WASM: Minerals, Energy and Chemical Engineering

Assessment of Fluid Transport Mechanisms in Shale Gas Reservoirs

Maria Nadia Testamanti

This thesis is presented for the Degree of
Doctor of Philosophy
of
Curtin University

November 2018

Declarations

To the best of my knowledge and belief this thesis contains no material previously published by any other person except where due acknowledgement has been made.

This thesis contains no material which has been accepted for the award of any other degree or diploma in any university.

Signature: .....

Date: .....

Abstract

Despite the numerous advances in oilfield and laboratory technologies over the past two decades, the assessment of pore scale phenomena in shale reservoirs remains a challenge. The evaluation of pore structure and flow properties from shale core analysis can be particularly difficult, owing to the abundance of nanoscale pore sizes and low permeability. A better understanding of the pore systems and gas transport mechanisms will lead to more representative shale reservoir models, and ultimately to better developmental and business decisions. In this thesis, pore structure and matrix permeability are characterised from experimental studies on shales, aiming to elucidate the complex interplay between the physical and flow properties. A combination of laboratory techniques have been applied in this research, on two shale sample sets from the Carynginia and Goldwyer formations, in Western Australia. The shale pore systems are characterised by the mercury intrusion porosimetry (MICP), low pressure nitrogen (LP-N_2) and carbon dioxide (LP-CO_2) adsorption methods, while matrix permeability are determined from quasi steady-measurements. In addition, nuclear magnetic resonance (NMR) serves as the principal probing tool linking pore structure and permeability data, to evaluate its potential for the petrophysical characterisation of shales.

The challenges in the signal acquisition, data inversion and interpretation of results from one-dimensional NMR experiments are examined, and guidelines more suitable for shale applications are proposed. An optimised methodology for the estimation of free and bound pore volumes (FFI, BVI) from transverse relaxation experiments (T_2) are developed, based on the experimental and analytical determination of two threshold cut-offs. A good agreement is observed between the $T_{2\ \text{cut-off}}$ identified by both approaches and also consistent with findings from 2D–NMR measurements, which show that the threshold cut-offs delimit distinct proton populations.

The associations between pore structure, fluid types and mineralogy in shales are characterised from LP-CO_2 and LP-N_2 adsorption, 1D– and 2D–NMR and MICP tests. The particular compositional controls on specific surface area are different in each sample set, but generally associated with organic richness, total clay and relative illite+smectite content. A possible correlation also emerges between the FFI/BVI after applying the $T_{2\ \text{cut-off}}$, characteristic pore sizes from MICP and N_2 tests, and compositional data.

The interrelationships between matrix permeability and its evolution, pore structure and composition are investigated, based on gas permeability tests on core samples from the Goldywer Formation. Non-linearity is observed in Klinkenberg plots at low pore pressures, presumably related to the substantial rarefaction effects arising from the particular experimental conditions of this study. Gas permeability results are analysed based on existing flow models, and a new second order model is then proposed. The simultaneous poroelastic and gas slippage mechanisms are incorporated into this second order flow model, which yields a good adjustment with the experimental data. Pore structure and permeability data are finally integrated and contrasted with NMR results and shale composition, to evaluate their impact on gas transport properties and their evolution. Model parameters related to gas slippage appear to be more sensitive to characteristic pore sizes, whereas poroelastic behaviour appears to be linked with sample composition. This study also shows that there is potential to use the NMR technique for the estimation of fluid dynamic effects. Some counter-intuitive results are obtained by the application of the new second order slip flow model, so more research is still needed.

Acknowledgements

This PhD journey has been a truly life-changing experience for me. The write-up of this thesis has been the most arduous task I have ever undertaken and it would not have been possible without the support of many people – my thanks and appreciation to all of them for helping me get here.

I would like to express my sincere gratitude to my supervisor, Prof. Reza Rezaee for supporting my transition from MPhil to PhD student and his continuous encouragement. Thank you for entrusting me with the intellectual freedom to explore so many different ideas and pursue independent work, and for the reassurance during tough times. The academic and professional skills learned under his guidance will undoubtedly stay with me throughout my career. I would also like to thank my co-supervisor, Assoc. Prof. Ali Saeedi, for his early guidance with planning and conducting laboratory experiments. I am very grateful to all the support staff and faculty of the former Department of Petroleum Engineering for their help through my doctoral studies.

Special thanks to our former technical officer Bob Webb for his efforts in ensuring the safety of laboratory procedures and for helping to keep my long experiments undisturbed. Thanks should also go to Finder Energy and the Western Australian Department of Mines, Industry Regulation and Safety for providing the core samples used in this thesis (Approval Nos. G32825 & N00413). Much gratitude goes to Derek Winchester and Shane Kager from CSIRO, for trimming the shale samples used in this study. Thanks to Yujie Yuan and Dawei Pan for their assistance with the collection of some of my earliest nuclear magnetic resonance data. I gratefully acknowledge the help of Christopher Wong in developing some of the Matlab code that was used early on in this research. To Jie Zou, thank you for preparing the powdered samples used in some of my laboratory tests. Thanks to Lukman Johnson for running the Rock-Eval tests and providing the geochemical composition data for most of the samples used in this research. Many thanks to Pooya Hadian for acquiring and interpreting most of the XRD data presented in this thesis, sometimes at very short notice. I also acknowledge the technical officers in the chemical engineering laboratories, for providing access to specialised instruments and training for conducting adsorption studies. Part of this work was undertaken using XRD instrumentation (ARC LE170100199) at the John de Laeter Centre, Curtin University. This research was financially

supported by an Australian Government Research Training Program (RTP) and a Curtin Research Scholarship (CRS).

Many thanks to Andrew Lockwood for providing insightful feedback on earlier versions of Chapters 2 and 3, and for introducing me to the fascinating world of data science during my internship with Woodside Energy. I also thank Prof. Victor Calo for his timely help with valuable resources that helped me kick-start the writing of this thesis. I am grateful to the petroleum engineering faculty at Instituto Tecnologico de Buenos Aires, my undergraduate alma mater, who laid the foundations that ultimately made this PhD possible. A very special thanks to Juan Rosbaco and Ruben Caligari for valuable advice that led me to pursue further studies.

Much gratitude goes to all my former and current colleagues at the Unconventional Gas Research Group, especially: Yujie, Hongyan, Lukman, Jie, Pooya, Kai and Faranak, who have offered their support and friendship throughout this PhD. I would also like to extend my gratitude to the rest of the fellow PhD students, particularly Farjana and Mohsen for their continuous moral support. To Eghan, thanks for the infinite supply of cat pictures.

Special thanks to my Argentinian friends in Perth for the dinners, texts and laughs. To my friends back home and scattered around the world, thank you for your thoughts, well-wishes, and long-distance support over these past four years. To my beloved cats, thanks for making the task of writing this thesis a more enjoyable exercise.

I am deeply grateful to my mum Mabel Bilardo, my dad Miguel Testamanti, and my sister Eugenia, for always encouraging me in the pursuit of my educational endeavours. You were there during my earliest successes and failures, and inspired me to follow my dreams. I especially thank my parents for all their sacrifices and for teaching me the value of hard work: I would not be here without your efforts.

There are no words to convey how truly grateful I am to my dear husband, Martin Saura, for his unconditional support. He has been my best friend, my soul-mate, my lifeline: this work would not have been possible without you. After seeing me through the ups and downs of my personal, professional and academic life, your unrelenting faith in me has motivated me to strive tirelessly to achieve this milestone. Martin has shared every step of this amazing journey with me, and I dedicate this thesis to him.

"Basic research is what I'm doing when I don't know what I'm doing"

- Wernher von Braun

Table of Contents

[1]This section includes material from: Testamanti and Rezaee, 2019.

List of Figures

List of Tables

Acronyms

*e*PSD	*Equivalent* Pore Size Distribution
*e*SSA	*Equivalent* Specific Surface Area
CBW	Clay Bound Water
CPMG	Carr-Purcell-Meiboom-Gill
IUPAC	International Union of Pure and Applied Chemistry
LP-CO_2	Low-pressure Carbon Dioxide
LP-N_2	Low-pressure Nitrogen
MICP	Mercury Intrusion Porosimetry
NMR	Nuclear Magnetic Resonance
OM	Organic Matter
RMSE	Root Mean-Squared Error
SC	Sample Set Carynginia
SG	Sample Set Goldwyer
SNR	Signal-to-Noise Ratio
TOC	Total Organic Carbon

Symbols

α_p	Permeability Sensitivity to Effective Stress
A	Cross-sectional Area
b	Gas Slippage Coefficient
β_p	Slippage Sensitivity to Effective Stress
c	Dimensionless Adzumi Constant
d	Pore Diameter
δ	Kinetic Diameter of Gas Molecule
ℓ	Characteristic Pore Length
γ	Surface Tension
k	Permeability
k_B	Boltzmann Constant
k_g	Apparent Gas Permeability

k_∞ . . . . . .Klinkenberg-Corrected Permeability

k_L . . . . . .Extrapolated Permeability ($\sigma_{\text{eff},L}$)

$\mathrm{K_n}$ . . . . . .Knudsen Number

λ . . . . . .Gas Mean Free Path

L . . . . . .Sample Thickness

M . . . . . .Gas Molar Mass

μ . . . . . .Viscosity

P_{atm} . . . . . .Atmospheric Pressure

P_c . . . . . .Capillary Pressure

P_{conf} . . . . . .Confining Pressure

P_{down} . . . . . .Downstream Pressure

ϕ . . . . . .Porosity

P_p . . . . . .Mean Pore Pressure

P_{up} . . . . . .Upstream Pressure

Q_g . . . . . .Gas Flow Rate

R . . . . . .Universal Gas Constant

r . . . . . .Pore Radius

ρ_B . . . . . .Bulk Density

ρ_G . . . . . .Grain Density

σ_{eff} . . . . . .Effective Stress

T . . . . . .Temperature

$\mathrm{T_1}$ . . . . . .Longitudinal Relaxation

$\mathrm{T_2}$ . . . . . .Transverse Relaxation

t_C . . . . . .Characteristic Time

Θ . . . . . .Contact Angle

Θ_1 . . . . . .First Order Slip Coefficient

Θ_2 . . . . . .Second Order Slip Coefficient

w . . . . . .Pore Width

X . . . . . .Effective Stress Coefficient

z . . . . . .Gas Compressibility Factor

CHAPTER 1

Introduction

Natural gas is a key component of the global primary energy matrix. The World Energy Council (2016) reported that natural gas had "the potential to play a critical role in the grand transition to an affordable and environmentally sustainable energy future", with global policy-makers supporting its use as a "cleaner source of energy for power, transportation, residential, and industry purposes". The global quest for cleaner energy sources has progressively pushed the frontiers of resources exploration, with unconventional gas reservoirs becoming increasingly important in the face of dwindling conventional reserves. Conventional resources occur as discrete accumulations that are part of a larger petroleum system, where oil and gas is trapped by buoyancy within rocks that act exclusively as reservoirs. Hydrocarbons stored in these porous and permeable formations can hence be extracted by reasonably standard production methods. In contrast, unconventional resources exist as continuous accumulations over a large area, as a result of significantly different trapping mechanisms. Commercial production of hydrocarbons from unconventional reservoirs therefore requires the use of more specialized extraction techniques and important investments. Coal, shale and tight sandstone formations with potentially commercial volumes of hydrocarbon all fall under the unconventional reservoir category. Within a given petroleum system, shales may act as both source and trap and are thus also described as "self-sourcing reservoirs".

Shales have been traditionally studied for their importance as source rocks in petroleum systems. Shale pores were generally assumed to store only immobile water (Truman et al., 1989), with no potential to hold significant volumes of free gas due to their low effective porosity and permeability (Luffel, 1993). Despite this common belief, the success of several commercial shale plays over the past decade, aided by technological advances and favourable market conditions, has led to a renewed interest in these rocks for their potential as unconventional reservoirs. Although shales have been the subject of numerous research studies in recent years, much uncertainty still exists as to their petrophysical properties, owing to the difficulties in measuring the extremely small pore sizes and low permeabilities (both in the nanoscale). Understanding the pore systems and fluid

transport mechanisms in shales will lead to more representative reservoir models, which are crucial to improve the accuracy of reserves estimates and production forecasts, and ultimately make better development and business decisions. In this research work, experimental studies are carried out to characterise the pore structure and matrix permeability of shales, aiming to cast some light on the interplay between their physical and flow properties.

1.1. Terminology

Shale is a term frequently found in the literature, but no universal consensus has been reached to date on what it constitutes. There is a degree of ambiguity and inconsistency around the terminology utilised to define shales and their petrophysical properties, with various expressions representing the same property -and vice versa- depending on the context. The terminology that will be used throughout this thesis is explained in the below.

Pore Systems

A pore is defined as a "small interstice or open space" in the porous media that generally admits "the passage or adsorption of liquid or gas" (Stokes and Varnes, 1955). The summation of all the pore spaces constitutes the pore system (or pore volume) of sedimentary rocks, a crucial parameter for estimating potential hydrocarbon accumulations that can be quantified if the size and shape of the pores present is known. However, a precise description of pore sizes is generally complicated by the highly irregular nature of pore shapes found in reservoir rocks and requires the use of reference model systems. The characterization of pore structures based on models with well-defined geometrical shapes (e.g. cylinders, slits, prisms, etc.) can lead to interpretation errors when different systems are compared, so pore sizes should be carefully defined to remain consistent for any reference model used. The IUPAC recommends the use of pore width as a measure of size (Rouquerol et al., 1994), by defining an equivalent cylindrical pore diameter that can be classified into the following categories:

- Micropores for sizes narrower than 2 nm
- Mesopores for sizes between 2–50 nm
- Macropores for sizes wider than 50 nm

In this thesis, the definition of pore size (and corresponding classification) suggested by the IUPAC will be used, where size represents the equivalent diameter for a cylindrical-shaped pore.

Shales

Shales, mudrocks and mudstones are broad terms widely used by the petroleum industry to refer to fine-grained sedimentary rocks, yet the exact meaning of each of these words is not always evident. The diversity of definitions appears to originate from the nomenclature problem created by the dual connotation of particle size (texture) and mineralogy in the term clay, and is further complicated by the lack of universal classification scales (Weaver, 1991). Most of the current grain size scales have their roots in the scheme originally proposed by Udden (1898) and later modified by Wentworth (1922), which classifies any sediment finer than 1/256 mm as clays, and as silts if mean sizes are in the 1/16–2 mm range. Based on the Uden-Wentworth scale and earlier work by Ingram (1953), Folk (1980) uses the term mudrocks to describe all terrigenous rocks with a silt and/or clay content above 50%, distinguishing shales, as fissile indurated rocks, from the non-fissile mudstone (sub-equal silt and clay content). Despite the lack of uniformity in the terminology used by early authors, there is a general agreement that the particular term chosen (mudstone/mudrock/shale) is not indicative of mineralogical composition (Neuendorf et al., 2011), and that fissility is a structural characteristic of shale rocks (Twenhofel, 1939; Ingram, 1953; McKee and Weir, 1953; Pettijohn, 1975; Folk, 1980; and many others).

Throughout this thesis, the term mudrock will be used for fine-grained sedimentary rocks composed of clay and/or silt-sized particles, independent of mineralogy, while the term shale will be restricted to mudrocks exhibiting fissility. In addition, the term gas shale will be used in its broadest sense to refer to any shale rock that may hold economic quantities of gas in place.

Organic Matter

The broad term sedimentary organic matter (OM) describes all the deposits derived from "skeletons or tissues of living organisms" (Stokes and Varnes, 1955). The OM dispersed in sedimentary rocks can be further classified based on its solubility properties when exposed to usual organic solvents (i.e. chloroform, benzene, among others). The fraction of sedimentary OM which is insoluble in organic solvents is commonly known as kerogen, while the soluble fraction is designated with the term bitumen (Durand, 1980). In this thesis, the expression organic matter represents the OM found in sedimentary rock, where their solubility properties cannot be specified.

Porosity

The American Geosciences Institute defines porosity (ϕ) as the fraction of "the bulk volume of a rock or soil that is occupied by interstices, whether isolated or connected" (Neuendorf et al., 2011). In porous media, this property is contingent on the particular technique used for its determination, as some porosimetry methods may only access the interconnected pores (e.g. fluid intrusion techniques), while others may also have the ability to detect closed or isolated pores (e.g. radiation techniques). To avoid confusion, the IUPAC recommends that the methods used for measuring both pore volume and apparent volume of the sample are included when reporting experimental results (Rouquerol et al., 1994). For the purpose of this thesis, the term porosity represents the summation of all the pore spaces that can be accessed with a given porosimetry technique, in porosity units.

It should be noted that clay minerals, abundant in shales, have an excess of negative ions on their surface that attract cations from nearby formation water. This phenomena leads to the creation of an adsorption water layer that can be described by the electrical double layer theory (Saarenketo, 1998), where the free flow of molecules is restricted. The concept of clay-bound water (CBW) will be herein used to describe the immovable water in the adsorption layer, where the bulk volume irreducible (BVI) represents the pore volumes occupied by any bound fluid. In addition, effective porosity may generally be defined as the fraction of "the total volume of a given mass of soil or rock that consists of interconnected interstices" (Neuendorf et al., 2011). Since the shale matrix can be constituted by large volumes of clay minerals, the concept of effective porosity will be used in this thesis to denote the difference between total porosity and the bulk volume irreducible. Effective porosity is therefore equivalent to the pore volumes occupied by producible fluids, herein referred to as free fluid index (FFI) when derived from nuclear magnetic resonance measurements (Timur, 1969; Coates et al., 1997; Coates et al., 1998).

Permeability

The permeability of a porous medium is defined as "a measure of the relative ease of fluid flow under unequal pressure" (Neuendorf et al., 2011). In this thesis, the term permeability denotes the ability of the shale matrix to transmit fluid. In addition, gas and apparent permeability are used interchangeably to describe the property determined from laboratory tests on shale core samples, using gas as the probing fluid. The intrinsic or absolute permeability of a medium refers to the magnitude that would be measured if the probing fluid was instead liquid or

if gas slippage effects were negligible, as will be explained further in Chapter 5.

The reader should bear in mind that the permeability enhancement associated with induced hydraulic fractures and other stimulation treatments will not be addressed in this research study.

1.2. Background and Motivation

Over the past decade, the commercial success of several shale plays have been the driving force behind the sharp rise of natural gas production in the United States, in what has since come to be known as the "Shale Revolution" (World Energy Council, 2016). As this wave started to spread around the world, exploration efforts in recent years have lead to the successful development of shale plays outside of North America and a renewed scientific interest in shales. Although extensive research has been carried out on sandstone and carbonate reservoir rocks, the study of petrophysical properties in shales – or mudrocks – has been traditionally overlooked by the petroleum industry, despite accounting for two thirds of all sedimentary rocks (Schieber and Zimmerle, 1998). Until recently, relatively few published studies had focused on the assessment of shale pore structure and flow properties outside the scope of evaluating their source and seal potential (Brace, 1980; Davies et al., 1991; Dewhurst et al., 1998; Katsube and Scromeda, 1991; Katsube et al., 1992; Luffel and Guidry, 1992; Luffel, 1993). Since the onset of the "Shale Revolution", however, the petrophysical properties of shales have been the subject of numerous research efforts, which aimed to understand the mechanisms by which gas was stored and produced in these tight rocks, that had such a complex pore structure and low matrix permeability (Bustin et al., 2008; Loucks et al., 2012; Ross and Bustin, 2009; Clarkson et al., 2011; Clarkson et al., 2016; Aguilera, 2014; Ambrose et al., 2010; Nelson, 2009; Sondergeld et al., 2010; Javadpour et al., 2007; Zhang et al., 2015; Civan, 2017; Rassouli et al., 2017; Heller et al., 2014; Tinni et al., 2018; Wang et al., 2016; Gensterblum et al., 2015; and many others). These recent studies have shed light into the particularities of gas storage and transport mechanisms in shales, however, the interrelationships between the various petrophysical aspects controlling them is poorly understood. Furthermore, the lack of standardised laboratory workflows remains an obstacle for obtaining representative results.

The shale matrix generally comprises a wide range of pore sizes, so a combination of experimental methods is required for the assessment of properties controlling their gas storage capacity (Bustin et al., 2008; Loucks et al., 2012). Figure 1.1 shows the porosimetry techniques commonly used in

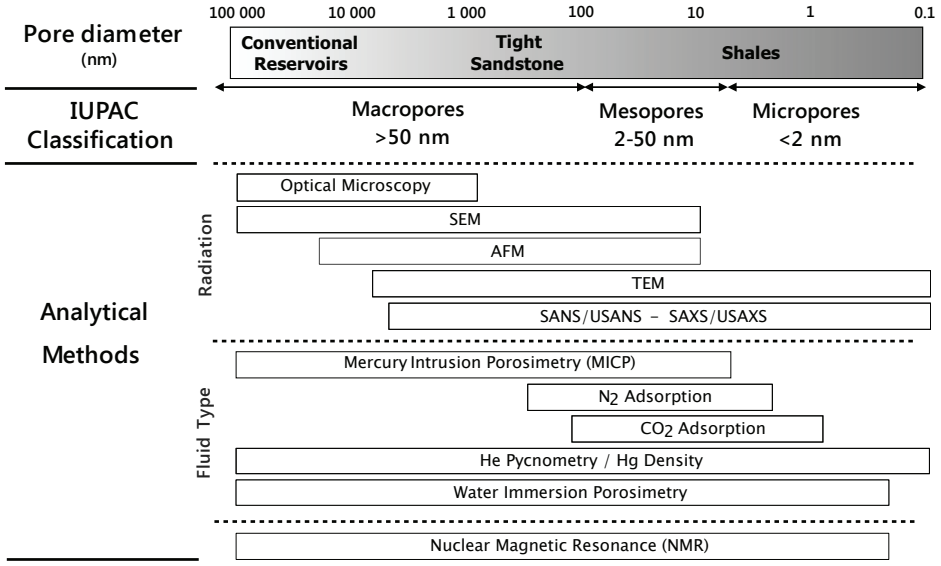

Figure 1.1. Core porosimetry methods and corresponding range of applicability (modified after Bustin et al. (2008)).

routine and special core analysis, as well as their pore size range of applicability. In this thesis, the pore systems of shale core samples have been characterised based on the mercury intrusion porosimetry (MICP), low pressure nitrogen (LP-N_2) and carbon dioxide (LP-CO_2) adsorption methods. In addition, nuclear magnetic resonance (NMR) has been utilised to study the distribution of pores sizes and fluid types in shales, allowing the indirect characterisation of their pore networks.

As a wireline logging tool, NMR is the only technique that can detect the reservoir fluid molecules directly. The estimation of porosity, pore size distribution and permeability from NMR logs is a well established practice in the petroleum industry (Dunn et al., 2002; Kenyon, 1997; Freedman, 2006; Prammer et al., 1996; Coates et al., 1997; Kleinberg, 1996), but its application in unconventional reservoirs is not straightforward. In shales, the complex pore network and mineralogy generally give rise to diffusion effects that would be otherwise negligible, creating additional difficulties in the acquisition and processing of NMR signal (Washburn, 2014; Saidian, 2015). Existing methodologies for the analysis of NMR data should consequently be revised and adapted for its use in shales, to avoid erroneous interpretations. Furthermore, the development of realistic shale reservoir models will necessarily require a good calibration between the well logging data and core analysis results. Notwithstanding the technological advances in recent years, the abundant nanoscale pores in the shale matrix give rise to unique challenges when

conducting tests on cores, hence the laboratory characterisation of pore systems and gas transport properties remains problematic. The optimisation of experimental methodologies will be paramount to reducing uncertainties in the assessment of pore structure and permeability, and therefore to estimating these petrophysical properties from NMR logs in shales eventually.

Due to the abundance of nanoscale pores, shales are less permeable to hydrocarbon flow than conventional reservoirs and the dominant gas transport mechanisms can also be significantly different . Significant investments are hence required for developing unconventional plays and the shale matrix permeability plays a pivotal role in determining their viability. In wells targeting shale gas reservoirs, the high initial production rates are possible thanks to extensive hydraulic fractures that release the free gas stored in the largest pores and natural microfractures. The gas originally adsorbed to the pore walls will desorb as the reservoir pressure declines, diffusing through the shale matrix and into the higher permeability channels. The stable gas flow rates that are commonly observed in shale reservoirs at later stages will be determined by the matrix permeability, as well as its behaviour under changing effective stresses. Whilst the gas transport mechanisms in shales have been the focus of a considerable amount of research in recent years, relatively few experimental studies have been published owing to the challenges in measuring such low permeabilities (Kang et al., 2011; Ghanizadeh et al., 2014; Zamirian et al., 2014; Heller et al., 2014; Letham and Bustin, 2016; Moghaddam and Jamiolahmady, 2016; Fink et al., 2017; Shen et al., 2018). The nanoscale pore sizes in shales, coupled with the heterogeneity in both mineralogy and texture, restrict the application of conventional core analysis workflows. These factors, along with the high level of uncertainty commonly associated with experimental results from shale core analysis, have been the main drivers of this research. The assessment of shale matrix permeability in the laboratory is no trivial task, especially due to the limited number of suitable core analysis techniques that do not require the use of high pore pressures Figure 1.2. Furthermore, the evaluation of experimental results generally requires more advanced flow models that can account for the simultaneous gas transport and poroelastic mechanisms, characteristic of shale reservoirs. In this thesis, permeability has been determined from quasi steady-measurements on shale cores and experimental results have been interpreted based on a modified gas flow model, considering the superposition of both poroelastic and fluid dynamic effects. In addition, nuclear magnetic resonance is used as the principal probing tool linking pore structure and permeability core data, in an attempt to cast some light on its potential for the petrophysical characterisation of shales.

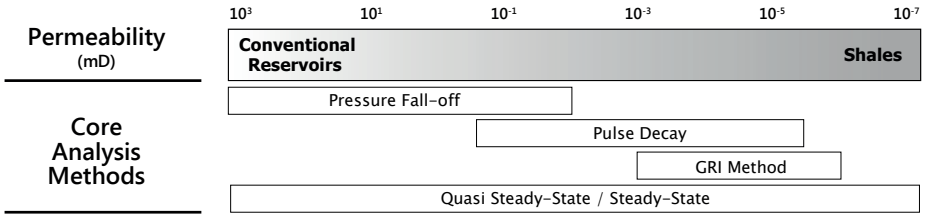

Figure 1.2. Core analysis techniques for permeability determination and corresponding range of applicability.

1.3. Research Objectives

This thesis aims to elucidate the interrelationships between pore structure, organic richness and mineralogy, matrix permeability, and how they may influence poroelastic behaviour. Whilst shales have been the subject of extensive research in recent years, no experimental study has been published to date which used an holistic approach to investigating these properties and their influence on gas storage and transport mechanisms. In particular, the following key objectives will be addressed in this research work:

1. **Optimisation of nuclear magnetic resonance methodologies for shale applications:** The challenges in the signal acquisition, data inversion and interpretation of results from one-dimensional NMR experiments are investigated, and guidelines more suitable for shale applications are proposed. A new methodology for the estimation of free and bound pore volumes from NMR measurements is introduced.

2. **Characterisation of pore structure and connectivity in shales:** Total and effective porosity, pore sizes, specific surface area and fluid types are determined from core analysis. Experimental results are contrasted and their connection to gas storage and flow mechanisms is explored. The relationships between pore structure, shale composition and NMR data are investigated.

3. **Experimental assessment of gas transport properties in shales:** Laboratory techniques are optimised for shale applications. Experimental permeability results are analysed based on two existing flow models, and a new second order model is proposed which incorporates both poroelastic and gas slippage effects. Pore structure and permeability data are integrated and contrasted with NMR results and shale composition, to evaluate their impact on gas transport properties and their evolution.

1.4. Thesis Outline

This thesis consists of six chapters, including this introductory chapter. Chapter 2 provides a description of the materials and methods used in subsequent chapters. Chapters 3 to 5 include the main results of this research study and corresponding discussions, each addressing one of the key objectives stated in the previous section. Finally, Chapter 6 summarises the conclusions from these chapters. The overall structure of the thesis is summarised below:

Chapter 1 provides the terminology used throughout this thesis and the context for the general research problem, and introduces the objectives addressed in subsequent chapters.

Chapter 2 describes the samples and provides a general overview of the experimental techniques used in this thesis. The relevant results from rock characterisation tests (XRD, Rock-Eval) and a summary of all the tests conducted are presented.

Chapter 3 focuses on the optimisation of the 1D–NMR technique for shale applications, exploring two sub-themes. First, a thorough assessment of the theoretical concepts and difficulties related to acquiring and processing 1D–T_2 signal in shales is presented, based upon both simulation and experimental NMR data. These insights provide the basis for the updated guidelines that are suggested for conducting 1D–NMR measurements on shales. The second part of the chapter presents a novel methodology for evaluating the FFI and BVI porosity fractions from relaxometry experiments, based on the determination of threshold cut-offs after saturating, centrifuging and oven-drying a set of shale core plugs. The experimental threshold cut-offs are then compared to coefficients identified by the analytical approach, proposed in the first part of the chapter.

Chapter 4 presents the experimental results from LP-CO_2 and LP-N_2 adsorption, 1D– T_2 and 2D–NMR T_1–T_2, and MICP tests on shale core samples. The pore structure, specific surface area and fluid types present in the pores are evaluated by the integration of results from different methods, and compared with compositional data. The potential implications of these findings on shale gas storage and flow properties, and the relationship to coefficients derived from the NMR methodologies proposed in Chapter 3 are discussed.

Chapter 5 presents the experimental results from quasi steady-state measurements on shale core discs and introduces a new modified flow model, adapted for the conditions of this study. Matrix permeability data is analysed following three distinct approaches: (i) a step-by-step method, accounting for poroelastic and slippage effects separately, (ii) a first order flow model, accounting for both poroelastic and slippage effects simultaneously, (iii) a newly proposed second order flow model, built upon the previous model and introducing a new term to account for the nonlinear effects observed in experimental results. The flow model parameters that were obtained based on this last approach, were then compared with compositional, porosimetry and NMR data, and their relationship to insights based on the methodology proposed in Chapter 3 is explored. The implications of these findings on the shale gas transport properties – and evolution under changing effective stresses – is finally discussed.

Chapter 6 summarizes the main findings of this research and provides concluding remarks.

1.5. List of Publications

From this thesis the following research outputs have been developed.

Published at, or Submitted to Peer Reviewed Journals

- **Testamanti, M. N.**, and Rezaee, R. (2019). Considerations for the Application of the NMR Technique in Shales. *Journal of Petroleum Science and Engineering*, *174*, 177–188.
- **Testamanti, M. N.**, and Rezaee, R. (2017). Determination of NMR $T_{2\,\text{cut-off}}$ for Clay Bound Water in Shales: A Case Study of Carynginia Formation, Perth Basin, Western Australia. *Journal of Petroleum Science and Engineering*, *149*, 497–503.

Conference Proceedings and Abstracts

- **Testamanti, M. N.**, Rezaee, R., Yuan, Y., and Pan, D. (2017). Determination of $T_{2\,\text{cut-off}}$ for Shale Reservoirs: A Case Study from the Carynginia Formation, Perth Basin, Western Australia. Extended abstract, *The APPEA Journal*, *57*, 664–668. Poster presentation at the APPEA Annual Conference and Exhibition, May 14–17, 2017, Perth, Western Australia.

- **Testamanti, M. N.**, Rezaee, R., and Zou, J. (2017). Porosity and Pore Size Distribution of Shales: A Case Study of the Carynginia Formation, Perth Basin, Western Australia. Extended abstract, The APPEA Journal, 57, 660–663. Presented at the APPEA Annual Conference and Exhibition, May 14–17, 2017, Perth, Western Australia.

- **Testamanti, M. N.**, Rezaee, R., and Wong, C. (2017). Gas Permeability Measurement of Shales Using the Quasi Steady-State Technique. Extended abstract, *The APPEA Journal*, *57*, 656–659. Presented at the APPEA Annual Conference and Exhibition, May 14–17, 2017, Perth, Western Australia.

- **Testamanti, N.**, Rezaee, R., and Saeedi, A. (2016). NMR $T_{2\text{ cut-off}}$ Determination for Shales. Poster presentation at *AAPG/SEG Annual International Conference and Exhibition*, 354–354, April 3–6, 2016, Barcelona, Spain.

In Preparation

- **Testamanti, M. N.**, and Rezaee, R. Experimental Assessment of Gas Transport Mechanisms in Shales.

- **Testamanti, M. N.**, and Rezaee, R. Characterization of Pore Structure and Fluid Types in Shales with the Carbon Dioxide and Nitrogen Gas Adsorption, Mercury Intrusion and Nuclear Magnetic Resonance Techniques.

Additional publications relevant to the thesis but not forming part of it

- Yuan, Y., Rezaee, R., Verrall, M., Hu, S. Y., Zou, J., and **Testamanti, N.** (2018). Pore Characterization and Clay Bound Water Assessment in Shale with a Combination of NMR and Low-Pressure Nitrogen Gas Adsorption. *International Journal of Coal Geology*, *194*, 11–21.

CHAPTER 2

Materials and Methods

Laboratory experiments to evaluate pore structure and gas flow capabilities in shales were conducted on twelve samples from the North Perth and Canning Basin, both located in Western Australia. All the samples studied can be categorised as marine-deposited shales, with variable mineralogy, clay content and geochemistry. This compositional variability facilitated the evaluation of its role as a control factor for fluid flow in shales. with an overview of the geological background and the sample selection process, before moving on to the details of the compositional characteristics for all the samples studied. Finally, the experimental techniques used throughout this thesis are briefly introduced.

2.1. Samples Description

The main chapters of this thesis include results from various petrophysical characterisation tests conducted on shale samples from the onshore Canning and North Perth Basin, both located in Western Australia (Figure 2.1). Samples from the Canning Basin were retrieved from the Ordovician Goldwyer Formation, while the North Perth samples belong to the Permian Carynginia Formation. In this section, a brief overview of both basins and geological setting of each shale formation is provided, along with a description of the mineralogical and geochemical composition of the samples used in this research study.

2.1.1. Geological Background and Selection of Samples

Goldwyer Formation (Canning Basin)

The intracratonic Canning Basin covers a total area of over 800,000 km^2, of which 730,000 km^2 are located onshore in northern Western Australia as indicated in Figure 2.1 (Geoscience Australia, 2018, July 14). Sediments of Paleozoic age are predominant in the onshore basin, where the depositional history spans the Early Ordovician to the Early Cretaceous (Figure 2.2a) over five major periods of sedimentation, each followed by an erosion period with or without tectonism (Towner and Gibons, 1983). Deposition of predominantly marine sediments in the Early Ordovician was initially prompted by a phase of

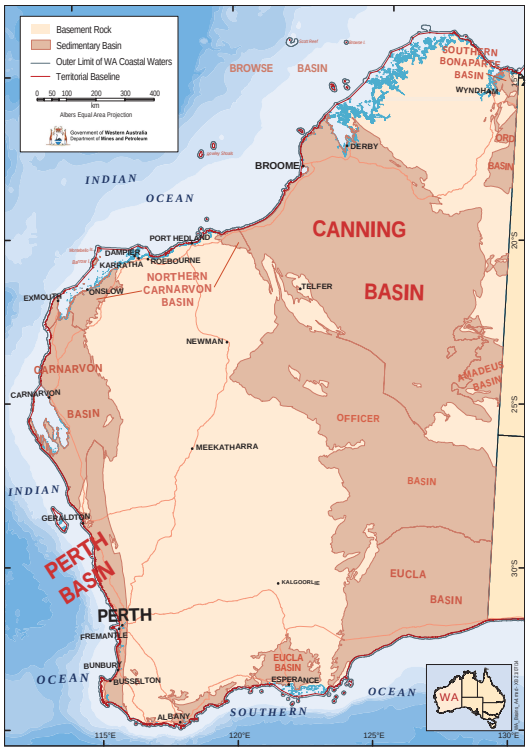

Figure 2.1 Map of sedimentary basins in Western Australia (modified from Western Australia Department of Mines and Petroleum, 2014)

extension and rapid subsidence. Ordovician sedimentary rocks include marine shales, overlain by extensive salt deposits of Late Ordovician to Silurian age. Thick carbonate reefs can be identified in the Devonian sequence, which was followed by erosion during the Carboniferous. Following the glaciation in the Early Permian, the final period of deposition included fluvio-deltaic and marine sediments during the Late Jurassic and Early Cretaceous. The offshore part of the basin contains younger sedimentary rocks, ranging from Permian to Early Cretaceous age (Western Australia Department of Mines and Petroleum, 2014). While exploration activity began in the early 1920s, this basin remains largely unexplored with less than four hundred wells drilled to date.

The onshore Canning basin has two major depocentres, trending in the north-westerly direction, separated by a mid-basin arch system. The northernmost includes the Fitzroy Trough and the Gregory Sub-basin, where rocks are predominantly of Paleozoic age with a thin section of Jurassic and younger sediments, and have an estimated thickness of up to 18,000 m (Yeates et al., 1984). The Kidson and Willara Sub-basins make up the southern major depocenter, which contains thinner sedimentary successions including claystone-limestone of Ordovician to Silurian age and Permo-Carboniferous non-marine clastic rocks (Towner and Gibons, 1983).

The Ordovician Goldwyer Formation has been identified as one of the source rocks in the onshore Canning Basin, with potential for significant unconventional resources. The Goldwyer Shale is predominantly comprised by mudstones and carbonates, deposited under reducing anoxic conditions. The uplifted sections of the Goldwyer Formations have been found to be oil prone, while deeper intervals are thought to be in the wet to dry gas window. The most organic-rich intervals are found across the upper member of the Goldwyer, while general TOC values are in the 1 to 5% range (Ghori and Haines, 2006). According to a report by the U.S. Energy Information Administration (2015), the Goldwyer Formation is estimated to hold about 235 Tcf of risked, technically recoverable shale gas, and nearly 10 billion barrels of condensate and shale oil.

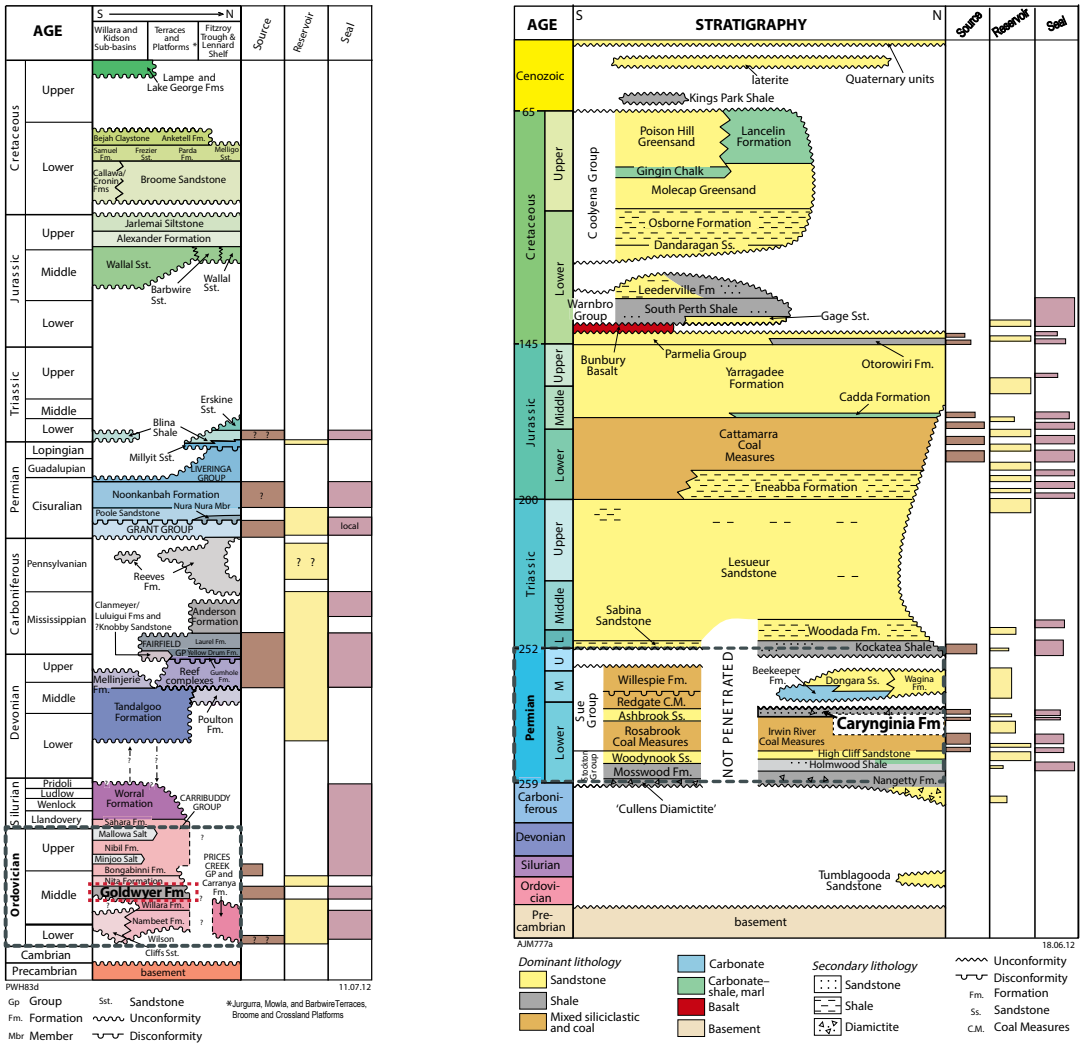

(a) Canning Basin **(b)** Perth Basin

Figure 2.2. Stratigraphic column and petroleum systems of the (a) onshore Canning Basin, and (b) onshore North Perth Basin (modified from Western Australia Department of Mines and Petroleum, 2014)

The core samples from the Goldwyer Formation used in this study were recovered from depths between 1300 and 1600 m within the same well, which was drilled to assess the unconventional hydrocarbon potential of the formation. Prior to sample selection, a visual inspection of all the core sections was conducted at the WA Core Library in late 2016. The samples were chosen to represent the different rock types and features identified, some of which are illustrated in Figure 2.3. Initially, vertical plugs of 1.5"–diameter and variable length were acquired from unpreserved cores. The samples were then re-trimmed at the CSIRO AARC laboratories in Perth, where each one was subdivided into three pieces. The cores were cut parallel to the bedding, using a specialised diamond wire cutting technique that avoids the use of lubrication fluid to prevent contamination. Two polished discs of similar thickness and a shorter core plug were obtained from each initial sample, with one of the discs being further sectioned into equal quarters. One of the quarter fragments was set aside for MICP tests, two were milled for other experiments and the remaining quarter was preserved. The same procedure was repeated for all the recovered Goldwyer shale samples that were used in this study.

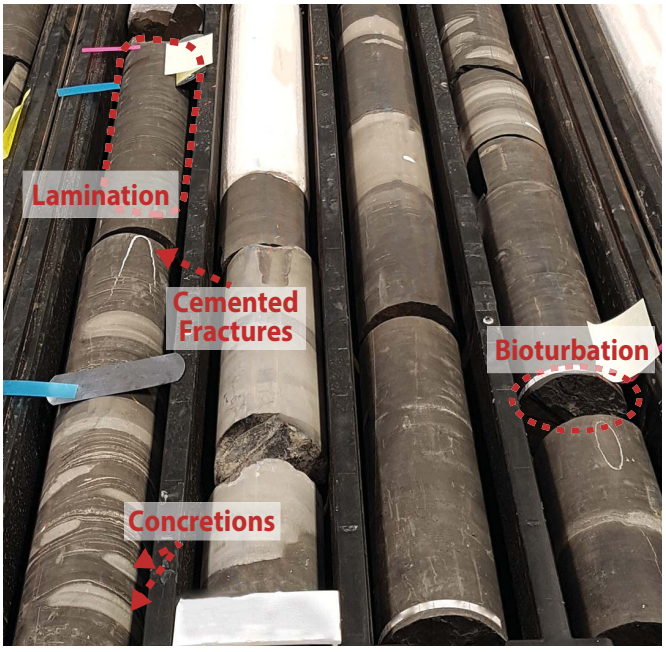

Figure 2.3. One of the core intervals inspected at the WA Core Library during the Goldwyer Formation sample selection process.

Carynginia Formation (Perth Basin)

The Perth Basin is a north-south trending sedimentary basin that covers a total area of over 170,000 km^2, half of which is found onshore in the southwest of Western Australia, as shown in Figure 2.1 (Geoscience Australia, 2018, July 14). It is bounded by the Darling Fault to the East, and extends offshore westerly to the edge of the continental crust (Hocking et al., 1994). The Perth Basin began forming during the break-up of Gondwana in the Permian, through the rifting of Australia and Greater India to the Cretaceous (Song and Cawood, 2000).

The onshore Perth Basin contains three north-trending depocentres with a maximum sediment thickness of 12,000 m, namely the Bunbury and Dandaragan troughs, and the Coolcalalaya Sub-basin (Hocking et al., 1994). Exploration activity in this basin began in the 1950s, and over three hundred and fifty wells have been drilled onshore to date. Despite exploration efforts, no commercial plays had been discovered in the onshore southern Perth Basin to 2014, while the northern portion of the basin contained 20 commercial oil and gas fields (Western Australia Department of Mines and Petroleum, 2014).

In the onshore northern Perth basin, the Dandaragan Trough covers the largest area, containing the deepest and thickest Permian to Cretaceous sedimentary succession (Mory and Iasky, 1994). Figure 2.2b shows some of the stratigraphic sections, which include argillaceous glacial-marine to deltaic rocks of Early Permian age (including the Carynginia Formation), Late Permian non-marine and shoreline siliciclastics to shelf carbonates, and non-marine to shallow marine siliciclastics of Triassic to Early Cretaceous age (Mory and Iasky, 1996). The onshore northern portion of Perth Basin contains the best prospects for unconventional resources, which could be hosting up to 32 Tcf of technically recoverable shale gas (U.S. Energy Information Administration, 2015).

The Permian Carynginia Formation has been signalled as one of the most prospective formations for shale gas exploration and production in the region. The Carynginia Shale is conformed by black to grey micaceous shale with interbedded sandstone and siltstone, deposited in a shallow marine environment. The average TOC content reported in the literature for this formation is 4%, which is found in the dry gas window over most of the onshore northern Perth Basin (U.S. Energy Information Administration, 2015). The U.S. Energy Information Administration (2015) report estimates that the Carynginia Shale could hold up to 25 Tcf of risked, technically recoverable shale gas reserves.

The Carynginia shale samples used in this thesis were recovered from an exploration well targeting unconventional gas resources, belonging to depths in

the 2780 to 2830 m range. The rock fragments and core plugs were readily available in the Department of Petroleum Engineering at Curtin University, but were originally sampled from unpreserved core stored at the WA Core Library. Some portions of the analysis presented in this thesis are based on raw experimental data originally reported by Al Hinai (2014) and Labani (2014), as will be specified in the relevant chapters. Whenever known, the particular sample preparation method before laboratory tests will also be explained.

2.1.2. Mineralogical and Geochemical Composition

Twelve core samples were used in this research study: six of them from the Carynginia and the remaining six from the Goldwyer Formation. Throughout this thesis, the two sample sets will sometimes be referred to as *SC* (Sample Set Carynginia) and *SG* (Sample Set Goldwyer) to avoid wordiness.

Mineralogical Characterisation

The mineralogical composition of shales was studied with the X-ray diffraction (XRD) technique. Laboratory tests were conducted on powdered samples at the John de Laeter Centre, in Curtin University. The quantitative characterisation of the mineral phases present was done on-site with the TOPAS software (Bruker). Detailed results from XRD analysis can be found in Table 2.1 and Table 2.2. Furthermore, XRD data was used to calculate normalised mineralogy to silicates, carbonates and clays for all the samples, which was then plotted onto a ternary diagram (Figure 2.4).

Shales deposited in marine environments tend to be rich in brittle minerals such as quartz, feldspars and carbonates, with relatively lower clay content, making them good candidates for hydraulic stimulation (De Silva et al., 2015). In contrast, lacustrine shale deposits often respond poorly to hydraulic stimulation, owing to the abundance of mud that increases their ductility (Katz and Lin, 2014). It should be noted that all the shale samples analysed in this thesis are from marine origin. Quartz/feldspars and clays were found to dominate the mineralogy across both sample sets, although the Carynginia shale samples presented a lower clay content (46–56%) than those from the Goldwyer Formation (56–70%). The ternary plot also suggests that the samples studied might have a mineralogy similar to other successful shale plays in the United Stated, such as the Marcellus Formation and the Pronghorn Member of the Bakken Shale. In addition, pyrite was identified in all the samples studied, which can indicate anoxic conditions during sedimentation (Slatt, 2013), favourable for the preservation of OM.

Beyond the total volume of clays, the type of clays present in the shale matrix can significantly impact their storage potential, as well as their response to stimulation treatments and future production performance. Smectite, typically associated with swelling behaviour and low thermal maturity rocks, was unsurprisingly only found in very small quantities in some of the Carynginia samples (below 2 %), and was absent in cores from the Goldwyer set. Similarly, kaolinite was present in only limited quantities in both groups, which is to be expected in Paleozoic shale formations or deep deposits (Weaver, 1991). The most abundant clay types identified in the SC group were mixed-layer illite/smectite followed by illite/mica, which was also found to be dominant in the SG samples.

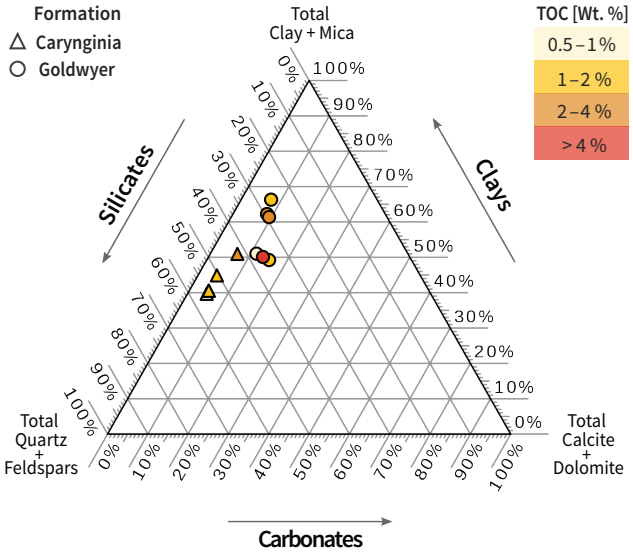

Figure 2.4. Compositional characterization of samples from the Carynginia and Goldwyer Formation. Mineralogical composition obtained from XRD tests; geochemical composition obtained from Rock-Eval pyrolisis.

Geochemical Characterisation

Geochemical analysis was completed based on the Rock-Eval methodology. During Rock-Eval pyrolysis, the rock sample is progressively heated in an inert atmosphere and the amount of hydrocarbons volatilised are measured using a flame ionisation detector (FID). The first peak observed in the FID pyrogram corresponds to S1, which represents the free hydrocarbons present in the sample as-received. The second peak detected is S2, which measures the amount of hydrocarbons formed during the thermal pyrolysis of kerogen present in the

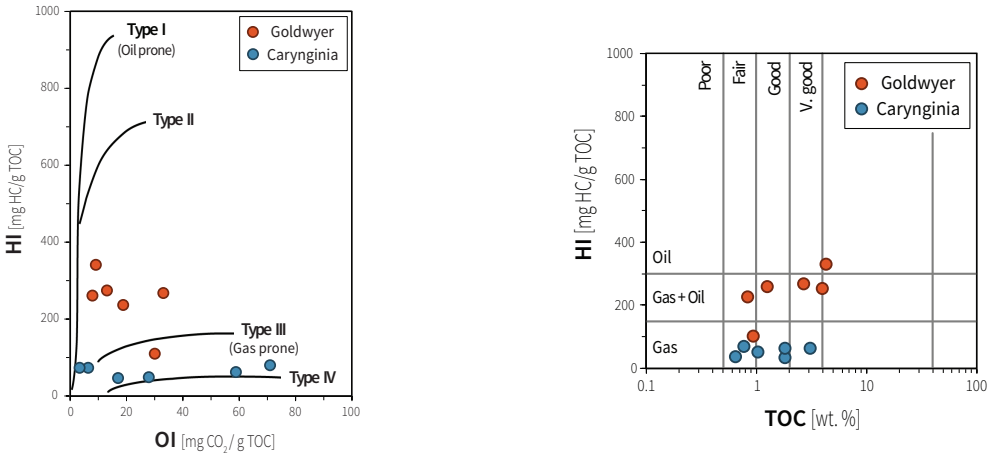

(a) **(b)**

Figure 2.5. (a) Modified Van Krevelen diagram showing the kerogen types; (b) TOC versus HI analysis to evaluate potential for hydrocarbon generation for the samples studied. The quantitative data can be found in Tables 2.1 and 2.2.

sample. The temperature at which the S2 peak occurs is also recorded as T_{max}, often used for evaluating the maturation levels of organic shales. The final peak recorded, S3, corresponds to the volume of CO_2 generated. The TOC represents the total organic carbon as wt.% of the rock sample, and is calculated as a function of S1 and S2. The source rock quality and kerogen type can be evaluated based on the Hydrogen (HI = S2/TOC) and Oxygen Index (OI = S3/TOC), while the Production Index (PI = S1/(S1+S2)) can be used to infer maturity. More information on the Rock-Eval technique can be found in Lafargue et al. (1998) and the references therein cited.

Tests were carried out on powdered samples with the Vinci Rock-Eval 6 apparatus located in the Department of Petroleum Engineering at Curtin University, and the Rocksix software (Vinci) was used for the quantitative analysis. The detailed results from Rock-Eval pyrolisis can be found in Table 2.1 and Table 2.2. The TOC of the Goldwyer samples range between 0.8–4.3 wt.%, whereas the Carynginia group has values from 0.6 to 3 wt.%. The average TOC is higher for the SG shales (2.3 wt.%), compared to the SC samples (1.5 wt.%) which, incidentally, is lower than the average TOC reported in the literature for the Carynginia Formation (U.S. Energy Information Administration, 2015). The Rock-Eval HI, OI and PI values collectively indicate that the OM is thermally mature for both SC and SG samples.

The modified Van Krevelen diagram of OI and HI values (Figure 2.5a) suggests a kerogen type III (gas-prone source rock) for all the SC samples as well as the deepest one from the SG group, while a kerogen type II (oil + gas/condensate

prone) is identified for the remaining SG samples. These kerogen classes (II/III) are consistent with shales of marine origin, in contrast with types I and IV which are associated with inert (over-mature) and lacustrine shales, respectively (Slatt, 2013). These initial interpretations are also supported by the comparison of TOC versus HI (Figure 2.5b), where the deepest SG and all six SC samples are again found in the gas generating region. As for the rest of the SG group, the most shallow sample appears in the oil generating region, whereas the four remaining are estimated to be in the condensate window.

Figure 2.6 shows the compositional associations for the two sample sets used in this thesis. The TOC of the SC samples shows a direct correlation with total clay content (left) and inverse with the quartz–feldspars abundance (right). Furthermore, the SC shales show a positive relationship – albeit weaker – between TOC and the sum of illite and smectite clay minerals (middle). The associations between geochemical and mineralogical composition are not as evident in the SG set, although a general positive trend is identified between TOC and silicates content (right). No clear relationships emerge from the comparison of TOC of the SG samples with total clay (left) and illite+smectite (middle) abundance. The dispersion observed in the Goldwyer graphs may be explained by the wider range of depths at which cores were retrieved (Table 2.3), with the six SG samples spanning ∼200 m, compared to the 45 m interval in the Carynginia set. The SG shales may thus have been subjected to considerably different depositional and diagenetic processes which would undoubtedly also affect the brittleness of the rock, yet a discussion of the particular mechanisms involved is beyond the scope of this thesis.

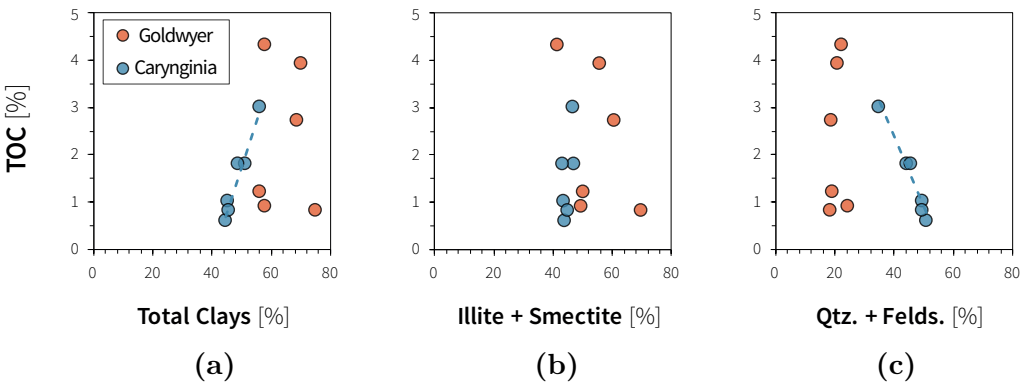

Figure 2.6. Compositional associations for the shale samples studied, comparing TOC with (a) total clay content; (b) sum of illite + smectite; (c) sum of quartz + feldspars.

2.2. Experimental Methods

This section gives a brief overview of all the experimental methods used in this thesis, for the assessment of pore structure and flow capabilities on the shale samples previously presented.

2.2.1. Nuclear Magnetic Resonance

All laboratory Nuclear Magnetic Resonance (NMR) experiments were carried out on a low field Magritek bench-top Rock Core Analyzer, located in the Department of Petroleum Engineering at Curtin University (Figure 2.7). The instrument probe can accommodate cylindrical core samples with a maximum diameter of 1" and 1.5", using the P29 probe and the P54 probe, respectively. The magnet operates at a stable temperature of 30°C and atmospheric pressure, with a frequency of approximately 2 MHz.

The T_2 decays were measured using the Carr–Purcel–Meiboom–Gill CPMG pulse sequence (Carr and Purcell, 1954; Meiboom and Gill, 1958). The instrument allows a minimum CPMG echo-spacing of 40 µs (P29 RF probe) or 100 µs (P54 RF probe), under certain conditions. Before the samples were placed inside the magnet, they were tightly wrapped with a plastic film to prevent water evaporation and moisture absorption. The plastic wrap, Teflon probe and other parts of the instrument can contain small amounts of nuclei and may generate signals detectable during NMR measurements. This background noise was consequently obtained and subtracted from the signal measured in all cores, before its inversion. The inversion module in the Prospa software (Magritek) and a number of Matlab routines –purposely developed or adapted– were employed for the computation of T_2 distributions. The particularities of the NMR technique and the experimental methods used in this thesis will be expanded in Chapter 3.

Figure 2.7 NMR spectrometer used in this study.

2.2.2. Mercury Injection Porosimetry

The Mercury Injection Porosimetry (MICP) data for the six samples from the Carynginia Formation were previously reported by Al Hinai (2014), however, the exact methodologies utilised for sample preparation and data corrections performed were not known at the time of writing this thesis. Therefore, the analysis and results herein reported for the Carynginia shale samples have been obtained using only the raw data from previous MICP tests.

In the case of samples from the Goldwyer Formation, MICP experiments were performed commercially by the Particle & Surface Sciences Laboratory in Sydney, NSW. Prior to MICP tests, the shale core samples were cleaned by Soxhlet extraction. Before they can be considered as effectively clean, this cleaning technique requires several cycles of a distillation-extraction-reflux process applied to the rock samples, using both polar and non-polar solvents whenever hydrocarbons are present. A methanol/toluene azeotropic mixture, with a boiling point around 64°C, was used as solvent to minimize clay damage due to high temperature in the Soxhlet chamber containing the Goldwyer shale fragments. In addition, PTFE boiling chips were introduced in the Soxhlet flask –along with the solvent– to promote the formation of bubbles, which effectively reduces the temperature required to reach the solvent boiling point. After the Soxhlet cleaning process, the core chips were oven-dried under vacuum pressure to evaporate solvent residue.

All MICP experimental results presented in this thesis were acquired with a maximum injection pressure of 60,000 psia, which allows mercury to intrude pore sizes in the 3–3×10^{-5} nm range. MICP tests were performed on a Micromeritics Autopore IV 9500™ in all cases. The raw MICP results were initially corrected and then analysed with the Micromeritics MicroActive software to derive pore structure information. The theoretical background of this technique, along with the assumptions and methodologies utilised for obtaining the results reported in this thesis will be discussed in more detail in Chapter 4.

2.2.3. Low Pressure Gas Adsorption

The micro– (pore sizes <2 nm) and mesopores (pore sizes 2–50 nm) were studied using the Low-Pressure Nitrogen (LP-N_2) and Carbon Dioxide (LP-CO_2) Adsorption techniques. Experiments were performed on the Micromeritics instruments TriStar II (N_2) and TriStar II Plus (CO_2), both located in the Department of Chemical Engineering at Curtin University (Figure 2.8a). The Micromeritics MicroActive software was used for the analysis of laboratory results.

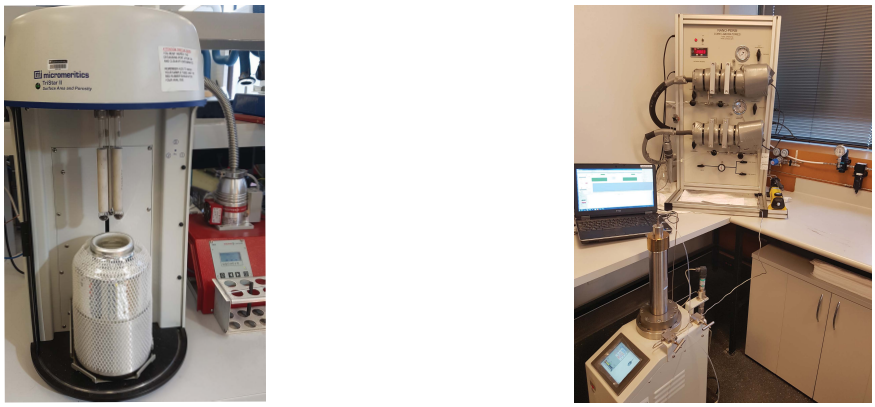

(a) (b)

Figure 2.8. Laboratory instruments used in this thesis for the measurement of shale properties: (a) Micromeritics TriStar instrument for low-pressure adsorption and desorption tests; (b) Nanopermeater for gas permeability tests.

The use of large core fragments in gas adsorption and desorption experiments can lead to unreliable results (Kuila, 2013), therefore all the tests performed in this study have been conducted on crushed rock samples. A homogenisation protocol was used for preventing sampling bias, following the particle size recommendations made by Labani (2014), with the ultimate goal of obtaining representative samples and results. The rock fragments were initially crushed using a mortar and pestle. A 60 mesh sieve was then used to separate the fraction of crushed rock with particle sizes < 250 µm. The process was repeated for the portion of rock fragments that could not pass through the sieve, until all the rock sample had been pulverised into the desired particle size. The samples were not subjected to any cleaning process to avoid extracting the organic matter, which would have altered further the original properties of the rock. Prior to analysis, gas impurities and moisture were removed from the samples utilising a Micromeritics VacPrep degassing station. The theory behind gas adsorption tests, procedures and methodology for converting isotherm curves into pore structure information will be explained further in Chapter 4.

2.2.4. Gas Permeability Measurements

Apparent gas permeability (k_g) can generally be obtained from tests where gas is axially injected through a cylindrical core sample (American Petroleum Institute, 1998). Under stationary and isothermal conditions, if the gas flow rate is low enough compared with the characteristic length of the porous sample studied, the Reynolds number and inertial effects will be minimised. Such system will be governed by Stokes Law, and thus permeability k_g may be calculated based

on the equation for gas derived from Darcy's law (Darcy, 1856):

$$k_g = \frac{2\mu P_r q_r z_m}{z_r G_f (P_1^2 - P_2^2)} \tag{2.1}$$

where the subindices *r*, *1*, *2* indicate the reference, upstream and downstream systems correspondingly, μ represents the gas viscosity, P is the measured pressure, q is gas flow rate and z_m/z_r is the ratio of gas deviation factor calculated at the mean pore pressure and the absolute reference pressure.

The gas permeability data presented in this thesis was determined for cylindrical shale core samples, based on the quasi steady-state technique proposed by Jannot and Lasseux (2012). In this method, the sample is placed inside a core holder that is connected to an upstream and downstream reservoir. The upstream reservoir is kept at a constant pressure, whereas a small differential pressure is applied at the core holder outlet, from which gas flow and in turn permeability is determined. The differential pressure applied and downstream reservoir volume are much smaller in magnitude than the corresponding upstream pressure and reservoir; so after certain conditions are met, the system can be considered to be quasi stationary. When a system meets the conditions for quasi steady-state flow and inertial effects are considered to be negligible, gas permeability k_g may also be calculated from Equation (2.1).

Quasi steady-state experiments were carried out to determine gas permeability on the shale samples previousy described. All tests were conducted in the Department of Petroleum Engineering laboratories at Curtin University (Figure 2.8b), at room temperature and using purified compressed air as the flooding gas. The injection pressure was controlled with a non-bleeding precision gas regulator and kept between 24 and 50 psi (relative pressure) for all tests, so as to minimise inertial effects. Pressure and temperature conditions were measured and recorded using a high precision pressure transmitter, and the necessary corrections were applied to minimise experimental errors. Gas flow rates were measured using a Core Laboratory Instruments NanoQ micro flow meter and recorded using the NANOK proprietary software supplied by the manufacturer. A high precision Vinci Technologies syringe pump was used to regulate the confining pressure, which was applied biaxially to the cores using water. This technique, along with the laboratory tests conducted and the particular gas flow mechanisms present in shales, will be explained in further detail in Chapter 5.

Table 2.1.
Mineralogical and geochemical composition of samples from the Goldwyer Formation (Canning Basin). The compositional values are reported in wt.% normalized to 100%, derived from XRD and Rock-Eval pyrolysis tests. The T_{max} values recorded during pyrolisis are reported in °C.

ID	Qtz	Feld	Plag	Cal	Dol	*Sum Carb*	Pyr	***Sum Non Clay***	Smec	I-S	I-M	Kao	Chl	***Sum Clay***	***TOC***	S1	S2	S3	HI	OI	T_{max}
SG-1	19	1	2	7	12	*19*	1	***42***	0	0	41	3	14	***58***	***4.28***	2.78	14.25	0.35	333	8	453
SG-2	17	1	2	4	2	*7*	2	***30***	0	0	56	3	11	***70***	***3.91***	3.18	9.95	0.29	254	7	454
SG-3	16	1	1	19	4	*23*	2	***44***	0	0	50	3	4	***56***	***1.24***	1.43	3.23	0.40	260	32	453
SG-4	16	2	1	3	1	*4*	2	***25***	0	0	70	1	4	***75***	***0.83***	1.24	1.90	0.15	229	18	456
SG-5	15	3	1	7	2	*9*	4	***31***	0	0	61	4	4	***69***	***2.68***	3.73	7.18	0.32	268	12	446
SG-6	22	1	1	7	8	*15*	3	***42***	0	0	49	2	7	***58***	***0.93***	1.10	0.96	0.27	103	29	456

Qtz = Quartz; *Feld* = Feldspars; *Plag* = Plagioclase; *Cal* = Total calcite; *Dol* = Total dolomite; *Pyr* = Pyrite; *Smec* = Total smectite; *Kao* = Total kaolinite; *I-S* = Total mixed-layer illite-smectite; *I-M* = Total illite + mica. *Obtained by XRD analysis.*

TOC = Total organic carbon (wt%); *S1* = Volatile hydrocarbon (HC) content (mgHC/g of rock); *S2* = Pyrolysable organic matter (mgHC/g of rock); *S3* = Carbon dioxide content (mgCO_2/g of rock); *HI* = Hydrogen index, S2×100/TOC (mgHC/gTOC); *OI* = Oxygen index, S3×100/TOC (mgHC/gTOC); T_{max} = temperature at which the S2 peak is recorded. *Obtained by Rock-Eval pyrolysis.*

Table 2.2.
Mineralogical and geochemical composition of samples from the Carynginia Formation (Perth Basin). The compositional values are reported in wt.% normalized to 100%, derived from XRD and Rock-Eval pyrolysis tests. The T_{max} values recorded during pyrolisis are reported in °C.

ID	Qtz	Feld	Plag	Cal	Dol	*Sum Carb*	Pyr	***Sum Non Clay***	Smec	I-S	I-M	Kao	Chl	***Sum Clay***	***TOC***	S1	S2	S3	HI	OI	T_{max}
SC-1	25	4	6	4	1	*5*	4	***44***	2	20	25	3	7	***56***	***3.03***	0.54	1.95	0.16	64	5	459
SC-2	35	2	7	0	2	*2*	3	***49***	1	30	16	2	3	***51***	***1.79***	0.18	0.64	0.28	36	16	459
SC-3	41	2	7	1	1	*2*	2	***54***	0	29	15	0	2	***46***	***1.02***	0.20	0.54	0.59	53	58	462
SC-4	42	2	7	0	3	*3*	1	***54***	2	29	15	0	1	***46***	***0.64***	0.13	0.25	0.17	39	27	458
SC-5	38	2	5	0	1	*1*	3	***51***	1	23	19	1	5	***49***	***1.82***	0.33	1.15	0.03	63	2	460
SC-6	41	2	7	0	2	*2*	2	***54***	0	30	15	0	1	***46***	***0.77***	0.34	0.53	0.54	69	70	463

Qtz = Quartz; *Feld* = Feldspars; *Plag* = Plagioclase; *Cal* = Total calcite; *Dol* = Total dolomite; *Pyr* = Pyrite; *Smec* = Total smectite; *Kao* = Total kaolinite; *I-S* = Total mixed-layer illite-smectite; *I-M* = Total illite + mica. *Obtained by XRD analysis.*

TOC = Total organic carbon (wt%); *S1* = Volatile hydrocarbon (HC) content (mgHC/g of rock); *S2* = Pyrolysable organic matter (mgHC/g of rock); *S3* = Carbon dioxide content (mgCO_2/g of rock); *HI* = Hydrogen index, S2×100/TOC (mgHC/gTOC); *OI* = Oxygen index, S3×100/TOC (mgHC/gTOC); T_{max} = temperature at which the S2 peak is recorded. *Obtained by Rock-Eval pyrolysis.*

2.3. Summary of Laboratory Experiments

The full list of experiments carried out on shale samples and included in this thesis can be found in Table 2.3 below, along with the core depths at which they were retrieved. The chapters where the corresponding results are first presented are also included.

Table 2.3.
List of laboratory experiments conducted on shale samples from the Carynginia and Goldwyer formations.

ID	Depth (m)	XRD	Rock Eval	1D–NMR T_2	2D–NMR T_1-T_2	MICP	LP-N_2 Ads.	LP-CO_2 Ads.	Gas Perm.
SC-1	2780	x	x	Sat.	–	x	x	–	–
SC-2	2782	x	x	Sat.	–	x	x	–	–
SC-3	2790	x	x	Sat.	–	x	x	–	–
SC-4	2794	x	x	Sat.	–	x	x	–	–
SC-5	2806	x	x	Sat.	–	x	x	–	–
SC-6	2825	x	x	Sat.	–	x	x	–	–
SG-1	1398	x	x	As-rec.	As-rec.	x	x	x	x
SG-2	1472	x	x	As-rec.	As-rec.	x	x	x	x
SG-3	1520	x	x	As-rec.	As-rec.	x	x	x	x
SG-4	1540	x	x	As-rec.	As-rec.	x	x	x	x
SG-5	1557	x	x	As-rec.	As-rec.	x	x	x	x
SG-6	1586	x	x	As-rec.	As-rec.	x	x	x	x
*Chapter **		*2*	*2*	*3, 4*	*4*	*4*	*4*	*4*	*5*

(*) Indicates the chapter numbers where the corresponding experimental results are first presented.
Sat. indicates NMR measurements on brine-saturated core plugs; *As-rec.* indicates NMR measurements on core plugs in their as-received state.

CHAPTER 3

Nuclear Magnetic Resonance for Shale Applications: T_2 Experiments

This chapter presents a methodology for the quantitative experimental analysis of NMR data in shales. Utilising both analytic and experimental approaches, two threshold cut-offs are identified and subsequently applied to T_2 distributions, by which the corresponding free and bound fluid fractions may be estimated. The first two sections lay out the context and the theoretical background of the NMR technique, including an overview of the most common signal acquisition and inversion methodologies. Section 3.3 presents a case study based on the analysis of T_2 data from measurements on real core samples and also obtained by simulation, to then reflect upon the best practices for acquiring and inverting T_2 signal in shales. In Section 3.4, an experimental procedure to conduct T_2 measurements and interpret NMR data in shales is proposed, stemming from the identification of two distinct $T_{2\,\text{cut-off}}$ on shale samples from the Carynginia Formation. The empirical threshold cut-offs from this systematic study are finally integrated with results determined analytically, drawing upon the comparison of T_2 distributions obtained by different inversion methods. The particular petrophysical interpretation of the free and bound fluid indices (FFI, BVI), derived from the application of $T_{2\,\text{cut-off}}$, is not within the scope of this chapter. Nonetheless, the NMR methodologies herein discussed serve as a base for the calculation of coefficients which will be used in subsequent chapters, where the connections with sample composition, pore structure and flow properties will also be examined.

3.1. Introduction

Nuclear magnetic resonance (NMR) is an established technique that has applications across a wide range of scientific disciplines, including medicine, material science and chemistry. One of the key features of this method is that measurements are non-invasive, so NMR is routinely used in the study of fluid-saturated porous media. This has proven particularly useful to the petroleum industry, where NMR tools are routinely used for the evaluation of

reservoirs (Jackson, 2001; Brown, 2001).

The analysis of NMR data obtained from wireline logging and laboratory measurements on cores can yield valuable information about the pore system and the different fluids present (e.g. Dunn et al., 2002; Kenyon, 1997; Freedman, 2002; Prammer et al., 1996; Coates et al., 1997). One-dimensional experiments are the most common application of the NMR technique for the study of porous media, and involve T_1 and T_2 measurements using low-field NMR spectrometers. Relaxometry experiments inspect the characteristic relaxation of the rock and fluids within its pores, which can be used to assess porosity and pore size distributions. A robust quantitative analysis of NMR results are thus essential, before reliable petrophysical parameters can be derived. The narrow pores and fast relaxation rates characteristic of shales, however, generate additional challenges for the acquisition and interpretation of NMR data.

Throughout this thesis, nuclear magnetic resonance is used as the principal probing tool linking the results from mineralogy, porosimetry and permeability characterisation methods. This chapter will examine the influence of various methodologies on the results obtained from laboratory NMR measurements in shales, aiming to cast some light on the best practices for T_2 data acquisition and inversion. For this purpose, both experimental results from NMR measurements on shales and simulated T_2 data will be analysed. Then, an alternative method for the experimental determination of T_2 cut-off values from NMR measurements on shale samples is presented, and results are later compared with the corresponding threshold values obtained analytically. The free and bound fluid fractions derived from the application of these $T_{2\ \text{cut-off}}$ are then interpreted solely based on the NMR results included in this chapter, while the integration with sample composition and porosimetry data will be discussed in Chapter 4.

3.2. Principles of NMR

NMR is a physical phenomenon that describes the response of atomic nuclei to an imposed magnetic field. The nucleus consists of neutrons and protons, which possess an intrinsic quantum property called spin. Atomic nuclei with odd numbers of protons and neutrons have non-zero spin, while atoms with even numbers have null spin. The NMR technique exploits the intrinsic magnetic momentum of all nuclei with a non-zero spin, which will absorb radio frequency energy when exposed to an external magnetic field of a certain strength that is specific to the nucleus. Adsorption resonance occurs when the

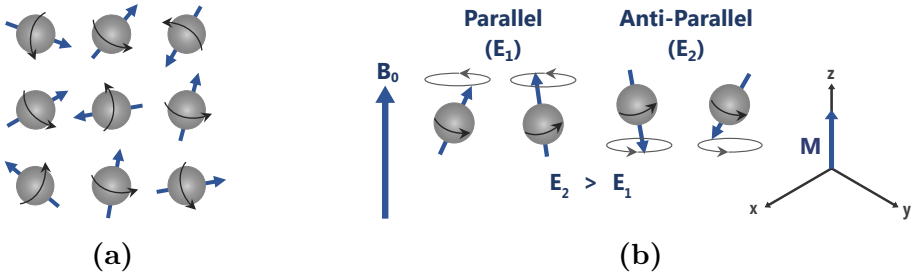

Figure 3.1. (a) In the absence of an external magnetic field, magnetic moment vectors of nuclei have no net magnetization and are randomly oriented; (b) when placed in a magnetic field B_0, nuclei will orient their spins either parallel or anti-parallel to the direction of the applied field and induce a net magnetization vector (M).

electromagnetic radiation has a particular frequency, known as resonance frequency, that is dependent on both the quantum properties of the nuclei and the field strength. The signals generated from the interaction of nuclear spins with the applied magnetic field can be detected and are thus recorded during NMR measurements. Unlike most of the nuclei found in the subsurface, the hydrogen nucleus generates a signal strong enough to be detected by the NMR logging tool, and is abundant in all reservoir fluids (Coates et al., 1998). In the petroleum industry, NMR logging tools are typically tuned to the magnetic resonance frequency of hydrogen protons, which maximizes the measured signal amplitude of the precessing nuclei.

During NMR measurements, a constant magnetic field B_0 is initially imposed on the nuclei. The torque exerted by B_0 on the individual magnetic moment of nuclei will cause them to precess about the magnetic field, a phenomenon known as Larmor precession. The precessing rate of spins is given by:

$$f = \frac{\gamma B_0}{2\pi} \tag{3.1}$$

where f is the Larmor – or precessional – frequency, and the gyromagnetic ratio γ is a proportionality constant, specific to each nucleus. The nuclear spins will be forced into low or high energy states, depending on whether the precessional axis is parallel or anti-parallel to the direction of B_0, as shown in Figure 3.1.

The majority of the precessing nuclei align parallel with B_0, as the low energy state is more stable. The resulting response is produced from this excess of low energy spins, that leads to a net magnetization vector (M). Using the semi-classical approach, the net magnetization can be calculated macroscopically as a function of time with the simplified Bloch equations (Bloch, 1946), written in

Figure 3.2. (a) Initial polarisation in the direction of the static magnetic field B_0; (b) an oscillating magnetic field B_1 (perpendicular to B_0) is subsequently applied.

vector notation as:

$$\frac{d\vec{M}(t)}{dt} = \gamma\vec{M}(t) \times \vec{B}(t) \tag{3.2}$$

Upon alignment – or polarization – of the nuclei in a direction parallel to the static magnetic field (designated as the longitudinal direction), the system is perturbed by a series of radio frequency (RF) pulses. The RF pulses form an oscillating magnetic field with an amplitude B_1, perpendicular to B_0, as shown in Figure 3.2. The net magnetization vector is then tilted to the transverse plane with a tip angle θ:

$$\theta = \gamma B_1 t_D \tag{3.3}$$

where t_D describes the duration of the applied oscillating magnetic field. After B_1 is turned off, the aligned nuclei will begin to dephase and eventually return to their previous thermodynamic state. The study of this process, known as relaxation, is the fundamental principle of NMR logging. When nuclei are placed in an external magnetic field, a net magnetization vector is induced along the z-axis. The NMR signal may be detected as long as the spins are coherent with one another, whereas loss of coherence results in the loss of signal. The NMR experiment moves the net magnetization vector from the z–axis to the xy plane, where is detected by the tool. In the petroleum industry, longitudinal (T_1) and transverse relaxation time (T_2) measurements are the key targets of NMR tools.

3.2.1. Longitudinal Relaxation (T_1)

Longitudinal or spin-lattice relaxation describes the process by which the longitudinal component of the magnetization vector (M_z) returns to thermodynamic equilibrium with its surroundings. The longitudinal relaxation rate, characterized by the time constant T_1, is derived from Equation (3.2) as:

$$M_z(t) = M_0 - [M_0 - M_z(0)]\ e^{-\frac{t}{T_1}} \tag{3.4}$$

where t describes the time over which the nuclei are exposed to the static magnetic field B_0, and M_0 is the equilibrium magnetization.

An Inversion Recovery (IR) pulse sequence can be used for the determination of T_1. In this sequence, a 180° pulse is initially applied to flip the magnetization vector along the longitudinal axis. After the pulse ceases, longitudinal relaxation is experienced by the spins as they return towards the initial equilibrium position M_0. Before equilibrium is reached, a 90° pulse is applied and the magnetization vector is rotated into the transverse plane. The longitudinal component of the magnetization vector M_z in the IR sequence is then described by:

$$M_z(t) = M_0\ (1 - 2e^{-\frac{t}{T_1}}) \tag{3.5}$$

T_1 may be defined as the time required for M_z to recover by a factor of e towards the equilibrium magnetization M_0. Or similarly, T_1 represents the time it takes the net magnetization to reach approximately 63% of its final value after being flipped by the 90° pulse, where 95% of the nuclear spins are polarized after an interval time equivalent to $3T_1$ (Coates et al., 1998). T_1 varies considerably with the strength of the applied magnetic field, making T_1 experiments impractical in reservoirs due to time-constraints and the poor signal-to-noise ratio (SNR) prevalent in subsurface measurements (Kleinberg et al., 1993). In contrast, T_2 values are typically much less reliant on field strength and allow data acquisition at commercially viable logging speeds.

3.2.2. Transverse Relaxation (T_2)

Transverse or spin-spin relaxation describes the process by which the transverse component of the magnetization vector M_{xy}, perpendicular to B_0, returns to its equilibrium magnetization M_0. Despite the complexity of the general T_2 phenomenon, the signal measured during T_2 measurements is fundamentally generated by the decoherence of the precessing nuclear spins in the transverse plane. The transverse relaxation rate is characterized by the time constant T_2, derived from Equation (3.2) as:

$$M_{xy}(t) = M_{xy}(0)\ e^{-\frac{t}{T_2}} \tag{3.6}$$

where T_2 represents the time at which M_{xy} has decayed to 37% of its initial magnitude.

In real systems, nuclei will not always precess with the same frequency. Instead, certain inhomogeneities will cause nuclear spins to have different resonant frequencies and eventually lead to loss of coherence (dephasing), which

produces a decaying signal in the transverse plane that is known as free induction decay (FID). The FID has a very short time constant $T_2{}^*$ (usually much smaller than T_2), and occurs due to inhomogeneities in the magnetic-fields and to the differences in the actual molecular relaxation mechanisms taking place in the measured substance. This decaying signal is not caused by a true relaxation mechanism, so its magnitude depends on the location of the spins relative to the applied magnetic field. The deviation from the ideal T_2 relaxation can be quantified with a spin-echo experiment, according to the equation:

$$\frac{1}{T_2{}^*} = \frac{1}{T_2} + \gamma \Delta B_0 \tag{3.7}$$

where ΔB_0 represents the magnetic field inhomogeneity. This principle is the basis for the Carr-Purcell-Meiboom-Gill (CPMG) pulse sequence, developed to account for the effect of decoherence on measured signals by refocusing the dispersed nuclear spins (Carr and Purcell, 1954; Meiboom and Gill, 1958).

3.2.2.1. Data Acquisition: The CPMG Pulse Sequence

The CPMG sequence involves an initial 90° RF pulse that tips the magnetization into the transverse plane. The loss of coherence suffered by the nuclei will induce an FID. After a time equivalent to half an echo-spacing (T_E), a 180° pulse will refocus the spins and the spin-echo (or simply echo) will be recorded by the NMR tool. This will then be followed by a series of 180° pulses, applied at an interval (T_E), which will produce a spin-echo train, as illustrated in Figure 3.3. It is worth noting that the dephasing caused by molecular interactions and diffusion cannot be reversed or avoided, so the CPMG pulse sequence can only be used to offset the loss of coherence resulting from B_0 inhomogeneities (Coates et al., 1998). Once a complete refocusing of all nuclei is no longer possible and the loss of coherence becomes irreversible, the spin-echo train will decay. T_2 may thus be defined as the time it takes for the nuclear spins to lose coherence with one another, and may either be shorter or equal to T_1. The measurement of T_2 decays are the primary target of NMR logging tools, from which T_2 distributions are derived by signal inversion.

3.2.2.2. Signal Processing

The prediction of observations for a particular system, based on the governing physics, is known as a *forward problem*. In contrast, *inverse problems* describe the process by which the parameters that characterize a physical system are inferred from experimental results. In NMR measurements, the decaying signals decomposed in the time domain describe a Laplace transform. Thus, obtaining

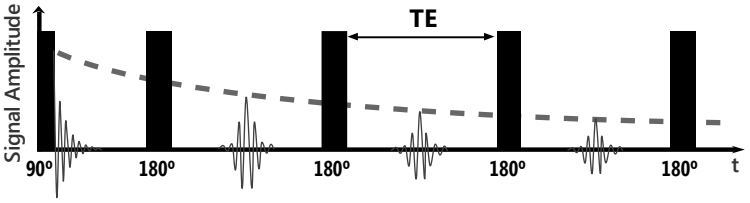

Figure 3.3. Schematic of CPMG pulse sequence and echo trains generated during T_2 experiments (dashed line), with an echo-spacing T_E (i.e. time between 180° pulses).

the distribution of characteristic T_2 relaxation times from the measured signal amplitudes requires an inversion of the Laplace transform. Different approaches can be used in solving the NMR inversion problem, so the use of a suitable method is crucial for obtaining T_2 distributions that can yield meaningful petrophysical information.

In the absence of experimental errors or noise, an ideal signal inversion problem can be represented by a linear relationship $Y=A \cdot X$, where Y is the measured data for a given system, A is the operator describing the physics of the problem, and X includes the model parameters to estimate. Noise is always part of the recorded T_2 data, as it cannot be suppressed from real NMR measurements. Consequently, a measured decaying NMR signal y(t) – in the time domain – has a structure similar to a Fredholm integral equation of the first kind (Polyanin and Manzhirov, 2008), as seen below:

$$y(t) = \int a(t, T_2)\, x(T_2)\, dT_2 + \xi \tag{3.8}$$

where $a(t,T_2)$ is the evaluation matrix (or *kernel*) that represents the physical problem, $x(T_2)$ is the unknown spectrum, and ξ is the experimental noise. The determination of $x(T_2)$ is the key objective of the T_2 inversion process.

The integral in Equation (3.8) acts as a low-pass filter that returns the smooth decaying signal y(t), by attenuating the high-frequency components in $x(T_2)$. These high frequency components, along with noise, will be amplified if $x(T_2)$ is directly estimated by an inversion of the recorded data y(t). Small perturbations in the measured data could lead to great variations in the spectra obtained, and such solutions are therefore said to be unstable. Furthermore, multiple distributions could produce similarly shaped T_2 decays (and vice versa) in the 1D–NMR inversion problem. Since the uniqueness and stability of solutions cannot be guaranteed, the NMR inversion problem is considered as *ill-posed*. In such cases, where a straightforward inversion to solve the problem stated in Equation (3.8) is not possible, estimating the T_2 spectra requires a

different approach that includes the use of regularization techniques (Polyanin and Manzhirov, 2008). The inversion of T_2 signal decay must be transformed into a numerical optimisation problem that can admit a unique solution, ensured by the introduction of constraints. The T_2 distribution will then be determined as the solution that best fits the measured data (under certain constraints).

Discretisation

The raw data recorded during NMR measurements is a complex signal, sampled at intervals T_E; however, only the real part of the NMR signal is generally used for further analysis in spectroscopy (Rutledge, 1996). The continuous integral in Equation (3.8) can be transformed into a linear algebraic system by discretisation, taking the form:

$$Y = AX + E \tag{3.9}$$

where $Y \in \mathbb{R}^m$ contains the data acquired at times t_i, $A \in \mathbb{R}^{m \times n}$ is the kernel matrix that represents the physical problem, $X \in \mathbb{R}^n$ is the distribution evaluated for the relaxation times T_{2j}, and $E \in \mathbb{R}^m$ is the error (or associated noise). In fluid-saturated rocks, the transverse relaxation components are assumed to decay exponentially, so Equation (3.9) can be rewritten as:

$$y_i = \sum_{j=1}^{N} x_j \, e^{-(t_i/T_{2j})} \quad i = 1, 2, ..., M \tag{3.10}$$

where the relaxation times T_{2j} are typically logarithmically spaced (Borgia et al., 1990; Whittall, 1996).

Singular Value Decomposition

The stability and computing cost of the NMR inversion problem can be improved by projecting the data onto a subspace, defined from a truncated singular value decomposition (SVD) of the kernel matrix (Mitchell et al., 2012; Hürlimann and Venkataramanan, 2002; Song et al., 2002; Venkataramanan et al., 2002). The matrix A can then be factorized by means of SVD as:

$$A = U \, \Sigma \, V^T \tag{3.11}$$

where $U \in \mathbb{R}^{m \times m}$ and $V \in \mathbb{R}^{n \times n}$ are orthogonal singular matrices, and $\Sigma \in \mathbb{R}^{m \times n}$ is a diagonal matrix of the singular values in descending order (Hansen, 1987).

The next step involves the compression of data by truncating the singular values in Σ. The inclusion of a large number of values enhances the effect of noise

in the spectrum, but limiting their number when the signal-to-noise ratio (SNR) is low may lead to solutions with artificially broad peaks (Song et al., 2005). Thus, only the first components of Σ that hold significant information should be retained, while those that contain mostly noise are to be discarded. The number of significant singular values $\tilde{n}_r$ depends on the condition number, calculated as the ratio of the largest to smallest singular values in the rank reduced Σ_r. The truncation level is commonly determined based on the SNR of the data (Mitchell et al., 2012; Song et al., 2005), and should satisfy the necessary conditions to ensure well-conditioned matrices (Hansen, 1987). The truncated matrices will be $\mathrm{U_r}$ (m×r), Σ_r (diagonal, r×r), $\mathrm{V_r}$ (n×r). The compressed data vector will then be calculated as $\mathrm{Y_r} = \mathrm{U_r^T\,Y}$, and the reduced kernel is $\mathrm{A_r} = \Sigma_\mathrm{r}\,\mathrm{V_r^T}$.

The truncated SVD approach can be used for regularisation, but requires previous knowledge about the solution to identify the optimal truncation value and cannot guarantee positive solution elements, so should thus be used in combination with other methods (Venkataramanan et al., 2002).

The NMR Optimisation Problem

The NMR data inversion process is equivalent to finding the best possible solution to an optimisation problem. Additional constraints are imposed on the algebraic system, which ensure that the $\mathrm{T_2}$ spectra obtained is physically representative of the real NMR phenomena in porous media. Since multiple possible solutions could fit the observed data relatively well, several numerical methods have been proposed to find the best possible result. Statistical tests, such as the sum of squared residuals (SSE) or the root-mean-squared error (RMSE), can be used to evaluate the optimality of the solution.

The problem described by Equation (3.9) can be solved with the non-negative least squares (NNLS-LH) method proposed by Lawson and Hanson (1974). The NNLS-LH solutions are obtained by minimising the misfit between the measured (Y) and predicted data ($\mathrm{A} \cdot \mathrm{X}$), subject to non-negativity constraints. Based on the dimensionality reduction explained, the NMR problem can be expressed as:

$$\underset{X_r \geqslant 0}{\arg\min} \parallel Y_\mathrm{r} - A_\mathrm{r}\, X_\mathrm{r} \parallel_2^2 \tag{3.12}$$

where $\parallel \cdot \parallel_2^2$ is the squared Euclidean L_2 norm. The NNLS method is very stable but convergence can be slow and solutions may consist of a few isolated peaks, as opposed to the smooth distributions associated with NMR relaxation in porous media (Whittall, 1996). Furthermore, solutions are quite sensitive to noise so adjacent components may be merged during the inversion process (Whittall, 1994).

The solutions to the general NMR inversion problem are generally found based on the methodology introduced independently by Twomey (1963) and Tikhonov (1963), which addresses both the non-negativity and smoothness requirements. In this method, a penalty smoothing term is included to avoid solutions featuring numerous sharp peaks that are not physically representative (despite being a good numerical fit). The problem described by Equation (3.12) is then extended to:

$$\underset{X_r \geqslant 0}{\arg\min} \parallel Y_r - A_r\, X_r \parallel_2^2 + \lambda \parallel L\, X_r - X_{r0} \parallel_2^2 \tag{3.13}$$

where L is the regularisation operator (matrix of additional constraints), and λ is a variable known as the regularization parameter. The L operator can regularise the solution via an L_0, L_1 or L_2 norm penalty function, often merely referred to as norm (or energy), slope or curvature smoothing (Dunn et al., 1994). The tuning parameter in Equation (3.13) controls the smoothness of the solution relative to the misfit term. Larger values of λ will dampen the smallest significant singular values (associated with noise) and thus lead to smoother solutions. The incorrect selection of λ can lead to either under- or over-smoothed spectra, so several methods have been developed to find the optimal λ_{opt} that provides the best trade-off between misfit and smoothness of solutions to return realistic T_2 distributions.

The Tikhonov regularisation described by Equation (3.13) may be implemented using a direct or an indirect approach. The direct approach involves an initial analysis to determine the optimal regularisation parameter which is later used to calculate the best possible solution, often using the NNLS-LH method (Lawson and Hanson, 1974). In contrast, the indirect approach finds the solution to the NMR problem with the help of auxiliary functions, such as the method proposed by Butler et al. (1981). Four methods for determining λ_{opt} used later in this chapter are described below: the *L-curve*, *GCV*, *BRD* and *UPEN*.

Choice of Regularisation Parameter

The *L-curve* method, proposed initially by Lawson and Hanson (1974) and further developed by Hansen (1992) and Hansen and O'Leary (1993), was one of the first algorithms introduced to solve the NMR inversion problem. The plot of the solution norm versus its corresponding residual norm, as a function of a given range of λ values results in an L-shaped curve as illustrated in Figure 3.2.2.2, giving its name to this method. The point at which the slope of the curve abruptly changes is then selected as the optimal smoothing coefficient λ_{opt}. The selection of the best regularization parameter may thus be somewhat arbitrary in the L-curve method, depending on the data analysed.

The *generalised cross-validation* (GCV) method, proposed by Golub et al.

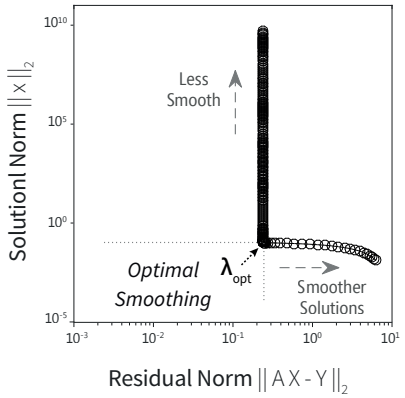

Figure 3.4 L-curve method: the solution norm $\|x\|_2$ is calculated for discrete λ values and plotted against the corresponding residual norm $\|AX - Y\|_2$. The horizontal part illustrates the residual norms that are most sensitive to errors, arising from the incorrect selection of λ. The vertical part illustrates the solution norms that are most sensitive to errors, arising from the amplification of random noise. The optimal λ_{opt} is located at the corner of the L-curve, either visually or using a numerical method such as the adaptive pruning algorithm (Hansen, 2015).

(1979), finds the optimal regularisation parameter λ_{opt} that minimises:

$$GCV(\lambda_{opt}) = \frac{\| Y_r - A_r X_{r,\lambda} \|_2^2}{[trace\,(\mathbb{I} - X_{r,\lambda})]^2} \tag{3.14}$$

where $\mathbb{I}$ is the identity matrix, and $X_{r,\lambda}$ is the solution calculated for a certain smoothing coefficient λ.

In the *Butler-Reed-Dawson* (BRD) method, an auxiliary convex function is minimised to find the λ_{opt} (instead of performing direct iterations over c_r) based on the discrepancy principle (Butler et al., 1981; Morozov, 1984). The regularisation parameter may be determined empirically as a function of a specified level of misfit in the data, such as RMSE. It is also common for solutions to be obtained based on the SNR of the data, generally defined as SNR $= M(0)/\sigma$, where σ is the noise standard deviation (Song et al., 2005). Using the Newton method, the estimated λ values are updated at each step as a function of $\sqrt{n_r}/\| c_r \|$ (Mitchell et al., 2012) and the misfit error is calculated as:

$$\chi(c_r, \lambda) = \frac{\lambda \| c_r \|}{\sigma} \tag{3.15}$$

The S-curve is commonly used to find the optimal regularisation parameter, which evaluates the sigmoidal shape displayed in the log-log graph of the misfit error, as a function of λ (Fordham et al., 1995). The optimal solution is found at the "heel" of the S-curve, where λ satisfies:

$$\frac{d(\log \chi(c_r, \lambda))}{d(\log \lambda)} = \text{TOL} \tag{3.16}$$

for a predetermined tolerance value (TOL) selected by the user.

The *UPEN* method introduced by Borgia et al. (1998) uses a quadrature regularisation function, where λ varies with the relaxation time to obtain a uniform application of the smoothing penalty term. The method was later refined, introducing a combination of regularisation functions to effectively

obtain variable smoothing (Borgia et al., 2000). In the second version of the UPEN method, the averaged signal within a defined window and the corresponding weight factors are used to provide feedback for a uniform penalty smoothing.

3.3. Considerations for the Acquisition and Inversion of NMR Data in Shales[1]

Different methodologies can be used to acquire NMR data and transform it into distributions that can yield useful petrophysical information, as reviewed in Section 3.2. Previous studies have suggested different approaches for the application of the NMR technique on shales (Washburn et al., 2015), but a universal standard is still lacking. The following subsections will examine the influence of different variables on the NMR results from cores, aiming to cast some light on the best practices for T_2 data acquisition and inversion in shales.

NMR data from real T_2 measurements on shale samples, and simulated T_2 decay curves were obtained for the purpose of this study. In Subsection 3.3.1, the impact of various acquisition parameters on the real T_2 signal measured in shales is analysed. All NMR experiments were carried out on a 2 MHz Magritek Rock Core Analyzer set to 30°C, equipped with either a P29 or P54 probe and using different settings. The real T_2 decays presented in this subsection were obtained on the same 1"–diameter core plug, in the *as-received* state, which was tightly wrapped in a plastic film to prevent moisture evaporation or absorption. The sample belongs to the Carynginia Formation, a dry gas prone shale section found in most of the northern Perth Basin (Mory and Iasky, 1996).

The inversion methods described earlier in this chapter are tested on synthetic T_2 data, and the analysis of results is presented in Subsection 3.3.2. The T_2 decays were generated to replicate the equivalent relaxation response that would be obtained from measurements on real shale samples. The *Lexus* module in the Prospa software (Magritek) was used for the BRD inversions, whereas the NNLS-LH/L-curve, NNLS-LH/GCV and UPEN algorithms were implemented in Matlab (Mathworks), using purposely written code. In the latter case, final computations were done using the NNLS function included in the MERA Toolbox for Matlab (Does, 2014).

[1]This section includes material from: Testamanti and Rezaee, 2019.

3.3.1. T_2 Data Acquisition

As explained in the previous section, the CPMG sequence involves the initial polarization of nuclear spins, followed by the application of a series of magnetic pulses or echoes N_E, spaced by a T_E time. Consecutive CPMG pulse trains are separated by a wait time or inter-experimental delay (T_W), during which the polarization of the system builds up. The parameters N_E, T_E, T_W, as well as the pulse specifications, are all necessary inputs of T_2 CPMG experiments and must be suitably chosen by the instrument's operator. The output of measurements will be a vector with the raw T_2 data, recorded at fixed intervals T_E. The sensitivity to different acquisition parameters is discussed below.

Inter-Experimental Delay

The magnitude of M_0 is estimated from the signal amplitude measured after the first RF pulse in the sequence. The T_W should thus be set to at least three times the expected T_1 value to allow a 95% polarization of the spins and avoid underestimating M_0. Shales have very fast relaxation rates, so generally short T_W times can be safely used for T_2 measurements. This is illustrated in Figure 3.5a, where the impact of the inter-experimental delay parameter on the measured M_0 of a shale core sample is examined. The T_2 decays were acquired with the P54 probe for 3,000 echoes, with a T_E = 100 µs and the same target SNR = 220 but using short and long T_W intervals, set to 3,000 and 20,000 ms respectively. Similarly shaped T_2 decay curves emerge from the graph, while the difference between the calculated M_0 was about 7%. The use of longer inter-experimental delays was therefore found to only marginally improve the estimation of M_0 values. The impact of the T_W parameter on the overall duration of measurements, however, becomes more significant in shales and should be evaluated against time constrains if applicable.

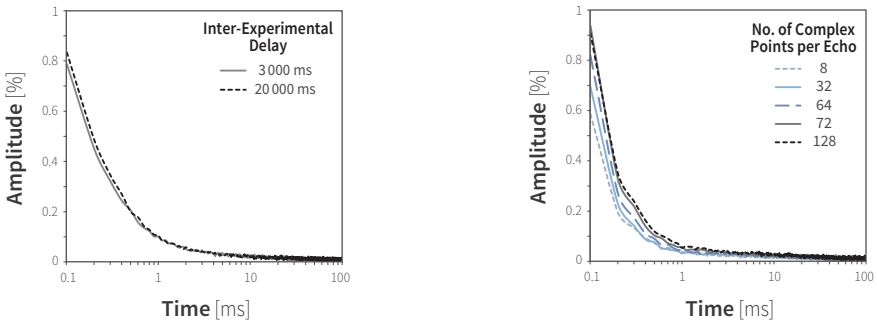

(a) **(b)**

Figure 3.5. T_2 decays from a shale core sample showing sensitivity of (a) M_0 to inter-experimental delay; (b) signal quality to number of complex points sampled per echo.

Signal-to-Noise Ratio

Despite being relatively weak, NMR signal can be detected owing to the abundance of hydrogen protons in the reservoir fluids. Improving the quality of the NMR data acquired can be seen as equivalent to reducing the experimental noise, which improves the effective SNR. After NMR signal is detected, the in-phase and quadrature signals for each spin-echo are sampled, according to the number of complex points and dwell time set by the user, and digitized in the spectrometer before being returned to the computer (Kleinberg, 1999). To improve the quality of NMR results, signal averaging – or stacking – is initially performed on the raw signal, followed by a phase correction. The final outputs are two data vectors, one containing the real components of the spin-echo train from which T_2 distributions will be obtained, and another containing the imaginary portion of the complex signal that represents the noise with zero mean (Coates et al., 1998).

The acquisition of a large number of echoes (N_E) allows the real part of the signal to decay to noise level, ensuring the detection of all the T_2 relaxation rates present in the core sample while improving the SNR of the NMR measurement. In practice, the experimental settings should satisfy the condition $N_E \geq T_{2,max}/3T_E$ to detect the full range of T_2 components (Coates et al., 1998). As observed in Figure 3.5a, shales have fast relaxation rates so most of the signal would be captured within the first few hundred milliseconds.

The SNR of the acquired data may also be enhanced by performing a signal averaging or stacking. This technique relies on the random feature of noise, as opposed to the reproducibility of the NMR signal, and therefore cannot filter out coherent noise. By averaging the signal from a number of successive scans N, the amplitude will grow at a rate of N whereas the growth rate of noise will be $\sqrt{N}$. The SNR improvement will then be proportional to $\sqrt{N}$ averaged, where the number of scans should be a multiple of 4 for a full phase cycling. Another method often used to improve the SNR of NMR data consists in increasing the number of complex points sampled per echo. The product of this sampling number (ideally a power of 2) and the dwell time will determine the total acquisition time (t_{acq}) for each spin-echo; the spectral width is given by the reciprocal of the dwell time. The minimum T_E available for the instrument will be limited by the acquisition time, and should be greater than t_{acq} plus an added delay to avoid artifacts in the signal due to the acoustic ringing of the probe. Nonetheless, the law of diminishing returns applies to both of the SNR enhancement techniques previously described and should be carefully considered when experimental parameters are selected. The acquisition of a large number

of points per echo may overheat the RF amplifier and thus damage the instrument, while an increase in the number of scans can extend the length of experiments considerably. Figure 3.5b shows the T_2 curves obtained from CPMG sequences on a real shale core sample, where the raw signal was sampled using a variable number of complex points. Measurements were conducted using Magritek's P29 probe, with 2,000 echoes and a T_E = 100 µs. Increasing the number of complex points sampled per echo from 8 to 32 leads to a 15% rise in the initial signal amplitude, similar to increasing the sampled points from 32 to 64, and then from 64 to 72. No substantial variations are observed between the curves acquired with 72 and 128 points per echo. The proportional rise in the noise standard deviation nonetheless prompts to question whether the increase in the first few data points could be in fact an artificial enhancement, caused by acoustic ringing effects (Gerothanassis, 1987). The use of a long acquisition delay is often recommended to prevent the collection of spin-echoes distorted by the probe free ringing, but that could also lead to the loss of valuable information in shales. Since most of the signal decay generally occurs in the first few data points, the application of post-acquisition filters and alternative data fitting techniques that can compensate for offset and acoustic ringing effects may be more suitable for processing NMR data in shales (Freedman, 2002; Venkataramanan et al., 2013; Salimifard et al., 2017).

Alternatively, the use of relatively larger core samples, where hydrogen nuclei are more abundant, can yield an improvement of the signal quality. Since this is not always possible, the use of instruments with smaller RF coils could be another option for achieving higher SNR levels during measurements.

Echo-Spacing (T_E)

The use of shorter T_E enables the earlier detection of NMR signal, desirable in the case of rocks with fast relaxing components. The number of complex points sampled per spin-echo, the pulse length and the acquisition bandwidth – along with the spectrometer's characteristics – will limit the minimum echo time that can be used for measurements. SNR will generally increase with decreasing T_E, as more data points will be generated (and recorded) at shorter intervals. The reduction in T_E also has the unintended consequence of accentuating acoustic ringing effects. The first echoes are generally more affected by the acoustic ringing of the probe which would consequently become part of the recorded signal, causing a very high initial amplitude followed by a coherent transient (Coates et al., 1998). This effect can be observed in Figure 3.6a, where the background signal acquired with a T_E of 40 µs shows a higher initial amplitude, compared to the curve obtained at a 100 µs echo-spacing.

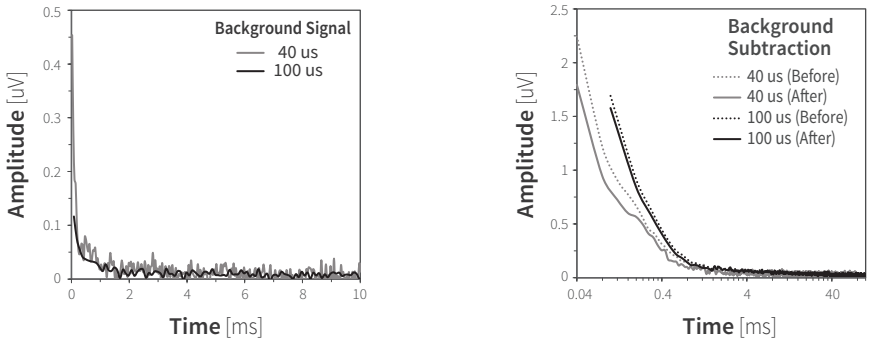

Figure 3.6. Effect of background signal (a), and its removal (b), on T_2 decaysacquired at different echo-spacing on a dry shale core sample using the Magritek's P29 probe.

The ringing noise can be filtered out to some extent by manipulating the digital filter bandwidth, at the expense of loss in sensitivity owing to the limitations on the minimum T_E possible (Salimifard et al., 2017), or attenuated by the use of smaller probes. The effect of random noise can be mitigated by subtracting the NMR signal corresponding to the instrument, from measurements on core samples. While background noise generally has little impact on results from high porosity rocks, it can contribute substantially to the NMR signal measured in shales (Saidian, 2015; Salimifard et al., 2017). It is therefore good practice to always obtain the background signal emitted by sample containers or plastic wraps and by the instrument itself, which should be then subtracted from the T_2 decays – prior to the data inversion. The effect of subtracting the background signal from T_2 measured in a real shale core sample is illustrated in Figure 3.6b, where experiments were conducted at 40 µs and 100 µs echo-spacings using a P29 probe. A greater portion of the fast T_2 components could be detected using a shorter T_E, although this difference becomes less significant beyond 0.5 ms. These fast T_2 relaxation rates are typically associated with organic and inorganic micropores, so short echo-spacings should be used whenever possible to investigate the full range of pore size ranges commonly found in the shale matrix.

A final point to consider is the issue of thermodynamic stability, crucial for T_2 measurements based on the CPMG pulse sequence. In core samples where narrow pores are abundant, the duration of experiments can increase considerably and span several hours. Failure to achieve isothermal conditions could lead to the underestimation of M_0, so core samples should always be allowed to stabilise to the magnet temperature prior to measurements. Alternatively, samples could be pre-heated before loading them into the spectrometer, provided that they are tightly sealed to avoid unintended fluid loss due to vaporisation.

3.3.2. T_2 Data Inversion

The ultimate goal of the T_2 inversion process is finding the spectrum that best represents the real relaxation mechanisms in the saturated porous media. Most NMR inversion methods can correctly find solutions for systems where the dominant T_2 components are sufficiently separated, so the choice of the inversion algorithm is not a significant source of concern. This, however, is not usually the case in complex porous systems with abundant small pore sizes such as shales. The shale matrix typically has a substantial clay and organic content, with protons susceptible to magnetisation that yield fast T_2 relaxation rates, often generating most of the total NMR signal acquired. Inversion algorithms must be therefore carefully selected, as the reconstructed signal should include sharper peaks at short T_2 times to accurately represent, not only the relaxation of fluids in smaller pores but also the clay bound water and solid organic matter present in shales. Caution must be nonetheless applied, to avoid artifacts in the spectrum at longer T_2 times that are not representative of real nuclei relaxation in larger pores.

The inversion algorithms described in the previous section were tested on a set of simulated T_2 decays emulating the relaxation rates commonly found in sandstones and shales, designated as case A and B in this study. The T_2 curves were obtained from distributions with the following distinctive features: (A) three peaks, centred on 2, 14 and 44 ms, displaying maximum normalised amplitudes of 20%, 50%, and 30% respectively; (B) four peaks, centred on 0.1, 2, 14 and 44 ms, displaying maximum normalised amplitudes of 20%, 40%, 30%, and 10% respectively. The T_2 components used as input for the simulations are indicated with black vertical lines in Figure 3.7. The T_2 decays were generated for 3,000 and 10,000 echoes, based on a 100 µs echo time. Gaussian noise was also added to the raw T_2 decay curves, to obtain SNR levels comparable to those of the experimental NMR data presented in the previous subsection.

Data Compression

Before inversion, the size of acquired data is reduced for computational efficiency purposes, and to filter out noisy values. The initial compression of NMR data can be computed with the TSVD method, which requires the selection of an optimal truncation value (Venkataramanan et al., 2002). Choosing this threshold incorrectly can lead to substantial attenuation of the shortest T_2 components (Prammer, 1994; Song et al., 2005), and consequent loss of valuable information in systems where fast components are expected. The optimal number of significant singular values required for the inversion was

analysed based on the L-curve method described in Hansen et al. (2007). The algorithm was implemented in MATLAB (MathWorks), using the Regularization Toolbox (Hansen, 2015). For the simulated T_2 decays analysed, a data reduction from the original number of data points to 25–50 significant values was generally found to produce stable solutions. Experimental noise could have a considerable impact on the T_2 spectra obtained from the inversion of NMR signal in shales, so the selection of an optimal truncation threshold is critical. Keeping a large number of singular values before inversion could compromise the identification of individual adjacent peaks in the T_2 spectrum, which can often lead to distributions featuring one broad peak at short T_2 times. The earliest data points recorded in shales will likely contain the most valuable information and must be preserved, while the noisy part of the T_2 curve should be pruned before inversion. The truncation criteria becomes more critical as the size of acquired data increases, relative to the time vector on which the inversion is evaluated. The impact of the data compression method can therefore be more significant in shales, when compared to other types of reservoirs.

Inversion Method

The incorrect selection of the NMR inversion algorithm may lead to gross interpretation errors, especially when the T_2 spectra are correlated to porosity and pore size distribution obtained from other core analysis methods. To assess the impact of NMR inversion algorithms in shales, the simulated T_2 curves were inverted for a logarithmically spaced vector with 200 points, within the range 0.01–600 ms for the simulated data from 3,000 echoes, and between 0.01–2,000 ms for the remaining cases. Solutions were regularised with the energy of the T_2 spectrum, also know as norm-smoothing, except for inversions based on the UPEN method. For the direct inversion approach using the NNLS-LH method, optimal smoothing coefficients were chosen based on the L-curve and GCV techniques, while distributions from indirect inversions were computed with the BRD and UPEN algorithms. The resulting T_2 distributions by different methods are presented in Figure 3.7, while the signal intensities are compared in Table 3.1. The goodness of fit of the four inversion methods were evaluated by the sum of absolute error (SAE), root-mean squared error (RMSE), peak signal-to-noise ratio (PSNR) and structural similarity index (SSIM) (Wang et al., 2004; Miao et al., 2008); the residual statistics are summarised and assessed against the original scores from the noisy data in Table 3.2.

No significant differences are observed between the total signal simulated, recovered and calculated by the four NMR inversions in case A, irrespective of

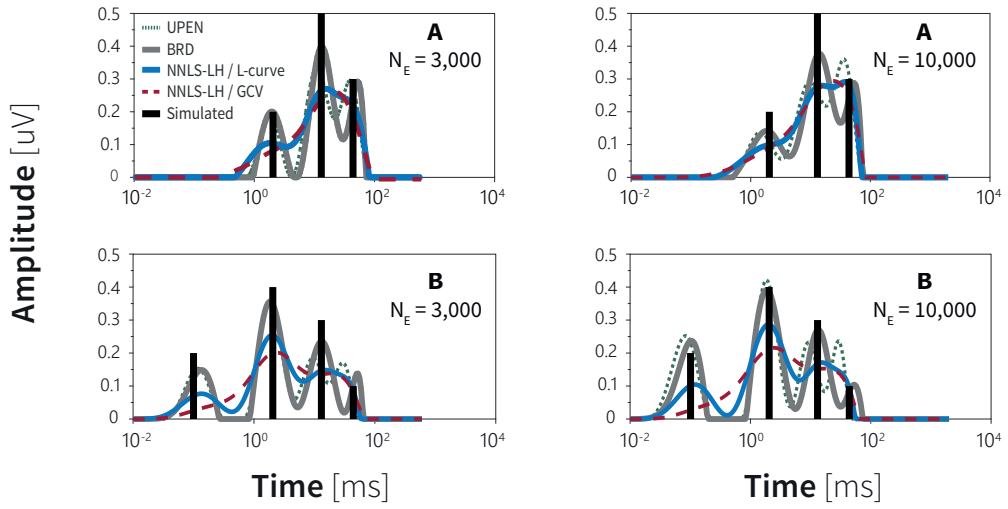

Figure 3.7. T_2 spectra for simulated T_2 data (black vertical lines), from decays obtained with 3,000 (left) and 10,000 echoes (right) and inverted by the NNLS-LH/Lcurve (blue), NNLS-LH/GCV (red dashes), BRD (grey) and UPEN (green dots) methods.

the number of echoes used (Table 3.1). In contrast, about 15% of the NMR signal in the simulated spectrum B is lost by the use of a 100 µs echo time, while the acquisition of a larger number of echoes has a minor positive effect on the amount of total signal intensity recovered. The contrast of case B inverted data reveals that the BRD and UPEN algorithms can closely reproduce the recovered signal amplitude (with an error <0.5%). The difference with inverted signal intensity is greater for the NNLS-LH technique, using either the L-curve (1-2%) or GCV criteria (2.5–4.5 %).

Figure 3.7 reveals that – in all cases – the direct inversion approach (NNLS-LH with L-curve and GCV) produces smoother T_2 spectra than the curves obtained by the BRD and UPEN algorithms. In conventional reservoirs, smooth solutions with broad spectral features are generally considered to be representative of the saturated porous media and therefore selected as the best fit. On the other hand, solutions including sharp peaks are discarded, while strong signals at short relaxation times are typically attributed to noise magnification from the inversion process. Based on common practice, T_2 curves determined by the combination of the NNLS-LH method with either the L-curve or GCV are less biased and would thus be preferred for evaluating petrophysical properties. However, the use of a single regularisation parameter in systems where adjacent peaks have different widths and amplitudes may also lead to either excessive broadening of narrow features, or sharpening of broad peaks (Borgia et al., 1998). This effect becomes apparent in the distributions obtained by NNLS-LH inversion with either the L-curve or GCV techniques, as no suitable λ_{opt} was found that could correctly

resolve the adjacent components centred on 12 and 44 ms. Instead, the individual features seem to emerge as a combined unique broad peak, visible in all the T_2 spectra generated by direct inversion. Since the NMR signal measured in shales will exhibit a sharp decay at short T_2 times where high experimental SNR levels are often unattainable, the lack of sensitivity to noise of the NNLS-LH inversion method is certainly a source of concern. Separating the contributions from individual fast relaxing T_2 components would likely be difficult with the use of inversion methods that apply a fixed amount of smoothing (e.g. NNLS-LH), however, the solutions would also be less biased and therefore more representative of global properties such as NMR porosity. On the other hand, noise-sensitive algorithms (e.g. BRD) may extrapolate the NMR signal well below the detection limit of the spectrometer and introduce significant bias in the determination of T_2 spectra, but could also help to distinguish individual adjacent peaks. This particular attribute could in turn facilitate the identification of threshold T_2 cut-offs, from which other coefficients with links to real petrophysical properties may be derived, as will be discussed later in this chapter.

Turning now to the overall accuracy of each method, it is evident from Figure 3.7 that that the contribution of individual peaks to the final T_2 spectra cannot be accurately distinguished by the use of forward inversion methods. The particular features in the simulated NMR data disappear after the NNLS-LH/GCV inversion (cases A, B), while the NNLS-LH/L-curve algorithm returns seemingly better fits with more precise peak locations (case B). Interestingly, the NNLS-LH/L-curve produces larger residuals than the NNLS-LH/GCV inversion, and has poorer PSNR, RMSE and SSIM scores (Table 3.2). The global performance of the NNLS-LH/L-curve method seems to improve when the number of echoes acquired increases (case B), matching the inversion quality metrics of the NNLS-LH/GCV algorithm. On the other hand, indirect NMR inversion approaches return T_2 distributions displaying well defined peaks. The BRD algorithm produces the best fits, in terms of both locating and estimating the amplitudes of the main peaks. The UPEN method is able to preserve the details of the original simulated data but fails to determine peak locations and amplitude correctly, while the weak associated PSNR, RMSE and SSIM scores render it the least reliable method out of the four herein analysed. Overall, the best fits are obtained with the BRD method, as confirmed by the superior inversion quality metrics. Surprisingly, the acquisition of a larger number of echoes appears to have a negative effect on T_2 inversions from the simulated dataset A, while a positive impact is observed for dataset B results.

Table 3.1.
Comparison of NMR signal intensity for the simulated T_2 datasets, inverted by the NNLS-LH/L-curve, NNLS-LH/GCV, BRD and UPEN methods.

Sample	No. Echoes	Original	Recovered	NNLS-LH (L-curve)	NNLS-LH (GCV)	BRD	UPEN
A	3,000	13.69	13.44	13.46	13.45	13.45	13.42
A	10,000	13.69	13.47	13.48	13.42	13.51	13.45
B	3,000	15.32	13.01	12.85	12.67	13.01	12.95
B	10,000	15.32	13.19	12.96	12.64	13.18	13.14

Table 3.2.
Goodness of fit for the simulated NMR data sets, inverted by the NNLS-LH/L-curve, NNLS-LH/GCV, BRD and UPEN methods. Errors are computed as the residuals between the original (Y) and predicted data ($Y^p = A\ X_\lambda$). Low RMSE, and high PSNR and SSIM values are indicative of good quality inversions.

Sample	No. Echoes	Original	NNLS-LH (L-curve)	NNLS-LH (GCV)	BRD	UPEN
			SAE $(\times 10^2)$			
A	3,000	8.22	1.57	1.50	1.46	1.71
A	10,000	18.70	5.48	5.39	5.16	5.67
B	3,000	4.15	1.67	1.63	1.39	1.82
B	10,000	10.16	5.40	5.37	5.03	5.56
			PSNR			
A	3,000	241	234	238	241	227
A	10,000	236	231	232	236	228
B	3,000	245	229	231	244	222
B	10,000	239	233	233	239	231
			RMSE $(\times 10^{-2})$			
A	3,000	41.12	6.76	6.46	6.24	7.33
A	10,000	36.95	7.01	6.91	6.59	7.25
B	3,000	21.83	7.13	7.02	6.02	7.72
B	10,000	19.27	6.83	6.83	6.39	7.02
			SSIM			
A	3,000	0.96	0.95	0.96	0.96	0.95
A	10,000	0.89	0.88	0.88	0.89	0.88
B	3,000	0.94	0.91	0.92	0.94	0.90
B	10,000	0.88	0.87	0.87	0.88	0.86

SAE: sum of absolute error; *PSNR*: peak signal-to-noise ratio; *RMSE*: root-mean squared error; *SSIM*: structural similarity index.

3.3.3. Best Practices for NMR Data Acquisition and Inversion in Shales

The acquisition and processing of NMR signal in shales is not a trivial task. The examples and analysis presented in this section provide important insights into the main factors influencing NMR results in shales, which can be summarised as:

- Good data acquisition practices favours the recording of good quality signals during NMR measurements, critical for reliable interpretations derived from inverted NMR data. The SNR of NMR signals can be improved by the acquisition of a large number of echoes along with signal averaging. Higher quality NMR data could be achieved by increasing the density of data points acquired, but this may also have the unwanted effect of enhancing experimental noise included in the recorded signals. Short echo spacing should be used during NMR measurements to facilitate the detection of fast relaxing T_2 components, abundant in shales. Prior to inversion, the corresponding post-processing techniques should be applied to the NMR raw decays to correct for the influence of noisy signals included in the recorded data.

- The fast relaxation rates in shales poses unique challenges for the inversion of NMR data. Direct inversion approaches (e.g. NNLS-LH + L-curve method) may result in very smooth T_2 distributions and the potential loss of valuable qualitative information in shales, but are likely more suitable to derive global petrophysical properties such as NMR porosity. Methods targeting noise level (e.g. BRD algorithm) may improve the quality of NMR inversion in shales but could also introduce significant bias into the solutions, so their use is recommended for the identification of individual components (and associated $T_{2\,\text{cut-off}}$ values) and qualitative interpretations.

The implications of these findings for the petrophysical characterisation of shales will become more evident in the next section, where the NMR technique is applied to study core samples from the Carynginia Formation. A new methodology is presented to determine experimental $T_{2\,\text{cut-off}}$ values, which are then compared with thresholds identified based on the approach used in this section.

3.4. Experimental Determination of Threshold T_2 cut-offs in Shales[2]

So far this chapter has focused on the principles of the NMR technique and the optimisation of experimental parameters, to obtain good quality raw and processed T_2 data in shales. The previous section laid out the foundations for the analytical determination of threshold cut-offs, based on the contrast of T_2 distributions inverted by different methods (i.e. applying fixed and variable regularisation), which will be used later in this chapter to characterise the pore volumes associated with free (FFI) and bound (BVI) fluids (Kenyon, 1997; Straley et al., 1991; Chen et al., 1998). Before exploring this approach further, this section will examine the connection between the 1D–NMR T_2 data measured in the laboratory and petrophysical properties. A novel experimental methodology will be presented to determine the threshold $T_{2\,\text{cut-off}}$ from NMR measurements on core plugs from the Carynginia Formation, acquired at different saturation levels. The analytical technique will then be integrated with the $T_{2\,\text{cut-off}}$ derived experimentally, to provide insights into the potentially producible and bound fluid fractions in shales.

3.4.1. NMR Petrophysics

The relaxation of hydrogen protons, abundant in reservoir fluids, and its quantification are the fundamental basis of the NMR technique applied to formation evaluation. NMR logging tools are thus considered to yield lithology-independent results, avoiding the pitfalls of traditional wireline logging methods (Kenyon, 1997; Anovitz and Cole, 2015). In saturated porous media, the NMR relaxation rate is a function of individual intrinsic (or bulk), surface and diffusion relaxation processes. The T_1 and T_2 relaxations in porous media are governed by the following equations (Bloembergen et al., 1948).

$$\frac{1}{T_1} = \frac{1}{T_{1,\text{bulk}}} + \frac{1}{T_{1,\text{surface}}} \tag{3.17}$$

$$\frac{1}{T_2} = \frac{1}{T_{2,\text{bulk}}} + \frac{1}{T_{2,\text{surface}}} + \frac{1}{T_{2,\text{diffusion}}} \tag{3.18}$$

[2]This section includes material from:

1. **Testamanti, M. N.**, and Rezaee, R. (2017). Determination of NMR $T_{2\,\text{cut-off}}$ for Clay Bound Water in Shales: A Case Study of Carynginia Formation, Perth Basin, Western Australia. *Journal of Petroleum Science and Engineering*, *149*, 497–503. I was the primary author.

The measured NMR data can be used to derive important reservoir properties such as porosity, pore size distribution and fluid type, as well as permeability and potential for hydrocarbon production (e.g. Timur, 1969; Kenyon et al., 1988; Prammer, 1994; Coates et al., 1998; Freedman, 2006; Dunn et al., 1994).

Porosity

One of the most critical parameters in the evaluation of hydrocarbon storage potential is the porosity of the reservoir rock. The NMR technique relies on the principle that signal amplitude at $t = 0$ is directly proportional to the net magnetization of the system, and thus to the total fluid-filled porosity (Kleinberg, 1999). Laboratory NMR porosity is estimated from the extrapolation of the first amplitude value recorded on brine-saturated core samples, and in combination with grain or bulk volume data obtained by any of the methods outlined in the API RP40 (American Petroleum Institute, 1998). The NMR spectrometer must be initially calibrated with a fluid sample of known volume with an assumed hydrogen index equal to 1 (Kenyon, 1997), ideally using the same saturating fluid and conducting all measurements at the same reference temperature. It is also important that the pore spaces in the rock are fully saturated for an accurate NMR porosity (and pore size distribution) assessment, as partially saturated pore volumes will shift the T_2 data toward shorter relaxation times (Kleinberg, 1999).

Pore Size Distribution

The T_2 rates measured in porous media arise from different bulk, surface and diffusion transverse relaxation processes (Equation (3.18)). In the *slow* diffusion regime, the measured relaxation rates are inversely proportional to the squared pore sizes (Brownstein and Tarr, 1979; Kleinberg et al., 1993). On the other hand, if T_2 is dominated by the relaxation of protons at the surface of pores, the system is said to be within the *fast* diffusion regime and the contribution from the last term in Equation (3.18) becomes negligible (Prammer et al., 1996). Furthermore, the $T_{2,\,\mathrm{bulk}}$ in water-saturated rocks is much longer than $T_{2,\,\mathrm{surface}}$, thus the transverse relaxation rates measured in such systems are directly proportional to the surface-to-volume ratio (S/V) of pores (Chen et al., 1998; Timur, 1969). Under such conditions, the T_2 spectra are considered to reflect the pore size distribution of the rock, relative to fluid type and viscosity.

When the first term and last term in Equation (3.18) are deemed negligible, the transverse relaxation of fluid-saturated rocks is governed by:

$$\frac{1}{T_2} \approx \rho_e \frac{S}{V} \tag{3.19}$$

where ρ_e is the surface relaxivity which, in general, cannot be precisely computed for complex porous systems. The *effective* coefficients ρ_e are instead determined empirically, from the comparison of NMR spectra to real pore size distribution curves obtained by other core analysis methods (Kleinberg, 1999; Lowell et al., 2004; Coates et al., 1998).

Unfortunately, the presence of multiple pore scales in shales can induce diffusional coupling effects, which violate the underlying hypothesis of Equation (3.19). This effect causes a shift in the T_2 curves, owing to the averaging of signal exchanged between the pores (Washburn, 2014), pushing the system relaxation into an *intermediate* diffusion regime (Kenyon, 1997). In such systems, direct correlations between 1D–NMR T_2 and pore size distributions are no longer valid, instead, the T_2 spectra indicate average pore sizes (Testamanti et al., 2017c).

Free Fluid and Bulk Volume Irreducible Model

The NMR data can provide additional information on the nature of pores and fluids, as well as the producibility potential of the rock. Protons associated with fluid in small pores and clay bound water are characterised by short T_2 relaxation times, whereas longer T_2 components can be correlated with fluid in larger pores and fractures. Protons in the solid matrix have even shorter characteristic T_2 times, typically in the order of 0.1 ms (Kleinberg, 1999). Based on these assumptions, a threshold T_2 parameter can be selected to distinguish between producible and irreducible pore fluids (Coates et al., 1998; Prammer et al., 1996; Chen et al., 1998). The portion of the T_2 distribution corresponding to movable fluids has an associated porosity fraction value known as *FFI* or free fluid index. The FFI is distinguished from the *BVI* (fraction of pores containing bound water) by a suitable $T_{2\,\text{cut-off}}$ value (see Figure 3.4.1). The $T_{2\,\text{cut-off}}$ parameter can be determined empirically from the comparison of NMR curves obtained for core samples at two different saturation levels, or assumed based on lithology in the absence of core NMR data (Straley et al., 1991; Coates et al., 1997; Chen et al., 1998).

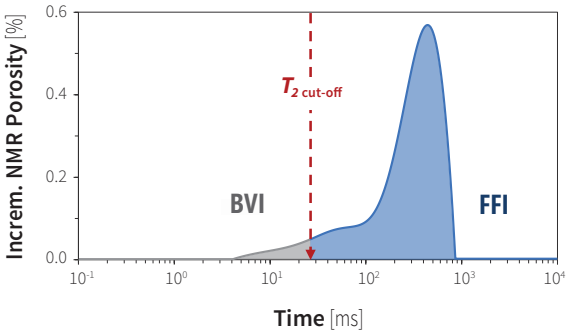

Figure 3.8 Producible (FFI) and bound (BVI) porosity fraction from the NMR T_2 distribution curve, estimated for a given $T_{2\ \text{cut-off}}$ value.

Several theoretical models have been developed to estimate permeability based on NMR relaxation data, from which the Coates model and the SDR (Schlumberger-Doll-Research) – or mean T_2 – model are the most widely used (Straley et al., 1991; Coates et al., 1997; Kenyon et al., 1988; Kleinberg, 1999). The Coates model can be applied to formations containing either water or hydrocarbons, whereas the SDR model can only be applied to rocks solely saturated with water. In the Coates model, permeability estimation depends of the $T_{2\ \text{cut-off}}$ value selected:

$$k_{\text{Coates}} = \left(\frac{FFI}{BVI}\right)^2 \left(\frac{\phi}{C}\right)^4 \tag{3.20}$$

where k is the matrix permeability, ϕ is the effective NMR porosity, and C is a constant specific to the formation. Using the SDR model, permeability is determined as a function of the geometric mean of the T_2 distribution:

$$k_{\text{SDR}} = CT_{2\text{gm}}^2\phi^4 \tag{3.21}$$

Relaxation Mechanisms in Shales

Hydrogen-rich particles confined to a bounded domain are often abundant in organic shales. Micro-porosity associated with kerogen, clays and particles adsorbed to the surface of the pore has a solid-like appearance from an NMR tool perspective (Washburn, 2014). These quasi-rigid molecules are typically absent in conventional reservoir rocks, where surface relaxation mechanisms are considered to dominate the measured T_2 signal decay provided that the applied magnetic field is homogeneous (Coates et al., 1998; Kleinberg, 1999; Kenyon, 1997). In very tight porous media, however, Brownian processes may arise from the abundance of molecules confined to a virtually restricted domain. The diffusing spins in a quasi-solid state would follow an approximately

motional-narrowing regime that can be described by a Gaussian distribution, influencing the shortest T_2 components in shales (Grebenkov, 2007; Washburn et al., 2015).

One of the inherent issues with NMR experiments is the limitation of signal acquisition in time, which can give way to distortions in the inverted spectrum that may appear as "feet" on either side of true peaks. These distinctive signatures could be the result of signal "leaks" or be in fact the signal from a separate peak that cannot be detected entirely due to spectrometer limitations (Eveleigh, 1996). The challenge is then to determine whether these features in the T_2 spectra are artifacts or if they have an actual physical meaning. For instance, relaxation rates below the first spin echo acquired are customarily excluded from the NMR data inversion, yet their decaying signal may still be partially detected in the earliest data points. If the mean of the fastest relaxing component is relatively close to the first T_2 data point acquired and measurement conditions ensure a high enough SNR, then some extrapolation can be safely done below the first real T_2 component (Moody and Xia, 2004). Furthermore, the actual detection of relaxing components below the threshold of the NMR instrument might be possible if stochastic resonance is generated. This naturally occurring phenomenon could be exploited by the dithering technique to amplify experimental noise and enhance the signal from very fast T_2 components that would generally be too weak to be detected (Pearce et al., 2008). Nonetheless, distinguishing between fast relaxing T_2 components produced by real relaxation mechanisms and those associated to ringing noise, would likely be an impossible task.

The degree of heterogeneity associated with shales, often displaying a wide separation between the smallest and largest pore scales, favours the broadening of features in NMR spectra (Watson and Chang, 1997). Additionally, the intricate shale pore network may induce large internal magnetic field gradients and thus the Brownian motion of spins, leading to deviations from the fast diffusion (Hürlimann, 1998; Song, 2000; Song, 2003; Washburn, 2014). These diffusion effects can be quantified based on laboratory 2D–NMR experiments, from which T_2 data corrections may be derived and the contribution from diffusion-induced signals estimated (Sun and Dunn, 2004). Unfortunately, obtaining sound results from borehole measurements remains impractical in shale reservoirs with the technology currently available, owing to the high levels of noise and consequently low SNR, and T_2 experiments thus remain as the most viable NMR data source to yield petrophysical information. One final point to consider is the impact of non-negligible internal gradients on the accuracy of NMR porosity determination, which may lead to its overestimation

(McPhee et al., 2015a). To minimise gradient-induced T_2 relaxation effects in shales, the use of larger core samples, low field spectrometers and short echo-spacings in the CPMG sequence, is recommended.

3.4.2. Methods and Materials

Six shale core plugs from the Carynginia Formation (SC) were used for the experimental study presented in this section. All NMR experiments were performed with a low field Magritek Rock Core spectrometer and P54 probe, suitable for 1.5" diameter samples, using the T_2 CPMG pulse sequence. The T_2 data was collected for 10,000 echoes at a 100 µs echo-spacing and 10,000 ms inter-experimental delay, with a minimum SNR value equal to 200. The pulse sequences were executed using a 16 µs acquisition time, with a 30 µs total delay.

The six SC core plugs were initially saturated with 30 g/l KCl brine, with the help of a manual pressure saturator. All samples were placed in the chamber and degassed overnight under vacuum pressure. After this, they were subjected to a 2,000 psi hydrostatic pressure for about 48 hours, until no significant pressure variations were observed in the chamber. The samples were then considered as fully saturated, their weight was recorded and T_2 experiments were performed. Next, the core plugs were separated into two subsets. Samples SC-3/SC-4 were left as control, while samples SC-1/SC-2/SC-5/SC-6 were subjected to desaturation by centrifugation and later by oven-drying (under vacuum) at increasing temperature. The experimental methodology for acquiring the NMR data on the four SC samples, summarised in Figure 3.9, was carried out as follows:

- Centrifugation

  The four shale samples were centrifuged at 4500 rpm for 26 hours, after which weights were recorded and T_2 was measured. Brine–air drainage curves can be derived from centrifugation experiments, and capillary pressure (P_c) at a particular radial distance ($r_{c\,i}$) is estimated from:

$$P_c = \frac{1}{2} \triangle \rho \, \omega^2 \, (R_c^2 - r_{ci}^2)$$

  where $\triangle\rho$ is the difference between the phase densities (brine–air), ω is the rotational speed, and R is the rotational radius of the centrifuge. For the particular centrifuge used in this study, the maximum capillary pressure achieved at a rotational speed of 4500 rpm was estimated to be ∼315 psi, which is deemed insufficient to remove the water from the smallest shale pores.

- Oven-drying

  Since the centrifuge available could not exert enough pressure to expel water from the smallest pores, a vacuum oven was employed to further desaturate the four shale samples. It is worth remembering that the boiling point of a liquid is the temperature at which its vapour pressure equilibrates with the ambient pressure. The use of a vacuum oven thus allows the vaporisation of water at lower temperatures, with the additional benefit of deterring oxidation reactions thanks to the absence of air in the chamber. While exposing shales to heat is generally not recommended, the use of a vacuum oven was deemed appropriate for identifying threshold $T_{2\ \text{cut-off}}$, owing to the impossibility of achieving irreducible saturation levels with a conventional laboratory centrifuge. In this study, the four samples were dried using a vacuum oven, at the following increasing temperatures: 50 and 60°C for 24 h; and then 80, 90, 100, 110 and 120°C until no further weight loss was observed at each drying temperature. After removing them from the oven, the cores were placed inside a sealed container and allowed to cool to the magnet temperature before T_2 was measured.

Gloves were utilised in manipulating the samples to avoid any possible contamination. For the case of re-saturated samples, weight was recorded after wiping the excess of water from the surface of core plugs. When samples had been oven-dried, they were placed in a sealed glass container and allowed to cool down to ambient temperature before weighting. Prior to NMR measurements, the core plugs were tightly wrapped with a plastic film to prevent any fluid evaporation and moisture absorption. The NMR signal from the instrument and

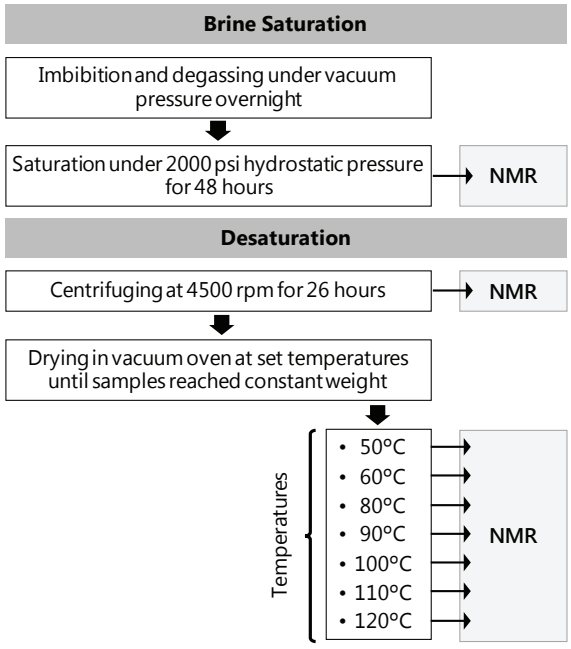

Figure 3.9 Flowchart summarising the procedure used for saturating and desaturating the four SC core plugs (SC-1/SC-2/SC-5/SC-6), upon which T_2 experiments were conducted and the experimental $T_{2\ \text{cut-off}}$ were calculated.

plastic film was collected separately and later subtracted from all shale measurements as background noise.

All T_2 decays were initially processed based on the non-negative least-squares (NNLS) method, using the Lawson and Hanson module in the Prospa software (Magritek), by which the T_2 distributions and porosity values originally reported in Testamanti and Rezaee (2017) were obtained. The NMR porosity values corresponding to this inversion method and the recorded weight loss after each oven-drying temperature were analysed for determining an optimal drying temperature value, which was capable of evaporating only the free fluid fraction from the shale cores. This temperature value was used as reference for calculating the $T_{2\ \text{cut-off}}$ after comparing the T_2 distributions from saturated and oven-dried samples, as illustrated in Figure 3.10. Samples SC-3/SC-4 were finally oven-dried at this optimal temperature to verify the $T_{2\ \text{cut-off}}$ values previously determined for the other subset of four samples.

In addition, the NMR data from the brine-saturated samples was inverted with the BRD, UPEN and NNLS-LH/GCV algorithms. The BRD inversion was performed in Prospa, using the *Asym* option in the *Lexus* module, while the UPEN and NNLS-LH/GCV algorithms were implemented in MATLAB (MathWorks). Prior to inversion, the raw NMR data was reduced via SVD.

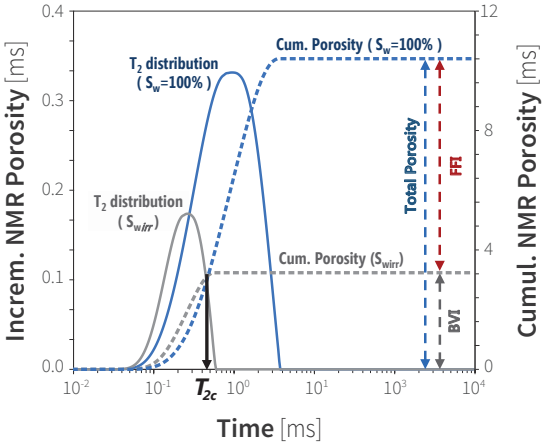

Figure 3.10 Methodology used to determine the experimental $T_{2\ \text{cut-off}}$ parameter (T_{2c} in the graph), based on laboratory NMR experiments on a sample brine-saturated (S_w=100%) and at irreducible saturation level ($S_{w,irr}$); modified from Testamanti and Rezaee (2017).

3.4.3. Results and Discussion

Repeatability of the results was determined based on samples SC-1 and SC-2, but for the sake of conciseness and clarity, the repeated tests are not shown in this subsection. More details on this can be found in Testamanti and Rezaee (Testamanti and Rezaee, 2017).

3.4.3.1. Experimental Results

- Fully saturated samples

  The T_2 distributions obtained by NNLS-LH inversion, on brine-saturated samples from the Carynginia set (SC-1/SC-2/SC-3/SC-4/SC-5/SC-6) are included in Figure 3.14. The main T_2 peaks are observed below 3 ms in all cases, suggesting small pore sizes. The unimodal T_2 distributions displayed by samples SC-1/SC-2/SC-5 are generally indicative of single dominant pore types, as is characteristic of shales with high clay content. In contrast, multiple peaks emerge from the T_2 distributions for the remaining three samples (SC-3/SC-4/SC-6), where a dominant peak is identified between 0.4–0.85 ms. In these last three samples, a significant amount of hydrogen protons appears to relax at T_2 times above 4 ms, that may correspond with larger pores present in silty shales. These three T_2 distributions also exhibit NMR signals even beyond 100 ms, which may be related to the presence of microfractures, likely induced during the re-saturation process.

- Centrifuged samples

  Figure 3.11 shows the T_2 distributions obtained by NNLS-LH inversion for the four SC samples, after brine-saturation and subsequent centrifugation. Very small weight losses in the range 0.2–0.45% were recorded for samples SC-1/SC-2/SC-5, while a 1.75% reduction was observed for sample SC-6. The magnitude of these weight differences can also be interpreted from the comparison of T_2 curves, before and after each core plug was centrifuged. After centrifugation, a signal reduction is identified on the four T_2 curves at longer transverse relaxation times, whereas the main peaks below 3ms remained mostly unaltered. These observations are generally explained by the expulsion of free water from the larger pore sizes and any microfractures present in the rock. The largest weight and NMR porosity reductions were recorded for sample SC-6, which also has the lowest clay content in the set.

  In conventional reservoir cores, irreducible saturation levels are normally achieved by the use of a laboratory centrifuge. A threshold $T_{2\,\text{cut-off}}$ can then be calculated to distinguish FFI from BVI, from the comparison of fully and partially saturated T_2 spectra (e.g. Straley et al., 1995; Chen et al., 1998). This threshold cut-off is directly related to capillary pressure and is indicative of the relative ease with which reservoir fluids may be produced. Upon inspection of the T_2 distributions, before and after centrifugation, this method was deemed inadequate to characterise the full extent of pore sizes in the shale matrix. While the capillary pressure exerted by the centrifuge

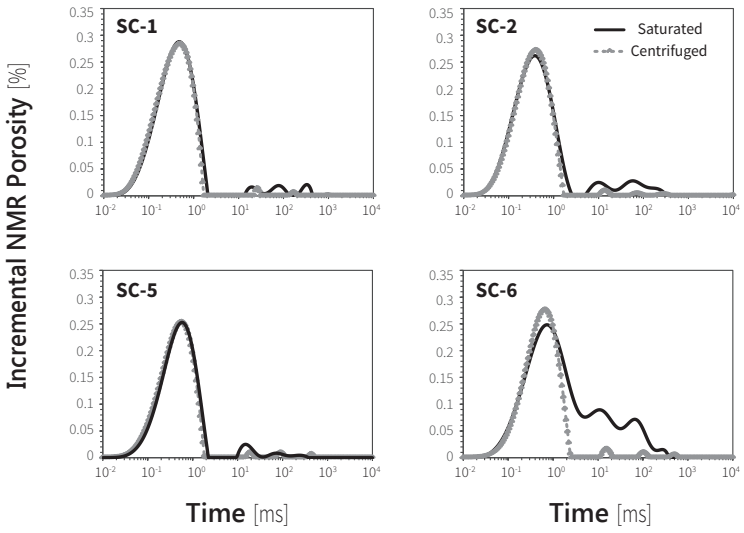

Figure 3.11. T_2 distributions from NMR experiments on four shale samples brine-saturated and after centrifugation, inverted by the NNLS-LH method.

seems to be enough to drain fluids from the larger pores and microfractures, it is insufficient to expel it from the smallest pore sizes (shorter T_2 times). The slight increase observed in the amplitude of the dominant peak could be interpreted as a redistribution of the water in the matrix pores, or as a shift arising from diffusional effects.

- Oven-dried samples

  Figure 3.12 shows the analysis of NMR porosity results and weight loss recorded for samples SC-1/SC-2/SC-5/SC-6, after being oven-dried at specific temperatures. From the graphs, the recorded weights and NMR porosities are seen to stabilise after core plugs were oven-dried at a temperature of 80°C. Beyond this point, no significant weight or NMR porosity reductions are observed.

  After fitting a power curve to these results for each sample, the change in trends was estimated to be in the 60–65°C range (Table 3.3). An dehydration temperature around 65°C was therefore selected and used to oven-dry samples SC-3 and SC-4, after which T_2 experiments were carried out. The T_2 distributions obtained by NNLS-LH inversion, on oven-dried samples from the Carynginia set (SC-1/SC-2/SC-3/SC-4/SC-5/SC-6) after stabilisation can be found in Figure 3.14.

  Although higher than the calculated boiling point of water for the vacuum oven used in this study (estimated around 35–45°C), this optimal

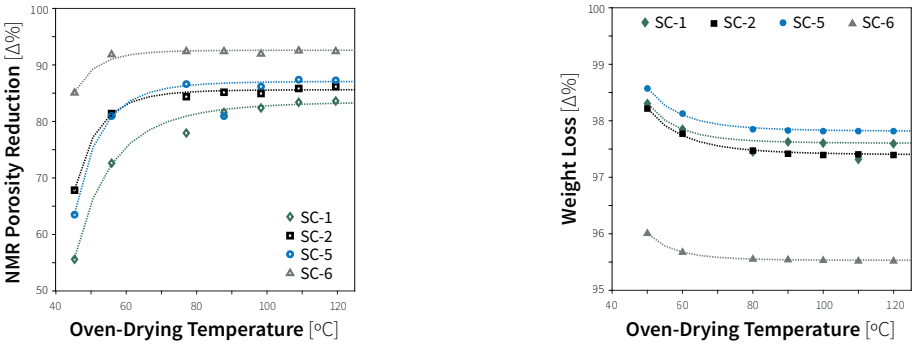

Figure 3.12. Effect of the oven-drying procedure on (a) NMR porosity reduction; (b) weight loss, recorded for each sample before NMR measurements. Adapted from Testamanti et al. (2017b).

dehydration temperature accelerates the desaturation process that would otherwise take days or weeks. The conversion of smectite to illite in shales has been largely documented in the literature (Hall et al., 1986; Singer and Müller, 1983; O'Brien and Slatt, 2012; Pytte and Reynolds, 1989; Srodon and Eberl, 1984), so the 65°C optimal oven-drying temperature was also selected to prevent unwanted changes in the pore structure that could arise from the instability of the mixed-layer illite-smectite clay types. In the original work presented in Testamanti and Rezaee (2017), abnormalities were observed in the T_2 data acquired after oven-drying the core plugs at 80°C and beyond 130°C, which were (for lack of a better explanation at the time) attributed to possible experimental errors. More recently, however, the temperature sensitivity of Carynginia shale samples was extensively analysed by Yuan et al. (2018), who found that the smectite to illite conversion process may start at around 80°C. For the Carynginia samples used in this thesis (and in the published study), mixed layer illite/smectite was the most abundant clay type and, therefore the abnormalities identified in Testamanti and Rezaee (2017) are now thought to have arisen from the abundance of these thermally sensitive clays.

3.4.3.2. Experimental Determination of Threshold $T_{2\ cut\text{-}off}$

The threshold T_2 cut-offs were obtained from the plot of the cumulative NMR porosity, after comparing the curves from fully-saturated cores, after centrifugation and oven-drying (Figure 3.10). Two threshold $T_{2\ cut\text{-}off}$ were determined after the samples were centrifuged and oven-dried: an upper T_{2U} and a lower T_{2L}, respectively. The upper thresholds T_{2U} were estimated in the

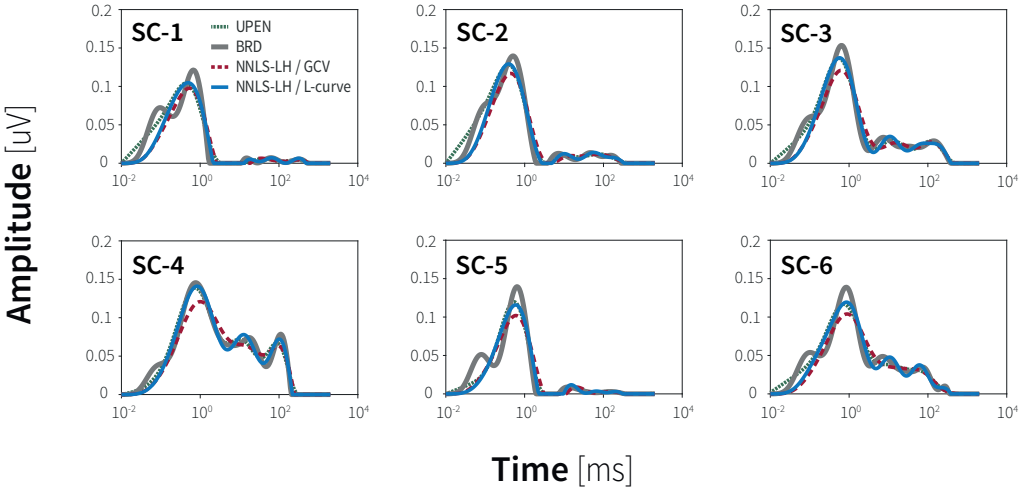

Figure 3.13. T_2 spectra for experimental decays from saturated shale core samples, obtained by the NNLS-LH/GCV, NNLS-LH/L-curve, BRD and UPEN methods.

range 1–2 ms for the four centrifuged core plugs. In the case of samples SC-3 an SC-4, an arbitrary threshold $T_{2U} = 2$ ms was applied, to obtain pseudo BVI and FFI indices comparable to experimental results using a centrifuge. For the six oven-dried samples, the lower T_{2L} were determined to be around 0.2–0.3 ms. The total, free and bound NMR porosity data, along with the corresponding T_{2L} and T_{2U}, have been summarised in Table 3.3. When permeability measurements cannot be carried out real core samples, the FFI/BVI ratio may indicate the potential pore volumes associated with producible fluids (Coates et al., 1998) which will be explored in subsequent chapters.

Although the use of common laboratory centrifuges is generally insufficient to characterise the whole pore system in the shale matrix, the associated BVI and FFI coefficients can still give useful indications of producibility. In centrifuged sample set, SC-2 and SC-6 expelled the largest fluid volumes and could thus be regarded as the most prospective intervals for producibility potential; however, both core plugs also presented visible fractures likely induced during the coring or re-saturation process. Sample SC-4 displayed the highest brine-saturated NMR porosity, however, fractures were also identified upon visual inspection of the core plug. Due to the abundance of highly sensitive minerals such as clays, a considerable fraction of the NMR porosity measured on shale cores could be associated with fluids in natural or induced fractures, thus failing to recognise these effects may lead to interpretation errors.

3.4.3.3. Comparison of T_2 Inversion Methods for the Analytical Determination of Threshold $T_{2\ cut\text{-}off}$

The T_2 raw data from experiments on the six brine-saturated SC core plugs were also inverted with the BRD, UPEN and NNLS-LH/GCV algorithms. The results are compared with the T_2 distributions initially obtained with NNLS-LH/L-curve inversion method, in Figure 3.13). The graph shows that the NNLS-LH/L-curve, NNLS-LH/GCV and UPEN methods produce similarly shaped T_2 curves, displaying one broad peak below 3 ms. In contrast, an additional peak seemingly emerges at short T_2 relaxation times, in some of the distributions obtained by BRD inversion.

The results from saturated core plugs obtained by BRD and NNLS-LH inversion are reproduced again in Figure 3.14 for clarification purposes, along with the T_2 distributions from oven dried samples (seen as dotted grey lines in the graph). While one broad peak can be observed at early times in the original T_2 spectra (NNLS-LH) from experiments in saturated shale core plugs, multiple peaks appear in the results from BRD inversion. When comparing these two curves to the spectra from oven-dried samples, the main peak in the T_2 distribution corresponding to the NNLS-LH method can be reinterpreted as the overlapped response of at least two individual features, which emerge on the T_2 curve obtained by the BRD inversion. A portion of the earliest peak in the BRD inverted curves fall below the detection limit of the spectrometer used, however, they may still represent the real NMR signals which are partially detected during T_2 measurements. The signal close to and below 0.1 ms has been associated with the transverse relaxation of structural hydroxyls in clays (Fleury et al., 2013; Washburn and Birdwell, 2013) and protons in solid organic matter (Washburn, 2014). Despite the uncertainty in the real amplitude and exact location of the additional peak distinguished by the BRD inversion around 0.1 ms, the feature is consistent with the NMR response expected in shales. The temperatures used in this study were not high enough to remove structural and bound water associated with clays (Prost et al., 1998), and therefore the signal below the calculated $T_{2\ cut\text{-}off}$ values is believed to originate from the relaxation of water bound to the surface of clays and solid organic matter.

Furthermore, two threshold cut-offs consistent with the experimental T_{2L}, T_{2U}, can be identified from the contrast of T_2 distributions obtained by the NNLH-LH and BRD algorithms. This analytical approach will be utilised in Chapter 4, to derive threshold cut-offs from T_2 data on the Goldwyer shale samples in "as-received" condition.

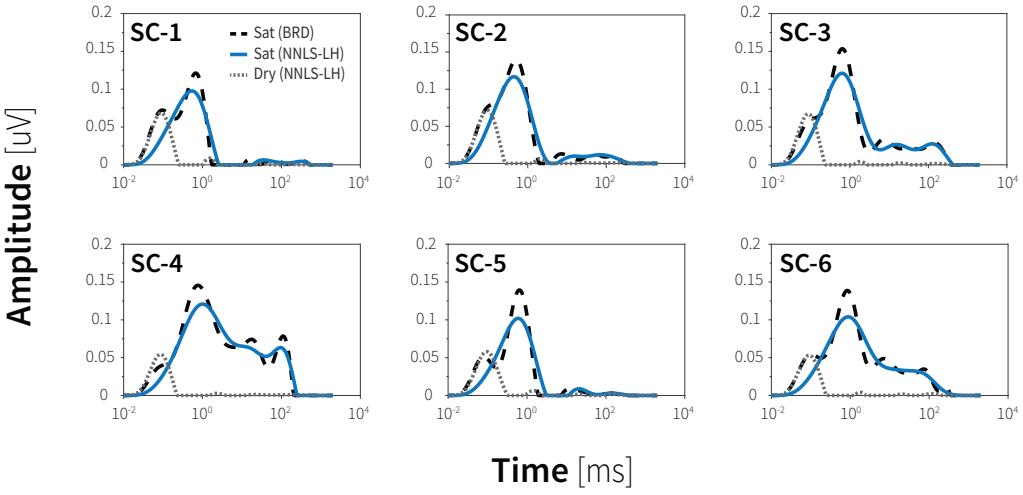

Figure 3.14. T_2 spectra from experimental decays on brine-saturated and oven-dried core samples, inverted by the NNLS-LH and BRD methods.

Table 3.3.
NMR porosity for brine-saturate core plugs, and free (FFI) and bound fluid saturation (BVI), calculated based on the threshold $T_{2\ \text{cut-off}}$ determined experimentally after centrifugation and oven-drying procedures.

Sample	NMR Porosity (%)	Centrifuge			Vacuum-Oven			Minimum Temperature (°C)
		$T_{2\ U}$ (ms)	FFI (U)	BVI (U)	$T_{2\ L}$ (ms)	FFI (L)	BVI (L)	
SC-1	10.0	1.43	0.08	0.92	0.26	0.67	0.33	64
SC-2	10.0	1.08	0.17	0.83	0.24	0.70	0.30	61
SC-3	11.5	2*	0.35	0.65	0.22	0.82	0.18	65*
SC-4	16.7	2*	0.54	0.64	0.23	0.88	0.12	65*
SC-5	8.0	1.76	0.06	0.94	0.30	0.71	0.29	60
SC-6	13.0	1.88	0.38	0.62	0.27	0.84	0.16	59

(*) Indicates real parameters used.

3.5. Conclusion

In this chapter, various aspects of the nuclear magnetic resonance (NMR) technique have been examined, with a focus on one-dimensional transverse relaxation (T_2) experiments for the ultimate petrophysical characterisation of shales. After describing the principles of the NMR phenomena and relaxometry experiments, a detailed analysis was conducted to investigate the different aspects involved in the T_2 signal acquisition and inversion process, with the objective of optimising T_2 measurements for shale applications. A methodology for the experimental determination of threshold T_2 cut-offs was then presented, and carried out on shale core samples from the Carynginia Formation. These are some of this chapter's highlights:

- Obtaining good quality NMR data can be difficult in shales. Increasing the number of scans results in extensive tests, but can also improve the experimental SNR. Alternatively, the SNR may be enhanced with the acquisition of a large number of data points, many of which will contain only noise. A good balance between noise and sensitivity to short T_2 components is essential.

- The fast relaxation rates in shales pose unique challenges for the inversion of NMR data. Direct inversion approaches (e.g. NNLS-LH/L-curve) result in very smooth T_2 distributions and the potential loss of valuable qualitative information. Methods targeting noise level, such as the BRD algorithm, can improve the quality of NMR inversion in shales but may also bias the results.

- An experimental method for the identification of $T_{2\,\text{cut-off}}$, and subsequent determination of free and bound fluid fractions in shales was proposed. The results presented indicate that a conventional laboratory centrifuge cannot generally exert enough capillary pressure to drive water out of the smallest shale pores. The use of a vacuum oven to desaturate shale cores may be a feasible method to determine secondary threshold $T_{2\,\text{cut-off}}$, provided the recommended 65°C temperature is not exceeded to avoid chemical changes in the clay types.

- An upper threshold cut-off $T_{2\,U}$ was distinguished from the experimental NMR data measured on centrifuged samples, calculated around 1–2 ms. A lower cut-off $T_{2\,L}$ was also determined after oven-drying the samples, and estimated to be within the 0.2–0.3 ms range. Overall, both experimental threshold cut-offs are consistent with findings derived from a more

analytical approach, which compared the shapes of the T_2 distributions of brine-saturated samples obtained by the NNLS-LH/L-curve and BRD inversion methods.

- The shape of the T_2 distributions at short times were found to be greatly influenced by the choice of inversion algorithm. The results presented highlight the importance of choosing an appropriate inversion method that can yield results that are representative of the real relaxation mechanisms in shales.

In the next chapter, the pore structure, connectivity and fluid types of shale samples will be investigated with different porosimetry techniques. The core analysis results are then compared with pseudo FFI/BVI coefficients determined from two threshold $T_{2\,\text{cut-off}}$, drawing upon the experimental and analytical methodologies presented in this chapter.

CHAPTER 4

Characterisation of Pore Structure and Fluid Types in Shales with the LP-CO_2 & N_2 Adsorption, MICP and NMR Techniques

This chapter examines the associations between pore structure and matrix composition in shales, and their role in the complex gas storage and transport mechanisms interplay. The introductory Section 4.1 gives a brief overview of the context and relevance of this research with regard to resource evaluation, before moving on to describe the laboratory pore characterisation methods used in this study in Section 4.2. The following Section 4.3 explains the experimental procedures and methodology used in low pressure adsorption (LP-GA), high pressure mercury porosimetry (MICP) and nuclear magnetic resonance (NMR) measurements on shale core samples from the Carynginia and Goldwyer formations. The experimental results from the different methods are then analysed, contrasted and compared with compositional data in Sections 4.4 and 4.5, for a better understanding of the petrophysical properties assessed in this chapter. Although this chapter includes some qualitative preliminary interpretations on producibility potential of the formations, a detailed discussion on the links between the pore structure attributes and gas transport mechanisms associated with shales is beyond its scope. This aspect will be investigated in the next chapter, which draws upon the entire thesis to address its final key research objective.

4.1. Introduction

Shale reservoirs are very heterogeneous and often have a highly variable mineralogical composition, presenting difficulties for the assessment of their storage and producibility potential. While many advances have been made in the stimulation and production fields, understanding the mechanisms by which gas is stored and flows in a shale formation remains a critical aspect for resource evaluation. In recent years, multiple studies have provided useful insights into these underlying processes, suggesting that therein could lie the fundamental

difference between non-commercial discoveries and economically viable shale plays. Despite the general consensus that the study of both gas storage and transport mechanisms hold the key to reducing exploration risks and optimising development strategies, the relationship between pore structure, mineralogy and permeability to gas in shales is still not fully understood.

The study of the gas adsorption and desorption phenomena is particularly important in shale reservoirs, as this mechanism plays a crucial role in the potential for gas storage and production. Most of the gas stored in shales can be found either as free gas in the inorganic pores, adsorbed to the surface of clay minerals and organic pores or dissolved in other organic phases (Javadpour et al., 2007). Initial production in these reservoirs necessarily requires hydraulic fracturing of the formation, yet as much as 85% of the total gas in place is found in a adsorbed state (Hill and Nelson, 2000). The pore structure will effect not only on how gas is stored in the rock matrix, but also on the preceding transport mechanisms within the formation that will determine its production behaviour (Bustin et al., 2008). Evaluating the gas flow properties inevitably requires a proper study into the shale pore surface, along with its porosity and pore size distribution. In this chapter, a range of laboratory techniques have been utilised to investigate the pore structure of shale core samples from the Carynginia and Goldwyer Formations. The interrelationships between these properties, mineralogical characteristics and organic richness may play an important role not only on the gas storage properties of the shale formation, but also in the assessment of producibility potential.

4.2. Background

Routine core analysis (RCA) can often provide all the petrophysical information required for the evaluation of conventional exploration projects. RCA techniques are generally insufficient for the characterisation of unconventional reservoir rocks and sometimes outright inapplicable, as a consequence of the variability in composition, pore scales and particle sizes present. A thorough assessment of shale properties can therefore only be achieved in the laboratory with a combination of multiple routine and special core analysis methods (Bustin et al., 2008; Chalmers et al., 2012; Josh et al., 2012). Low-pressure adsorption (LP-GA) methods are generally used to quantify the surface area and pore sizes of materials with a relatively large proportion of micro- and mesopores. Although they have not been traditionally utilised in the petroleum industry, these techniques offer the advantage of providing fast results and have thus becoming a popular choice for studying the

pore structure of tight rocks such as shales (Bustin et al., 2008; Chalmers et al., 2012). Based on the physisorption and capillary condensation phenomena, nitrogen (N_2 at 77 K) adsorption measurements can provide useful results in fine grained rocks with open pore sizes in the 2–300 nm range, whereas carbon dioxide (CO_2 at 273 K) may be used to characterise microporosity (Anovitz and Cole, 2015; Bustin et al., 2008; Rouquerol et al., 1994). Overall, the LP-GA technique can detect pore sizes in the 0.3–300 nm range depending on the gas employed, and it is regularly used in combination with high pressure mercury intrusion porosimetry (MICP) to evaluate a wider range of pore sizes (Lowell et al., 2004; Rouquerol et al., 1994). The MICP technique is particularly useful in shales for quantifying the portion of macropores and mesopores outside the reach of LP-GA measurements. At high pressures, pore sizes as narrow as 3 nm may be intruded by mercury, providing important information about the rock's resistance to the passage of non-wetting fluids through multiple pore scales. However, the absence of a real wetting phase and the impossibility to assess larger fractures poses limitations to the scalability of MICP core results to real reservoir behaviours. Nuclear magnetic resonance (NMR) is not affected by the shortcomings of the LP-GA and MICP methods, as the full range of pore sizes – accessible to hydrogen protons – can be detected with NMR measurements. In addition, information on the fluid types present and potential producibility of the rock, along with other petrophysical properties, can be derived from NMR data. It is worth remembering that the fluid composition and shale properties will be altered during the core retrieval and sampling process, which can lead to question the true representativeness of core analysis results at reservoir scale. Therefore, the real power of NMR lies on the possibility of correlating laboratory results acquired on cores to subsurface data measured with NMR wireline logging tools.

A comprehensive understanding of pore structure may be achieved in shales using the powerful combination of LP-GA, MICP and NMR methods. The main aspects of each technique and their use for pore characterisation in shales are explained in the next subsections.

4.2.1. Low Pressure Gas Adsorption

The adsorption phenomenon occurs at the gas-solid interface due to the interaction between the adsorbent, adsorptive and adsorbate, which indicate correspondingly the solid, the gas capable of being sorbed, and the fluid the adsorbed state (Sing et al., 1985; Lowell et al., 2004). The amount of gas or vapour that a solid surface can adsorb will depend not only on the adsorbent itself (i.e. the adsorbate-adsorbent interaction potential), but also on the

absolute temperature and pressure at which the interaction occurs. Furthermore, the reversibility of adsorption processes is controlled by the magnitude of interaction potentials between the solid surface and the gas/vapour molecules. Chemical adsorption (chemisorption) is irreversible, whereas physical adsorption (physisorption) is the reversible process behind gas adsorption pore characterisation methods, mainly driven by Van der Waal's forces (Gregg and Sing, 1982). Physisorption equilibrium can generally be achieved rapidly, allowing the quick calculation of pore surface area, while pore sizes and their distribution can be estimated from the study of the capillary condensation phenomena when pores are fully saturated with the adsorptive (Lowell et al., 2004).

For a particular gas-solid interface, the adsorption/desorption isotherms are constructed from laboratory measurements carried out at a constant temperature. Before conducting the tests, the solids must be degassed to ensure a clean surface that will allow the adsorption of molecules. This is usually achieved by heating the adsorbent under vacuum, at the maximum temperature allowed by the solid without altering its nature (Sing et al., 1985). Known volumes of gas are later injected into and withdrawn from the system, and the quantity adsorbed is calculated for a range of relative pressure points P/P° after a certain equilibration time has been achieved (Rouquerol et al., 1994). The first layer of gas will adsorb on the solid surface at lower relative pressures, and additional adsorbate layers will form as the pressure increases. The plot of quantity adsorbed versus P/P°, at a constant temperature, defines the isotherm of the gas-solid system.

In real porous materials, the reversibility of physisorption is often violated over certain pressure ranges P/P°, causing adsorption hysteresis (Sing and Williams, 2004). The shape of the isotherm curves and the corresponding adsorption-desorption hysteresis loops can then yield additional information about the pore shapes and sizes present in the solid. The IUPAC guidelines presented in Sing et al. (1985) identify six types of isotherms (Type I to VI in Figure 4.1a) and four hysteresis patterns (H1 to H4 in Figure 4.1b) associated with the physisorption and capillary condensation phenomena in most solids , based on the work of de Boer et al. (1966), Gregg and Sing (1982), Burgess et al. (1989), Everett (1967), and Brunauer (1945) among others. According Sing et al. (1985), physisorption isotherms may be classified as:

- The reversible Type I isotherm, typical of microporous materials with relatively small external surfaces. The amount adsorbed is governed by the accessible micropore volumes.
- The reversible Type II isotherm, associated with non-porous or

macroporous solids, represents unrestricted monolayer-multilayer uptake (the point B indicates the beginning of multilayer adsorption).
- The reversible Type III isotherm, indicative of weak interactions between the adsorbent and adsorptive.
- The type IV isotherm, associated with mesoporous solids, represents the initial monolayer-multilayer adsorption followed by capillary condensation. Similar to Type II curves at lower pressures, Type IV isotherms are characterised by an adsorption-desorption hysteresis loop.
- The type V isotherm also indicates weak adsorbent-adsorptive interaction and is accompanied by hysteresis.
- The type VI isotherm represents the layer-by-layer adsorption on a solid with uniform non-porous surface.

The Type I, II and IV isotherms are the most commonly exhibited by rock samples (Anovitz and Cole, 2015). According to the hysteresis loops in physisorption isotherms, Sing et al. (1985) differentiates between:

- The Type H1 curve, typical of mesoporous solids with a narrow range of uniform pore sizes.
- The Type H2 loop, indicative of materials without well-defined pore size distributions and shapes. The abrupt change observed in the desorption curve has been associated with pore-blocking/percolation and cavitation-induced evaporation processes over a range of pore throat sizes (Thommes et al., 2015).
- The Type H3 curve, observed in solids comprised by plate-like particles such as clays.
- The Type H4 loop, associated with narrow slit-shaped pores. The sharp increase of adsorbate amount at lower pressures represents the filling of micropores.

More recently, the IUPAC has expanded the original classification presented in Sing et al. (1985) and now includes two particular cases identified for Type I & IV isotherms and the H2 loop, and an additional hysteresis loop (Type H5) characteristic of mesoporous solids with open and partially blocked pores (for more information see Thommes et al. (2015)). In addition, some hysteresis loops exhibit a sharp drop in the desorption branch that represents the forced closure of the isotherm, caused by a phenomenon known as *tensile strength effect* (Gregg and Sing, 1982; Lowell et al., 2004). Isotherms where this forced closure point can be identified may indicate a considerable volume of pores with sizes below 4 nm (Groen et al., 2003; Kuila, 2013), and renders the desorption branches unusable for pore size distribution analysis.

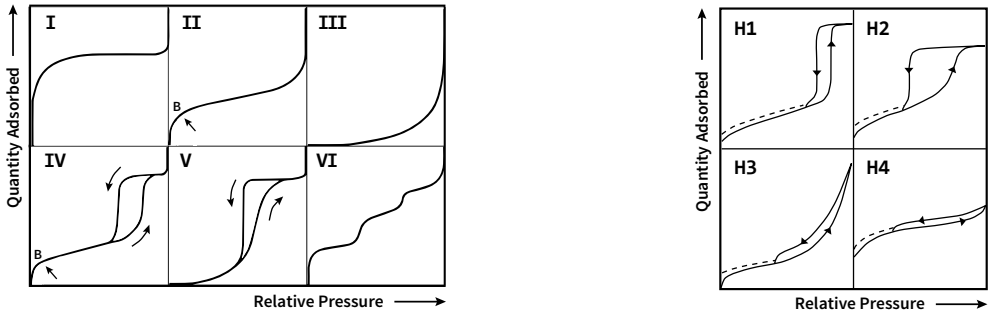

(a) **(b)**

Figure 4.1. Classification of (a) physisorption isotherms; (b) hysteresis loops (modified after Sing et al., 1985).

The Brunauer-Emmett-Teller (BET) is the most widely used method to determine pore surface area from the physisorption isotherm data (Brunauer et al., 1938). Isotherms are initially adjusted to the linear form of the BET equation:

$$\frac{P}{n(P^\circ - P)} = \frac{1}{n_m C} + \frac{C-1}{n_m C}\frac{P}{P^\circ} \tag{4.1}$$

where n is the amount adsorbed at the relative pressure P/P°, n_m is the monolayer capacity and C is an empirical constant related to the shape described by the isotherm (Rouquerol et al., 1994). Generally the application of BET linear model is restricted to the portion of the isotherm that falls in the P/P° range 0.05–0.30 (Sing et al., 1985). One of the pitfalls of the BET method is its oversimplified theoretical model, extended from the Langmuir model to represent multilayer adsorption mechanisms, which often cannot describe the real underlying processes that take place in complex porous solids (Thommes et al., 2015). Rouquerol et al. (2007) presented an improvement to the BET method, optimising its application for solids containing micropores. The specific surface area (SSA) of pores in the solid may be calculated as:

$$\mathrm{SSA_{BET}} = n_m a_m L \tag{4.2}$$

where a_m is the molecular cross-sectional area (i.e. the area occupied by each adsorbate molecule in the complete monolayer) and L is the Avogadro constant (Rouquerol et al., 1994). It should be noted that the BET and other similar method can only yield an approximation to the surface area of pores, hence this property will be referred to as *equivalent* specific surface area (*e*SSA) in this thesis. The BET-Rouquerol technique was used to quantify surface area in samples from the Goldwyer Formation, however, the values yielded from measurements on the Carynginia shales were found to be inconsistent with results from other methods.

This technique was deemed unsuitable for the estimation of surface area in the SC samples and more advanced methods were consequently explored, as explained below.

Classical models for pore size analysis from physisorption isotherm data are based on the Kelvin equation (Sing et al., 1985; Lowell et al., 2004). Among these methods, the Barrett-Joyner-Halenda (BJH) model has often been a method of choice for the characterisation of gas shales (Anovitz and Cole, 2015; Clarkson et al., 2011; Kuila, 2013; Bustin et al., 2008). One of the main issues with classical methods is –just like in the BET model– their oversimplified approach to the complex physisorption and capillary condensation mechanisms that occur in mesopores, which results in a great underestimation of pore sizes (Lowell et al., 2004). It is worth mentioning that all these classical methodologies were developed considering the extremely limited computational capabilities at a time when most analysis required the manual calculation of results, which explains their hitherto popularity. In their latest revision of recommended practices for the evaluation of pore surface area and pore size distribution from physisorption data, the IUPAC found classical models to be unsuitable for the analysis of narrow mesopores and categorically recommends against their use (Thommes et al., 2015). Some improvements were possible with the introduction of various semi-empirical models that applied corrections to a number of classical methods, but still failed to achieve a realistic representation of pore sizes. Over the last few decades, however, advancements in computer have allowed the development of more complex models that describe the real processes that occur in micro- and mesopores, based on the fundamental principles of statistical mechanics. The density functional theory (DFT), for instance, represents a superior approach to describe the adsorbate configuration at the molecular level and yields more reliable pore size results over the full nanopore range (Thommes et al., 2015). In the DFT model and similar approaches, the pore size distribution (PSD) function is obtained by solving an ill-posed numerical problem, which is fundamentally similar to the NMR inversion problem analysed in the previous chapter. The same methodologies are also be applied to stabilise the problem and approximate the solutions. The key difference between the physisorption PSD and NMR inversion problem will be the kernel function used. A number of kernel functions have been developed to account for the different pore shapes and heterogeneity of adsorbents, some of them even based on semi-classical models, which may also be used to derive pore surface area information (Landers et al., 2013). When a kernel compatible with the real nanoporous system is used, the DFT model can provide a more accurate representation of the shale pore system

(Adesida et al., 2011; Labani et al., 2013; Wang et al., 2014; Zhang et al., 2017; Wei et al., 2016; Akkutlu and Fathi, 2012). In this thesis, pore size distribution from LP-N_2 and LP-CO_2 adsorption experiments has been obtained by the DFT method, assuming slit-shaped pores. In addition, the DFT model was used to derive *e*SSA in Carynginia shale samples, as it was found to yield more realistic results than the BET-Rouquerol method.

4.2.2. Mercury Intrusion Porosimetry

The High Pressure Mercury Intrusion (MICP) porosimetry technique involves the controlled injection of a non-wetting phase (mercury) into a chamber that contains small fragments of core sample, with air assumed as the wetting phase. Due to its high surface tension, mercury cannot enter pores in the absence of external forces (Lowell et al., 2004). The underlying physical principle of the MICP method can be explained by the equation introduced by (Washburn, 1921), which describes the pressure P_c at which mercury must be injected before it can intrude a capillary radius r:

$$P_c = \frac{-2\gamma cos\Theta}{r} \tag{4.3}$$

where γ is the surface tension and Θ is the contact angle between mercury and the rock. It is evident from Equation (4.3) that only the interconnected pores can be assessed with the MICP method, and the force required to intrude them is inversely proportional to the pore throat sizes present in the rock (Anovitz and Cole, 2015). During MICP tests, mercury is pumped into the chamber until the maximum pressure allowed by the penetrometer is reached (typically ∼60,000 psia for instruments used in shale studies), while the injected volume is obtained for a number of set pressure values. As the pressure in the system increases, mercury will intrude the smallest pore throats, up to a width of approximately 3 nm at a maximum pressure of 60,000 psi (Webb, 2001). The cumulative mercury volume up to this point is then used for deriving porosity and density, among other parameters. After the injection stops, the pressure in the chamber will drop as the mercury is progressively expelled from the pores. Some mercury remains inside the pores even after the pressure falls to zero, so the intrusion and extrusion cumulative volume curves will form an open hysteresis loop (Lowell et al., 2004). In addition, the intrusion-extrusion process has been found to be thermodynamically equivalent to gas adsorption-desorption and comparable isotherm curves can be obtained from both methods (Lowell and Shields, 1981; Lowell et al., 2004; Webb, 2001).

Surface area of the intruded pores (dS) may be estimated as a function of the cumulative volume (dV) injected up to a certain pressure. If the surface values

are normalised by the sample weight, a specific surface area can be estimated that is comparable with results from other methods. The surface area calculation is independent of pore geometry (Rootare and Prenzlow, 1967; Webb, 2001), but depends on the contact angle chosen:

$$dS = -\frac{PdV}{\gamma|cos\Theta|} \tag{4.4}$$

In the absence of more accurate data, a good agreement can generally be obtained between the surface area calculated from MICP and gas adsorption by assuming an advancing contact angle between 130 and 140° (Lowell et al., 2004). Previous studies suggest that advancing contact angles around 130° are suitable for MICP analysis on quartz rich materials (Kloubek, 1981), whereas values of at least 140° are more appropriate for dolomite and organic rich solids (Schowalter, 1979). More recently, Wang et al. (2016) reported contact angles above 150° for the smallest pores in shale, obtained from molecular dynamics models purposely developed. As expected, the contact angle of mercury generally varies depending on whether the substance is advancing over a dry surface or receding from a wetted surface (Adam, 1964), with higher values associated with intrusion. In this thesis, an advancing contact of 140° was used to process intrusion MICP data for all the samples. The receding contact angle was adjusted between 104 and 106°, consistent with other values found in the literature (Lowell et al., 2004; Kloubek, 1981; Schowalter, 1979). Since the surface area derived from MICP only represents the pores accessible to mercury at the maximum injection pressure, the calculated values will be referred to as *equivalent* specific surface area (*e*SSA) in this thesis.

When it comes to the experimental procedure, significant errors can arise if the amount of sample measured is much smaller than the size of the penetrometer bulb used, or the porosity too low. The most common baseline error compensation method is known as *blank correction* and generally involves running blank tests to account for thermal and instrument compressibility effects (Webb, 2001). The acquired data from the blank run are later subtracted from real samples results, to offset the negative sample size effect. Alternatively, blank corrections may be effected based on equations that take into account material properties (Sigal, 2009). Some instrument manufacturers have also adapted general equations for specific penetrometers and offer these blank corrections through their proprietary software. Increasing the sample mass and selecting an appropriate penetrometer ultimately help to minimise baseline errors, which was the approach used in this study.

Material compressibility effects can also lead to considerable errors in the

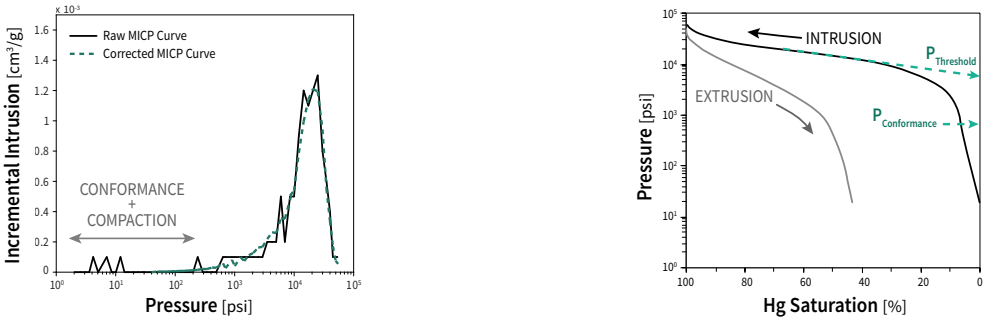

(a) **(b)**

Figure 4.2. Example graphical output and normalisation procedure for the raw MICP data (a) Incremental intrusion curve showing the effect of conformance and compression. (b) Visualisation of conformance ($P_{Conformance}$) and threshold pressure ($P_{Threshold}$).

interpretation of MICP data, which can be particularly accentuated in samples with low to moderate porosity. As the test begins, mercury will enter the chamber and fill all the voids around the sample. An initial response can be identified in the incremental intrusion curve as the mercury conforms to the sample at low pressures; this artifact is known as *conformance effect* and is caused by the surface roughness of the rock (Brown, 2015). As the chamber pressure increases, the sample will be compacted by mercury before the threshold pressure is reached and pore throats are finally intruded. Compaction continues even after initial pore throat intrusion; however, compaction effects above the threshold pressure cannot be easily recognised from the MICP data and are therefore usually included with conformance (Brown, 2015). Conformance effects can be particularly significant in shales, so the raw MICP curves must be carefully inspected and corrected to avoid an incorrect characterisation of the pore system. An example of the conformance effect on the intrusion curve and the corresponding correction is shown in Figure 4.2a.

Several models have been proposed over the years to derive permeability values from MICP curves (Pittman, 1992; Swanson, 1981; Katz and Thompson, 1986; and many others). Originally proposed by Swanson (1981), the threshold pressure is often selected as the "apex" of the cumulative curve, as illustrated in Figure 4.2b. This point indicates the pressure at which the smaller pore sizes – accessible to mercury – are intruded, and is considered as a key factor controlling permeability in unconventional reservoirs (Rezaee et al., 2012). The determination of conformance (entry) and threshold pressure can be subjective to some extent, so it is essential that MICP data analysis is carried out on raw intrusion curves to assure a consistent interpretation criterion. It is worth noting that errors in the estimation of contact angles could lead to

misinterpretations of entry and threshold pressures derived from MICP equivalent pore size distributions, and therefore have not been used for this purpose here. In this thesis, the MICP threshold pressures for shale samples have been determined graphically, at the point of inflexion in the cumulative curves upon which the first rapid increase is observed. The values obtained were then cross-checked with the methodology explained in Comisky et al. (2011).

4.2.3. Nuclear Magnetic Resonance

The measurement of longitudinal and transverse relaxation has traditionally been the main application of NMR in the petroleum industry. Transverse relaxation (T_2) is governed by the contribution of bulk ($1/T_{2\,B}$), surface ($1/T_{2\,S}$) and diffusion processes:

$$\frac{1}{T_2} = \frac{1}{T_{2B}} + \frac{1}{T_{2S}} + \frac{1}{T_{2D}} \tag{4.5}$$

In contrast, longitudinal relaxation (T_1) is only affected by bulk ($1/T_{1\,B}$) and surface ($1/T_{2\,S}$) relaxation mechanisms, according to the equation:

$$\frac{1}{T_1} = \frac{1}{T_{1B}} + \frac{1}{T_{1S}} \tag{4.6}$$

In one-dimensional relaxometry experiments, the resulting NMR signal in the saturated porous media is essentially governed by the two equations above (Kenyon, 1997), and may be used for estimating porosity, pore size distribution and even permeability (Coates et al., 1998; Kleinberg et al., 1993; Prammer et al., 1996). Unfortunately, obtaining petrophysical information from 1D–NMR T_1 or T_2 measurements becomes much more difficult in complex porous media such as shales. While T_2 experiments are preferred in conventional reservoirs, they may not be sufficient for the characterisation of shale reservoirs due to the possible overlapping of the fast relaxing components. In the case of T_1 measurements, although they are not affected by magnetic field inhomogeneities or other molecular diffusion mechanisms, some overlapping may still occur. The shortfalls of 1D–NMR measurements can be overcome with the use of more advanced multidimensional NMR techniques (Sun, 2007; Hürlimann et al., 2003; Washburn and Birdwell, 2013; Kausik et al., 2011). In particular, the contrast between measured T_1 and T_2 can provide useful information in shales. During T_1–T_2 measurements, the signal is acquired from an inversion recovery pulse sequence followed by a CPMG echo train (English et al., 1991). The resulting 2D–NMR data is then inverted for creating T_1–T_2 maps, where the different fluids in the rock may be identified based on their location (Song et al., 2002;

Birdwell and Washburn, 2015; Fleury and Romero-Sarmiento, 2016).

For heterogeneous systems in the fast-diffusion relaxation regime (Brownstein and Tarr, 1979), equations (4.5) and (4.6) can be rewritten as:

$$\frac{1}{T_i} = \frac{f_B}{T_{iB}} + \frac{f_S}{T_{iS}} \tag{4.7}$$

where f_B represents the fraction of bulk molecules within a pore, f_S is the fraction of molecules close to the pore surface, and $1/\mathrm{T_i}$ is the total measured relaxation rate, for either longitudinal (i = 1) or transverse (i = 2) relaxation. In the absence of gradient effects where Equation (4.7) is valid, the relaxation time of water in nanopores should theoretically be in the range 0.1–1 ms for surfaces relaxivities between 1 and 10 µm/s (Fleury and Romero-Sarmiento, 2016). However, Equation (4.7) becomes invalid for protons in nanopores with heavily restricted mobility, and the use of a different relaxation model that can account for dipolar interactions is required (Bloembergen et al., 1948). As a result, much shorter relaxation times will be measured for fluid molecules that are virtually immobile, typically below the detection limit of most commercial low field spectrometers. In addition, the diffusive exchange between pores, also known as pore coupling (Grunewald and Knight, 2009), may be significant in shales and could in turn lead to T_2 distributions that are not a reflection of real pore sizes (Fleury and Soualem, 2009; Washburn, 2014).

Based on the proposition that different proton populations will have distinctive associated T_1/T_2 values, recent studies have shown that the fluids present in shales may be identified in T_1–T_2 maps (Tinni et al., 2014; Birdwell and Washburn, 2015; Fleury and Romero-Sarmiento, 2016; Singer et al., 2016; Khatibi et al., 2019; Romero-Sarmiento et al., 2017). Using a low-field 2 MHz NMR instrument, Tinni et al. (2014) performed T_1–T_2 measurements on sandstone and shale core samples and found that movable fluids have a lower T_1/T_2 ratio than those immobile. The authors then propose that the magnitude of the T_1/T_2 contrast will be determined by the molecular weight of the fluids. This conclusion is supported by the work of Birdwell and Washburn (2015), who demonstrated experimentally that the geochemical properties of oil shales can be correlated to certain features in T_1–T_2 maps. Fleury and Romero-Sarmiento (2016) and Romero-Sarmiento et al. (2017) expanded previous observations by studying the signatures of different fluids in T_1–T_2 maps, acquired on isolated kerogen and shale samples with a high frequency 23.7 MHz spectrometer. Their main findings can be summarised as:

- Hydroxyls in the clay structure typically have an associated NMR signal below 0.1 ms and cannot be distinguished with most standard low-field

spectrometers.

- The signal emitted by protons in the solid organic matter has high associated T_1/T_2 values, but may be overlapped with hydroxyls depending on the level of maturity.

- Water has an associated T_1/T_2 value close to 2, even for molecules in the interlayer of clays.

- Methane, both in the free and adsorbed state, can be found close to the line $T_1/T_2 \approx 1$.

- The associated T_1/T_2 ratios of lighter oils will be higher than for water, whereas the relaxation contrast of heavy (residual) oils would be even higher (Korb et al., 2014; Tinni et al., 2014; Rylander et al., 2013).

Fleury and Romero-Sarmiento (2016) also note that the use of a lower frequency NMR spectrometer would result in smaller T_1/T_2 ratios, however, the location of the different fluids in the T_1–T_2 maps (illustrated in Figure 4.3) would not be greatly affected. This view seems to be supported by a recently published study (Khatibi et al., 2019) that explores the relationship between geochemical properties of shales samples and the fluid signatures in the corresponding T_1–T_2 maps, acquired with a high frequency spectrometer. Collectively, these studies indicate that the 2D–NMR technique based on the T_1/T_2 contrast can be a valuable tool for fluid mapping in shales. In this thesis, T_1–T_2 maps acquired on the six Goldwyer samples were utilised for evaluating the fluid types present.

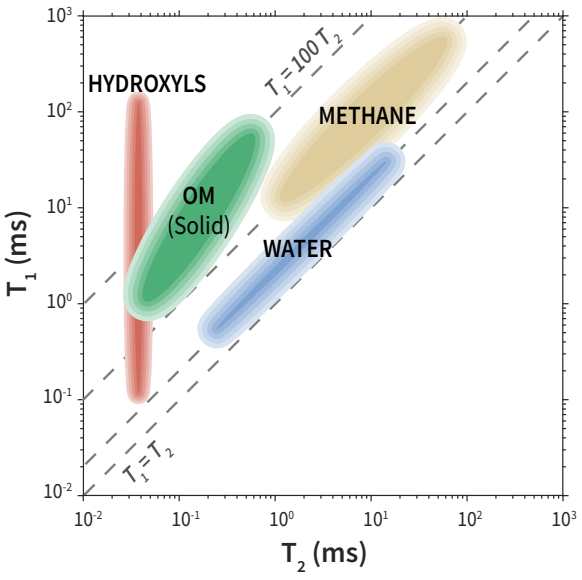

Figure 4.3 T_1–T_2 map showing the different regions associated with hydroxyls, solid organic matter (OM), water and methane in shales (modified after Fleury and Romero-Sarmiento (2016)).

4.3. Materials and Methods

The pore structure of the twelve shale samples from the Carynginia and Goldwyer Formations was studied based on a combination of NMR, MICP, and LP-CO_2 and LP-N_2 gas adsorption tests. The individual methodologies and application to each sample set are described below.

Low Pressure Gas Adsorption

- **Nitrogen**

The shale mesopores were investigated with LP-N_2 tests, conducted on all core samples at 77K. Prior to measurements, the powdered samples were degassed overnight to remove adsorbed gases and other volatile impurities from the rock surfaces, at a temperature of 90°C. In addition, isothermal jackets were placed around the sample tubes to ensure a uniform temperature during measurements. Adsorption and desorption isotherm curves were measured using between 40 and 60 points. The *equivalent* specific surface area of the SG samples was calculated based on the BET-Rouquerol method, whereas the DFT surface model was considered to be more representative in the case of SC samples. Equivalent pore size distributions (*e*PSD) were obtained based on the Broeckhoff-de Boer kernel function for slit-shaped pores in oxidic materials (de Boer et al., 1966), which works reasonably well for pore sizes above 7 nm (Lowell et al., 2004).

- **Carbon Dioxide**

In addition to LP-N_2, the micropore structure of the SG samples was also studied with LP-CO_2 experiments. The sample preparation and experimental procedure was the same as for the N_2 tests, but only adsorption isotherms were measured in the case of CO_2 analysis. To obtain (*e*PSD), the recorded data was interpreted based on a model derived from the density functional theory (DFT), assuming CO_2 adsorption on a carbonaceous material with slit-shaped pores (Tarazona, 1985; Tarazona et al., 1987).

Mercury Intrusion Porosimetry

The MICP experimental data was collected for pressure points in the range 1.5–60,000 psi, which allows the assessment of equivalent pore sizes between 3 and 3×10^5 approximately. Small rock fragments weighting 8–14 g were used for tests on samples with relatively lower clay content (<35% wt.), while smaller 1–4 g core chips were used for testing those samples that were richer in clay.

Before mercury was injected into the chamber, shale samples were degassed at a 25 µmHg vacuum pressure. In all cases, the experimental data was collected using a reference equilibration rate of at least 0.001 µL/g/s.

The raw MICP data was corrected for conformance effects based on the methodology originally proposed by Bailey (2011) and later applied in Comisky et al. (2011). The resulting MICP data was then fitted to a third degree spline and normalised, as suggested in Lenormand (2003). The correction procedure on the cumulative curves, along with the indicative conformance and threshold pressures is exemplified in Figure 4.2b. The term *entry pressure*, as used in subsequent sections, refers to the point beyond which conformance effects can no longer be clearly identified ($P_{conformance}$ in the aforementioned figure).

After making conformance effect corrections, the equivalent specific surface area (*e*SSA) was calculated at the first maximum point (or peak value) identified in the incremental area curve to procure comparable values across the whole sample set. Pore throat sizes were calculated based on the Washburn equation for a surface tension of 0.485 N/m, with an advancing contact angle assumed as 140° and a receding contact angle around 105°. Pore size distributions were approximated from the linear pore volume per unit radii distributions (dV/dr), based on a cylindrical pore model (Lowell et al., 2004; Webb, 2001).

Nuclear Magnetic Resonance

▪ T_2 Measurements on Saturated Samples

The NMR data analysed in this chapter for the six samples from the Carynginia Formation (SG) was obtained from T_2 measurements on saturated core plugs, based on the methodology specified in Section 3.4.2. The detailed NMR results for the SC samples can be found in Table 3.3.

▪ T_1–T_2 and T_2 Measurements on Samples As-Received

The NMR methodology described in Section 3.4.2 was not used on the six samples from the Goldwyer Formation. Instead, 2D–NMR T_1–T_2 measurements were conducted on SG core plugs with a 1.5" diameter in their *as-received* state, using the same spectrometer previously described and a P54 probe. In the case of the SG samples, longitudinal and transverse relaxation experiments were performed consecutively, where the NMR signal was obtained with a free induction decay (FID) pulse sequence immediately followed by a CPMG echo train. The FID sequence consisted generally of 40 logarithmically spaced values, whereas the number of CPMG pulses were adjusted to capture the full decay curve for the minimum echo time possible in the instrument, while minimising

the total measurement time. The 2D–NMR signal was then analysed and T_1–T_2 maps were created for the six SG samples. The inversion algorithm was written in Matlab, using the NNLS function included in the MERA Toolbox (Does, 2014) for the final calculation. Prior to inversion, the 2D–NMR data was compressed via SVD (Song et al., 2002). The inversion problem was regularised for minimum energy (Dunn et al., 1994) and solutions were computed with the Lawson & Hanson non-negative least squares (LH-NNLS) algorithm (Lawson and Hanson, 1974), where the regularization parameter was automatically selected based on the generalised cross-validation (GCV) method (Golub et al., 1979).

In addition, 1D–NMR T_2 curves were measured on the SG samples (as-received) with a 50 µs echo-spacing, 64 points per echo and a minimum signal-to-noise level of 240. The T_2 decays were inverted using both fixed and variable smoothing methods, based on the NNLS-LH (Lawson and Hanson, 1974) and the Butler-Reeds-Dawson (BRD) approach (Butler et al., 1981). The insights gained from the inspection of T_1–T_2 maps and T_2 distributions obtained by the BRD algorithm, were combined and two distinct T_2 cut-off values were subsequently identified (T_{2L}, T_{2U}). The T_{2L} and T_{2U} thresholds from the Goldwyer set are also consistent with the $T_{2cut-off}$ values found experimentally in the previous chapter, which were determined after comparing the T_2 spectra from brine-saturated SC core plugs with measurements after centrifuging (T_{2U}) and oven-drying T_{2L} the samples. The associated pseudo free-to-bound fluid ratios – FFI/BVI (L), FFI/BVI (U) – were then calculated from T_2 data obtained by NNLS-LH inversion, and compared with the median pore radii and widths, derived from MICP and LP-N_2 adsorption tests.

4.4. Results

4.4.1. Carynginia Shales

- LP-N_2 Adsorption

  Figure 4.4a shows the results obtained from LP-N_2 adsorption tests on the SC samples. The curves can be best represented by Type IV isotherms, as physisorption hysteresis is present (Brunauer et al., 1938). The shape of the isotherms suggests that pore networks are generally dominated by meso- and macropores, with minor contribution from micropores except in the case of samples SC-1 and SC-5. The curves also describe a Type H3 hysteresis loop, mostly visible in the SC-1 and SC-5 graphs, which are associated with clay particles slit-shaped pores (Sing et al., 1985).

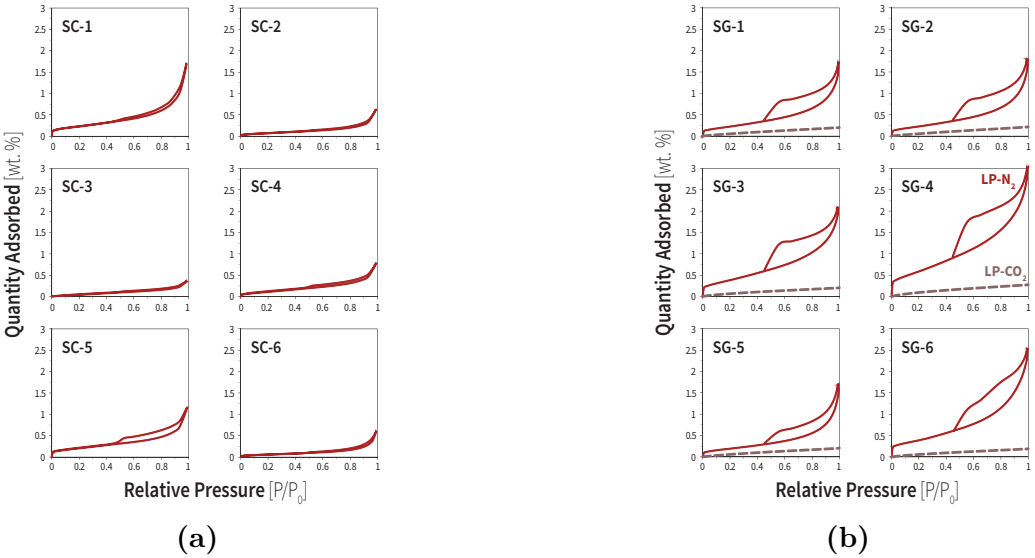

Figure 4.4. Normalised isotherm curves from LP-N_2 (solid lines) and LP-CO_2 (dashed lines) adsorption tests on samples from the (a) Carynginia Formation, Perth Basin; (b) Goldwyer Formation, Canning Basin.

- MICP Porosimetry

  Figure 4.5a shows the conformance corrected MICP curves for the SC samples, normalised for mercury intrusion. The highest entry pressures are observed for samples SC-1 and SC-2, whereas SC-6 and SC-4 display the lowest ones.

  Samples SC-1 and SC-2 are likely to have the most uniform pore size distributions, due to the more abrupt increment at low normalised mercury saturation, without further visible changes to the rate of intrusion. Since most of the intrusion occurs at higher pressure, SC-1 and SC-2 are also presumed to have the largest proportion of narrow pore sizes in the Carynginia set. Samples SC-3 and SC-5 also exhibit a gradual intrusion of mercury in the capillary pressure curves that is consistent with uniform pore sizes, but the lower entry pressure suggests generally wider pores. In contrast, the more stepwise intrusion observed in the SC-4 and SC-6 curves could be indicative of significant compression beyond the initial entry point, which may be related to the presence of a wider and continuous range of pore sizes.

  The MICP (effective) porosity and estimated threshold pressures for the SC samples are presented in Table 4.1. The lowest threshold pressures are observed for SC-4 and SC-6, whereas the highest values correspond to samples SC-1 and SC-2. The porosity ranges between 2.5–3.5% for the Carynginia set, with a mean value around 2.9%.

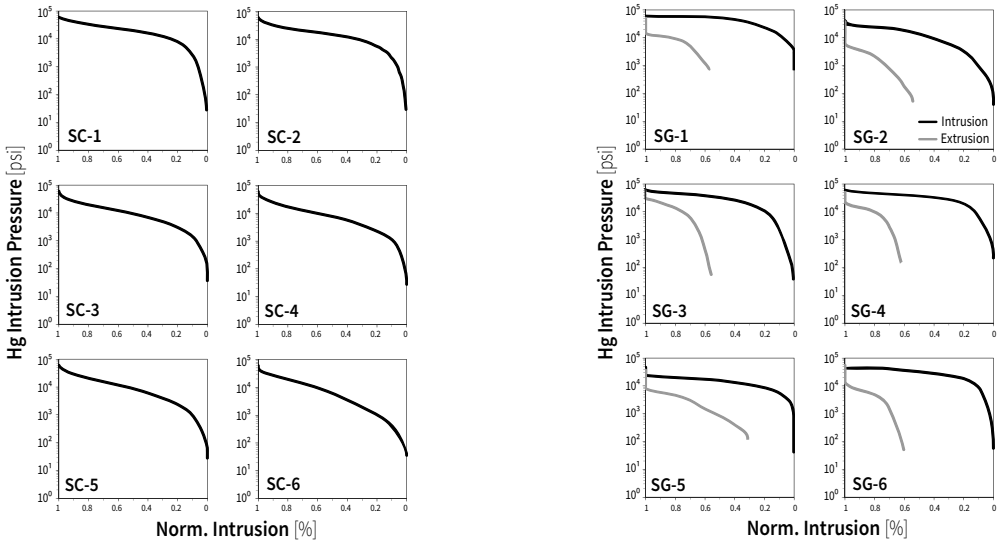

Figure 4.5. Normalised capillary pressure curves after conformance effects correction, derived from MICP intrusion (black) and extrusion (gray) tests on samples from the (a) Carynginia Formation, Perth Basin; (b) Goldwyer Formation, Canning Basin.

Table 4.1.
Results from MICP and 1D–NMR T_2 tests on samples from the Carynginia and Goldwyer formations. Parameters derived from MICP include effective porosity (ϕ_{MICP}), threshold pressure (P_{thresh}) and mean (r_{mean}), median (r_{med}) and geometric mean ($r_{\mathrm{geo\,mean}}$) pore radii. Parameters derived from NMR include the lower T_{2L} cut-off values identified and the corresponding $\frac{\mathrm{FFI}}{\mathrm{BVI}}$(L), and upper T_{2U} and associated $\frac{\mathrm{FFI}}{\mathrm{BVI}}$(U).

Sample	MICP					NMR T_2				
ID	ϕ_{MICP} (%)	P_{thr} (psi)	r_{mean} (nm)	r_{med} (nm)	r_{geom} (nm)	ϕ_{NMR} (%)	T_{2L} (ms)	$\frac{\mathrm{FFI}}{\mathrm{BVI}}$(L) (%)	T_{2U} (ms)	$\frac{\mathrm{FFI}}{\mathrm{BVI}}$(U) (%)
SC-1	3.5	4,900	6.8	23.5	19.8	10.0	0.3	2.03	1.4	0.09
SC-2	2.9	4,250	9.9	47.8	36.8	10.0	0.2	2.33	1.1	0.20
SC-3	2.7	1,650	14.1	93.6	62.8	11.5	0.2	4.56	2.0	0.54
SC-4	2.7	950	27.9	162.0	139.1	16.7	0.2	7.33	2.0	1.17
SC-5	3.1	1,700	10.8	36.7	52.0	8.0	0.3	2.45	1.8	0.06
SC-6	2.5	800	11.7	68.5	93.5	13.0	0.3	5.25	1.9	0.61
SG-1	2.8	14,500	5.7	8.3	9.9	–	0.2*	2.18	1.4	0.04
SG-2	1.5	6,600	11.7	33.7	27.8	–	0.2*	2.62	1.4	0.09
SG-3	3.2	7,200	5.7	19.9	16.8	–	0.2*	3.41	1.4	0.06
SG-4	4.9	13,400	4.0	11.7	9.9	–	0.2*	4.29	1.5	0.04
SG-5	1.3	4,800	9.9	40.2	16.8	–	0.2*	2.87	1.4	0.17
SG-6	3.9	10,050	6.8	14.1	11.7	–	0.2*	3.65	1.5	0.03

(*) Indicates T_2 measurements on "as-received" SG core plugs

- NMR T_2 Distributions

  The T_2 distributions corresponding to brine-saturated samples from the Carynginia Formation, inverted with the NNLS-LH and BRD algorithms are shown in Figure 4.6a. The vertical lines indicate the lower T_{2L} (leftmost) and upper T_{2U} (rightmost) threshold values, identified from the comparison with T_2 measurements on centrifuged and oven-dried samples (presented in the previous chapter).

  The relevant lower and upper T_2 cut-off values used for the calculation of FFI/BVI ratios are summarised in Table 4.1. The smallest values of FFI/BVI (L), between 2–2.5, are displayed by samples SC-1/SC-2/SC-5, which coincidently are the most organic rich of the Carynginia set. Sample SG-4 shows the highest values of associated lower FFI/BVI (L) coefficient (around 7.3), as well as upper FFI/BVI (U) ratio (around 1.2). Out of the remaining five samples, three of them exhibit FFI/BVI (U) values below 0.25 (SC-1/SC-2/SC-5), while the other two are around 0.6 (SC-3/SC-6). Interestingly, the smallest FFI/BVI (U) ratios in the SC set are observed for samples with the smallest characteristic pore lengths (derived from MICP/LP-N_2 adsorption tests).

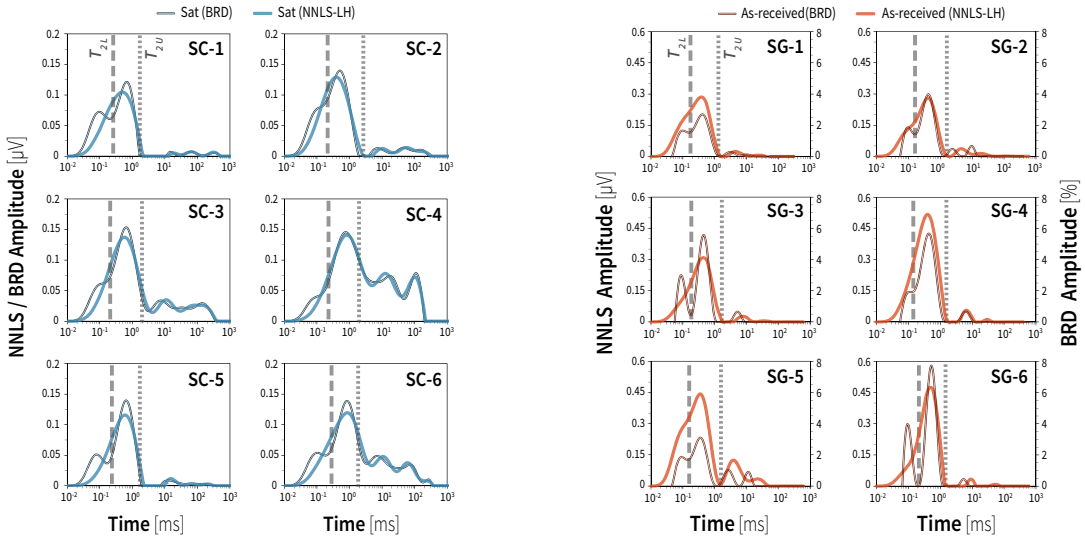

Figure 4.6. NMR T_2 distributions, obtained by NNLS-LH and BRD inversion from measurements on: (a) brine-saturated core plugs from the Carynginia Formation (SC), Perth Basin (presented earlier in Chapter 3); (b) "as-received" core plugs from the Goldwyer Formation (SG), Canning Basin.

4.4.2. Goldwyer Shales

- LP N_2 and CO_2 Adsorption

  Figure 4.4b shows the isotherm curves acquired on Goldwyer shales from LP-N_2 and LP-CO_2 adsorption tests. The LP-N_2 curves are best represented by Type IV isotherms, which are characterised by their hysteresis loops (Brunauer et al., 1938), and suggest the presence of generally significant micro-, meso- and macropore volumes. The shapes of the isotherms are associated with H3 hysteresis loops, characteristic of materials comprised by plate-like particles with slit-shaped pores (Sing et al., 1985).

  The LP-CO_2 adsorption results indicate that micropores are present in all samples, but no significant differences can be observed in the different the isotherm curves. The influence of sample composition on LP-N_2 and LP-CO_2 results will be analysed in the next section.

- MICP Porosimetry

  The conformance corrected MICP capillary pressure curves for the SG samples are shown in Figure 4.5b. The entry pressures for the Goldwyer shale samples are generally higher than those identified in the MICP curves of the Carynginia set, which suggests the presence of narrower pores.

  The breakdown of the MICP (effective) porosity values and estimated threshold pressures for the SG samples can be found in Table 4.1. A wider range of porosity values are observed in the Goldwyer set, compared to the more uniform results for the SC samples. Porosity across the sample set varies between 1.3 and 4.9 %, with SG-2 and SG-5 displaying the lowest values. Turning now to to estimated threshold pressures, the lowest value is seen for sample SG-5, whereas SG-1 and SG-4 have the highest ones.

  The hysteresis cycles formed by the intrusion and extrusion curves can be interpreted qualitatively, to gain insights on the prospective fluid transport properties of reservoir rocks. Care should still be exercised when deriving producibility interpretations from samples with considerable carbonates content, as the force exerted by the intruding mercury at a high pressure could eventually open up pathways to pores that were previously isolated. From the Goldwyer MICP graph, the gradual decline observed in the extrusion curve for SG-5 suggests that this sample could potentially offer the least resistance to the flow of non-wetting fluids.

- NMR T_1–T_2 Maps

The T_1–T_2 maps of the six SG samples (Figure 4.7) are dominated by the signal of components with T_2 below 0.1 ms, commonly associated with hydroxyls and solid organic matter (OM). The portion corresponding to each of these proton populations cannot be distinguished along the T_1 axis in any of the six charts. The low frequency of the NMR spectrometer used for measurements could be one of the reasons for this inability to differentiate between the hydroxyls and OM peak. However, another possible explanation for the merge of these features could be the inversion algorithm by which the T_1–T_2 maps were obtained. As mentioned in the previous chapter, inversion methods based on variable smoothing may be more suitable to analyse NMR data in shales than algorithms using a unique regularisation parameter. Unfortunately, attempts to extend a variable smoothing algorithm for 2D mapping of NMR data were unsuccessful during this research study. For this reason, the T_1–T_2 maps were calculated based on a combination of the NNLS Lawson & Hanson and GCV inversion methods (Lawson and Hanson, 1974; Golub et al., 1979), which use a fixed smoothing approach to solutions. Some studies have reported successful implementations of variable smoothing algorithms in two dimensions for the analysis of NMR data (Song et al., 2002; Bortolotti et al., 2016), so further research into the use of similar techniques in shales would be worthwhile.

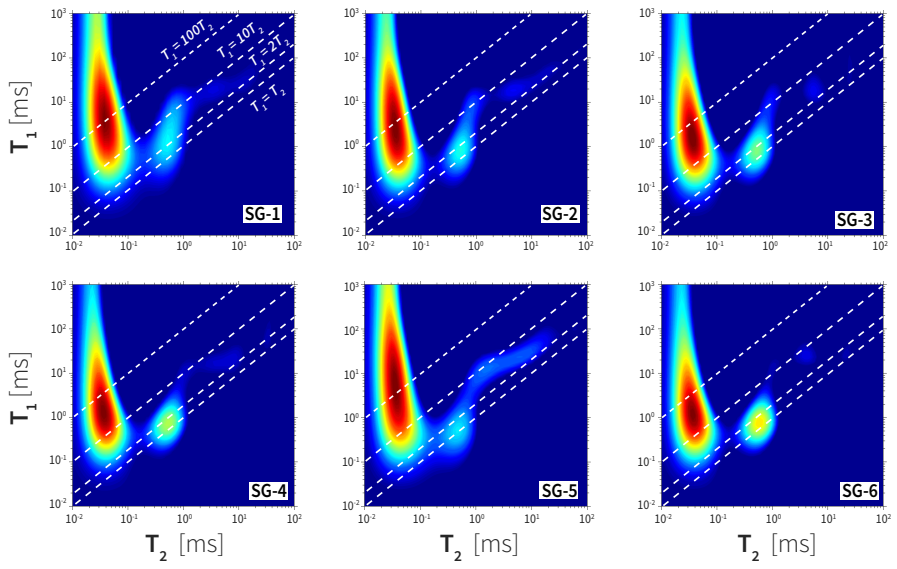

Figure 4.7. T_1–T_2 maps, acquired on "as-received" core plugs from the Goldwyer Formation, Canning Basin.

A secondary peak with T_2 between 0.1 and 1 ms can also be identified in all maps, though its amplitude (indicated by the colour intensity) varies across the sample set. Based on studies reviewed in Section 4.2.3, this feature is generally indicative of water filling the smallest pore spaces or associated with clays. The intensity of this secondary peak appears to be higher in samples SG-3/SG-4/SG-6, which coincidentally show the lowest TOC values.

A third feature, with a T_1/T_2 approximately in the range 2–10, can be distinguished in some of the maps. Some authors have proposed that the location of these T_1–T_2 features can be correlated with water in larger pores, gas and other light hydrocarbons (Romero-Sarmiento et al., 2017; Tinni et al., 2014; Khatibi et al., 2019). These peaks are more evident in samples SG-1, SG-2 and SG-5, which also show the highest measured TOC content in the Goldwyer group, suggesting signatures that are more likely indicative of gas and/or light oil, rather than water. However, there is no way to ascertain the real origin of these potentially hydrocarbons, as they could correspond to either relatively light oil that was preserved in the core samples (due to the tight nature of the pores) or to gas possibly generated during the NMR measurements (due to the partial vaporisation of light components in the solid organic matter when exposed to the 30°C magnet temperature).

- NMR T_2 Distributions

  Figure 4.6b shows the T_2 distributions from 1D–NMR measurements on SG core plugs "as-received", obtained by the NNLS-LH and BRD inversion algorithms. The vertical lines indicate the lower T_{2L} (leftmost) and upper T_{2U} (rightmost) threshold values, identified from the visual inspection of T_1/T_2 maps and the T_2 spectra inverted with the BRD method.

  All the lower and upper T_2 cut-off values, and associated pseudo FFI/BVI coefficients, can be found in Table 4.1. The lower T_{2L} is identified around 0.2 ms for the six SG samples, whereas the upper T_{2U} value is ∼1.5 ms. The pseudo FFI/BVI (L) ratios are between 2.2–4.3, whereas the FFI/BVI (U) are much lower in the 0.03–0.2 range. The smallest FFI/BVI (L) ratios are observed for the most organic rich samples of the SG set, similar to the trends identified earlier from inspection of the SC results. In contrast, the FFI/BVI (U) values appear to be more likely correlated to pore sizes, with the lowest ratios displayed by samples with the smallest characteristic pore lengths in the set.

4.5. Discussion

This section discusses the results and petrophysical properties derived from the different porosimetry methods, that are relevant to the assessment of gas storage and transport mechanisms in shales.

4.5.1. Specific Surface Area from Different Methods

Figure 4.8a shows the comparison of *e*SSA from LP-CO_2 adsorption tests on the Goldwyer samples, to results derived from other porosimetry methods. Positive correlations – with p-values < 0.05 – are observed in the plot of *e*SSA results from both MICP and LP-N_2 techniques, against the corresponding values from LP-CO_2 adsorption. The calculated correlation coefficient (R) is lower for the comparison with MICP *e*SSA data, which is expectable as the pore scales accessible to LP-CO_2 are well below the smallest pore sizes where mercury can intrude. A wide range of *e*SSA values are seen across the results from both MICP and LP-N_2 methods, whereas the values derived from LP-CO_2 adsorption are in the range 1.5–2.5 m^2/g.

Turning now to the comparison of *e*SSA from MICP and LP-N_2 adsorption tests for the twelve shale samples, a much stronger agreement is seen between the results from each porosimetry technique across both sample sets (Figure 4.8b). The SC set shows *e*SSA values between 1.4–5.5 m^2/g from MICP results, and in the range 3.5–6.8 m^2/g from LP-N_2 adsorption. In the case of SG samples, the *e*SSA results from MICP tests are in the range 0.9–11 m^2/g, whereas the

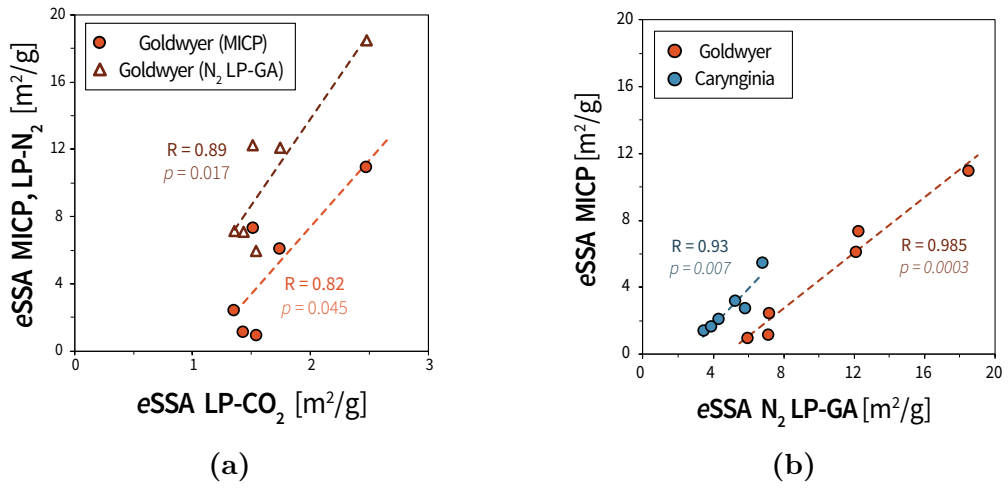

Figure 4.8. Comparison of *equivalent* specific surface area derived from: (a) LP-CO_2 versus LP-N_2 adsorption and MICP tests on samples from the Goldwyer Formation; (b) LP-N_2 adsorption versus MICP tests on samples from the Carynginia and Goldwyer formations.

values derived from LP-N_2 adsorption are between 6–18.5 m^2/g. The differences in magnitude observed for the *e*SSA from each technique is certainly consistent with the methodological differences in surface area calculation, as both methods quantify the area of inorganic pores but differ in the range of sizes that they can screen. The high correlation coefficients and low *p*-values observed in the comparison of *e*SSA results from different sources provide reassurance for the global integration of experimental data.

Relationship between *e*SSA and Composition

- LP-CO_2 Adsorption

  The comparison of *e*SSA from LP-CO_2 adsorption tests ($eSSA_{LP-CO_2}$) on the Goldwyer samples shows a weak positive correlation with the total clay content (Figure 4.9a). In addition, a moderate negative relationship (R = 0.69, *p*-value = 0.13) is observed between $eSSA_{LP-CO_2}$ and TOC (Figure 4.9b). The plot of $eSSA_{LP-CO_2}$ versus the sum of illite and smectite clay minerals (I+S) reveals a strong uphill trend, with a correlation coefficient close to 0.8 and *p*-value marginally above 0.05 (Figure 4.9c).

  The graphs below thus indicate that the *e*SSA of SG samples, quantified from LP-CO_2 adsorption tests, may vary inversely with TOC, and directly with the abundance of clay minerals that are generally associated with larger specific surface areas (I+S).

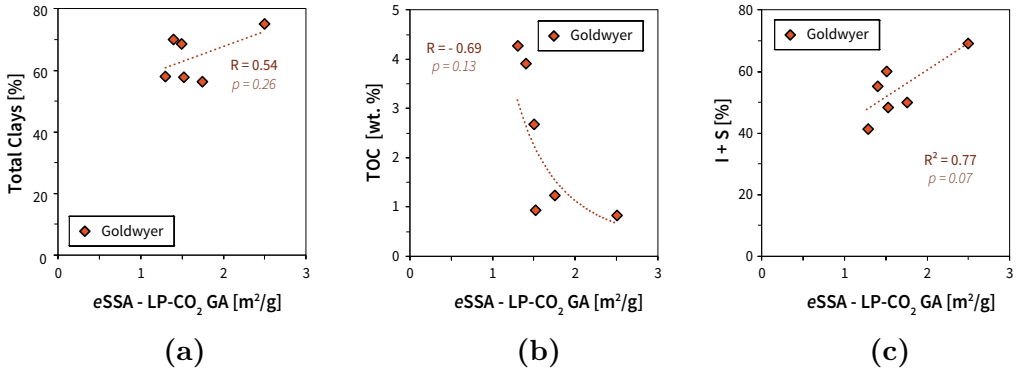

Figure 4.9. Compositional associations for the shale samples studied, comparing equivalent specific surface area (*e*SSA) derived from LP-CO_2 adsorption tests with (a) Total clay content; (b) TOC; (c) sum of illite+smectite clay minerals (I+S).

- LP-N_2 Adsorption

  Figure 4.10 shows the associations between the *e*SSA from LP-N_2 adsorption tests ($e\text{SSA}_{\text{LP}-\text{N}_2}$), and the mineralogical and geochemical composition of the shale samples studied. Uphill trends are generally observed in the comparison of $e\text{SSA}_{\text{LP}-\text{N}_2}$ versus total clay content, with a strong correlation emerging for the SC samples (p-value < 0.01) but a very weak one seen in the SG set (Figure 4.10a). In addition, the comparison of $e\text{SSA}_{\text{LP}-\text{N}_2}$ from LP-N_2 adsorption with TOC reveals a very strong positive relationship (R = 0.98) for the SC samples, and strong but negative correlation (R = 0.81) for the SG shales (Figure 4.10b). In both sample sets, the $e\text{SSA}_{\text{LP}-\text{N}_2}$ shows a similar uphill-trending correspondence with the abundance of I+S clay minerals (Figure 4.10c).

  The $e\text{SSA}_{\text{LP}-\text{N}_2}$ of the Goldwyer samples is therefore suspected to vary directly with the sum of illite and smectite clay content and inversely with TOC, which is consistent with previous findings from the inspection of $e\text{SSA}_{\text{LP}-\text{CO}_2}$ data. The analysis of LP-N_2 adsorption results also indicates that the *e*SSA in the Carynginia set may be directly influenced by the TOC and total clay content of the samples.

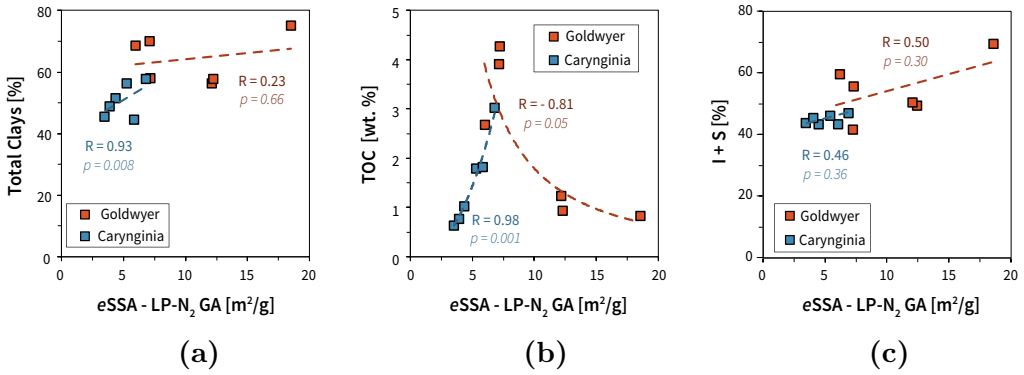

Figure 4.10. Compositional associations for the shale samples studied, comparing equivalent specific surface area (*e*SSA) from LP-N_2 adsorption tests with: (a) total clay content; (b) TOC; (c) sum of illite+smectite (I+S) clay minerals.

- MICP Porosimetry

  The results of the correlation analysis between *e*SSA from MICP tests ($e\text{SSA}_{\text{MICP}}$) and composition, for both sample sets, are presented in Figure 4.11. The plots show a strong positive correlation between

$e\text{SSA}_{\text{MICP}}$ of the Carynginia samples and total clay content (Figure 4.11a), as well as TOC levels (Figure 4.11b), while a weak uphill trend (R = 0.67, p-value = 0.14) emerges from the comparison with the content of I+S clay minerals (Figure 4.11c). In contrast, the comparison between eSSA in the Goldwyer set and TOC shows a strong negative correlation (R = 0.85, p-value = 0.03), whereas the corresponding plots with total clay and I+S content exhibit weak uphill trends.

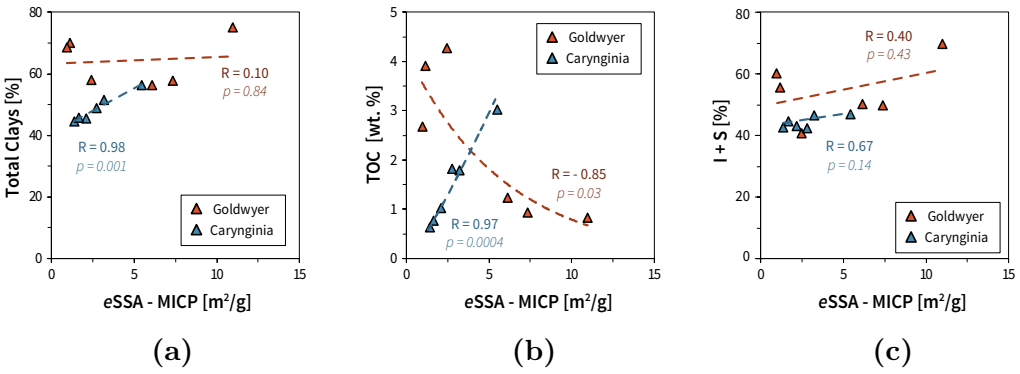

Figure 4.11. Compositional associations for the shale samples studied, comparing equivalent specific surface area (eSSA) derived from MICP tests with: (a) total clay content; (b) TOC; (c) sum of illite+smectite (I+S) clay minerals.

While the magnitude of eSSA from different porosimetry methods is not directly comparable, similar general trends emerge from their comparison with various geochemical and mineralogical properties. The analysis suggests that the organic richness and total clay content of the Carynginia shale samples may exert direct influence over the measured eSSA, showing additional weaker links to the abundance of illite and smectite clay groups. On the other hand, the eSSA of the Goldwyer samples appears to be inversely correlated to TOC levels, and – to a lesser extent – directly influenced by the sum of illite and smectite content. As explained in Chapter 2, all the Carynginia samples used in this thesis are found in the dry gas window, whereas most of the Goldwyer shales are gas + oil (or condensate) prone. Although the trends observed in this subsection must be interpreted with caution due to the small sample size, it would be interesting to assess whether these compositional relationships effect any control on the type of hydrocarbon generated by each shale formation.

4.5.2. Influence of Sample Preparation on MICP Results

When the MICP porosity results between both sample sets were compared (Table 4.1), an unexpected pattern was identified among the SC samples. Within the Carynginia set, the highest MICP porosities were displayed by samples SC-1, SC-2 and SC-5, which coincidentally also have the highest estimated threshold pressures and measured TOC. These porosity values appear to be inconsistent with the mineralogical composition of the samples, which may be highlighting a potential problem during the sample preparation stage. For instance, Burger et al. (2014) have reported differences in the porosity values measured in organic rich shale samples before and after Dean Stark cleaning, presumably caused by the dissolution of solid organic matter components.

As explained earlier, MICP data for the six samples from the Carynginia Formation were originally reported by Al Hinai (2014), but the particular sample preparation procedures prior to tests are not known. Based on the current analysis of results, the use of a harsh solvent core cleaning method before MICP measurements appears to be a plausible explanation for the counter-intuitive porosity values that were observed in the most organic-rich SC samples. Combining the Dean-Stark method with a pure toluene organic solvent can speed-up the core cleaning process and is generally the first choice for conventional rocks (American Petroleum Institute, 1998). However, the use of toluene in organic-rich shales may have the unwanted effect of dissolving the solid organic matter that conforms the matrix, as well as altering the clay structures due to the toluene high boiling point (∼111°C). Distillation methods using a methanol/toluene azeotropic mixture (boiling point ∼64°C) may increase the length of cleaning procedures considerably, but are also more gentle on clays and solid organic matter. As inferred from the examination of MICP data on SC and SG samples, gentler core cleaning methods are more suitable for shales and can lead to more consistent core analysis results.

An investigation into the effect of sample preparation – particularly degassing temperature – on the results obtained by LP-N_2 and LP-CO_2 adsorption tests falls outside the scope of this thesis. Recent work by Yuan et al. (2018) on samples from the Carynginia Formation, however, found that temperatures above 75°C may affect the shale structure so a wider study on this topic is recommended for future research.

4.5.3. Equivalent Pore Size Distribution

Figure 4.12 shows the comparison of MICP, LP-N_2 and LP-CO_2 (SG samples only) *e*PSD. The *e*PSD from MICP tests were approximated with the function

dV/dr (differential intrusion per linear pore radii), while the ratio dV/dw (differential volume per linear pore width) was used for the LP-N_2 and LP-CO_2 data.

The *e*PSD from LP-N_2 adsorption results appears as a multimodal distribution for the SC samples, and as a right-skewed distribution on the SG set. The agreement between the shape of LP-N_2 adsorption and MICP curves is relatively weak for the Carynginia shales, but stronger in the Goldwyer samples. As observed in Figure 4.12b, the full spectra of pore sizes present in the SG samples can be described by combining the *e*PSD from LP-N_2 adsorption and MICP measurements with the LP-CO_2 adsorption curves. The SC set shows generally larger mean (w_{mean}), median (w_{med}) and geometric mean (w_{geom}) pore widths determined from LP-N_2 adsorption than SG samples (Table 4.2). The *e*PSD LP-CO_2 statistics show that the w_{mean}, w_{med} and w_{geom} range between 0.41–0.53 nm in the Goldwyer set. Interestingly, the characteristic pore lengths of SG samples, determined by the different porosimetry methods, do not show any evident relationship with either their *e*SSA or sample composition. Despite correlating to different pore scales (pore width versus radius), the similarity of *e*PSD from LP-N_2 adsorption and MICP tests on the SG samples suggests that the cylindrical pore shape assumed by the latter method may be inadequate for this data set. While beyond the scope of this thesis, it would be interesting to investigate further into the suitability of the pore shapes assumed by each model for the analysis of shales.

The *e*PSD from MICP seen in the graphs is mostly unimodal for all the shales samples. Turning now to the curves statistics (Table 4.1), the calculated mean (r_{mean}), median (r_{med}) and geometric mean (r_{geom}) pore radii for the SG samples are generally lower than the values in the SC set. The larger dispersion of r_{mean}, r_{med} and r_{geom} observed for each sample in the SC set suggests the presence of narrow as well wider pore throats, compared to the narrower range of pore throat sizes found in SG shales. When threshold pressure is also taken into consideration, samples SC-1/SC-2 might possibly offer the highest resistance to fluid flow in the Carynginia group, whilst SC-4 could have the best producibility potential. In the Goldwyer group, samples SG-1/SG-4 could potentially have the worst producibility potential, whereas SG-2/SG-5 might have the best one. Overall, permeability to non-wetting fluids is likely to be higher for samples from the Carynginia Formation, in comparison to the Goldwyer shales.

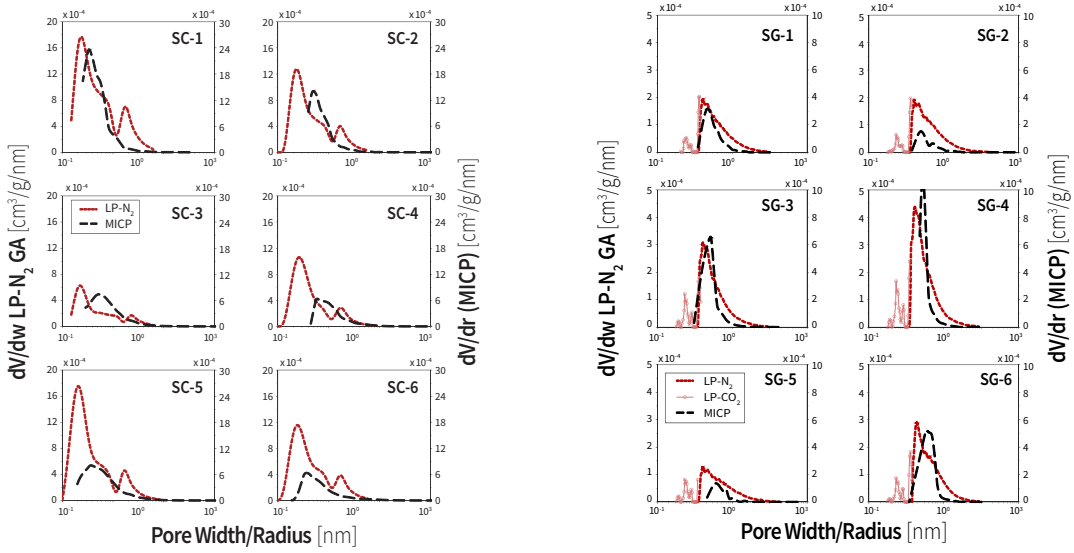

Figure 4.12. Comparison of equivalent pore size distribution (dV/dw and dV/dr) showing the results for: (a) SC shale samples, obtained from MICP (black) and LP-N_2 adsorption (red) curves; (b) SG shale samples, obtained from MICP (black), LP-N_2 (red) and LP-CO_2 (light red) adsorption curves.

It is worth noting that NMR T_2 measurements are sensitive to diffusion effects, which can arise from the differences of saturating fluid types, as seen from T_1–T_1 maps. In addition, diffusional coupling may be induced by the multiple pore scales found in shales (Washburn, 2014), ranging from nano-sized pores to larger natural or artificially-induced fractures. When diffusion effects are significant, the NMR response in shales will be averaged and consequently shifted horizontally, indicating average pore sizes only (Testamanti et al., 2017c). A direct correlation of T_2 distributions to *e*PSD obtained from other porosimetry techniques is therefore often invalid, as diffusion effects in shales cannot generally be ignored. Since direct comparisons of distributions may lead to erroneous interpretations, pseudo coefficients were obtained instead from the application of threshold values onto NMR T_2 distributions, and will be contrasted in the next subsection with other characteristic parameters derived from MICP and LP-N_2 adsorption tests.

4.5.4. Analysis of 1D–NMR Results

Two sets of free-to-bound fluid (FFI/BVI) coefficients were calculated for each sample set from NMR T_2 distributions obtained by NNLS-LH inversion, after applying the lower $T_{2\,L}$ and upper $T_{2\,U}$ cut-off values previously identified (Table 4.1). Both sets of FFI/BVI ratios (L, U) were then compared with

Table 4.2.
Equivalent pore size distribution statistics from LP-N_2 and LP-CO_2 adsorption tests on samples from the Carynginia and Goldwyer Formations: mean (w_{mean}), median (w_{med}) and geometric mean (w_{geom}) pore width.

Sample ID	LP-N_2 Adsorption			LP-CO_2 Adsorption		
	w_{mean} (nm)	w_{med} (nm)	w_{geom} (nm)	w_{mean} (nm)	w_{med} (nm)	w_{geom} (nm)
SC-1	14.1	20.1	12.6	–	–	–
SC-2	15.0	21.4	10.5	–	–	–
SC-3	19.0	24.0	14.1	–	–	–
SC-4	24.0	48.7	15.9	–	–	–
SC-5	15.0	25.5	12.6	–	–	–
SC-6	20.1	28.7	15.0	–	–	–
SG-1	5.8	10.5	4.1	0.48	0.52	0.43
SG-2	7.8	16.9	5.8	0.43	0.48	0.41
SG-3	5.8	11.9	4.6	0.48	0.53	0.45
SG-4	4.6	10.5	3.7	0.48	0.53	0.43
SG-5	8.3	15.9	6.2	0.45	0.52	0.43
SG-6	5.8	10.5	4.6	0.45	0.52	0.43

porosimetry results from MICP and LP-N_2 adsorption tests, as well as sample composition. The outcomes of this analysis are explained below.

Relationship between FFI/BVI and Composition

The comparison of the lower FFI/BVI (L) ratios with TOC and total clay content are shown in the top row of Figure 4.13. In both sample sets, a strong negative correlation emerges between FFI/BVI (L) and TOC. When the total clay content is plotted against the FFI/BVI (L), a strong downhill relationship is again found for the SC samples, whereas the SG shales exhibit opposite trends – albeit not statistically significant (p-value > 0.05). It is worth remembering that NMR measurements on the Goldywer samples were conducted on "as-received" core plugs, so the FFI/BVI ratios calculated could have been affected by the significant diffusion effects expected.

The relationships between the upper FFI/BVI (U) coefficients and both total clay and TOC content are negative-trending for the SC samples, yet the corresponding p-values are marginally above 0.05 (bottom row of Figure 4.13). In the case of SG samples, the plot of TOC and total clay content against the

FFI/BVI (U) ratios reveals uphill trends, however, the low correlation coefficients and high p-values indicate the absence of significant relationships between the variables.

The analysis suggests that sample composition is more likely to be associated with the lower $T_{2\,L}$ cut-off and corresponding FFI/BVI (L) coefficients, than with the upper $T_{2\,U}$ threshold. The organic richness of the samples, in particular, is presumably linked to the T_2 signal detected below the lower $T_{2\,L}$ cut-off. Furthermore, the analysis conducted in Section 4.5.1 showed strong correlations between TOC abundance and the *e*SSA for all samples, suggesting that it may be possible to find relationships between the FFI/BVI (L) coefficients and the petrophysical properties associated with gas storage potential in shales. As seen from the T_1–T_2 maps, distinguishing between the multiple phenomena that can lead to overlapped responses at short T_2 relaxation times is virtually impossible using only 1D–NMR data. This poses additional challenges for interpreting the FFI/BVI ratios as indicative of shale gas storage potential, however, it would be interesting to explore this topic further in the future.

Comparison of FFI/BVI and Porosimetry Data

The MICP porosity values for the SC samples are significantly lower than the NMR porosity from brine-saturated core plugs (Table 4.1). This is naturally expected due to the fundamental differences of each method, as MICP quantifies effective porosity whereas NMR detects the signal from all the hydrogen protons in the fluid-saturated sample, which is more closely related to the total porosity of the rock. Having discussed the influence of harsh core cleaning methods in shales and the limitations of each porosimetry technique, it is no surprise that the NMR porosity from SC samples do not match the trends in MICP results.

The relationships between the free-to-bound fluid ratios (FFI/BVI) and characteristic pore lengths are also explored in Figure 4.14 (top row). In each case, the pore dimensions were approximated as the median pore radii and widths, derived from MICP and LP-N_2 adsorption tests respectively. Figure 4.14 shows a good direct correlation between the FFI/BVI (L) of the SC samples and the median pore radii (MICP) and widths (LP-N_2). In contrast, the corresponding relationships are not as evident in the plot of SG results, which may be due to the presence of different fluid types in the samples. A strong positive correlation also emerges from the comparison of FFI/BVI (U) and the median pore radii (MICP) and widths (LP-N_2) in the SC samples (bottom row of Figure 4.14). In addition, a good direct correspondence can now be observed on the plot of FFI/BVI (U) ratios for the SG samples against their

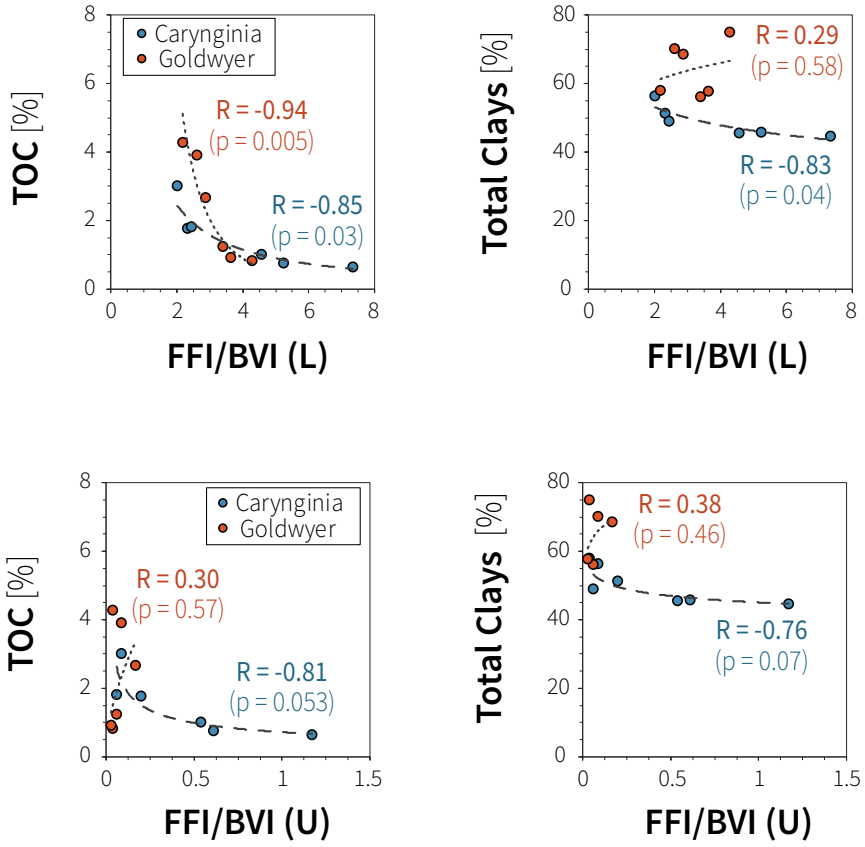

Figure 4.13. Comparison of TOC and total clay content, with the FFI/BVI ratios calculated based on (top) a lower $T_{2\,L}$ cut-off (0.2–0.3 ms); (bottom) an upper $T_{2\,U}$ cut-off (1.1–2.0 ms). The T_2 distributions for SC samples were acquired from core plugs brine-saturated, centrifuged and oven-dried. The SG samples were measured in "as-received" state.

characteristic pore lengths.

The analysis presented indicates that the impact of diffusion on NMR T_2 measurements is likely greater towards shorter relaxation times, affecting the calculation of FFI/BVI (U) coefficients. These effects might become more significant when multiple fluid types and pore scales are present, as inferred from the inspection of correlation plots for the SG samples. Overall, the FFI/BVI (L) ratios seem to be more likely associated with rock composition – in particular TOC, while the characteristic pore lengths may have more influence on the FFI/BVI (U) coefficients determined for each sample. Furthermore, if the FFI/BVI (U) ratios are interpreted as pseudo producibility indices, the graphs suggest that the resistance to fluid flow would be lower for samples with wider dominant pore sizes.

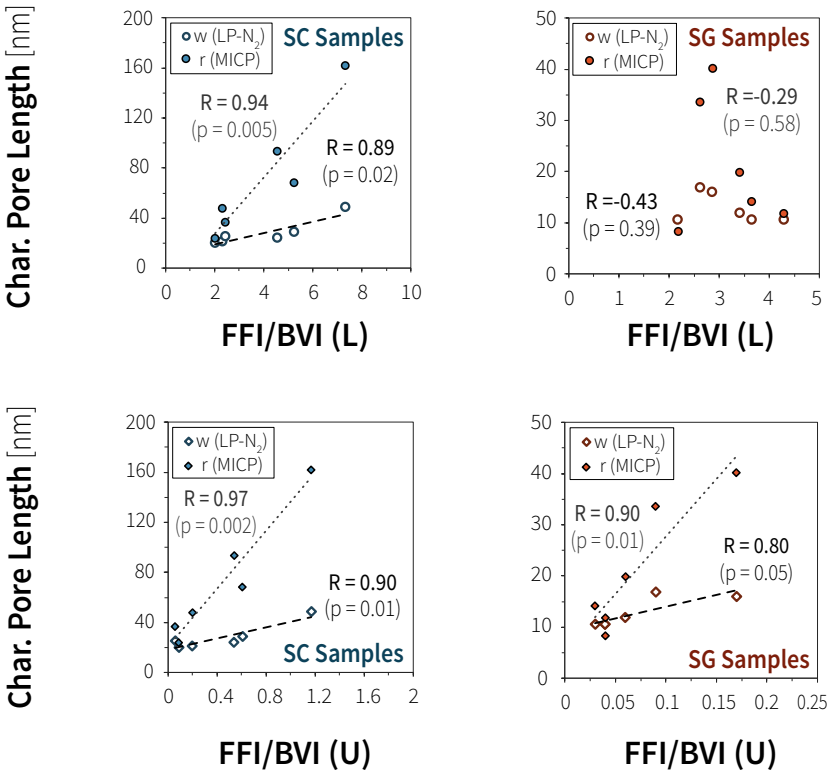

Figure 4.14. Comparison of median pore radii (r) and widths (w), from MICP and LP-N_2 tests respectively, with the FFI/BVI coefficients calculated from (top) a lower $T_{2\,L}$ value (0.2–0.3 ms); (bottom) an upper $T_{2\,U}$ value (1.1–2.0 ms). The $T_{2\,cut\text{-}off}$ for SC samples were determined experimentally from brine-saturated, centrifuged and oven-dried core plugs; the $T_{2\,cut\text{-}off}$ for SG shales were derived analytically from NMR measurements on core plugs "as-received".

4.6. Conclusion

This chapter has explored the relationships between pore structure, fluid types and matrix composition in shales. The pore networks of twelve samples from the Carynginia and Goldwyer formations were studied using the MICP, NMR, LP-CO_2 and LP-N_2 adsorption techniques; the experimental results were later contrasted and compared with the mineralogical and geochemical data. Taken together, the findings presented in this chapter indicate that gas storage and transport properties of these formations are likely dependent on multiple simultaneous mechanisms. Distinguishing between each of them can be a difficult task – or even outright impossible, however, the integration of multiple porosimetry techniques allows a greater understanding of the underlying phenomena.

The total clay content, organic richness and clay types in the shale matrix, may all exert control over the type and amount of hydrocarbons produced, as

well as the producibility potential of the formation, but do so differently in each case. The equivalent specific surface area from the different porosimetry methods appears to correlate more strongly to TOC levels, although divergent trends were observed for each sample set. The gas storage potential of the Carynginia and Goldwyer formations might thus be associated to organic richness, which for the SG samples may also be favoured by the relative abundance of certain clay types (illite + smectite), or by the total clay content in the case of the SC shales. Depositional and diagenetic processes are undoubtedly responsible for the present mineralogical and geochemical composition of the formation, and the results presented in this chapter suggest that they may ultimately play a crucial role in the gas storage and transport capabilities of shales.

The outcomes of laboratory tests on shales may also depend on the choice of sample preparation and core cleaning procedures. Harsh methods such as pure organic solvent distillation can expedite the core cleaning process, but may also lead to inconsistent porosimetry results in shales. Gentler techniques such as distillation based on azeotropic mixtures might help to prevent the dissolution of solid-like organic matter and alteration of clay structures comprising the shale matrix, and should thus be used whenever possible.

The 2D–NMR T_1–T_2 technique can yield valuable information about fluid types and sizes in shales. The analysis of T_1–T_2 maps, combined with insights derived from the application of fixed and variable smoothing inversion methods on 1D–NMR data, were used for identifying two distinct cut-off values (a lower $T_{2\,L}$, an upper $T_{2\,U}$) on T_2 distributions from both sample sets. Based on these thresholds, two free-to-bound fluid ratios (L, U) were calculated and compared with rock composition data, as well as characteristic pore lengths from other porosimetry methods. The FFI/BVI (L) coefficients showed a greater degree of correspondence with sample composition (stronger with TOC), while the FFI/BVI (U) appeared to correlate to dominant pore sizes. Notwithstanding the limited sample size used in this study, these findings suggest that there could be a link between the FFI/BVI (L) coefficients and petrophysical properties related to gas storage, whilst the FFI/BVI (U) ratios might hint at the producibility potential of the shale formation.

The next chapter will continue to explore some of the ideas above, in relation to the characterisation of flow properties in shales. The interplay between shale composition, pore structure and permeability evolution will also be discussed, to address the main research objective of this thesis.

CHAPTER 5

Experimental Assessment of Gas Transport Mechanisms in Shales

The final chapter of this thesis will investigate the different gas transport mechanisms in shales and how the interrelationships with the petrophysical parameters, identified in previous chapters, will affect prospective producibility. The first section highlights the most critical aspects of the evaluation of gas flow properties in shales that motivated this study. The next section of this chapter reviews the gas storage and transport mechanisms characteristic of shales, which are analysed throughout this thesis. The third section explains the experimental methodology utilised for permeability measurements on shale core samples from the Goldwyer Formation. The experimental results are then presented, before moving on to the discussion of permeability–effective stress models for the interpretation of permeability data. A second order gas flow equation is finally proposed and the parameters obtained by this method are extensively analysed.

5.1. Introduction

In recent years, the ever-growing global demand for secure energy sources with reduced carbon footprint has extended the frontiers of hydrocarbon exploration. The successful development of multiple North American shale gas plays over the last two decades have placed these unconventional reservoirs in the limelight, and the resilience of the Shale Revolution –even through the most recent energy price downturn– has prompted a renewed interest in shale oil and gas resources all around the world (B. Z., 2018). Evaluating the true potential of shale reservoirs is becoming increasingly important for many countries such as Australia, which is estimated to hold vast shale gas reserves that could be key for overcoming possible natural gas shortages in the near future (World Energy Council, 2016; Kehoe, 2017). In this context, understanding the complex gas storage and transport mechanisms associated with shales will be crucial to assess the viability of these unconventional plays (Figure 5.1).

The shale matrix, with its intricate pore network and diverse composition, has direct influence over hydrocarbon storage and transport properties that will

ultimately control the producibility and prospective recovery in shale gas reservoirs. Previous chapters of this thesis have addressed the difficulties in describing the pore structure in shale cores, often due to limitations in the available techniques, and discussed the main factors that affect their gas storage potential. With shale matrix permeabilities often in the nanodarcy range, characterising their gas transport mechanisms can be an even more arduous task that requires purposely developed core analysis techniques and instruments. Permeability measurements in shales can also be very time-consuming and extend over several days or weeks, thus the impact of laboratory conditions on results must also be assessed. Furthermore, the interpretation of permeability data itself requires special consideration, as the abundant narrow pore and pore throat sizes in the shale matrix can lead to deviations in fluid flow behaviour and restrict the applicability of Darcy's law. Production from shales will thus be controlled by various transport processes, which will act differently depending on the pore scales and development stage of the reservoir. This final chapter will investigate the contribution of these transport mechanisms to gas flow in shales, presenting the results from permeability measurements on Goldwyer shale samples. Having previously examined the possible control factors for gas storage potential, their impact and implications on the prospective producibility of shale reservoirs will also be assessed.

5.2. Gas Storage and Transport Mechanisms in Shales

5.2.1. Gas Storage in Shales

In shale reservoirs, the total gas in place exists as a mixture of free, adsorbed and dissolved gas (Javadpour et al., 2007; Wang and Reed, 2009; Sondergeld et al., 2010). The production of free gas, mainly stored in the non-organic shale matrix and natural fractures, is generally dominant during the early stages of development and the high initial flow rates typically observed in new wells are achieved by extensive hydraulic fracturing of the formation. In contrast, the gas adsorbed to the pore walls and dissolved in the solid organic matter are associated with the stable flow rates commonly seen in wells at later production stages, with their contribution becoming more important as the reservoir pressure drops (Valkó and Lee, 2010; Clarkson, 2013; Gensterblum et al., 2015).

5.2.2. Gas Transport in Shales

Despite the abundance of narrow pore throats, extensions of Darcy's law and other fundamental fluid flow equations commonly used in the petroleum industry may still be used in shale reservoirs, depending on the length scales and as long as their limitations are recognised. This requires a good comprehension of the underlying gas transport processes, which are inherently different from those associated with conventional reservoir rocks. Yet these processes have been traditionally studied from the cap or source rock perspective in shales, with most of the literature focusing on their role as both source and reservoir only being published in the last decade (Gensterblum et al., 2015).

The flow mechanisms naturally occurring in the nanoscale shale pores are significantly different than the mass transport processes along the hydraulic fractures and closer to the borehole, as illustrated in Figure 5.1. In new wellbores, the gas stored in the largest pores is initially contacted by induced hydraulic fractures and flows into the borehole under a gas slippage or even continuum flow regime. Gas production from smaller pores ensues, before non-equilibrium conditions prompt the desorption of gas originally absorbed to the surface of clays and solid organic matter (Javadpour et al., 2007). Brownian processes are dominant in the solid organic matter (molecular scale), where

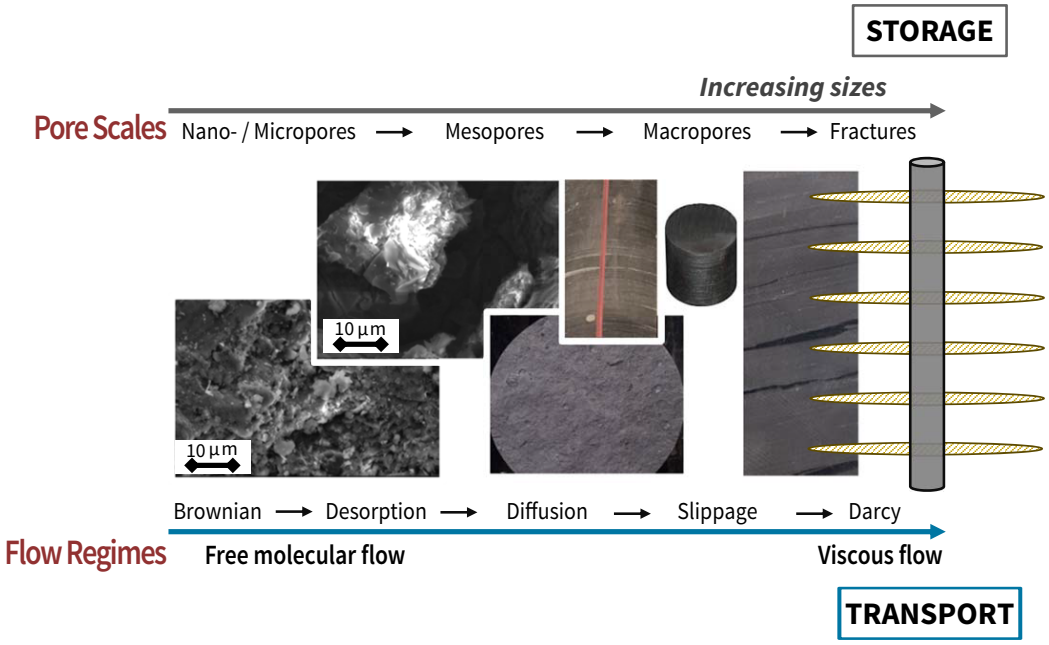

Figure 5.1. Illustration of the multiple gas storage and transport mechanisms that are present in shale reservoirs.

movement of gas molecules is caused by concentration imbalances and non-equilibrium conditions. In the nanoscale pores, diffusion mechanisms govern gas flow and therefore cannot be modelled by Darcy's equation (Akkutlu and Fathi, 2012; Singh et al., 2014; Zhang et al., 2015; Civan, 2010; Darabi et al., 2012; Javadpour, 2009).

Gas Flow Regimes

Flow regimes can be differentiated based on the Knudsen number K_n (Javadpour and Ettehadtavakkol, 2015), which relates the mean free path of gas (λ) and the characteristic length (ℓ) of the porous medium:

$$K_n = \frac{\lambda}{\ell} \tag{5.1}$$

Additionally, the mean free path λ is defined as:

$$\lambda = \frac{k_B T}{\sqrt{2}\pi\delta^2 P} \tag{5.2}$$

where k_B is the Boltzmann constant, T is the temperature, P is the absolute pressure and δ is the kinetic diameter of the gas molecule. According to their Knudsen numbers, flow regimes governed by the Navier-Stokes equations may be classified into viscous/Darcy flow for K_n <0.001, or slip flow (Klinkenberg) for K_n between 0.001–0.1, as illustrated in Figure 5.2. Knudsen numbers in the range 0.1–10 are associated with transition flow, whereas K_n >10 indicates the free molecular flow regime, for which the traditional Navier-Stokes equations are no longer valid (Sondergeld et al., 2010; Javadpour and Ettehadtavakkol, 2015).

The transport properties of shales can be determined from core-flooding experiments, where gas is forced through a core sample. At very low Knudsen numbers, the mean free path of gas molecules is significantly smaller than the characteristic pore diameters so gas will behave like a viscous fluid while flowing through the porous media. Darcy gas flow can be described with the equation introduced by Darcy (1856), adapted for compressible fluids:

$$Q_g(P_{atm}) = \frac{k_g\, A\, ({P_{up}}^2 - {P_{down}}^2)}{2\, P_{atm}\, \mu\, L} \tag{5.3}$$

where Q_g represents the volumetric outflow rate measured at the atmospheric (or reference) pressure P_{atm}, k_g is the Darcy permeability to gas, μ is the gas viscosity,

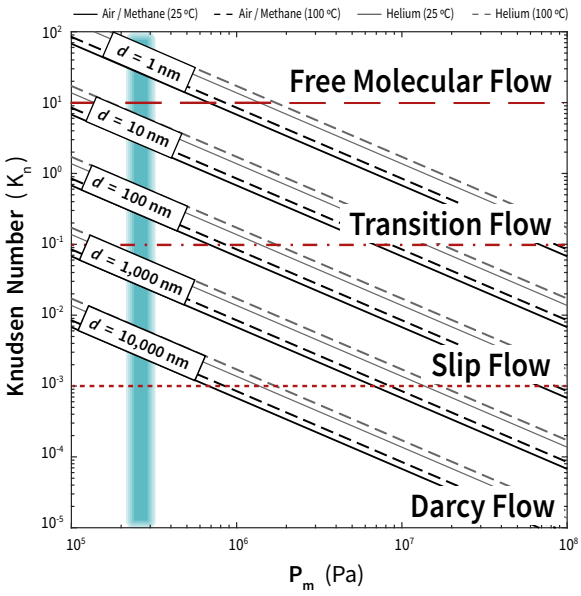

Figure 5.2 Knudsen numbers (K_n) as a function of mean pore pressure (P_m) for various mean pore sizes (d), indicating the gas flow regimes for helium and air/methane (at 25, 100 °C). The pore pressure ranges used in this experimental study are highlighted.

A is the cross-sectional area (perpendicular to flow) and L is and thickness (along the direction of flow) of the porous medium, and P_{up} and P_{down} are the upstream and downstream absolute pressures, respectively (American Petroleum Institute, 1998; McPhee et al., 2015b). Equation (5.3) is widely known as Darcy's law for isothermal (inert) gas flow though porous media, valid under the assumptions of negligible inertial effects and a non-reactive medium to the flowing fluid, and is analogous to the Hagen–Poiseuille law for fluid flow along pipes. It should be noted that no significant inertial macroscopic effects are generally observed in tight rocks at small pressure differentials (American Petroleum Institute, 1998; Jin et al., 2015). Since the experimental study presented in this chapter was carried out under such conditions and only matrix permeability was considered, inertial corrections to Darcy's law will not be covered in this thesis but a rigorous analysis on this matter can be found in Lasseux and Valdés-Parada (2017).

Rarefaction effects increase significantly at very large Knudsen numbers, resulting in mean free paths of gases that are equal or greater than the characteristic length of the porous medium. The gas flow will then be dominated by the interactions between gas molecules and the solid surface, giving rise to a phenomenon known as Knudsen diffusion (Knudsen, 1909). Mass transport due to diffusion processes are governed by the fundamental equation known as Fick's first law, where the concentration gradient ($\nabla\varphi$) is related to the diffusion flux (J) by a coefficient (D):

$$J = -D\,\nabla\varphi \tag{5.4}$$

The parameter D, sometimes referred to as *diffusivity*, depends on the squared velocity of the diffusing discrete particles, which varies with the particle sizes,

fluid viscosity and temperature. Under the free molecular regime, gas movement through a porous medium no longer describes a viscous flow and will instead be controlled by the random motion of the sum of discrete particles.

Two intermediate cases can be distinguished at Knudsen numbers in the range 0.001–0.1, depending on the relative influence of the underlying mechanisms in Darcy and free molecular flow. As Kn increases and the mean free path of gas molecules approach the characteristic pore sizes of the medium, the interactions between the individual molecules and the pore walls become more frequent, causing deviations from the physical principles of Darcy's law. When viscous forces are still dominant over diffusion processes, this phenomenon is known as gas slippage or Klinkenberg effect (Knudsen effect in other disciplines) and can be described by a semi-empirical model extended from Darcy's equation. Klinkenberg (1941) showed that the k_g determined in Equation (5.3) represents the apparent permeability to gas of the porous medium and approximates a limiting value (k_∞) at infinite pore pressures. The calculated k_g values can be linearly correlated with the reciprocal mean pore pressure ($P_p = \frac{P_{up}+P_{down}}{2}$) at which measurements were conducted, according to:

$$k_g = k_\infty \left(1 + \frac{b}{P_p}\right) \tag{5.5}$$

where k_∞ is commonly denominated the Klinkenberg-corrected –or absolute– permeability, and b is an empirical parameter that depends on the porous medium and gas properties. At Knudsen numbers above ∼0.1, diffusion effects become much more prominent and have a greater influence over the macroscopic gas flow than viscous forces. The interactions in the region closest to the solid surface, known as Knudsen layer, are not considered in the original equation proposed by Klinkenberg (1941) thus a different formulation should be used to quantify the contribution from molecular diffusion mechanisms under these particular conditions. Slippage effects may then be quantified from the relationship between the parameter b and pore geometry, derived after combining the Hagen–Poiseuille and Knudsen equations. Assuming cylindrical pores, b is related to the effective mean pore diameter (d) of the system as follows:

$$b = \frac{8\, c\, \lambda\, P_p}{d} \tag{5.6}$$

where the dimensionless coefficient c is known as the Adzumi constant and has a value around 0.9–1 for simple gases, at high and low pressures respectively, and ∼0.7 for hydrocarbon gas mixtures (American Petroleum Institute, 1998; Adzumi, 1937; Klinkenberg, 1941). For slit-shaped pore geometries, the relationship above

is transformed into:

$$b = \frac{16\, c\, \mu}{w} \left(\frac{2\, R\, T}{\pi\, M} \right)^{1/2} \tag{5.7}$$

where R is the universal gas constant, M is the gas molar mass, and indicates the effective mean pore widths (Randolph et al., 1984). Shale gas reservoirs generally fall under the viscous, slip and transition flow regimes so various models have been proposed in recent years based on the Hagen–Poiseuille equation with computational efficiency in mind (Javadpour, 2009; Darabi et al., 2012; Civan, 2010). Most equations for the study of gas flows in tight porous media stem from the work by Beskok and Karniadakis (1999), who incorporated both slippage and diffusion mechanisms into the Navier-Stokes equations (based on simple channel, pipe and duct geometries) and proposed a unified model to describe gas transport suitable for the full range of Knudsen numbers.

Factors Affecting Permeability in Shales

Several studies have shown that permeability is a highly anisotropic property in shales, strongly influenced by changes in effective stress and pore pressure (Kwon et al., 2001; Ghanizadeh et al., 2014; Fink et al., 2017; Heller et al., 2014; Shen et al., 2018; Letham and Bustin, 2016; Sinha et al., 2013; Moghaddam and Jamiolahmady, 2016). Mineralogy will also play an important role, not only as an indirect controlling factor for gas slippage but also influencing the poroelastic behaviour of shale reservoirs (Kwon et al., 2004; Ghanizadeh et al., 2014; Heller et al., 2014; Fink et al., 2017). The complex interrelationship between the mineralogical composition and fabric of the rock and the pore sizes present affects the Knudsen number, which in turn determines the dominant gas flow regime (Chalmers et al., 2012; Loucks et al., 2012; Bustin et al., 2008; Javadpour and Ettehadtavakkol, 2015).

From equations (5.1) and (5.2), gas slippage effects are found to be directly influenced by the characteristic pore sizes in the rock, as well as the type of flowing gas and pore pressure and temperature conditions. These effects are illustrated in Figure 5.2, which shows that the Knudsen number will increase with decreasing pore sizes and pressures. In addition, slippage effects will be enhanced by gas molecules with smaller kinetic diameters (such as Helium) and higher gas temperatures. Deviations from the linear relationship depicted by Equation (5.5) have also been reported from simulation studies at sufficiently low pore pressures and diameters (i.e. high Knudsen numbers), for which second order equations were found to yield more accurate representations of real gas transport mechanisms (Tang et al., 2005; Fathi et al., 2012).

The stress-dependence of transport properties in shales has been the focus of

a number of recent studies (Kwon et al., 2001; Tinni et al., 2012; Ghanizadeh et al., 2014; Heller et al., 2014; Fink et al., 2017; Shen et al., 2018), which found that confining pressure variations generally have a greater impact on matrix permeability than pore pressure. These observations have significant implications for the assessment of producibility potential in shale gas reservoirs, as the core permeability measured under large effective stresses could hint at the future behaviour during the depletion stage. Pore structures will be affected by the increasing weight of the lithostatic column as the reservoir pressure drops, resulting in narrower effective pore apertures. Nonetheless, the impact of stress-induced pore size restrictions might be partly mitigated by the concurrent desorption of gas molecules from the pore walls, which will further intensify gas slippage effects prompted by the lower pore pressures.

The matrix permeability in shales will be governed by the intricate interrelationship of gas slippage and poroelastic effects, as well as their corresponding controlling factors. Thus, identifying the predominance and relative contribution of each mechanism to the macroscopic gas flow will be greatly beneficial for a better understanding of the storage and transport properties in shale reservoirs, across the different production stages. Despite the proliferation of published petrophysical studies in recent years, only a few of them have investigated experimentally the multiple controlling factors for shale matrix permeability and their dependence on pore structural changes (Sinha et al., 2013; Heller et al., 2014; Zamirian et al., 2014; Letham and Bustin, 2016; Fink et al., 2017; Shen et al., 2018). The last main chapter of this thesis will thus focus on this under-explored area, trying to shed some light on the underlying convoluted poroelastic and mass transport mechanisms in shale gas reservoirs. For this purpose, gas permeability measurements were conducted on six shale samples from the Goldwyer Formation, at various mean pore and confining pressures over a 12–month period. An analysis on the apparent permeability –as determined from laboratory tests– is provided in the current study, followed by a discussion on the processes governing gas flow in shales. Gas permeability results are then integrated with experimental data from pore characterisation techniques, to assess the impact of the various control factors on both gas storage and transport properties. The implications of these findings and their significance for evaluating producibility potential in shales are also discussed.

5.3. Materials and Methods

Samples

Polished shale discs with a length ∼1 cm and diameter ∼3.8 cm (1.5") were used in this study, sub-sampled parallel to the bedding from the six Goldwyer samples selected at the WA Core Library. Upon receipt, the samples were tightly wrapped in plastic and stored away in airtight containers to preserve their original "as-received" state for future studies. Discs were trimmed at the CSIRO ARRC laboratories utilising a specialised diamond-wire technique that requires no lubrication fluid beyond air. Samples were not subjected to any cleaning or drying process prior to gas permeability measurements, so as to avoid further alterations other than from the coring process itself. The most relevant characteristics for the six samples tested have been summarised in Table 5.1 below.

Table 5.1.
Core plug dimensions (length, diameter), organic content (TOC) and mineralogy (silicates, carbonates, clays, illite+smectite) of the samples used in this study.

Sample	Dimensions		Composition				
ID	Len (cm)	Diam (cm)	TOC (wt. %)	Qtz.* (wt. %)	Carb. (wt. %)	Clays (wt. %)	I+S** (wt. %)
SG-1	1.03	3.84	4.3	22.3	18.9	58.0	41.3
SG-2	1.04	3.83	3.9	20.8	6.7	70.2	55.8
SG-3	0.93	3.83	1.2	19.1	22.6	56.3	50.1
SG-4	0.97	3.82	0.8	18.5	4.1	75.1	69.7
SG-5	1.03	3.83	2.7	18.7	9.1	68.7	60.5
SG-6	1.00	3.84	0.9	24.6	14.9	57.8	49.4

(*) Sum of quartz, feldspars and plagioclase.
(**) Sum of illite and smectite clay minerals.

Supplementary Porosimetry Data

The characteristic pore lengths for the six shale samples have been estimated from MICP and LP-N_2 data, presented in the previous chapter. The mean pore radii and pore widths, calculated as the median values from MICP and LP-N_2 equivalent pore size distributions are included in Table 5.2 for comparison purposes, along with the calculated MICP threshold pressures.

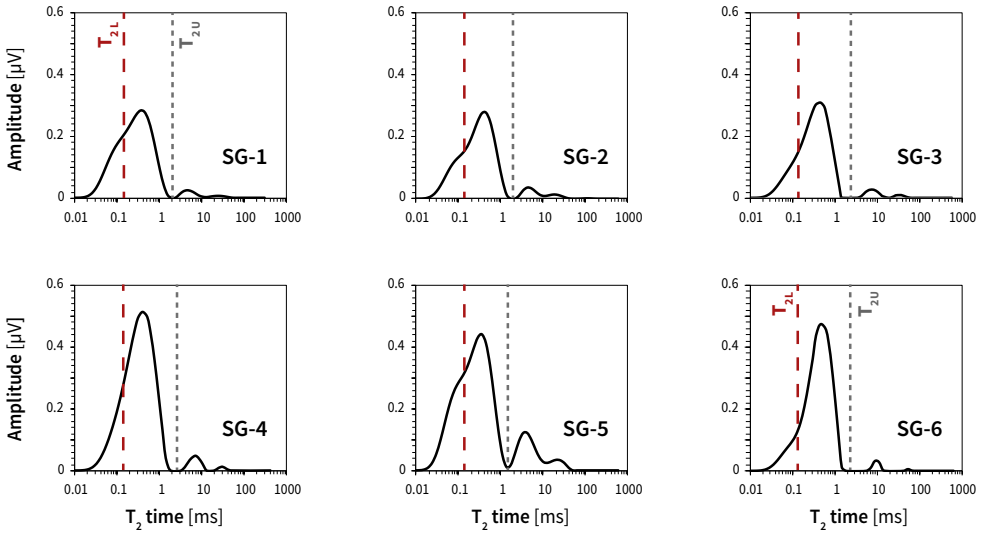

Figure 5.3. T_2 distributions acquired on the companion SG core plugs, in "as-received" condition. The lower and upper T_2 cut-off values used in the calculation of free fluid indices are indicated with red ($T_{2\,L}$) and grey ($T_{2\,U}$) dashed lines, respectively.

NMR T_2 experiments were also conducted on the six companion SG core plugs, in their "as-received" condition, and T_2 distributions were subsequently calculated (Figure 5.3). Two T_2 cut-off values were distinguished upon visual inspection of the T_1–T_2 maps shown earlier (**Figure 4.6b**), a lower one $T_{2\,L}$ estimated to be around 0.15–0.20 ms and an upper one $T_{2\,U}$ at 1.4 ms. Pseudo free fluid indices (FFI_L^*, FFI_U^*) were then constructed based on the T_2 thresholds identified, as the sum of normalised signal ($T_2 > T_{2\,\text{cut-off}}$). The estimated lower and upper T_2 thresholds and the associated pseudo FFI values are presented in Table 5.2.

Permeability Measurements

A core-flooding rig equipped with two hydrostatic core holders, to allow for simultaneous tests, was utilised in this study. Apparent gas permeabilities were determined with a Nano-Perm™ flow-meter system (Core Laboratories), inspired on the quasi steady-state method proposed by Jannot and Lasseux (2012) that –in turn– built up on the work of Brace et al. (1968), Jones (1997) and Cui et al. (2009). Several modifications were made to the original set-up and methodology to reduce uncertainties and correct for real gas effects. Purified compressed air was used in all measurements for a more realistic representation of the gas flow mechanisms in shale reservoirs, as it yields Knudsen numbers similar to methane Figure 5.2.

Core discs are initially placed inside a vessel that is attached to an infinitely large upstream reservoir, under constant pressure, and a much smaller downstream reservoir, where pressure is regulated by an electronic valve controlled from a computer (Figure 5.4). The core holder is also connected to a high precision syringe pump (Vinci Technologies), which uses water to apply a biaxial confining pressure to the –isolated– core samples and keeps it constant throughout the prolonged full test sequence. During measurements, a non-bleeding pressure regulator controls the gas inflow into the core holder and maintains the pressure P_{up} stable. The outlet valve is initially in a closed position as gas passes through the core and starts entering the tiny downstream chamber, where the variable $P_{down}(t)$ is recorded. Once the pressure in the downstream reservoir reaches a certain threshold value (significantly smaller than P_{up}), the outlet valve opens and the collected gas is released. The pressure at the downstream subsequently drops to zero and gas flow rate is estimated from the slope of $P_{down}(t)$ versus time recorded for that cycle, and is then repeated multiple times to minimise experimental errors. Furthermore, the upstream absolute pressure and temperature conditions are continuously monitored with two Keller PA-33 digital transmitters (accuracy ± 0.05 %) installed at the core holder inlets, which enables a more precise calculation of the gas viscosity and deviation factors used in permeability determination. After sufficient time is allowed to ensure pseudo stationary flow conditions, the apparent gas permeability can be determined as follows:

$$k_g = \frac{2\,\mu\,z\,L\,a_q}{A\,P_p\,(P_{up} - P_{down})} \tag{5.8}$$

Table 5.2.
Summary of porosimetry results, including mean pore radius (r_p from MICP tests), mean pore width (w_p from LP-N_2 tests), and the $T_{2\ cut\text{-}off}$ values used for the calculation of pseudo free fluid indices (normalised) from 1D–NMR tests on "as-received" core plugs.

Sample	MICP		LP-N_2	NMR			
ID	P_{thresh} (psi)	r_p (nm)	w_p (nm)	T_{2L} (ms)	FFI_L* (norm. %)	T_{2U} (ms)	FFI_U* (norm. %)
SG-1	14,500	16.5	10.5	0.17	0.66	1.41	0.04
SG-2	6,600	67.3	16.9	0.17	0.72	1.40	0.07
SG-3	7,200	39.7	11.9	0.18	0.77	1.39	0.05
SG-4	13,400	23.5	10.5	0.15	0.81	1.45	0.04
SG-5	4,800	80.3	15.9	0.15	0.74	1.40	0.15
SG-6	10,050	28.1	10.5	0.19	0.83	1.40	0.04

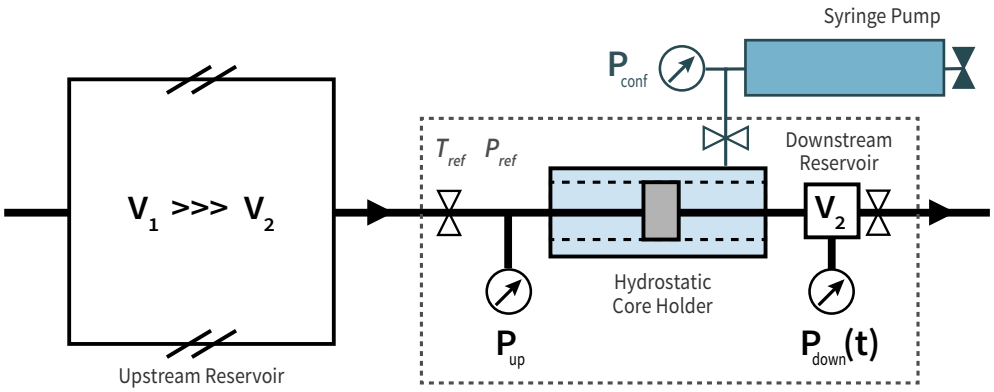

Figure 5.4. Simplified diagram of the experimental set-up used for gas permeability measurements. The gas inlet pressure (P_{up}) is adjusted with a non-bleeding precision regulator, while an electronic valve regulates the small pressure differential at the downstream (P_{down}). The confining pressure in the biaxial core holder is controlled by a Vinci syringe pump filled with water. All pressure transmitters have an internal temperature compensation loop for better accuracy.

where μ is the real gas viscosity, z is the real gas compressibility –or deviation– factor, L is the length –or thickness– of the disc-shaped core sample and A is its cross-sectional area ($A = \pi\, diam^2$), and a_q represents the mass flow factor as a function of the rate of change of $P_{down}(t)$ in time. The gas viscosity is calculated from Sutherland's equation (Haynes, 2014) while the gas z-factor was determined as the largest real root that solves the original Peng-Robinson equation of state (Peng and Robinson, 1976), for the real mean pressure and temperature conditions as recorded by the corresponding digital pressure transmitter and air. In addition, the characteristic time (t_C) to reach quasi-steady state was estimated from the equation suggested by Jannot and Lasseux (2012) for the particular experimental conditions:

$$t_C \approx \frac{\phi\, \mu\, L^2}{k_g\, P_{up}} \tag{5.9}$$

One of the main advantages of this method lies in the feasibility of conducting measurements at low pore pressures (below 60 psi for our particular gas pressure regulator), which minimises inertial effects and makes the use of Equation (5.3) possible. The effect of net stress on gas transport properties can therefore be studied using much lower confining pressures than with other methods, which in turn reduces the risk of damaging the delicate pore structures in the shale matrix. In addition, the risk of gas and confining fluid leaks –a common issue in shale permeability measurements– are greatly minimised.

Measurements were performed for various pore pressures in the range 24–50

psi and 250–2000 psi confining pressures. The slip and transition flow regimes were expected to dominate the macroscopic gas transport across the shale cores for the particular experimental conditions in this study, as seen by the estimated range of Knudsen numbers indicated in Figure 5.2. The test sequence –at each confining stress– started with a 72 hours pre-stressing period: the pressure was gradually increased during the first 24 hours and left for 48 hours to ensure uniform poroelastic effects. This was followed by a 24 hours period of gas injection, after which the actual measurements began. Depending on the availability of equipment and other external factors, around 8–12 weeks were needed to acquire a full data set of pore-pressures/confining-stresses for two shale samples using purified compressed air. The stability of experimental conditions during such prolonged tests becomes critical. The laboratory temperature was controlled by an air conditioning equipment, whereas an acrylic screen and insulation material around the core holders ensured isothermal conditions for the rig. Periods where the atmospheric pressure and ambient temperature (± 0.5 °C) remained stable were identified from the recorded data and those permeability values were selected for further analysis, so as to avoid inconsistencies across the data set and when comparing results from different samples. The impact of unstable laboratory conditions and other experimental challenges encountered are examined below.

Sources of Experimental Error

The stability of laboratory conditions, such as room temperature or pressure, is not as critical for permeability measurements performed in conventional reservoir rocks as it is in tight porous media. Tests in shale samples can extend over several hours –or even days– and any changes to ambient conditions may leave footprints on results. Figure 5.5 illustrates the impact of fluctuating room temperature on the gas permeability measured for a shale core sample from the SC set, before and after introducing modifications to the equipment. In both cases, purified dry compressed air was injected at 30 psi under a confining pressure of 1000 psi. For the leftmost chart results, the confining stress was applied with a manual pump utilising hydraulic oil at the beginning of the test, without any kind of insulation on the equipment or further adjustments. An air conditioner controlled the room temperature during the day but was turned off in the evening, causing differences of more than 5 °C. At 20 °C, the thermal volumetric expansion coefficient of hydraulic oil is almost 3 times that of water, so even small changes in the room temperature can result in great differences on the effective confining stress. For this particular example, the variation in ambient temperature induced discrepancies in the confining pressure effectively

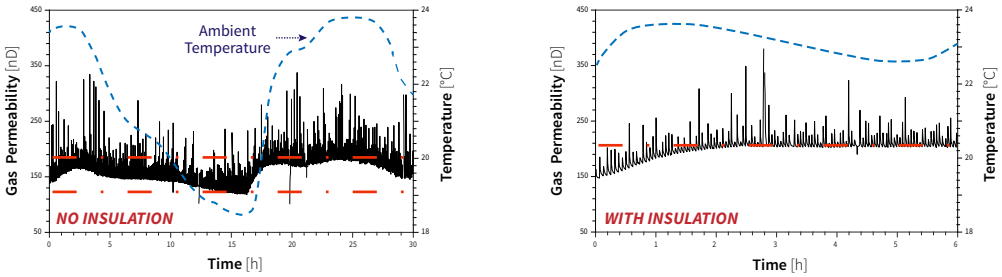

Figure 5.5. Effect of variable ambient temperature on gas permeability results from measurements on a shale sample, with gas injected at 30 psi under a confining pressure of 1000 psi (Adapted from Testamanti et al., 2017a). Left: before installing insulation, confining stress applied with a manual pump and hydraulic oil. Right: after installing insulation, confining pressure applied with a high precision syringe pump and water.

applied to the core of 15–20% (compared to the initial settings) but hiked to 40% for stress values above 2000 psi. Gas pressure, viscosity, density and compressibility are also affected by non-isothermal conditions, which gave rise to differences of more than 45% in the gas permeability obtained without accounting for real gas effects. To ensure stabilised ambient conditions, heavy insulation was installed during the trial stage before conducting further tests. Furthermore, the confining fluid was replaced by water and a high precision syringe pump was installed to provide constant confining pressure conditions at all times. All the measured data were also corrected for real gas effects and recalculated based on the Keller PA-33 transmitter logged data, using purposely written Matlab code. The test was then repeated after implementing all the corresponding modifications and the results are shown in the rightmost chart of Figure 5.5. Under normal running conditions, the temperature measured at the core holder inlet remains relatively constant (23 $\pm$ 0.5 °C) and the associated fluctuations in the gas permeability values are generally below 5% for all tests. In addition, all the pressure transmitters installed include temperature compensation feedback, so the potential effects of the 0.5 °C difference on instruments is considered to be minimal and do not require further corrections.

With regards to the differences arising from human error, average discrepancies in the interpreted permeability values using a late-time approach were between 8 and 12 % for all the tests on SG samples. A uniform criteria for the analysis of experimental data is thus paramount for obtaining consistent results across different sample sets. Having examined the various experimental factors that could affect the permeability data during laboratory measurements, the effect of sample dimensions on tests will be scrutinised next.

Length of Shale Samples and Tests

The length of the core samples tested has a direct influence on the duration of permeability measurements, as observed from Equation (5.9). To demonstrate this effect, gas permeability tests were conducted on two cylindrical companion samples of the Carynginia shale SC-5, trimmed to different lengths. A 1"–wide–by–1/4"–long (∼2.5 × 0.6 cm) thin disc was cut from "as-received" unpreserved core and then embedded into a 1 1/2"–resin sleeve. A thick core plug with a 1.5"–diameter–by–1 7/8"–length (∼3.8 × 4.8 cm), originally cut from the same unpreserved core but subsequently subjected to a harsh solvent cleaning and drying process, was tested for comparison. The differential outflow pressure recorded during laboratory measurements performed at a 40 psi gas inflow pressure and 1000 psi confining pressure are shown in Figure 5.6. In the graph, the approximate characteristic times (t_C) indicate the point after which pseudo steady-state conditions are achieved and apparent gas permeability can be calculated from Equation (5.8). The thickest core plug required a stabilisation time around ten times longer than the thin disc sample, which showed signs of pseudo stationary conditions within the first 30 minutes of the experiment. The length of shale samples should therefore be minimised whenever possible, so as to reduce the duration of laboratory tests and associated errors that may consequently arise. One caveat of this proposition is, however, that the decrease of experimental errors could potentially be negated by an increase in *core-end effects*. The quantification of such errors was not possible during the course of this research but should be evaluated in future studies.

Figure 5.6 also reveals that the differential downstream pressure rates – proportional to outflow rate and thereby permeability – for the clean shale core

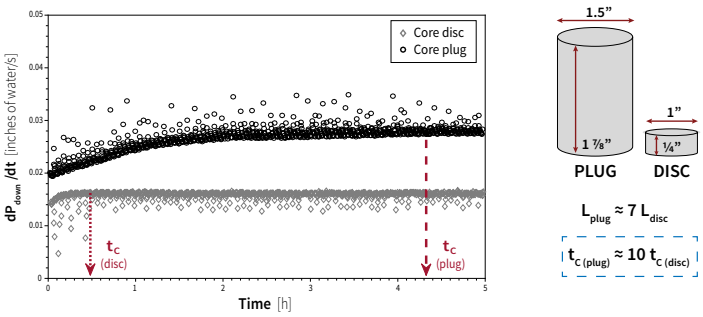

Figure 5.6. Effect of sample thickness on the length of gas permeability tests, comparing the differential downstream pressure rate ($dP_{down}(t)/dt$) versus duration (hours) for a thick core plug and a thin disc shale sample (adapted from Testamanti et al., 2017a). Tests conducted with purified compressed air, at 40 psi inflow pressure and 1000 psi confining pressure.

plug are twice as much as the measured values for the "as-received/unpreserved" disc sample, illustrating the great impact of common core cleaning processes. Since they may lead to significant differences in permeability measurements and yield results that do not reflect the real properties of the rock, no core cleaning procedures were employed before testing the SG samples.

5.4. Results

The results of permeability measurements at various confining and mean pore pressure combinations are presented in Figure 5.7 (for full results see Appendix A), where the apparent gas permeability was plotted versus inverse mean pore pressure for comparison to the linear Klinkenberg equation (5.5). The lowest permeability values are seen for samples SG-1 and SG-4, whereas SG-5 appears to be the most permeable to gas. Interestingly, a non-linear effect was observed in the results from measurements at pore pressures below ∼32 psi, suggesting a possible deviation from the expected Klinkenberg phenomenon.

Concave-up non-linear effects in Klinkenberg plots from measurements on shales were studied by Fathi et al. (2012) and later reported by Zamirian et al. (2014), while Moghaddam and Jamiolahmady (2016) observed concave-down trends in experimental permeability results obtained at higher pore pressures. Non-linear behaviour could nonetheless have multiple underlying causes beyond the fluid dynamics and poroelastic phenomena, including errors associated with laboratory conditions. Noise in the permeability data due to experimental errors was, however, deemed unlikely for the reasons examined in the previous section. To test the hypothesis that the observed deviations were not related to procedural inaccuracies or unstable experimental conditions, permeability measurements were repeated on both the core plug and thin disc from sample SC-5, but over a wider range of confining and pore pressures. The results from these additional tests are presented in Figure 5.8 for comparison purposes, where non-linear effects are absent and the gas permeability data is seen to align to the Klinkenberg linear equation in both cases. Experimental errors were thus ruled out as the potential source of non-linearity in the results from SG samples, which is instead suspected to arise from the various gas transport phenomena associated with extremely narrow pores sizes. For instance, results from porosimetry methods reveal that the characteristic lengths in sample SC-5 are around 26 nm assuming slit-shaped pore widths (from LP-N_2 tests) and close to 100 nm for cylindrical pore diameters (from MICP tests). In comparison, the characteristic pore widths and diameters, as estimated from porosimetry tests (Figure 5.2), are considerably smaller across the SG sample

set so it is reasonable to assume that the dominant gas transport mechanisms will also differ. The non-linear behaviour observed in results from SG samples will be analysed in the next section, as the simultaneous effects of gas transport and poroelastic mechanisms on shale matrix permeability are explored.

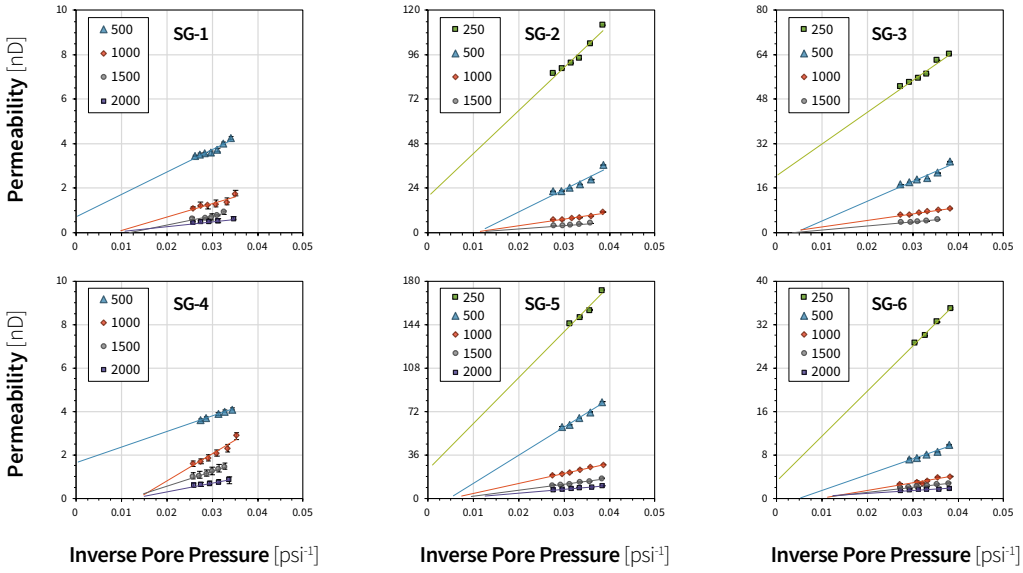

Figure 5.7. Results from gas permeability measurements carried out on six shale samples from the Goldwyer Formation at different confining pressures, plotted against the corresponding inverse mean pore pressure ($1/P_p$). Purified compressed air was utilised in all laboratory tests, for P_{up} in the range 24–50 psi and P_{conf} between 250–2500 psi. Non-linearity (deviation from Klinkenberg behaviour) is observed at very low pore pressures.

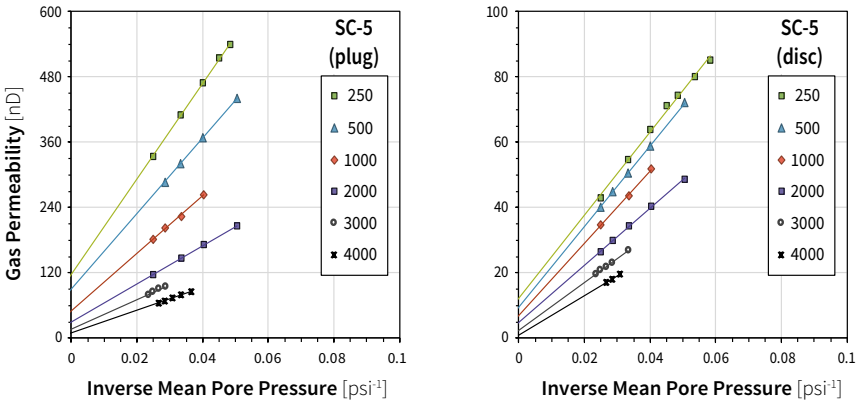

Figure 5.8. Results from gas permeability measurements conducted on two Carynginia shale samples companion of SC-5: a thick core plug (after a harsh solvent cleaning and drying process) and a thin disc (from as-received/unpreserved core). Tests were conducted for confining pressures of 250–4000 psi and inflow pressure of 5–60 psi, with gas permeability results conforming to the linear Klinkenberg equation.

5.5. Discussion

5.5.1. Gas Transport Mechanisms

The suitability of the Klinkenberg equation (5.5) for the interpretation of gas transport phenomena was evaluated by fitting permeability results to a straight line (Figure 5.7). Upon closer inspection, the graph shows that the extrapolated or Klinkenberg-corrected permeability coefficients are generally negative for confining pressures over 1000 psi (Table 5.3), in agreement with previous research findings by Fathi et al. (2012) and Zamirian et al. (2014). Furthermore, Mathur et al. (2016) carried out an experimental study on shale permeability and found that transition flow prevailed for pore pressures below 250 psi, later concluding that second order corrections were necessary for the characterisation of gas transport in this regime. The pore pressures used in the current study were below that range, ultimately suggesting a violation of the underlying physical principles of the Klinkenberg equation.

Fathi et al. (2012) conducted molecular dynamics simulations for capillary tubes of different widths and argued that under the transition flow regime, the linear Klinkenberg model neglects the kinetic effects of gas molecules bouncing-back against the pore walls that would ultimately lead to a permeability enhancement. This effect was accounted for in their proposed "double-slip" extended Klinkenberg equation:

$$k_g = k_\infty \left[1 + \left(\frac{b}{P_p}\right)^2 \left(\frac{L_{KE}}{\lambda}\right)\right] \tag{5.10}$$

where k_∞ is the extrapolated permeability, b is the same gas slippage coefficient described in Equation (5.5), λ is the mean free path of gas molecules and L_{KE} is a length scale associated with their kinetic energy due to the interaction with pore walls. The experimental results were then plotted against the squared inverse mean pore pressure, as shown in Figure 5.9, and a straight line was fitted to evaluate their agreement with the "double-slip" model. The slope and intercept parameters that were obtained for each flow model are summarised in Table 5.3. The analysis shows that the extrapolated permeability values determined from Equation (5.10) are positive in all cases, suggesting that a second order model may be better suited for the interpretation of experimental results.

The permeability enhancement associated with gas slippage was also estimated for both the Klinkenberg and "double-slip" models. Figure 5.10 compares the corresponding permeability increase for each model, derived from the parameters obtained by regression on equations 5.5 and 5.10. At first glance, the magnitude of

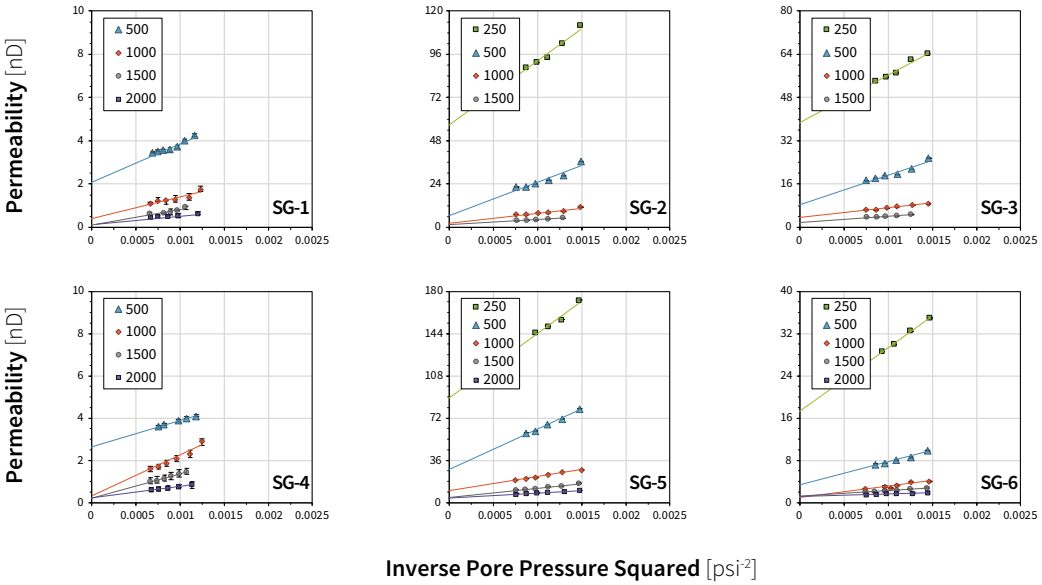

Figure 5.9. Double-slip Klinkenberg correction applied on gas permeability results from tests on six shale samples from the Goldwyer Formation at different confining pressures, plotted against the corresponding inverse mean pore pressure squared ($1/P_p{}^2$).

gas slippage effects on measured permeability would seem to increase along with confining pressure. This observation is then confirmed numerically, by fitting the data points to second degree polynomials which reveal a direct relationship between quadratic coefficients and confining stress. Furthermore, the rate of permeability enhancement due to gas slippage is found to vary differently across the sample set. Slippage effects appear to be more significant for samples SG-1/SG-4/SG-6 and less so for SG-2/SG-3/SG-5, suggesting a correlation between their magnitude and the characteristic pore sizes in the shale matrix (Table 5.2).

The study by Fathi et al. (2012) proposed that kinetic effects due to the interaction of gas molecules with the pore wall should only be significant for narrow capillaries in the transition flow regime. Based on this premise, the authors showed that the normalised coefficients $(L_{KE}/\lambda)(b/P_p)$ would consequently become negligible for gas flowing through large capillaries. In real reservoirs, however, pore diameters do not remain constant but are controlled by the balance between internal and external forces acting upon them. Soft rock types such as coals and shales, are particularly sensitive to the changes in effective stress that occur due to reservoir depletion. The composite of poroelastic and dynamic mass transport processes will control the evolution of the shale matrix permeability (Figure 5.11). As the reservoir pressure declines with production, the pores in the shale matrix are compacted and there is a consequent reduction in apparent permeability. This negative trend from poroelastic origin could be ultimately offset by the increase in fluid dynamic

effects that arise with increasing average Knudsen numbers, leading to the characteristic slow-declining production curves of shale gas reservoirs. These coexisting processes could then indirectly control the long-term shale gas recovery potential, so understanding their progression with effective reservoir pressure is of paramount importance. In the following subsection, the interplay between gas transport and poroelastic mechanisms, and their effect on matrix permeability will be analysed.

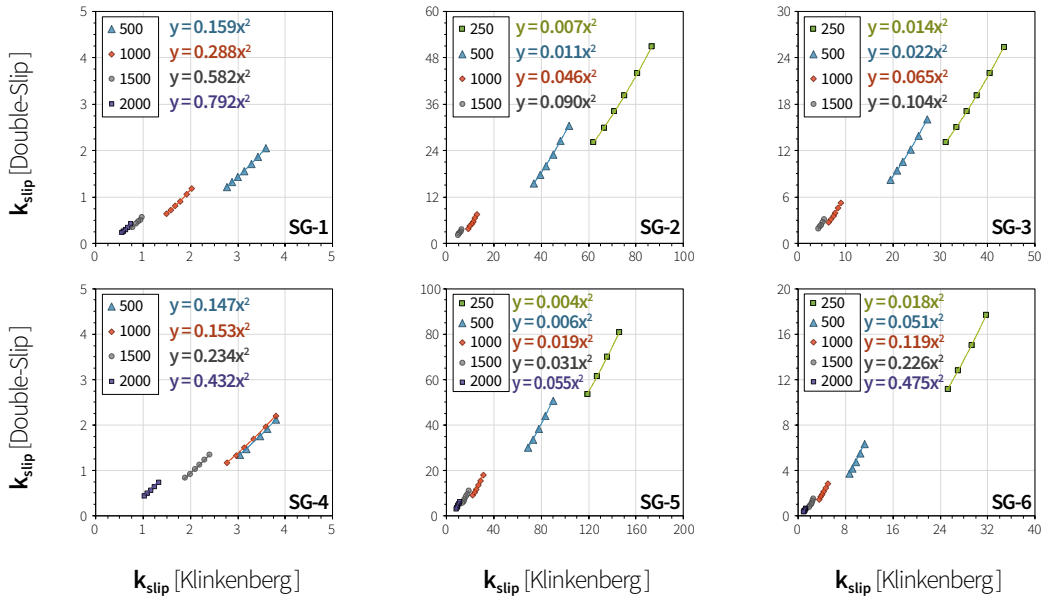

Figure 5.10. Comparison of the permeability enhancement due to gas slippage (k_{slip}) for various mean pore/confining pressure combinations, as estimated from the corresponding terms of the Klinkenberg and "double-slip" equations. All results were fitted to a second degree polynomial for illustration purposes.

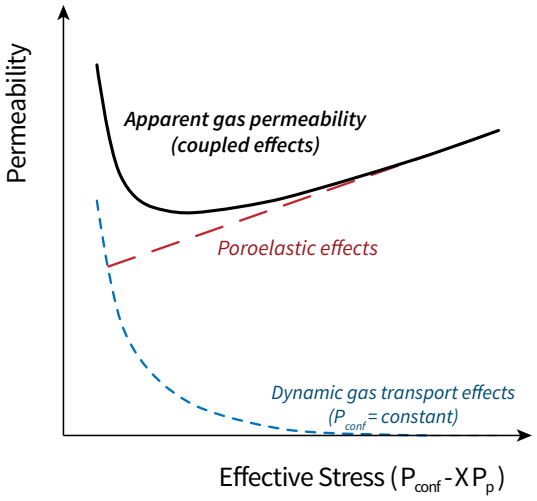

Figure 5.11 Evolution of matrix permeability over the production life of shale gas reservoirs, due to the coexisting poroelastic and fluid dynamic effects (modified from Fink et al., 2017).

Table 5.3.
Model parameters obtained for the original Klinkenberg (first order model) and double-slip (second order) flow equations.

Sample	$P_{Conf.}$	Klinkenberg Model			Double-Slip Model		
ID	(psi)	Slope (psi^{-1})	Intercept (nD)	R^2	Slope (psi^{-2})	Intercept (nD)	R^2
SG-1	500	105	-0.6	0.90	1,760	2.1	0.92
	1,000	58	-0.4	0.88	955	0.4	0.90
	1,500	30	-0.1	0.87	521	0.3	0.89
	2,000	21	-0.1	0.92	350	0.2	0.94
SG-2	250	2,212	22.5	0.95	33,694	58.4	0.96
	500	1,334	-17.3	0.90	20,380	4.3	0.93
	1,000	332	-2.7	0.96	5,056	2.7	0.97
	1,500	175	-1.3	0.97	2,766	1.4	0.98
SG-3	250	1,140	20.6	0.96	17,498	39.0	0.97
	500	711	-3.0	0.91	10,975	8.4	0.93
	1,000	235	-0.2	0.98	3,586	3.6	0.99
	1,500	153	-0.7	0.97	2,439	1.7	0.98
SG-4	500	110	0.5	0.99	33,694	2.2	0.99
	1,000	107	-1.2	0.93	20,380	0.4	0.95
	1,500	73	-0.9	0.95	5,056	0.2	0.95
	2,000	39	-0.4	0.94	2,766	0.1	0.95
SG-5	250	3,800	24.0	0.94	54,834	89.4	0.95
	500	2329	-10.7	0.98	34364	28.4	0.99
	1,000	799	-2.9	0.99	12,059	10.2	0.99
	1,500	491	-2.9	0.95	7,514	5.0	0.96
	2,000	278	-0.4	0.99	4,213	4.1	0.99
SG-6	250	826	3.2	0.99	11,982	17.4	0.99
	500	293	-1.5	0.97	4,376	3.4	0.98
	1,000	129	-1.0	0.86	1,978	1.2	0.87
	1,500	68	-0.2	0.97	1,046	1.3	0.98
	2,000	32	-0.7	0.98	487	1.2	0.98

5.5.2. Considerations for the Analysis of Coupled Gas Transport and Poroelastic Mechanisms

The relationship between permeability, pore and confining pressure is examined in Figure 5.12, where the difference between the slippage terms in equations (5.5) and (5.10) has been plotted against its corresponding mean pore pressure. The diffusion effects in the graphs are more evident at lower confining stresses, as indicated by the data points which describe apparent quadratic polynomial curves. In contrast, the magnitude of the differences between

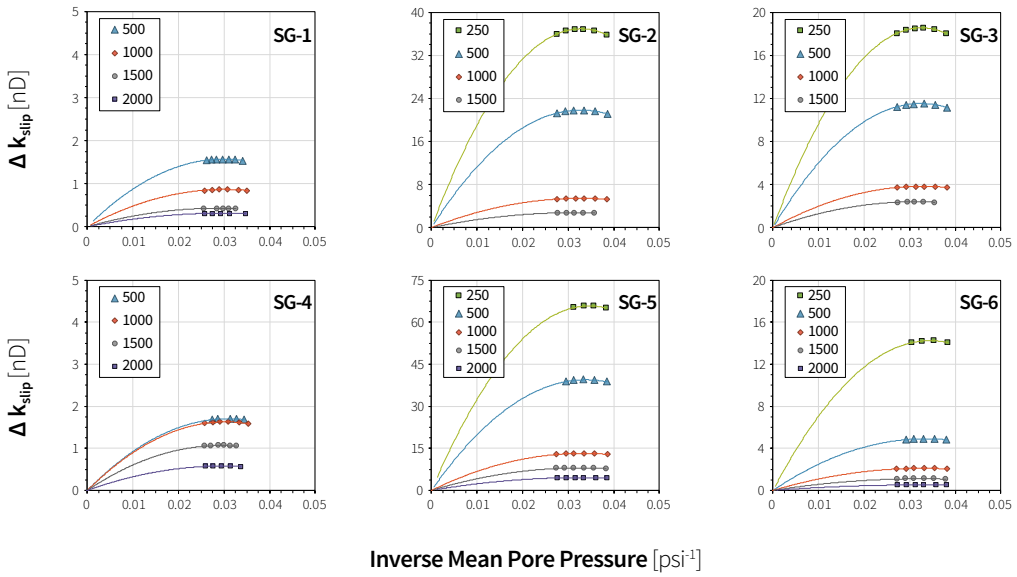

Figure 5.12. Gas slippage correction (Δk_{slip}), calculated as the difference between the corresponding terms in the Klinkenberg ($k_\infty b\ P^{-1}$) and "double-slip" ($k_\infty b^2\ P^{-2}\ L_{KE}/\lambda$) flow equations, as a function of inverse mean pore pressure.

slippage-enhanced permeability from the Klinkenberg and "double-slip" models decreases at increasing confining pressure, as the second order effects become negligible. The more linear permeability reduction observed at higher confining stress is then consistent with the theoretical evolution that is expected in shale gas reservoirs (Figure 5.11), controlled by coupled poroelastic and fluid dynamic processes. While the experimental results herein presented provide further support for the conceptual premise explored by other authors (Heller et al., 2014; Letham and Bustin, 2016; Moghaddam and Jamiolahmady, 2016; Mathur et al., 2016; Fink et al., 2017), the data must be interpreted with caution as permeability measurements were not carried out at reservoir conditions. The combination of findings nonetheless suggests that it may be possible to characterise the apparent gas permeability of the shale matrix associated with each mechanism. The complex interplay between mass transport and poroelastic phenomena can ultimately play a key role in the long-term productivity of shale reservoirs, and so a more comprehensive approach is required for its study. In this research, the sensitivity of permeability to both pore (P_p) and confining pressure (P_{conf}) was evaluated with respect to effective stress (σ_{eff}), according to:

$$\sigma_{eff} = P_{conf} - X\ P_p \tag{5.11}$$

where the effective stress coefficient X is a property of the rock (Cheng, 2016). Poroelastic materials where confining pressure variations effect a greater impact on permeability than pore pressure will have an associated $X \leq 1$. The particular

case of X=1 describes the Terzaghi effective stress that is commonly used in soil mechanics but generally unsuitable to characterise clay-rich rocks (Kwon et al., 2001; Heller et al., 2014; Fink et al., 2017; Letham and Bustin, 2016). Using Equation (5.11) as a starting point, this chapter will now move on to evaluate the suitability of forward and multi-parameter regression models, for the assessment of the coupled poroelastic and gas transport mechanisms on the matrix permeability of shales.

5.5.2.1. Forward Evaluation

A forward methodology was initially chosen to study the evolution of apparent gas permeability of the shale matrix, where the effective stress coefficient was approximated as X=1. Although this value is likely higher than what would be expected in shales (Kwon et al., 2001), the methodological error associated is considered to be relatively low due to the pore pressure levels used in this study. Based on the methodology presented in (Letham and Bustin, 2016), gas permeability results can then be correlated to effective stress by adjusting the measured data to a general power law:

$$k = k_L \, {\sigma_{\text{eff}}}^{\alpha_p} \tag{5.12}$$

Similarly, the gas slippage coefficient can be adjusted to a power law in the form:

$$b = b_L \, {k_{\infty,i}}^{\beta_L} \tag{5.13}$$

where the coefficients b_L and β_L are obtained as the best fits to the data.

The power laws and effective stress parameter (X) describing the measured permeability, according to the forward methodology, are presented in Figure **??**. The experimental data were fitted by linear regression analysis and goodness of fit was evaluated based on the coefficient of determination (R^2), also indicated in the graph. The permeability–effective stress power laws in Figure **??** reveal that sample SG-2 and SG-5 have the highest extrapolated permeability values (k_L), around 620 and 240 µD respectively. In contrast, the lowest k_L value is identified for sample SG-4, around 5 µD. The k_L values observed in the graph seem to correlate with characteristic pore lengths measured in the samples (Table 5.1), whereas no trends emerge upon inspection of the power law exponents (α_p).

The quadratic term in the "double-slip" Equation Equation (5.10) was later subtracted from the experimental results, to estimate the slippage-corrected matrix permeability of the samples. The graphical analysis shown in Figure **??** suggests that the error associated with the incorrect determination of the

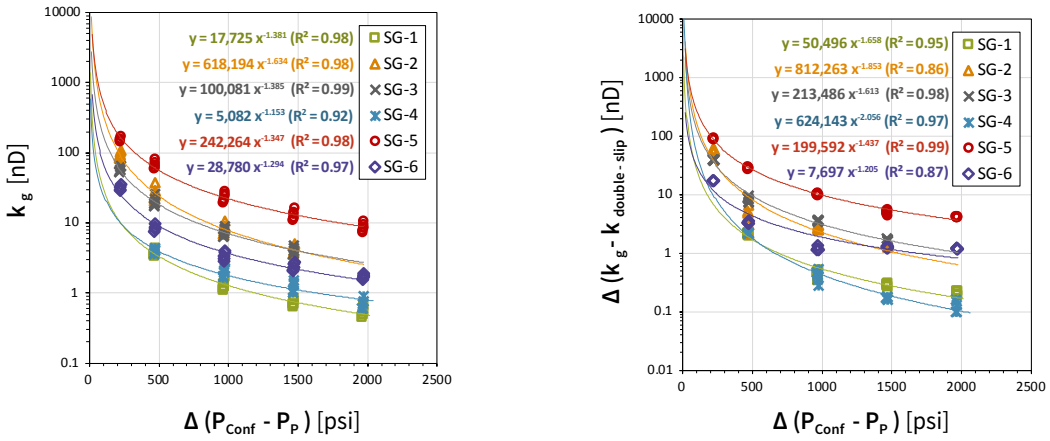

Figure 5.13. Gas permeability (k_g) versus simple effective stress ($\sigma_{eff} = P_{conf} - P_p$), calculated for: (a) measured gas permeability (k_g); (a) slippage-corrected permeability, based on the double-slip model ($k_{corr} = k_g - k_{slip}$).

coefficient X and the slippage-enhanced permeability is likely greater for higher effective stresses, which may be inferred from the wider spread observed in data points. This agrees with the previous interpretation of results, as permeability evolution in this region should theoretically be dominated by poroelastic processes, generally following a linear trend. At lower effective stress, the corrected permeability values appear to align almost perfectly for constant confining pressures, illustrating the relative low influence of poroelastic effects. In this region, the gas flow regime would be governed by dynamic transport mechanisms which – in this case – appear to be correctly characterised by the double-slip model.

It is worth noting that relying on R^2 coefficients alone for evaluating the suitability of the forward method may be insufficient, and could even lead to the incorrect interpretation of results. For instance, the gas permeability data herein presented violates the hypothesis of linearity assumed by the methodology proposed by Letham and Bustin (2016), so the validity of any results derived from this model requires careful consideration. The potential flaws in the current forward approach are highlighted in Figure 5.14, which shows the relationship between the gas slippage parameter and extrapolated Klinkenberg permeability for the six shale samples. At first glance, the calculated R^2 below 0.50 indicates that the current method would not be a suitable choice for fitting the experimental permeability results. Then, according to Equation (5.13), all data points should conform to a power law but this is not observed in the graph. A change in trends can be instead identified

for all samples, which might signal the transition from dynamic gas transport to poroelastic-dominated permeability regime. The analysis presented indicates that such transition may occur at confining pressures between 500-1000 psi for the system studied, but the characterisation of relative contributions to measured matrix permeability is not feasible with the current method. The suitability of multi-parameter regression models will be analysed next, to assess whether some of the fundamental pitfalls aforementioned can be offset by the use of more complex representations which consider the simultaneous gas transport and poroelastic mechanisms that control matrix permeability in shales.

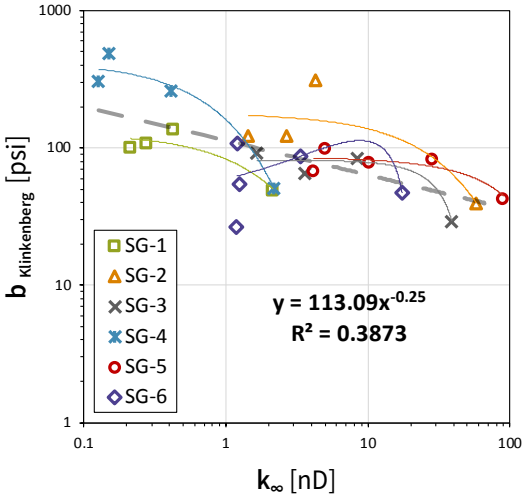

Figure 5.14 Gas slippage parameter (b) versus extrapolated Klinkenberg permeability (k_∞), obtained at different confining pressures. The coefficient k_∞ was derived using the Double-Slip equation, whereas b was estimated with the Klinkenberg method.

5.5.2.2. Multi-Parameter Regression Models

In this analysis, two approaches were chosen to study the combined poroelastic and gas transport phenomena:

1. Multi-regression analysis to determine the parameters in permeability–effective stress power laws, based on the extension of the linear Klinkenberg equation proposed by Fink et al. (2017). Both poroelastic and gas slippage effects are considered in this model, where the apparent gas permeability (k_g) is adjusted to:

$$k_g = k_L \left[\frac{P_{\text{conf}} - X\, P_{\text{p}}}{\sigma_{\text{eff},L}} \right]^{\alpha_p} \left[1 + \frac{b_0 + \beta_p \left(P_{\text{conf}} - X\, P_{\text{p}} \right)}{P_{\text{p}}} \right] \tag{5.14}$$

where k_L represents the permeability extrapolated from the Klinkenberg equation for an effective stress $\sigma_{\text{eff},L} = 1$, the coefficient β_p is a measure

of the sensitivity of the slippage parameter (b) to effective stress, and b_0 is the gas slippage coefficient at zero effective stress (in pressure units). While the experimental results presented in this thesis appear to violate the assumptions in the model by Fink et al. (2017), the objective of the current assessment is to test the hypothesis in Fink et al. (2018) who argue that non-linear behaviour stems from the incorrect interpretation of effective stress states rather than deviations from the Klinkenberg model.

2. Multi-regression analysis to determine the parameters in permeability–effective stress power laws, while also accounting for the non-linear effects observed in the measured data. The experimental results were fitted to a second order slip model in the form:

$$k_g = k_\infty \left(1 + \frac{\Theta_1}{P_p} + \frac{\Theta_2}{P_p^2}\right) \tag{5.15}$$

where Θ_1 and Θ_2 are the first and second order slip coefficients, respectively (a full derivation of the expression above can be found in Tang et al., 2005). It is worth noting that most second order slip models found in the literature and extended to shale gas reservoirs have been developed from simulation studies where porous media is represented as an ideal bundle of straight, cylindrical and parallel capillary tubes, made of an organic material (Beskok and Karniadakis, 1999; Kazemi and Takbiri-Borujeni, 2015; Tang et al., 2005; Fathi et al., 2012; Gupta et al., 2018; and many others). While this rather simplistic approach cannot be used to accurately model the full extent of gas transport phenomena in complex porous media such as organic shales, the same underlying mechanisms are considered to prevail. For this reason, the coefficients Θ_1 and Θ_2 were reformulated as a function of the gas slippage parameter b, such that $\Theta_i = \theta_i b$. This approach was later found to coincide with the fundamental idea behind the expansion of Klinkenberg's equation proposed by Moghadam and Chalaturnyk (2014), however, the current work differs in that no assumptions are made on the concavity of apparent gas permeability in the presence of significant rarefaction effects, while the existence of a non-ideal porous medium is addressed by the introduction of the empirical coefficients Θ_i. The value of Θ_1 was set to 1, to test whether this representation was more suitable to separate the overlapping first and second order effects. The extrapolated Klinkenberg permeability (k_∞) was then modelled after a power law and the coefficient b was rewritten as a function of effective stress, similar to the methodology

presented in Fink et al. (2017). The complementary set of equations used in the current model are shown below.

$$\Theta_1 = \theta_1 b \tag{5.16a}$$

$$\Theta_2 = \theta_2 b \tag{5.16b}$$

$$k_\infty = k_L \left(\frac{\sigma_{\text{eff}}}{\sigma_{\text{eff},L}} \right)^{\alpha_p} \tag{5.16c}$$

$$b(\sigma_{\text{eff}}) = b_0 + \beta_p \, \sigma_{\text{eff}} \tag{5.16d}$$

The results for the cases considered in the current analysis, summarised in Table 5.4, are discussed below.

Case 1: Multi-Parameter Regression Analysis for First Order Slip Model

For the case herein evaluated, Equation (5.14) was fitted to the full range of experimental data by a non-linear least squares method. The equation was solved based on a trust-region algorithm included in Matlab's Optimization Toolbox™, using a threshold value $\Delta \leq 10^{-3}$ between iterations as convergence criteria. Based on the initial solutions to the unconstrained minimization problem, variable constraints were defined and later imposed on the model to determine the parameters presented in Table 5.4. Figure 5.15a illustrates the analysis conducted for solving the first order equation considered in this case.

The effective stress coefficients (X) from this model are in the range 0.61–0.84. This is consistent with the observations by Fink et al. (2017) and Fink et al. (2018), who argued that the Terzaghi principle does not hold for shale samples. The extrapolated permeability values (k_L) yielded by this model are generally lower than those by the forward method, except for sample SG-1. By the current approach, the power law coefficients (α_p) are determined to be in the range -1.25–1.60. The k_L values appear to be correlated with mean pore sizes, whereas composition may have greater influence on the α_p parameters. In the case of the gas slippage coefficient b_0 and effective stress sensitivity β_p, values were around 31–40 (in psi) and 0.002–0.025 respectively, while no evident relationships were found with either sample composition or characteristic pore lengths.

In shale gas reservoirs under production, the effective stress will increase with declining reservoir pressure, triggering simultaneously: (1) a reduction in permeability due to poroelastic effects; (2) an enhancement in permeability due to increased gas slippage from the reduction of pore sizes and pressures. The main advantage of the method proposed by Fink et al. (2017) lies in its ability to consider the coupling of both poroelastic and slippage phenomena,

particularly important for understanding how the shale matrix permeability will evolve at different production stages. Nonetheless, using a first-order slippage equation could lead to the misinterpretation of experimental results when significant rarefaction effects are present. The presence of non-linearity in Klinkenberg plots from shale samples has been attributed to the overestimation of effective stress caused by the incorrect characterisation of the parameter X (e.g. Letham and Bustin, 2016; Fink et al., 2017). However, this does not fully explain the experimental permeability results herein presented. The low pore pressures used in this study, combined with the narrow pore sizes identified in the samples, would undoubtedly give rise to significant permeability enhancement – regardless of the confining stress used. This becomes evident in Figure 5.2, where the possible Knudsen numbers place the tight samples studied in the transition flow regime region. Under these conditions, the assumptions behind Equation (5.14) are violated and therefore a first order slippage equation would be unsuitable for interpreting the experimental permeability results, regardless of the effective stress state used. The next approach evaluated will be therefore based on a second order extension of the Klinkenberg equation, to account for the rarefaction effects present and address the methodological issues herein identified.

Case 2: Multi-Parameter Regression Analysis for Second Order Slip Model

The effective stress coefficients (X) from this model varied between 0.78–0.90 for the six samples studied, which is more in line with values reported in the published literature (Heller et al., 2014; Letham and Bustin, 2016; Fink et al., 2017). The effective stress sensitivity of permeability (α_p) and slippage (β_p) were in the range of -1.30–1.67 and 0.006–.019, respectively. The extrapolated permeability (k_L) ranged between 4.2–244.9 µD, while the slippage coefficient at zero net stress (b_0) showed values around 20–40 (in psi). The second order coefficients (θ_2^2) were found to vary between 0.15–1.60 for the six samples analysed.

The X and k_L values are generally higher with the second order equation, whereas the α_p coefficients show no significant differences with the results obtained by the first order model ($< 5\%$). When it comes to the b_0 parameters, the results for samples with the largest mean pore sizes (SG-2/SG-5) are similar to those by the previous model, while lower values are found for samples with narrower characteristic pore lengths. The differences between the gas permeability predicted by this model and the experimental values, indicated as the root mean-squared error (RMSE) in Table 5.4, are lower than in the previous case. It is also worth noting that solutions from this method appeared to be less sensitive to changes in seed values than in the previous model, making

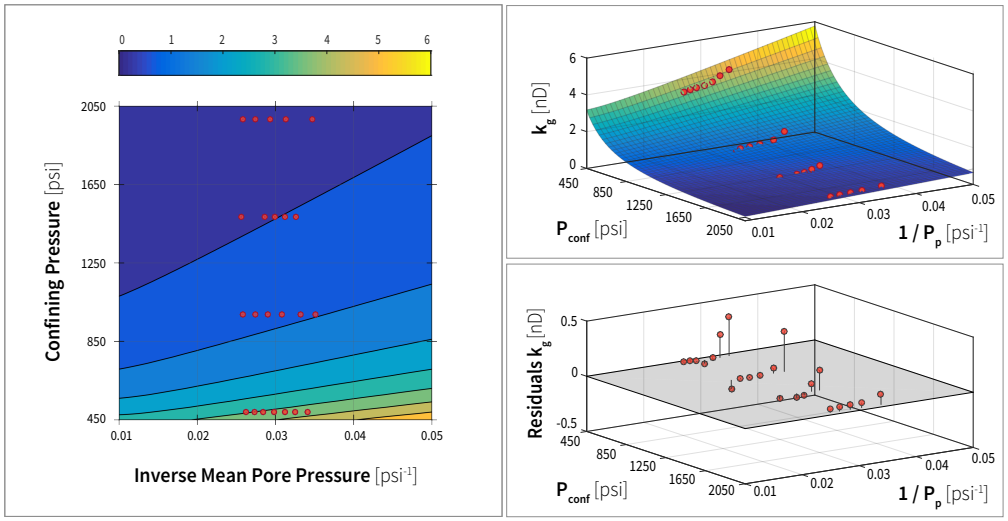

(a) First Order Model

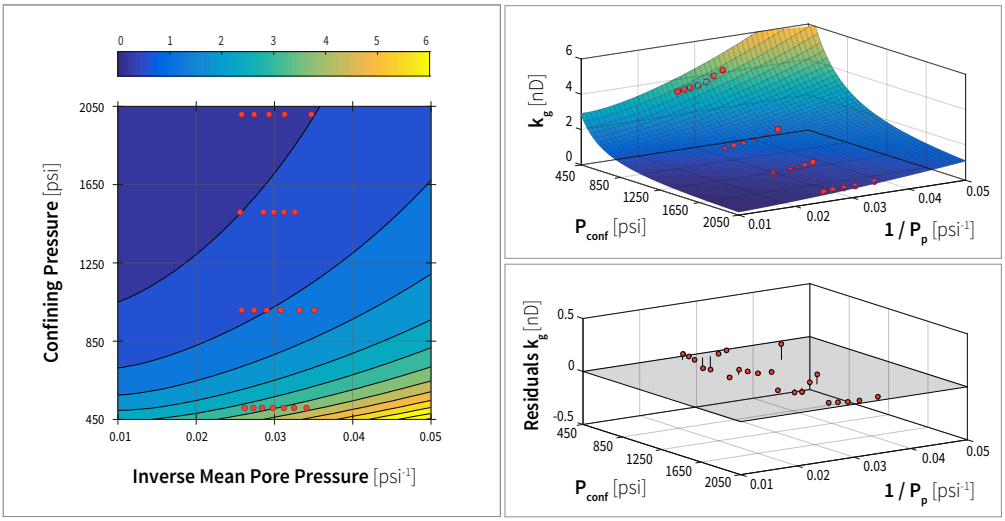

(b) Second Order Model

Figure 5.15. Example of analysis conducted on sample SG-1 to determine the model parameters, assuming a first (case 2, top panel) and second order gas slippage equation (case 3, bottom panel). Left and top right figures in each panel show the combined poroelastic and gas slippage effects on permeability (k_g), at various confining (P_{conf}) and inverse mean pore pressures ($1/P_p$). Bottom right figures show the residuals obtained when predicting gas permeability, based on the best fit for either the original data points that conform to the linear Klinkenberg equation (case 2) or the full data set (case 3). The permeability isolines suggest that the first order model may underestimate the contribution from rarefaction effects to total gas flow at low mean pore pressure.

the determination of optimal coefficients more straightforward. After considering the introduction of the two additional parameters in the equation, however, the improvements observed become less significant. The strong dependence of non-linear least-squares methods on seed values (variable constraints) for obtaining the optimal model parameters should also be recognised, as it can introduce additional bias into the process and ultimately skew the regression results. This issue is often unavoidable in the analysis of experimental data, regardless of its nature, so employing consistent criteria for the introduction of different model constraints are critical for obtaining analogous solutions. In the current study, the multi-parameter permeability models were constrained based on a uniform – albeit arbitrary – methodology, by selecting lower and then upper bound parameter values that minimised the RSME of the solutions. It is therefore possible to obtain dissimilar results – and conclusions – if a different regression method and/or criteria are utilised.

As expected, the effective stress coefficients obtained by both methods suggest that the Terzaghi principle (X=1) is invalid for the samples studied. Looking at Figure 5.15, the second order equation seemingly has the ability to predict the greater enhancement of apparent permeability at lower mean pore pressures (P_p) more accurately than the first order model. When the measured gas permeability is dominated by poroelastic mechanisms or where contribution from diffusion is likely negligible, the values estimated from both methodologies are closer in magnitude. In this region, first order models provide a reasonable approximation for interpretation of gas permeability results in shales. Ultimately, the choice of a second order equation to model matrix permeability should be contingent on the number of experimental data points available for fitting, as well as the flow system under study. The inherent risk of over-parametrisation requires great caution when applying these complex methods over a limited number of data points, as they can yield well numerically fitting solutions that are nevertheless disconnected from the physical principles behind the equations. This potential issues will be addressed in the final part of this chapter, which examines the relationships between the optimal parameters obtained by the second order model and rock properties derived from other experimental methods.

5.5.2.3. Analysis of Coefficients Determined by Multi-Parameter Regression on Second Order Model

Pore Structure and Gas Transport Mechanisms in Shales

The second order model results for the coefficients X, k_L, b_0 and θ_2^2 were plotted against the characteristic pore radii (r_{MICP}) and widths (w_{LP-N_2}) of the samples,

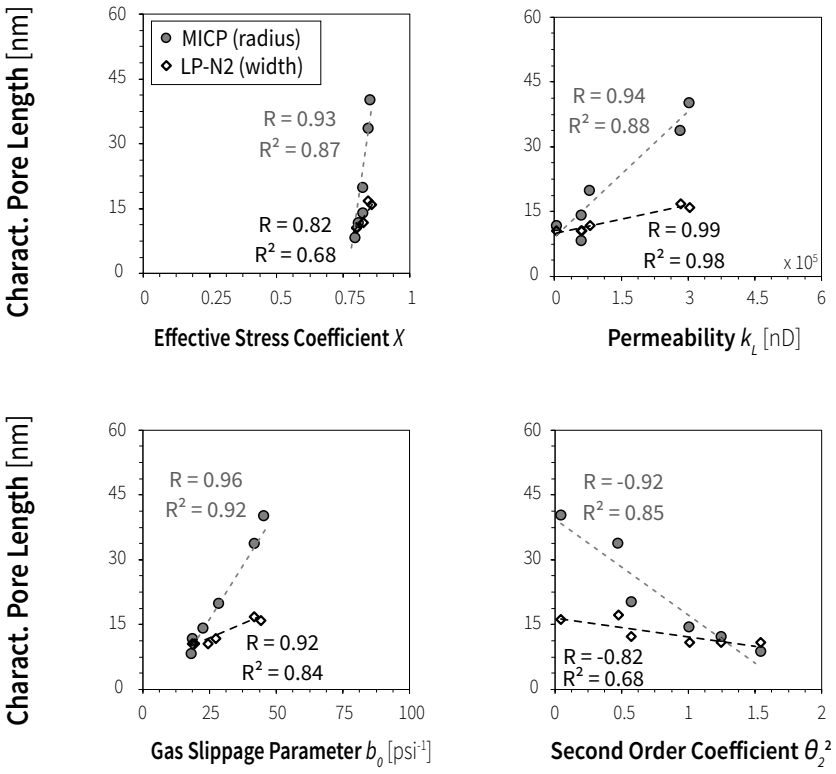

Figure 5.16. Relationships between various second order model parameters (case 2) and characteristic pore lengths, based on mean pore radii from MICP tests (cylindrical pores) and widths from LP-N_2 measurements (slit-shaped pores). The corresponding linear correlation coefficient (R) and coefficient of determination (R^2) are also indicated.

determined from MICP and LP-N_2 tests respectively (Figure 5.16). A strong positive linear relationship ($R > 0.82$) is observed between characteristic pore lengths and the coefficients X, indicating that the pore size distribution of the rock likely has great influence over the ruling effective stress laws. The k_L and b_0 parameters also show a strong uphill correlation ($R > 0.92$) with both r_{MICP} and w_{LP-N_2}. In addition, a strong albeit negative linear relationship ($R < -0.82$) is seen between the second order coefficients θ_2^2 and the mean pore radii and widths determined experimentally for the SG samples.

Turning now to the MICP threshold pressure of the samples (Figure 5.17), strong negative linear relationships ($R < -0.80$) emerged from the plots against the effective stress coefficient (X), the extrapolated permeability (k_L) and the gas slippage coefficient (b_0). A moderate downhill correlation ($R = 0.50$) was observed with the slippage sensitivity to effective stress parameter (β_p), however, the low coefficient of determination ($R^2 = 0.33$) indicates a very weak linear relationship between both variables at best.

Overall, the graphs suggest that the characteristic pore lengths in the shale matrix may have a great direct impact on the dominant gas transport

mechanisms, as well as an indirect effect over the poroelastic behaviour of the reservoir. The positive trends emerging between pore sizes and gas slippage parameters, however, result counter-intuitive when comparing them to Equations 5.6 and 5.7 and should caution that the parameters being evaluated are likely not equivalent.

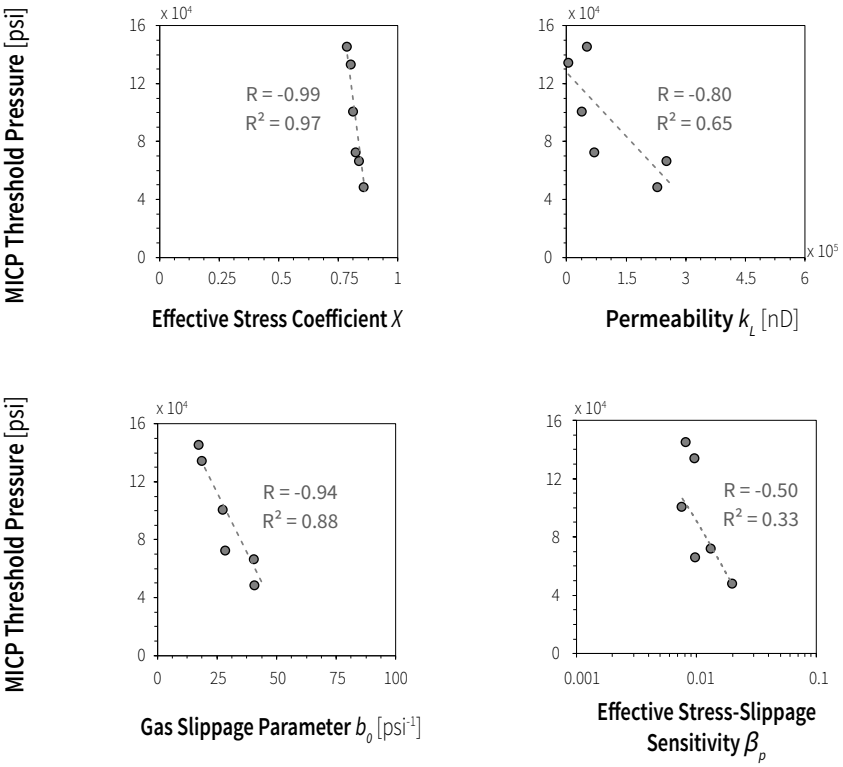

Figure 5.17. Relationships between threshold pressure determined from MICP tests and various second order model parameters (case 2), with their corresponding linear correlation coefficient (R) and coefficient of determination (R^2).

NMR T_2 Measurements and Gas Flow in Shales

The relationships between various second order model parameters and FFI from T_2 experiments were also explored in Figure 5.18, to investigate the potential use of NMR data for permeability prediction. The FFI (L) and FFI (U) were calculated after applying lower and upper cut-off values to the normalised cumulative T_2 amplitude, indicated as $T_{2\,L}$ and $T_{2\,U}$ in Table 5.2. The plots revealed a deviation in the FFI (L) calculated for sample SG-1, likely associated with the high measured TOC content which can cause the shifting of NMR signal towards low T_2 times, as well as its underestimation due to the impossibility of detecting full components below the detection threshold of the

instrument (0.1 ms). The FFI (L) for sample SG-1, highlighted in red in the graphs, was therefore excluded from further analysis.

Downhill correlations are seen between FFI (L) and effective stress coefficient (X), power law exponent (α_p), extrapolated permeability (k_L) and gas slippage parameter (b_0). In contrast, moderate-to-strong positive linear relationships emerge from the comparison of the same model parameters with the FFI (U) of the samples (R: 0.78–0.83; R^2: 0.60–0.69). This combination of findings, while preliminary, provides some support for the conceptual premise that 1D–NMR measurements could potentially be used for deriving permeability interpretations. Nonetheless, caution must be applied due to the small sample size used in this research study and potential unsuitability of the second order model in its current form. Further work is thus needed to determine whether these findings can be generalised or if the trends herein observed are simply a serendipitous, yet random, occurrence.

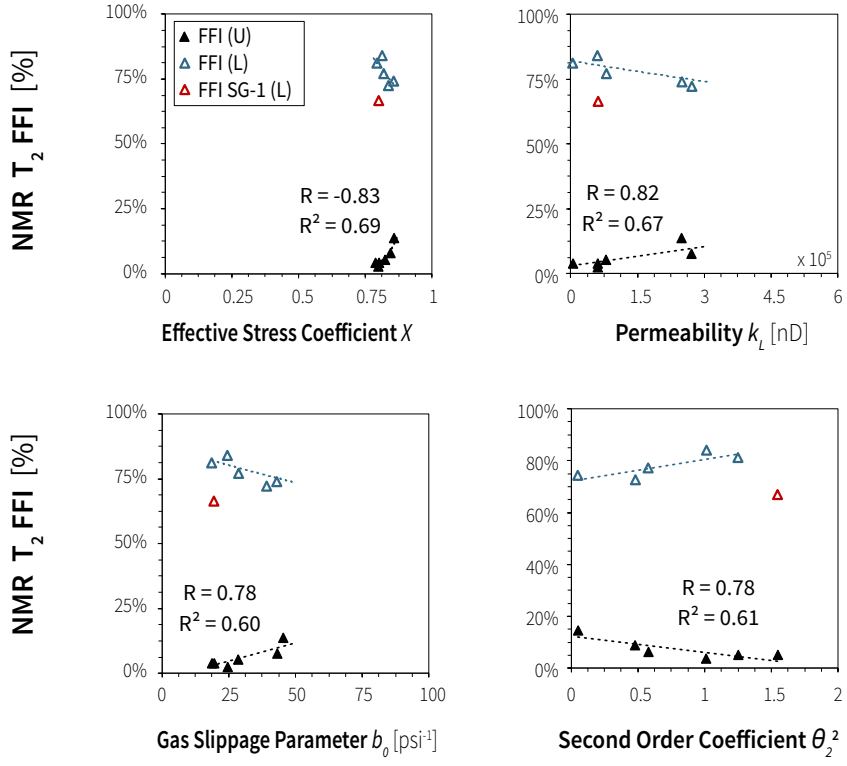

Figure 5.18. Relationships between free fluid indices (FFI), obtained from NMR T_2 measurements on *as-received* core samples, and various second order model parameters (case 2). The FFI (L) was calculated as the normalised amplitude above a lower $T_{2\,L}$ in the range 0.15–0.20 ms, whereas FFI (U) was determined for an upper threshold $T_{2\,U}$ value around 1.4–3.3 ms. The FFI (L) for sample SG-1, highlighted in red, was not considered in the analysis.

Matrix Composition and Poroelastic Behaviour in Shales

The last analysis conducted in this study explored the relationships between sample composition and effective stress sensitivity of permeability (given by α_p) and gas slippage (indicated by β_p), illustrated in Figure 5.19.

The plot of β_p parameters (leftmost chart) showed linear relationships with the sum of illite and smectite clay minerals (I+S, $R^2 = 0.56$ uphill), and with the total quartz and feldspars content (QF, $R^2 = 0.44$ downhill). On the other hand, a negative trend was observed in the plot of β_p and the samples' TOC, yet with a very low coefficient of determination ($R^2 = 0.15$). Turning now to the analysis of α_p exponents, the plot reveals uphill correlations with QF ($R^2 = 0.28$) and TOC ($R^2 = 0.70$), and a downhill trend in the correspondence with I+S ($R^2 = 0.57$).

Based on this information, a ratio of (QF+TOC)/(I+S) was constructed and compared to the β_p and α_p coefficients (rightmost chart), revealing moderate-to-strong negative linear relationships with R values equal to -0.74 and -0.77 respectively. Remembering that causation cannot be inferred from correlation, this last plot is a mere illustration of the complexity of the shale matrix, which poses unique challenges for correctly understanding and predicting the evolution of gas permeability – and therefore production – under real reservoir conditions.

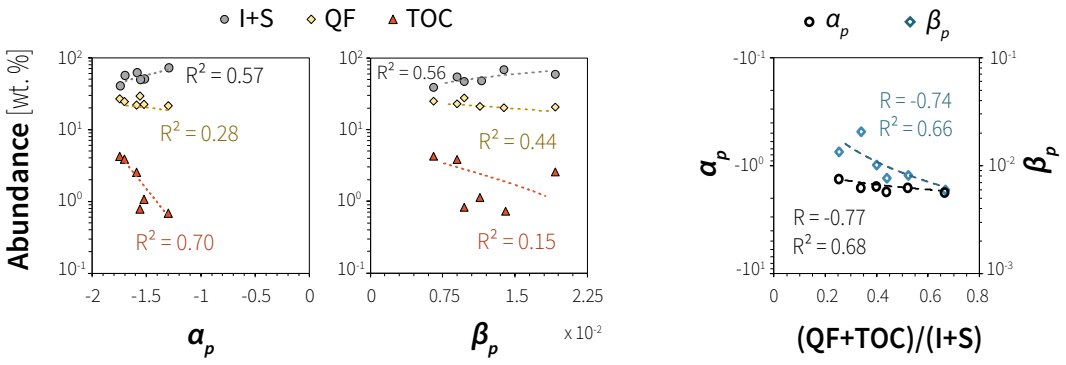

Figure 5.19. Compositional associations for slippage–effective stress (β_p) and permeability–effective stress α_p sensitivity parameters, on the six Goldwyer shale samples studied.

Table 5.4.
Summary of experimental settings and effective stress–permeability model parameters obtained for the cases outlined in Subsection 5.5.2.2. The root-mean squared error (RMSE) for the measured permeability is indicated for each of the cases considered, calculated by non-linear regression.

Sample	**Case 1**							
ID	X	k_L (µD)	α_p			b_0 (psi)	β_p	RMSE
SG-1	0.61	30.52	-1.60			36.16	0.012	0.14
SG-2	0.82	195.70	-1.58			39.83	0.002	4.44
SG-3	0.76	55.53	-1.43			42.20	0.025	1.69
SG-4	0.73	3.93	-1.25			31.25	0.010	0.30
SG-5	0.72	199.60	-1.48			39.96	0.014	6.80
SG-6	0.84	23.23	-1.49			40.05	0.060	3.27
	Case 2							
ID	X	k_L (µD)	α_p	θ_1	θ_2^2	b_0 (psi)	β_p	RMSE
SG-1	0.78	43.95	-1.67	1	1.60	20.00	0.006	0.08
SG-2	0.87	244.90	-1.66	1	0.43	40.20	0.008	2.00
SG-3	0.87	73.13	-1.50	1	0.50	29.90	0.010	0.74
SG-4	0.80	4.19	-1.30	1	1.23	21.33	0.013	0.24
SG-5	0.90	210.70	-1.53	1	0.15	40.53	0.019	6.55
SG-6	0.82	36.96	-1.53	1	1.05	28.45	0.009	0.97

5.5.3. Limitations of this Research Study

The study presented in this chapter has potential limitations that stem from both the experimental methodology and interpretations of results. First and foremost, findings cannot be generalised owing to the small sample size used in this research and therefore statistical tests should only be regarded as indications of possible relationships. While tests were carried out on "as-received" shale core samples to avoid possible structural changes, the absence of pore blockages or more complex phenomena related to the presence of native reservoir fluids cannot be ascertained in the current study. When it comes to methodological technicalities, the use of core discs was found to decrease the tests duration significantly, yet the short length-to-width ratio could also inadvertently induce errors associated with boundary effects. Furthermore, the pore and confining pressures at which permeability was

measured are significantly lower than those at reservoir conditions, restricting the direct extrapolation of results. It is also worth mentioning that core samples were only evaluated over a narrow range of effective stresses due to time constraints, which might be insufficient for the assessment of geomechanical effects on shale permeability.

The technical difficulties associated with the evaluation of permeability in shales are also reflected in the relative low number of experimental studies found in the literature, compared to other research areas. Very few published studies have conducted permeability measurements on shale samples at such low pore pressures or under conditions comparable to the experiments included in this chapter (e.g. Fathi et al., 2012; Zamirian et al., 2014; Mathur et al., 2016; Moghadam and Chalaturnyk, 2016), which poses additional difficulties when interpreting results. When the contribution of slip flow to total gas flow is significant, the decoupling of gas transport and poroelastic mechanisms in shales may not be possible. Under such conditions, the concept of "intrinsic" or Klinkenberg-corrected permeability can lose its significance, particularly when evaluating soft porous materials (Gensterblum et al., 2014). The use of multi-parameter equations may hence lead to erroneous interpretations of the underlying causes of non-linear behaviour similar to that observed in Figure 5.7. Second-order methods with numerous independent variables in particular, can yield numerically fitting albeit inconsistent results, as explained recently by Fink et al. (2018). In the current study, this might be evidenced by the counter-intuitive direct correspondence between characteristic pore length of the samples and the gas slippage parameter b_0 obtained by a second order multi-parameter equation (Figure 5.16). On the other hand, small associated second order coefficients (θ_2^2) were obtained for the samples showing the strongest linear behaviour of the set (SG-2/SG-3/SG-5). This suggests that while a multi-parameter second order equation does capture more complex effects, they may still be incorrectly characterised as a result of – for instance – the absence of adsorption, pore geometry or organic matter considerations in the equation itself. The introduction of additional parameters might then be tempting; however, the associated increase in uncertainty and bias could only be offset by acquiring a large number of data points, which would ultimately be impractical due to the complexity of experimental permeability determination in shales.

5.6. Conclusion

The main factors affecting the duration of tests and potential sources of error have been extensively discussed in this chapter, and the length of the samples was found to have great influence on the time to reach pseudo-stationary flow. Thin core disks are thus preferred to minimise the test duration that can otherwise lead to significant errors, derived from variations in the reference (laboratory) conditions. The trade-off with the increase in *core-end* effects and associated errors should be evaluated in future work.

Experimental permeability data, measured at various confining and mean pore pressures on samples from the Goldwyer Formation, was presented. Non-linear effects were observed in the gas permeability data at lower mean pore pressures, likely associated with significant rarefaction effects due to the abundance of narrow dominant pore lengths. The first order Klinkenberg equation failed to account for non-linearity and yielded negative values of extrapolated permeability at increasing confining stress. The second order "double-slip" model returned more consistent values and the graphical analysis showed that it can account for both the linear and non-linear behaviours at different confining pressures.

A second order multi-parameter regression model was finally proposed, considering both rarefaction and poroelastic effects on matrix permeability, to evaluate whether the contribution of each mechanism could be quantified. The second order model parameters were then compared with experimental data from MICP, LP-N_2 and NMR measurements, as well as sample composition. Relationships emerged from the comparison of model coefficients related to gas slippage and MICP/LP-N_2 characteristic pore lengths, MICP threshold pressure, and NMR free fluid indices. In contrast, the poroelastic behaviour, defined by the sensitivity of permeability and gas slippage coefficient to effective stress, appeared to be more likely influenced by the shale matrix composition. The preliminary findings presented in this chapter provide some support to the case for the use of second order flow models, which may ultimately lead to a greater understanding of the controls behind matrix permeability evolution in shale gas reservoirs. Several questions remain unanswered at present, that stem not only from the counter-intuitive relationships observed in some of the results, but also from the lack of published research on this topic. Further studies, which take into account the issues highlighted in this chapter, will need to be undertaken for a proper characterisation of the interplay between poroelastic and dynamic gas transport mechanisms.

CHAPTER 6

Conclusion

This thesis set out to cast some light on the interrelationships between composition, pore structure, gas transport properties and poroelastic behaviour in shales, while also assessing the suitability of nuclear magnetic resonance as a petrophysical characterisation tool. Experimental and analytical approaches were combined to explore the pore fluid distributions (free, bound fluid indices) from T_2 experiments on shale samples, based on the identification and subsequent application of thresholds cut-offs. The NMR coefficients derived (FFI, BVI) were correlated with pore structure and compositional core data, to understand the possible controls on gas storage and flow attributes, as well as the proton populations distinguished by each threshold $T_{2\ \text{cut-off}}$. These insights were then integrated with results from gas permeability tests on shale discs, to investigate the interplay between composition, pore structure and permeability evolution. A flow model was finally proposed which considered the influence of both fluid dynamics and poroelastic effects, to interpret the measured gas permeability data (in the presence of significant rarefaction) and assess the particular gas transport mechanisms in shales. The main findings and conclusions from this research are summarised below in Section 6.1, while directions for future work are suggested in Section 6.2.

6.1. Conclusions

This section is divided into three subsections, each addressing one of the research objectives outlined in the introductory chapter (1.3). The main highlights, findings and conclusions of each chapter, relevant to the corresponding topic, are indicated.

6.1.1. Optimisation Nuclear Magnetic Resonance Methodologies for Shale Applications

Chapter 3 examined the sole use of 1D–NMR experiments for the petrophysical characterisation of shales, using a twofold approach.

- A systematic study was conducted, utilising both real and synthetic T_2 data, to shed light upon the best practices for NMR signal acquisition and inversion in shales. The evidence from this study suggests that:
  - Improving the quality of NMR signal is deemed equivalent to enhancing the signal-to-noise ratio (SNR) of measurements. This may be achieved with an increase in the number of scans, the complex points sampled per echo, or the density of data points acquired (using shorter echo-spacings), as well as the use of larger core samples or smaller magnet probes.
  - Enhancing the SNR of the measured data will lead to a magnification of the experimental noise on the fastest T_2 components. The use of post-acquisition filters or other data reduction techniques before inversion is thus recommended, to mitigate the impact of noisy signals and prevent misinterpretations of T_2 distributions.
  - The choice of NMR inversion method can greatly effect the shape of T_2 distributions, particularly at short T_2 times.
  - Inversion methods which apply variable regularisation (e.g. BRD) are useful for distinguishing the contribution from adjacent T_2 components and making qualitative petrophysical interpretations, but may also extrapolate NMR data well below the detection limit of spectrometer and yield significantly biased T_2 spectra.
  - Inversion methods which apply fixed amounts of regularisation (e.g. NNLS-LH) cannot individualise adjacent peaks in the T_2 distributions, but they are also less susceptible to bias and thus more appropriate for quantifying attributes such as NMR porosity, or free and bound fluid fractions (FFI, BVI).

- An optimised methodology was proposed for estimating the free and bound fluid indices (FFI, BVI) in shales from NMR T_2 measurements, combining both experimental and analytical techniques. Based on the identification and subsequent application of different threshold $T_{2\,\text{cut-off}}$, the corresponding FFI and BVI fractions are estimated from T_2 experiments on clean, re-saturated core samples from the Carynginia Formation (SC). The most noteworthy methodological aspects and empirical findings are:
  - The $T_{2\,\text{cut-off}}$ may be determined experimentally from the comparison of cumulative T_2 curves, acquired on shale core samples at different

saturation levels (i.e. after brine-saturation, centrifugation, oven-drying procedures).

- The $T_{2\,\text{cut-off}}$ may also be derived analytically from the comparison of T_2 distributions, obtained by different inversion methods (i.e. fixed and variable regularisation) from brine-saturated shale samples.
- Two threshold $T_{2\,\text{cut-off}}$ were determined experimentally, by comparing the T_2 distributions of brine-saturated core plugs from the Carynginia Formation, to the spectra obtained: after centrifugation ($T_{2U} \sim$ 1–2 ms); after vacuum oven-drying ($T_{2L} \sim$ 0.2–0.3 ms). The experimental $T_{2\,\text{cut-off}}$ are consistent with the thresholds identified analytically, upon inspection of the T_2 distributions obtained from brine-saturated samples by a fixed (NNLS-LH/L-curve) and variable (BRD) smoothing inversion algorithms.

Chapter 4 added to the above, drawing upon the integration of 1D–NMR T_2 and 2D–NMR T_1–T_2 data acquired on "as-received" shale samples from the Goldywer Formation (SG).

Overall, this research has shown that threshold $T_{2\,\text{cut-off}}$ may be identified upon inspection of:

- 1D–NMR T_2 distributions from brine-saturated SC core samples, obtained by BRD inversion
- 2D–NMR T_1–T_2 maps from "as-received" SG core samples, obtained by a 2D mapping of the NNLS-LH algorithm
- 1D–NMR T_2 distributions from "as-received" SG core samples, obtained by BRD inversion

These analytical $T_{2\,\text{cut-off}}$ are also consistent with the T_{2L}, T_{2U} determined experimentally. Furthermore, the analysis of T_1–T_2 maps provide support to the premise that these threshold cut-offs are, indeed, delimiting different proton populations.

6.1.2. Characterisation of Pore Structure and Connectivity in Shales

Chapter 4 investigated the associations between pore structure, fluid types and mineralogy in shales, based on the integration of experimental data from LP-CO_2 and LP-N_2 adsorption, 1D– and 2D–NMR and MICP tests on core samples. The main findings of this study can be summarised as:

- Harsh core cleaning methods may dissolve the organic matter and alter the clay structures in shales, consequently distorting porosimetry results.
- The equivalent specific surface area (*e*SSA) appears to be more sensitive to sample composition. In particular:
  - The *e*SSA of Carynginia samples may be influenced by TOC (direct correlation) and total clay content (direct correlation).
  - The *e*SSA of Goldwyer samples may be influenced by TOC (inverse correlation) and sum of illite+smectite clay content (direct correlation).
- 2D–NMR T_1–T_2 maps can be useful to assess pore sizes and fluid types in shales, as well as threshold $T_{2\,\text{cut-off}}$ to identify the different proton populations.
- Two pseudo FFI/BVI coefficients were calculated for each sample, according to the threshold cut-offs (T_{2L}, T_{2U}) determined either experimentally or analytically. The relationships between these ratios and compositional and porosimetry data were also explored:
  - The FFI/BVI (T_{2L}) appear to be more sensitive to TOC (SC/SG samples) and clay content (SC samples).
  - The FFI/BVI (T_{2U}) appear to be more sensitive to dominant pore sizes in the shale matrix.

  This preliminary analysis suggests that there might be a link between the FFI/BVI (T_{2L}) ratios and gas storage properties, and between the FFI/BVI (T_{2U}) and producibility potential in shales, however, more research is still needed.

6.1.3. Experimental Assessment of Gas Transport Mechanisms in Shales

Chapter 5 investigated the interplay between matrix permeability and its evolution, pore structure and composition in shales. The results from gas permeability tests on core samples from the Goldywer Formation were presented, where non-linear effects were observed at low pore pressures. The common Klinkenberg equation and the "double-slip" extended Klinkenberg model were assessed for the interpretation of experimental matrix permeability data. A second order slip flow model was then proposed, considering poroelastic mechanisms in the presence of significant rarefaction. The main findings of this research can be summarised as:

- Permeability tests on shales are very sensitive to unstable ambient conditions.
- Inertial effects are mitigated by conducting measurements at low pore pressures, but rarefaction effects may be substantial.
- The Klinkenberg equation fails to account for the mechanisms behind the gas permeability data measured in the transition flow regime (i.e. at high confining stress and low pore pressure), but all experimental results can be fitted with the "double-slip" model.
- A second order slip flow model (considering poroelastic behaviour) could be more suitable to interpret gas permeability data in the presence of significant rarefaction effects. When using multi-parameter equations, however, a large number of data points are required to achieve consistent results. The interrelationships between the second order model parameters, compositional and porosimetry data were studied:
  - The model parameters linked to gas slippage appear to be more sensitive to the characteristic pore lengths in the shale matrix.
  - The model parameters linked to poroelastic behaviour appear to be more sensitive to sample composition.
  - It is possible that FFI/BVI (T_{2U}) coefficients may correlate to model parameters linked to gas slippage, although further research on this is needed.
  - Some counter-intuitive relationships were observed, which could indicate the misrepresentation of effects in the equation proposed.
- Overall, as the pressure in shale gas reservoirs declines:
  - The permeability evolution due to poroelastic mechanisms might be controlled (directly or indirectly) by the same petrophysical properties associated with gas storage potential.
  - The permeability evolution due to fluid dynamics mechanisms might be controlled (directly or indirectly) by the relative abundance of narrow pore sizes in the shale matrix.

6.2. Recommendations for Future Work

This thesis has addressed several challenges in the petrophysical characterisation of shales, to advance the understanding of the complex

interplay between flow properties, pore structure, matrix composition and poroelastic mechanisms. The limited sample size used in this study undoubtedly requires a careful interpretation of results, and considerably more work will be needed to assess the validity of the findings herein presented at larger scales or its applicability to other shale reservoirs. In particular, the following possible avenues for research have been identified:

- Explore the use of inversion methods with variable smoothing for the analysis of 2D–NMR data. In addition, further research should be conducted on the use of 2D–NMR T_1–T_2 maps to directly quantify pore sizes and fluid types.

- Investigate the impact of sample preparation and degassing – or drying – temperature on pore size distribution results, obtained by low pressure gas adsorption and mercury intrusion porosimetry tests on shales.

- Investigate the relationships between:

  - FFI/BVI (T_{2L}) and eSSA, and ultimately their connection to gas storage properties in shales;
  - FFI/BVI (T_{2U}) and flow model parameters, and ultimately the correlation with gas transport mechanisms in shales;

  to evaluate the possibility of estimating petrophysical properties from NMR measurements.

- Conduct additional permeability tests on the same or similar shale samples, under comparable experimental conditions, to check for deviations from Klinkenberg behaviour and rule out other sources of nonlinear effects:

  - using higher inflow pressures, thus lowering the Knudsen numbers and gas slippage effects;
  - using other probing gasses;
  - using clean core samples, thus reducing the uncertainties related to the presence of pore fluids other than the probing gas;
  - over a wide range of confining and pore pressure combinations, to understand the evolution of matrix permeability under variable poroelastic and dynamic gas transport effects.

- Assess the validity of the second order gas flow model proposed or with modifications, utilising permeability data on samples from other shale formations.

Bibliography

Adam, N. K. (1964). The chemical structure of solid surfaces as deduced from contact angles. In *American chemical society* (Chap. 2, pp. 52–56).

Adesida, A. G., Akkutlu, I., Resasco, D. E., & Rai, C. S. (2011). Characterization of Barnett Shale Kerogen Pore Size Distribution using DFT Analysis and Grand Canonical Monte Carlo Simulations. In *Spe annual technical conference and exhibition*. Denver, Colorado, USA.

Adzumi, H. (1937). Studies on the flow of gaseous mixtures through capillaries. III. The flow of gaseous mixtures at medium pressures. *Bulletin of the Chemical Society of Japan*, *12*(6), 292–303.

Aguilera, R. (2014). Flow Units: From Conventional to Tight-Gas to Shale-Gas to Tight-Oil to Shale-Oil Reservoirs. *17*(2), 190–208.

Akkutlu, I. Y. & Fathi, E. (2012). Multiscale Gas Transport in Shales With Local Kerogen Heterogeneities. *SPE Journal*, *17*(04), 1002–1011.

Al Hinai, A. S. H. (2014). *Investigation of gas shale pore structure and its influence on transport properties* (Doctoral dissertation, Curtin University).

Ambrose, R. J., Hartman, R. C., Diaz Campos, M., Akkutlu, I. Y., & Sondergeld, C. (2010). New Pore-scale Considerations for Shale Gas in Place Calculations. Pittsburgh, Pennsylvania, USA: Society of Petroleum Engineers.

American Petroleum Institute. (1998). *Recommended Practices for Core Analysis* (2nd ed.). Washington, DC, USA: American Petroleum Institute.

Anovitz, L. M. & Cole, D. R. (2015). Characterization and Analysis of Porosity and Pore Structures. *Reviews in Mineralogy and Geochemistry*, *80*(1), 61–164.

B. Z. (2018). How the Shale Oil Industry Survived the Crisis? Retrieved from http://lebanongasnews.com/wp/how-the-shale-oil-industry-survived-the-crisis/

Bailey, S. (2011). Closure and Compressibility Corrections to Capillary Pressure Data in Shales.

Beskok, A. & Karniadakis, G. (1999). Report: A model for flows in channels, pipes, and ducts at micro and nano scales. *Microscale Thermophysical Engineering*, *3*(1), 43–77.

Birdwell, J. E. & Washburn, K. E. (2015). Multivariate Analysis Relating Oil Shale Geochemical Properties to NMR Relaxometry. *Energy & Fuels*, *29*(4), 2234–2243.

Bloch, F. (1946). Nuclear Induction. *Phys. Rev. 70*(7-8), 460–474.

Bloembergen, N., Purcell, E. M., & Pound, R. V. (1948). Relaxation effects in nuclear magnetic resonance absorption. *Physical Review*, *73*(7), 679–712.

Borgia, G. C., Brown, R. J. S., & Fantazzini, P. (2000). Uniform-Penalty Inversion of Multiexponential Decay Data. *Journal of Magnetic Resonance*, *147*(2), 273–285.

Borgia, G. C., Fantazzini, P., & Mesini, E. (1990). Water 1H spin-lattice relaxation as a fingerprint of porous media. *Magnetic Resonance Imaging*, *8*(4), 435–447.

Borgia, G., Brown, R., & Fantazzini, P. (1998). Uniform-penalty inverstion of multiexponential decay data. *Journal of Magnetic Resonance*, *132*(132), 65–77.

Bortolotti, V., Brown, R. J. S., Fantazzini, P., Landi, G., & Zama, F. (2016). Uniform Penalty inversion of two-dimensional NMR relaxation data. *Inverse Problems*, *33*(1), 15003.

Brace, W. F. (1980). Permeability of crystalline and argillaceous rocks. *International Journal of Rock Mechanics and Mining Sciences and Geomechanics*, *17*(5), 241–251.

Brace, W. F., Walsh, J. B., & Frangos, W. T. (1968). Permeability of granite under high pressure. *Journal of Geophysical Research*, *73*(6), 2225–2236.

Brown, A. A. (2015). Interpreting Permeability from Mercury Injection Capillary Pressure Data. In *Aapg 2015 annual convention and exhibition* (Vol. 41660, pp. 3–5).

Brown, R. J. S. (2001). The Earth's-field NML development at Chevron. *Concepts in Magnetic Resonance*, *13*(6), 344–366.

Brownstein, K. R. & Tarr, C. E. (1979). Importance of Classical Diffusion in NMR Studies of Water in Biological Cells. *Physical Review*, *A 19*(6), 2446–2453.

Brunauer, S. (1945). Physical adsorption. *The adsorption of gases and vapors*, *1*, 226.

Brunauer, S., Emmett, P. H., & Teller, E. (1938). Adsorption of Gases in Multimolecular Layers. *Journal of the American Chemical Society*, *60*(2), 309–319.

Burger, J., McCarty, D., Peacher, R., & Fischer, T. (2014). Sample Preparation for Unconventional Analysis: a Case for Solvent Extraction. In *International symposium of the society of core analysts* (p. 9). Avignon, France.

Burgess, C. G. V., Everett, D. H., & Nuttall, S. (1989). Adsorption hysteresis in porous materials. *Pure and Applied chemistry*, *61*(11), 1845–1852.

Bustin, R. M., Bustin, A. M. M., Cui, A., Ross, D., & Pathi, V. M. (2008). Impact of Shale Properties on Pore Structure and Storage Characteristics. In *Spe shale gas production conference*. Fort Worth, Texas, USA: Society of Petroleum Engineers.

Butler, J. P., Reeds, J. A., & Dawson, S. V. (1981). Estimating Solutions of First Kind Integral Equations with Nonnegative Constraints and Optimal Smoothing. *SIAM Journal on Numerical Analysis*, *18*(3), 381–397.

Carr, H. Y. & Purcell, E. M. (1954). Effects of Diffusion on Free Precession in Nuclear Magnetic Resonance Experiments. *Physical Review*, *94*(3), 630–638.

Chalmers, G. R. L., Ross, D. J. K., & Bustin, R. M. (2012). Geological controls on matrix permeability of Devonian Gas Shales in the Horn River and Liard basins, northeastern British Columbia, Canada. *International Journal of Coal Geology*, *103*, 120–131.

Chen, S., Arro, R., Minetto, C., Georgi, D., & Liu, C. (1998). Methods For Computing Swi And BVI From NMR Logs. In *Spwla 39th annual logging*

symposium. Keystone, Colorado, USA: Society of Petrophysicists and Well-Log Analysts.

Cheng, A. H.-D. (2016). *Poroelasticity* (1st ed.). Theory and Applications of Transport in Porous Media. Oxford, Mississippi, USA: Springer.

Civan, F. (2010). Effective Correlation of Apparent Gas Permeability in Tight Porous Media. *Transport in Porous Media*, *82*(2), 375–384.

Civan, F. (2017). Comprehensive Modeling of Nanopore Gas Storage and Transport Including Absorption, Adsorption, and Confinement Effects in Shale-Gas Reservoirs. Austin, Texas, USA: Unconventional Resources Technology Conference.

Clarkson, C. R. (2013). Production data analysis of unconventional gas wells: Review of theory and best practices. *International Journal of Coal Geology*, *109-110*, 101–146.

Clarkson, C. R., Haghshenas, B., Ghanizadeh, A., Qanbari, F., Williams-Kovacs, J. D., Riazi, N., ... Deglint, H. J. (2016). Nanopores to megafractures: Current challenges and methods for shale gas reservoir and hydraulic fracture characterization. *Journal of Natural Gas Science and Engineering*, *31*, 612–657.

Clarkson, C. R., Jensen, J. L., & Blasingame, T. (2011). Reservoir Engineering for Unconventional Reservoirs: What Do We Have to Consider? The Woodlands, Texas, USA: Society of Petroleum Engineers.

Coates, G. R. G., Marschall, D., Mardon, D., Galford, J., Mardon, D., Marschall, D., ... Marschall, D. (1997). A New Characterization Of Bulk-Volume Irreducible Using Magnetic Resonance. *The Log Analyst*, *39*(01).

Coates, G. R., Xiao, L., & Prammer, M. G. (1998). *NMR logging: principles and applications*. Halliburton Energy Services.

Comisky, J. T., Santiago, M., McCollom, B., Buddhala, A., & Newsham, K. E. (2011). Sample Size Effects on the Application of Mercury Injection Capillary Pressure for Determining the Storage Capacity of Tight Gas and Oil Shales. In *Canadian unconventional resources conference*. Calgary, Alberta, Canada: Society of Petroleum Engineers.

Cui, X., Bustin, A. M. M., & Bustin, R. M. (2009). Measurements of gas permeability and diffusivity of tight reservoir rocks: different approaches and their applications. *Geofluids*, *9*(3), 208–223.

Darabi, H., Ettehad, A., Javadpour, F., & Sepehrnoori, K. (2012). Gas flow in ultra-tight shale strata. *Journal of Fluid Mechanics*, *710*, 641–658.

Darcy, H. (1856). *Les fontaines publiques de la ville de Dijon: exposition et application des principes à suivre et des formules à employer dans les questions de distribution d'eau*. Les fontaines publiques de la ville de Dijon. Exposition et application des principes à suivre et des formules à employer dans les questions de distribution d'eau: ouvrage terminé par un appendice relatif aux fournitures d'eau de plusieurs villes au filtr. Dalmont. arXiv: arXiv:1011.1669v3

Davies, D. K., Bryant, W. R., Vessell, R. K., & Burkett, P. J. (1991). Porosities, Permeabilities, and Microfabrics of Devonian Shales. In R. H. Bennett, W. R. Bryant, M. H. Hulbert, W. A. Chiou, R. W. Faas, J. Kasprowicz,

. . . T. Yamamoto (Eds.), *Microstructure of fine-grained sediments: From mud to shale* (Chap. 10, pp. 109–119). New York, NY: Springer New York.
De Silva, P. N. K., Simons, S. J. R., Stevens, P., & Philip, L. M. (2015). A comparison of North American shale plays with emerging non-marine shale plays in Australia. *Marine and Petroleum Geology*, *67*, 16–29.
de Boer, J. H., Lippens, B. C., Linsen, B. G., Broekhoff, J. C. P., van den Heuvel, A., & Osinga, T. J. (1966), *21*(4), 405–414.
Dewhurst, D. N., Aplin, A. C., Sarda, J., & Yang, Y. (1998). Compaction-driven evolution of porosity and permeability in natural mudstones: An experimental study. *Journal of Geophysical Research: Solid Earth*, *103*(B1), 651–661.
Does, M. D. (2014). Multi-Exponential Relaxation Analysis (MERA) Toolbox.
Dunn, K.-J., LaTorraca, G. A., & Bergman, D. J. (2002). *NMR in Porous Media*. Elsevier.
Dunn, K.-J., LaTorraca, G. A., Warner, J. L., & Bergman, D. J. (1994). *On the Calculation and Interpretation of NMR Relaxation Time Distributions*. New Orleans, Louisiana, USA: Society of Petroleum Engineers.
Durand, B. (1980). *Kerogen: Insoluble Organic Matter from Sedimentary Rocks*. Editions technip.
English, A. E., Whittall, K. P., Joy, M. L. G., & Henkelman, R. M. (1991). Quantitative Two-Dimensional time Correlation Relaxometry. *Magnetic Resonance in Medicine*, *22*(2), 425–434.
Eveleigh, L. J. (1996). Chapter 1 Fourier transform and signal manipulation. In D. N. Rutledge (Ed.), *Data handling in science and technology* (Vol. Volume 18, pp. 1–24). Elsevier.
Everett, D. H. (1967). Solid-Gas Interface. *Chemistry in Britain*, *3*(8), 341.
Fathi, E., Tinni, A., & Akkutlu, I. Y. (2012). Correction to Klinkenberg slip theory for gas flow in nano-capillaries. *International Journal of Coal Geology*, *103*, 51–59.
Fink, R., Letham, E. A., Krooss, B. M., & Amann-Hildenbrand, A. (2018). Caution when comparing simulation results and experimental shale permeability data: Reply to "Comments on "Apparent permeability of gas shales – Superposition of fluid-dynamic and poro-elastic effects" by Fink et al. " by Moghaddam. *Fuel*, *234*, 1545–1549.
Fink, R., Krooss, B. M., Gensterblum, Y., & Amann-Hildenbrand, A. (2017). Apparent permeability of gas shales – Superposition of fluid-dynamic and poro-elastic effects. *Fuel*, *199*, 532–550.
Fleury, M., Kohler, E., Norrant, F., Gautier, S., M'Hamdi, J., & Barré, L. (2013). Characterization and Quantification of Water in Smectites with Low-Field NMR. *The Journal of Physical Chemistry C*, *117*(9), 4551–4560.
Fleury, M. & Romero-Sarmiento, M. (2016). Characterization of shales using T_1–T_2 NMR maps. *Journal of Petroleum Science and Engineering*, *137*, 55–62.
Fleury, M. & Soualem, J. (2009). Quantitative analysis of diffusional pore coupling from T_2–store–T_2 NMR experiments. *Journal of colloid and interface science*, *336*(1), 250–9.
Folk, R. L. (1980). *Petrology of Sedimentary Rocks*. Hemphill Publishing Company.

Fordham, E. J., Sezginer, A., & Hall, L. D. (1995). Imaging Multiexponential Relaxation in the (y, LogeT1) Plane, with Application to Clay Filtration in Rock Cores. *Journal of Magnetic Resonance, Series A*, *113*(2), 139–150.

Freedman, R. (2002). Processing NMR data in the presence of coherent ringing.

Freedman, R. (2006). Advances in NMR Logging. *Journal of Petroleum Technology*, *58*(1), 60–66.

Gensterblum, Y., Ghanizadeh, A., Cuss, R. J., Amann-Hildenbrand, A., Krooss, B. M., Clarkson, C. R., ... Zoback, M. D. (2015). Gas transport and storage capacity in shale gas reservoirs - A review. Part A: Transport processes. *Journal of Unconventional Oil and Gas Resources*, *12*, 87–122.

Gensterblum, Y., Ghanizadeh, A., & Krooss, B. M. (2014). Gas permeability measurements on Australian subbituminous coals: Fluid dynamic and poroelastic aspects. *Journal of Natural Gas Science and Engineering*, *19*, 202–214.

Geoscience Australia. (2018, July 14). Canning Basin. Retrieved July 14, 2018, from http://www.ga.gov.au/scientific-topics/energy/province-sedimentary-basin-geology/petroleum/offshore-northwest-australia/canning

Gerothanassis, I. P. (1987). Methods of avoiding the effects of acoustic ringing in pulsed fourier transform nuclear magnetic resonance spectroscopy. *Progress in Nuclear Magnetic Resonance Spectroscopy*, *19*(3), 267–329.

Ghanizadeh, A., Gasparik, M., Amann-Hildenbrand, A., Gensterblum, Y., & Krooss, B. M. (2014). Experimental study of fluid transport processes in the matrix system of the European organic-rich shales: I. Scandinavian Alum Shale. *Marine and Petroleum Geology*, *51*, 79–99.

Ghori, K. & Haines, P. (2006). Paleozoic petroleum systems of the canning basin: A review. In *Aapg 2006 international conference and exhibition* (10120). Perth, Australia.

Golub, G. H., Heath, M., & Wahba, G. (1979). Generalized Cross-Validation as a Method for Choosing a Good Ridge Parameter. *Technometrics*, *21*(2), 215–223.

Grebenkov, D. S. (2007). NMR survey of reflected Brownian motion. *Reviews of Modern Physics*, *79*(3), 1077–1137.

Gregg, S. J. & Sing, K. S. W. (1982). Adsorption, surface area and porosity. *Journal of the Electrochemical Society*, *114*(11), 371.

Groen, J. C., Peffer, L. A. A., & Pérez-Ramírez, J. (2003). Pore size determination in modified micro-and mesoporous materials. Pitfalls and limitations in gas adsorption data analysis. *Microporous and Mesoporous Materials*, *60*(1), 1–17.

Grunewald, E. & Knight, R. (2009). A laboratory study of NMR relaxation times and pore coupling in heterogeneous media. *Geophysics*, *74*(6), E215–E221.

Gupta, N., Fathi, E., & Belyadi, F. (2018). Effects of nano-pore wall confinements on rarefied gas dynamics in organic rich shale reservoirs. *Fuel*, *220*, 120–129.

Hall, P. L., Astill, D. M., & McConnell, J. D. C. (1986). Thermodynamic and structural aspects of the dehydration of smectites in sedimentary rocks. *Clay Minerals*, *21*(4), 633–648.

Hansen, P. C. (1992). Numerical tools for analysis and solution of Fredholm integral equations of the first kind. *Inverse Problems*, *8*(6), 849.

Hansen, P. C. (2015). *Regularization Tools for Matlab*.

Hansen, P. C., Jensen, T. K., & Rodriguez, G. (2007). An adaptive pruning algorithm for the discrete L-curve criterion. *Journal of Computational and Applied Mathematics*, *198*(2), 483–492.

Hansen, P. & O'Leary, D. (1993). The Use of the L-Curve in the Regularization of Discrete Ill-Posed Problems. *SIAM Journal on Scientific Computing*, *14*(6), 1487–1503.

Hansen, P. C. (1987). The truncatedSVD as a method for regularization. *BIT Numerical Mathematics*, *27*(4), 534–553.

Haynes, W. M. (2014). *CRC handbook of chemistry and physics* (95th ed.) (W. M. Haynes, Ed.). Boca Raton, FL, USA: CRC press.

Heller, R., Vermylen, J., & Zoback, M. (2014). Experimental investigation of matrix permeability of gas shales. *AAPG Bulletin*, *5*(5), 975–995.

Hill, D. G. & Nelson, C. R. (2000). Gas productive fractured shales: an overview and update. *Gas Tips*, *6*(3), 4–13.

Hocking, R. M., Mory, A. J., & Williams, I. R. (1994). An Atlas of Neoproterozoic and Phanerozoic Basins of Western Australia. In P. Purcell & R.R. (Eds.), *The sedimentary basins of western australia: Proceedings of petroleum exploration society of australia symposium, perth, 1994* (July 1994, pp. 21–43). Perth, Australia: Petroleum Exploration Society of Australia.

Hürlimann, M. D. & Venkataramanan, L. (2002). Quantitative Measurement of Two-Dimensional Distribution Functions of Diffusion and Relaxation in Grossly Inhomogeneous Fields. *Journal of Magnetic Resonance*, *157*(1), 31–42.

Hürlimann, M. D., Flaum, M., Venkataramanan, L., Flaum, C., Freedman, R., & Hirasaki, G. J. (2003). Diffusion-relaxation distribution functions of sedimentary rocks in different saturation states. *Magnetic Resonance Imaging*, *21*(3), 305–310.

Hürlimann, M. D. (1998). Effective Gradients in Porous Media Due to Susceptibility Differences. *Journal of Magnetic Resonance*, *131*(2), 232–240.

Ingram, R. L. (1953). Fissility of Mudrocks. *GSA Bulletin*, *64*(8), 869–878.

Jackson, J. A. (2001). Los Alamos NMR well logging project. *Concepts in Magnetic Resonance*, *13*(6), 368–378.

Jannot, Y. & Lasseux, D. (2012). A new quasi-steady method to measure gas permeability of weakly permeable porous media. *Review of Scientific Instruments*, *83*(1), 15113.

Javadpour, F. & Ettehadtavakkol, A. (2015). Gas Transport Processes In Shale. In R. Rezaee (Ed.), *Fundamentals of gas shale reservoirs* (Chap. 11). Wiley Online Books. Wiley Online Library.

Javadpour, F., Fisher, D., & Unsworth, M. (2007). Nanoscale Gas Flow in Shale Gas Sediments. *Journal of Canadian Petroleum Technology*, *46*(10), 55–61.

Javadpour, F. (2009). Nanopores and Apparent Permeability of Gas Flow in Mudrocks, Shales and Siltstone. *Journal of Canadian Petroleum Technology*, *48*(08), 16–21.

Jin, Y., Uth, M., Kuznetsov, A. V., & Herwig, H. (2015). Numerical investigation of the possibility of macroscopic turbulence in porous media: a a direct numerical simulation study. *Journal of Fluid Mechanics*, *766*, 76–103.

Jones, S. C. (1997). A Technique for Faster Pulse-Decay Permeability Measurements in Tight Rocks. *SPE Formation Evaluation*, *12*(1), 19–26.

Josh, M., Esteban, L., Delle Piane, C., Sarout, J., Dewhurst, D. N., & Clennell, M. B. (2012). Laboratory characterisation of shale properties. *Journal of Petroleum Science and Engineering*, *88*, 107–124.

Kang, S. M., Fathi, E., Ambrose, R. J., Akkutlu, I. Y., & Sigal, R. F. (2011). Carbon dioxide storage capacity of organic-rich shales. *SPE Journal*, *16*(04), 842–855.

Katsube, T. J. & Scromeda, N. (1991). Effective porosity measuring procedure for low porosity rocks. *Geological Survey of Canada; Current Research, Part E*, 291–297.

Katsube, T. J., Williamson, M., & Scromeda, N. (1992). Effective porosity of tight shales from the Venture Gas Field, offshore Nova Scotia. *Geological Survey of Canada; Current Research, Part D*, 111–119.

Katz, A. J. & Thompson, A. H. (1986). Quantitative prediction of permeability in porous rock. *Physical Review B*, *34*(11), 8179–8181.

Katz, B. & Lin, F. (2014). Lacustrine basin unconventional resource plays: Key differences. *Marine and Petroleum Geology*, *56*, 255–265.

Kausik, R., Minh, C. C., Zielinski, L., Vissapragada, B., Akkurt, R., Song, Y., ... Blair, E. (2011). Characterization of Gas Dynamics in Kerogen Nanopores by NMR. In *Spe annual technical conference and exhibition* (pp. 1–16). Denver, Colorado, USA: Society of Petroleum Engineers.

Kazemi, M. & Takbiri-Borujeni, A. (2015). An analytical model for shale gas permeability. *International Journal of Coal Geology*, *146*, 188–197.

Kehoe, J. (2017). Lessons from the US for Australia's energy crisis.

Kenyon, W. E. (1997). Petrophysical Principles of Applications of NMR Logging. *The Log Analyst*, *38*(02).

Kenyon, W. E., Day, P. I., Straley, C., & Willemsen, J. F. (1988). A Three-Part Study of NMR Longitudinal Relaxation Properties of Water-Saturated Sandstones. *SPE Formation Evaluation*, *3*(3), 622–636.

Khatibi, S., Ostadhassan, M., Xie, Z. H., Gentzis, T., Bubach, B., Gan, Z., & Carvajal-Ortiz, H. (2019). NMR relaxometry a new approach to detect geochemical properties of organic matter in tight shales. *Fuel*, *235*, 167–177.

Kleinberg, R. L. (1996). Utility of NMR T_2 distributions, connection with capillary pressure, clay effect, and determination of the surface relaxivity parameter $\rho 2$. *Magnetic Resonance Imaging*, *14*(7–8), 761–767.

Kleinberg, R. L. (1999). Nuclear Magnetic Resonance. In P. B. T. Wong (Ed.), *Methods in the physics of porous media* (Chap. 9, Vol. 35, pp. 337–385). Experimental Methods in the Physical Sciences. Academic Press.

Kleinberg, R. L., Straley, C., Kenyon, W. E., Akkurt, R., & Farooqui, S. A. (1993). Nuclear Magnetic Resonance of Rocks: T_1 vs. T_2. In *Spe annual technical conference and exhibition*. Houston, Texas, USA: Society of Petroleum Engineers.

Klinkenberg, L. J. (1941). The Permeability Of Porous Media To Liquids And Gases. *Drilling and Production Practice*.

Kloubek, J. (1981). Hysteresis in porosimetry. *Powder Technology*, *29*(1), 63–73.

Knudsen, M. (1909). Die Gesetze der Molekularstromung und der inneren Reibungsstromung der Gase durch Rohren. *Annalen der Physik*, *333*(1), 75–130.

Korb, J.-P., Nicot, B., Louis-Joseph, A., Bubici, S., & Ferrante, G. (2014). Dynamics and Wettability of Oil and Water in Oil Shales. *The Journal of Physical Chemistry C*, *118*(40), 23212–23218.

Kuila, U. (2013). *Measurement and interpretation of porosity and pore-size distribution in mudrocks: The whole story of shales* (Doctoral dissertation, Colorado School of Mines).

Kwon, O., Kronenberg, A. K., Gangi, A. F., & Johnson, B. (2001). Permeability of Wilcox shale and its effective pressure law. *Journal of Geophysical Research: Solid Earth*, *106*(B9), 19339–19353.

Kwon, O., Kronenberg, A. K., Gangi, A. F., Johnson, B., & Herbert, B. E. (2004). Permeability of illite-bearing shale: 1. Anisotropy and effects of clay content and loading. *Journal of Geophysical Research: Solid Earth*, *109*(10).

Labani, M. M. (2014). *An Investigation into the Interrelationship between Petrophysical Properties of Potential Gas Shale Reservoirs from Western Australia* (Doctoral dissertation, Curtin University).

Labani, M. M., Rezaee, R., Saeedi, A., & Hinai, A. A. (2013). Evaluation of pore size spectrum of gas shale reservoirs using low pressure nitrogen adsorption, gas expansion and mercury porosimetry: A case study from the Perth and Canning Basins, Western Australia. *Journal of Petroleum Science and Engineering*, *112*, 7–16.

Lafargue, E., Marquis, F., & Pillot, D. (1998). Rock-Eval 6 Applications in Hydrocarbon Exploration, Production, and Soil Contamination Studies. *Revue de l'Institut Français du Pétrole*, *53*(4), 421–437.

Landers, J., Gor, G. Y., & Neimark, A. V. (2013). Density functional theory methods for characterization of porous materials. *Colloids and Surfaces A: Physicochemical and Engineering Aspects*, *437*, 3–32.

Lasseux, D. & Valdés-Parada, F. J. (2017). On the developments of Darcy's law to include inertial and slip effects. *Comptes Rendus - Mecanique*. A century of fluid mechanics: 1870–1970, *345*(9), 660–669.

Lawson, C. L. & Hanson, R. J. (1974). 26. Examples of Some Methods of Analyzing a Least Squares Problem. In *Solving least squares problems* (Chap. 26, pp. 199–206).

Lenormand, R. (2003). Interpretation of mercury injection curves to derive pore size distribution. In *International symposium of the society of core analysts*. Pau, France: Society of Core Analysts.

Letham, E. A. & Bustin, R. M. (2016). Klinkenberg gas slippage measurements as a means for shale pore structure characterization. *Geofluids*, *16*(2), 264–278.

Loucks, R. G., Reed, R. M., Ruppel, S. C., & Hammes, U. (2012). Spectrum of pore types and networks in mudrocks and a descriptive classification for matrix-related mudrock pores. *AAPG Bulletin*, *96*(6), 1071–1098.

Lowell, S., Shields, J. E., Thomas, M. A., & Thommes, M. (2004). *Characterization of Porous Solids and Powders: Surface Area, Pore Size*

and Density (B. Scarlett, Ed.). Particle Technology Series. Kluwer Academic Publishers. eprint: 9809069v1 (arXiv:gr-qc)

Lowell, S. & Shields, J. E. (1981). Equivalency of mercury porosimetry and gas adsorption. *Powder Technology*, *29*(2), 225–231.

Luffel, D. L. (1993). *Advances in Shale Core Analysis*. Gas Research Institute.

Luffel, D. & Guidry, F. (1992). New Core Analysis Methods for Measuring Reservoir Rock Properties of Devonian Shale. *Journal of Petroleum Technology*, *44*(11), 1184–1190.

Mathur, A., Sondergeld, C. H., & Rai, C. S. (2016). Comparison of Steady-State and Transient Methods for Measuring Shale Permeability. In *Spe low perm symposium* (p. 22). Denver, Colorado, USA: Society of Petroleum Engineers.

McKee, E. D. & Weir, G. W. (1953). Terminology for Stratification and Cross-stratification in Sedimentary Rock. *GSA Bulletin*, *64*(4), 381–390.

McPhee, C., Reed, J., & Zubizarreta, I. (2015a). Chapter 11 - Nuclear Magnetic Resonance (NMR). In J. R. Colin McPhee & Z. Izaskun (Eds.), *Developments in petroleum science* (Chap. 11, Vol. Volume 64, pp. 655–669). Elsevier.

McPhee, C., Reed, J., & Zubizarreta, I. (2015b). Chapter 5 - Routine Core Analysis. In J. R. Colin McPhee & Z. Izaskun (Eds.), *Core analysis a best practice guide* (1st, Chap. 5, Vol. Volume 64, pp. 181–268). Developments in Petroleum Science. Elsevier.

Meiboom, S. & Gill, D. (1958). Modified Spin-Echo Method for Measuring Nuclear Relaxation Times. *Review of Scientific Instruments*, *29*(8), 688–691.

Miao, J., Huo, D., & Wilson, D. L. (2008). Quantitative image quality evaluation of MR images using perceptual difference models. *Medical Physics*, *35*(6), 2541–2553.

Mitchell, J., Chandrasekera, T. C., & Gladden, L. F. (2012). Numerical estimation of relaxation and diffusion distributions in two dimensions. *Progress in Nuclear Magnetic Resonance Spectroscopy*, *62*, 34–50.

Moghadam, A. A. & Chalaturnyk, R. (2016). Analytical and Experimental Investigations of Gas-Flow Regimes in Shales Considering the Influence of Mean Effective Stress. *SPE Journal*, *21*(02), 557–572.

Moghadam, A. A. & Chalaturnyk, R. (2014). Expansion of the Klinkenberg's slippage equation to low permeability porous media. *International Journal of Coal Geology*, *123*, 2–9.

Moghaddam, R. N. & Jamiolahmady, M. (2016). Fluid transport in shale gas reservoirs: Simultaneous effects of stress and slippage on matrix permeability. *International Journal of Coal Geology*, *163*, 87–99.

Moody, J. B. & Xia, Y. (2004). Analysis of multi-exponential relaxation data with very short components using linear regularization. *Journal of Magnetic Resonance*, *167*(1), 36–41.

Morozov, V. A. (1984). *Methods for solving incorrectly pose problems* (Z. Nashed, Ed.). New York: Springer.

Mory, A. & Iasky, R. (1994). Structural Evolution of the Onshore Northern Perth Basin, Western Australia. In *The sedimentary basins of western australia: Proceedings of petroleum exploration society of australia symposium, perth, 1994* (pp. 781–789). Perth, Australia.

Mory, A. J. & Iasky, R. P. (1996). *Stratigraphy and structure of the onshore northern Perth Basin, Western Australia*. Western Australia: Western Australia Geological Survey.

Nelson, P. H. (2009). Pore-throat sizes in sandstones, tight sandstones, and shales. *American Association of Petroleum Geologists Bulletin*, *93*(3), 329–340.

Neuendorf, K. K. E., Mehl Jr., J. P., & Jackson, J. A. (2011). Glossary of Geology (5th Edition). American Geosciences Institute.

O'Brien, N. R. & Slatt, R. M. (2012). *Argillaceous Rock Atlas*. Springer New York.

Pearce, C. E. M., Abbott, D., McDonnell, M. D., & Stocks, N. G. (2008). Stochastic resonance: its definition, history, and debates. In *Stochastic resonance: From suprathreshold stochastic resonance to stochastic signal quantization* (pp. 6–46). Cambridge University Press.

Peng, D. Y. & Robinson, D. B. (1976). A New Two-Constant Equation of State. *Industrial and Engineering Chemistry Fundamentals*, *15*(1), 59–64.

Pettijohn, F. J. (1975). *Sedimentary rocks*. Harper International Edition. Harper & Row Limited.

Pittman, E. D. (1992). Relationship of Porosity and Permeability to various Parameters Derived from Mercury Injection Capillary Pressure curves for Sandstones. *AAPG Bulletin*, *76:2*(2), 191–198.

Polyanin, A. D. & Manzhirov, A. V. (2008). *Handbook of Integral Equations: Second Edition* (2nd ed.). Handbooks of Mathematical Equations. CRC Press.

Prammer, M. G., Drack, E. D., Bouton, J. C., & Gardner, J. S. (1996). Measurements of Clay-Bound Water and Total Porosity by Magnetic Resonance Logging. *Log Analyst*, *37*(6), 61–69.

Prammer, M. (1994). *NMR Pore Size Distributions and Permeability at the Well Site*. New Orleans, Louisiana, USA: Society of Petroleum Engineers.

Prost, R., Benchara, A., & Huard, E. (1998). State and location of water adsorbed on clay minerals: consequences of the hydration and swelling-shrinkage phenomena. *Clays and Clay Minerals*, *46*(2), 117–131.

Pytte, A. M. & Reynolds, R. C. (1989). The Thermal Transformation of Smectite to Illite. In N. D. Naeser & T. H. McCulloh (Eds.), *Thermal history of sedimentary basins* (pp. 133–140). New York, NY: Springer New York.

Randolph, P., Soeder, D., & Chowdiah, P. (1984). Porosity and Permeability of Tight Sands. In *Spe unconventional gas recovery symposium* (pp. 57–66). Pittsburgh, Pennsylvania, USA: Society of Petroleum Engineers.

Rassouli, F., Ross, C., Zoback, M., & Andrew, M. G. (2017). Shale Rock characterization using multi-scale imaging. In *51st us rock mechanics/geomechanics symposium*. San Francisco, California, USA: American Rock Mechanics Association.

Rezaee, R., Saeedi, A., & Clennell, B. (2012). Tight gas sands permeability estimation from mercury injection capillary pressure and nuclear magnetic resonance data. *Journal of Petroleum Science and Engineering*, *88–89*, 92–99.

Romero-Sarmiento, M. F., Ramiro-Ramirez, S., Berthe, G., Fleury, M., & Littke, R. (2017). Geochemical and petrophysical source rock characterization of the Vaca Muerta Formation, Argentina: Implications for unconventional

petroleum resource estimations. *International Journal of Coal Geology*, *184*, 27–41.

Rootare, H. M. & Prenzlow, C. F. (1967). Surface areas from mercury porosimeter measurements. *The Journal of Physical Chemistry*, *71*(8), 2733–2736.

Ross, D. J. K. & Bustin, R. M. (2009). The importance of shale composition and pore structure upon gas storage potential of shale gas reservoirs. *Marine and Petroleum Geology*, *26*(6), 916–927.

Rouquerol, J., Avnir, D., Fairbridge, C. . W., Everett, D. . H., Haynes, J. M., Pernicone, N., ... Unger, K. . K. (1994). *Recommendations for the characterization of porous solids*. IUPAC.

Rouquerol, J., Llewellyn, P., & Rouquerol, F. (2007). Is the bet equation applicable to microporous adsorbents? *Studies in Surface Science and Catalysis*, (160), 49–56.

Rutledge, D. N. (1996). *Signal Treatment and Signal Analysis in NMR* (1st ed.). Elsevier Science.

Rylander, E., Singer, P. M., Jiang, T., Lewis, R., McLin, R., & Sinclair, S. (2013). NMR T_2 distributions in the Eagle Ford shale: Reflections on pore size. In *Spe usa unconventional resources conference 2013* (2010, pp. 426–440). The Woodlands, Texas, USA: Society of Petroleum Engineers.

Saarenketo, T. (1998). Electrical properties of water in clay and silty soils. *Journal of Applied Geophysics*, *40*(1), 73–88.

Saidian, M. (2015). *Effect of Rock Composition and Texture on Pore Size Distribution in Shales: application in low field Nuclear Magnetic Resonance* (Doctoral dissertation, Colorado School of Mines).

Salimifard, B., Dick, M., Green, D., & Ruth, D. W. (2017). Optimizing NMR Data Acquisition and Data Processing Parameters for Tight-Gas Montney Formation of Western Canada. In *International symposium of the society of core analysts*. Vienna, Austria: Society of Core Analysts.

Schieber, J. & Zimmerle, W. (1998). *The history and promise of shale research* (P. Sethi, J. Schieber, & W. Zimmerle, Eds.). Stuttgart, Germany: Schweizerbart Science Publishers.

Schowalter, T. T. (1979). Mechanics of Secondary Hydrocarbon Migration and Entrapment. *AAPG Bulletin*, *63*(5), 723.

Shen, Y., Pang, Y., Shen, Z., Tian, Y., & Ge, H. (2018). Multiparameter Analysis of Gas Transport Phenomena in Shale Gas Reservoirs: Apparent Permeability Characterization. *Scientific Reports*, *8*(1), 2601.

Sigal, R. F. (2009). A methodology for blank and conformance corrections for high pressure mercury porosimetry. *Measurement Science and Technology*, *20*(4), 45108.

Sing, K. S. W., Everett, D. H., Haul, R. A. W., Moscou, L., Pierotti, R. A., Rouquerol, J., & Siemieniewska, T. (1985). Reporting Physisorption Data for Gas/Solid Systems with Special Reference to the Determination of Surface Area and Porosity. *Pure and Applied Chemistry*, *57*(4), 603–619.

Sing, K. S. W. & Williams, R. T. (2004). Physisorption Hysteresis Loops and the Characterization of Nanoporous Materials. *Adsorption Science & Technology*, *22*(10), 773–782.

Singer, A. & Müller, G. (1983). Chapter 3 Diagenesis in Agrillaceous Sediments. In G. Larsen & G. V. Chilingar (Eds.), *Diagenesis in sediments and*

sedimentary rocks (Vol. 2, pp. 115–212). Developments in Sedimentology. Elsevier.

Singer, P. M., Chen, Z., & Hirasaki, G. J. (2016). Fluid Typing and Pore Size in Organic Shale Using 2D NMR in Saturated Kerogen Isolates. *Petrophysics*, *57*(3), 604–619.

Singh, H., Javadpour, F., Ettehadtavakkol, A., & Darabi, H. (2014). Nonempirical Apparent Permeability of Shale. *SPE Reservoir Evaluation & Engineering*, *17*(3), 414–424.

Sinha, S., Braun, E. M., Determan, M. D., Passey, Q. R., Leonardi, S. A., Boros, J. A., ... Kudva, R. A. (2013). Steady-State Permeability Measurements on Intact Shale Samples at Reservoir Conditions - Effect of Stress, Temperature, Pressure, and Type of Gas. In *Spe middle east oil and gas show and conference*. Manama, Bahrain: Society of Petroleum Engineers.

Slatt, R. M. (2013). Unconventional Resource Shales. In R. M. Slatt (Ed.), *Stratigraphic reservoir characterization for petroleum geologists, geophysicists, and engineers* (2nd ed., Chap. 12, Vol. 61, pp. 553–620). Elsevier B.V.

Sondergeld, C. H., Newsham, K. E., Comisky, J. T., Rice, M. C., & Rai, C. S. (2010). Petrophysical Considerations in Evaluating and Producing Shale Gas Resources. In *Spe unconventional gas conference*. Pittsburgh, Pennsylvania, USA: Society of Petroleum Engineers.

Song, Y.-Q. (2000). Determining Pore Sizes Using an Internal Magnetic Field. *Journal of Magnetic Resonance*, *143*(2), 397–401.

Song, Y. (2003). Using internal magnetic fields to obtain pore size distributions of porous media. *Concepts in Magnetic Resonance Part A*, *18A*(2), 97–110.

Song, Y.-Q., Venkataramanan, L., & Burcaw, L. (2005). Determining the resolution of Laplace inversion spectrum. *The Journal of Chemical Physics*, *122*(10), 104104.

Song, T. & Cawood, P. A. (2000). Structural styles in the Perth Basin associated with the Mesozoic break-up of Greater India and Australia. *Tectonophysics*, *317*(1), 55–72.

Song, Y.-Q., Venkataramanan, L., Hürlimann, M. D., Flaum, M., Frulla, P., & Straley, C. (2002). T_1—T_2 Correlation Spectra Obtained Using a Fast Two-Dimensional Laplace Inversion. *Journal of Magnetic Resonance*, *154*(2), 261–268.

Srodon, J. & Eberl, D. (1984). Illite. *Reviews in Mineralogy and Geochemistry*, *13*(1), 495.

Stokes, W. L. & Varnes, D. J. (1955). *Glossary of selected geologic terms with special reference to their use in engineering*. Denver: Colorado Scientific Society.

Straley, C., Morriss, C. F., & Kenyon, W. E. (1991). NMR In Partially Saturated Rocks: Laboratory Insights On Free Fluid Index And Comparison With Borehole Logs. In *Spwla 32nd annual logging symposium*. Midland, Texas, USA: Society of Petrophysicists and Well-Log Analysts.

Straley, C., Morriss, C., & Kenyon, W. E. (1995). NMR in partially saturated rocks: laboratory insights on free fluid index and comparison with borehole

logs. In *Log analyst* (Vol. 36, *1*, pp. 40–56). Society of Petrophysicists and Well-Log Analysts.

Sun, B. (2007). In situ fluid typing and quantification with 1D and 2D NMR logging. *Magnetic Resonance Imaging*, *25*(4), 521–524.

Sun, B. & Dunn, K.-J. (2004). Methods and limitations of NMR data inversion for fluid typing. *Journal of Magnetic Resonance*, *169*(1), 118–128.

Swanson, B. (1981). A Simple Correlation Between Permeabilities and Mercury Capillary Pressures. *Journal of Petroleum Technology*, *33*(12), 2498–2504.

Tang, G. H., Tao, W. Q., & He, Y. L. (2005). Gas slippage effect on microscale porous flow using the lattice Boltzmann method. *Physical Review E - Statistical, Nonlinear, and Soft Matter Physics*, *72*(5), 56301.

Tarazona, P. (1985). Free-energy density functional for hard spheres. *Physical Review A*, *31*(4), 2672–2679.

Tarazona, P., Marconi, U. M. B., & Evans, R. (1987). Phase equilibria of fluid interfaces and confined fluids. *Molecular Physics*, *60*(3), 573–595.

Testamanti, M. N. & Rezaee, R. (2019). Considerations for the acquisition and inversion of NMR T2 data in shales. *Journal of Petroleum Science and Engineering*, *174*, 177–188.

Testamanti, M. N., Rezaee, R., & Wong, C. (2017a). Gas Permeability Measurement of Shales Using the Quasi Steady-State Technique. *The APPEA Journal*, *57*, 656–659.

Testamanti, M. N., Rezaee, R., Yuan, Y., & Pan, D. (2017b). Determination of T_2 cut-off for Shale Reservoirs: A Case Study from the Carynginia Formation, Perth Basin, Western Australia. *The APPEA Journal*.

Testamanti, M. N., Rezaee, R., & Zou, J. (2017c). Porosity and Pore Size Distribution of Shales: A Case Study of the Carynginia Formation, Perth Basin, Western Australia. *The APPEA Journal*, *57*, 660–663.

Testamanti, M. N. & Rezaee, R. (2017). Determination of NMR T_2 cut-off for Clay Bound Water in Shales: A Case Study of Carynginia Formation, Perth Basin, Western Australia. *Journal of Petroleum Science and Engineering*, *149*, 497–503.

Thommes, M., Kaneko, K., Neimark, A. V., Olivier, J. P., Rodriguez-Reinoso, F., Rouquerol, J., & Sing, K. S. (2015). Physisorption of gases, with special reference to the evaluation of surface area and pore size distribution. *International Union of Pure & Applied Chemistry*, *87*(9-10), 1051–1069.

Tikhonov, A. (1963). Solution of Incorrectly Formulated Problems and the Regularization Method. *Soviet Math. Dokl. 5*, 1035–1038.

Timur, A. (1969). Producible Porosity And Permeability Of Sandstone Investigated Through Nuclear Magnetic Resonance Principles. *SPWLA*, *10*(1), 23–26.

Tinni, A., Fathi, E., Agarwal, R., Sondergeld, C. H., Akkutlu, I. Y., & Rai, C. S. (2012). Shale Permeability Measurements on Plugs and Crushed Samples. In *Spe canadian unconventional resources conference* (p. 14). Calgary, Alberta, Canada: Society of Petroleum Engineers.

Tinni, A., Sondergeld, C., & Rai, C. (2014). NMR T_1–T_2 response of moveable and non-moveable fluids in conventional and unconventional rocks. In

International symposium of the society of core analysts, avignon, france (pp. 8–11).

Tinni, A., Sondergeld, C., & Rai, C. (2018). New Perspectives on the Effects of Gas Adsorption on Storage and Production of Natural Gas From Shale Formations. *Petrophysics*, *59*(1), 99–104.

Towner, R. & Gibons, D. (1983). *Geology of the onshore Canning Basin, Western Australia*. Bureau oj Mineral Resources, Geology and Geophysics. Canberra, Australia.

Truman, R. B., Howard, W. E., & Luffel, D. L. (1989). *Shale Porosity - Its Impact On Well Log Modeling And Interpretation*. Denver, Colorado, USA: Society of Petrophysicists and Well-Log Analysts.

Twenhofel, W. H. (1939). Environments of origin of black shales. *AAPG Bulletin*, *23*(8), 1178–1198.

Twomey, S. (1963). On the Numerical Solution of Fredholm Integral Equations of the First Kind by the Inversion of the Linear System Produced by Quadrature. *Journal of the ACM*, *10*(1), 97–101.

U.S. Energy Information Administration. (2015). *Technically Recoverable Shale Oil and Shale Gas Resources: Australia*. U.S. Energy Information Administration ({EIA}).

Udden, J. A. (1898). *Mechanical composition of wind deposits*. Augustana Library publications. Lutheran Augustana Printers.

Valkó, P. P. & Lee, W. J. (2010). A Better Way To Forecast Production From Unconventional Gas Wells. In *The spe annual technical conference and exhibition*. Florence, Italy: Society of Petroleum Engineers.

Venkataramanan, L., Gruber, F. K., Habashy, T. M., Akkurt, R., Vissapragada, B., Lewis, R. E., & Rylander, E. (2013). Methods of investigating formation samples using NMR data.

Venkataramanan, L., Song, Y. Q., & Hürlimann, M. D. (2002). Solving Fredholm integrals of the first kind with tensor product structure in 2 and 2.5 dimensions. *IEEE Transactions on Signal Processing*, *50*(5), 1017–1026.

Wang, F. P. & Reed, R. M. (2009). Pore Networks and Fluid Flow in Gas Shales. In *Spe annual technical conference and exhibition*. New Orleans, Louisiana, USA: Society of Petroleum Engineers.

Wang, S., Javadpour, F., & Feng, Q. (2016). Confinement Correction to Mercury Intrusion Capillary Pressure of Shale Nanopores. *Scientific reports*, *6*, 20160.

Wang, Y., Zhu, Y., Chen, S., & Li, W. (2014). Characteristics of the nanoscale pore structure in northwestern hunan shale gas reservoirs using field emission scanning electron microscopy, high-pressure mercury intrusion, and gas adsorption. *Energy and Fuels*, *28*(2), 945–955.

Wang, Z., Bovik, A. C., Sheikh, H. R., & Simoncelli, E. P. (2004). Image quality assessment: from error visibility to structural similarity. *IEEE Transactions on Image Processing*, *13*(4), 600–612.

Washburn, E. W. (1921). Note on a method of determining the distribution of pore sizes in a porous material. *The Proceedings of the National Academy of Sciences*, *7*(4), 115–116.

Washburn, K. E. (2014). Relaxation mechanisms and shales. *Concepts in Magnetic Resonance Part A*, *43A*(3), 57–78.

Washburn, K., Anderssen, E., Vogt, S., Seymour, J. D., Birdwell, J. E., Kirkland, C. M., & Codd, S. L. (2015). Simultaneous Gaussian and exponential inversion for improved analysis of shales by NMR relaxometry. *Journal of Magnetic Resonance*, *250*, 7–16.

Washburn, K. E. & Birdwell, J. E. (2013). Updated methodology for nuclear magnetic resonance characterization of shales. *Journal of Magnetic Resonance*, *233*, 17–28.

Watson, A. T. & Chang, C. T. P. (1997). Characterizing porous media with NMR methods. *Progress in Nuclear Magnetic Resonance Spectroscopy*, *31*(4), 343–386.

Weaver, C. E. (1991). *Clays, muds, and shales*. Developments in Sedimentology. Elsevier Science.

Webb, P. (2001). An Introduction To The Physical Characterization of Materials by Mercury Intrusion Porosimetry with Emphasis On Reduction And Presentation of Experimental Data. *Micrometrics Instrument Corp.* 23.

Wei, M., Zhang, L., Xiong, Y., Li, J., & Peng, P. (2016). Nanopore structure characterization for organic-rich shale using the non-local-density functional theory by a combination of N2and CO2adsorption. *Microporous and Mesoporous Materials*, *227*, 88–94.

Wentworth, C. K. (1922). A Scale of Grade and Class Terms for Clastic Sediments. *The Journal of Geology*, *30*(5), 377–392.

Western Australia Department of Mines and Petroleum. (2014). *Western Australia's Petroleum and Geothermal Explorer's Guide - 2014 Edition*. Petroleum Division and Geological Survey of Western Australia.

Whittall, K. P. (1994). Analysis of Large One-Dimensional and Two-Dimensional Relaxation Data Sets. *Journal of Magnetic Resonance, Series A*, *110*(2), 214–218.

Whittall, K. P. (1996). Analysis of NMR Relaxation Data. In D. N. Rutledge (Ed.), *Signal treatment and signal analysis in nmr* (Chap. 3, Vol. Data Handl, pp. 44–67). Elsevier.

World Energy Council. (2016). *World Energy Resources: Unconventional gas, a global phenomenon*.

Yeates, A. N., Gibson, D. L., Towner, R. R., & Crowe, R. W. A. (1984). Regional Geology of the Onshore Canning Basin, W.A. In P. Purcell (Ed.), *The canning basin w.a.: Proceedings of geological society of australia / petroleum exploration society of australia symposium, perth, 1984* (Chap. Basin Geol, pp. 23–55). Perth, Australia: Geological Society of Australia.

Yuan, Y., Rezaee, R., Verrall, M., Hu, S. Y., Zou, J., & Testamanti, N. (2018). Pore Characterization and Clay Bound Water Assessment in Shale with a Combination of NMR and Low-Pressure Nitrogen Gas Adsorption. *International Journal of Coal Geology*, *194*, 11–21.

Zamirian, M., Aminian, K. K., Ameri, S., & Fathi, E. (2014). New Steady-State Technique for Measuring Shale Core Plug Permeability. In *SPE/CSUR unconventional resources conference – canada* (p. 11). Calgary, Alberta, Canada: Society of Petroleum Engineers.

Zhang, L., Xiong, Y., Li, Y., Wei, M., Jiang, W., Lei, R., & Wu, Z. (2017). DFT modeling of CO2 and Ar low-pressure adsorption for accurate nanopore structure characterization in organic-rich shales. *Fuel*, *204*, 1–11.

Zhang, P., Hu, L., Meegoda, J. N., & Gao, S. (2015). Micro/Nano-pore Network Analysis of Gas Flow in Shale Matrix. *Scientific Reports*, *5*, 13501.

APPENDIX A

Measured Matrix Permeability Data

Table A.1.
Apparent permeability to air for sample SG-1.

Sample SG-1		
Confining Pressure (psi)	Pore Pressure (psi)	Measured Permeability (nD)
500	29.3	4.3 ± 0.30
500	30.8	4.0 ± 0.20
500	32.1	3.7 ± 0.30
500	33.6	3.6 ± 0.30
500	35.2	3.6 ± 0.25
500	36.6	3.5 ± 0.15
500	38.1	3.4 ± 0.10
1000	28.5	1.7 ± 0.20
1000	30.1	1.4 ± 0.25
1000	32.5	1.3 ± 0.20
1000	34.5	1.3 ± 0.10
1000	36.5	1.2 ± 0.10
1000	38.8	1.1 ± 0.05
1500	30.7	0.9 ± 0.05
1500	32.1	0.8 ± 0.02
1500	33.5	0.7 ± 0.10
1500	35.0	0.7 ± 0.02
1500	39.0	0.6 ± 0.05
2000	28.8	0.6 ± 0.05
2000	32.0	0.5 ± 0.05
2000	34.1	0.5 ± 0.02
2000	36.5	0.5 ± 0.03
2000	38.8	0.5 ± 0.02

Table A.2.
Apparent permeability to air for sample SG-2.

Sample SG-2		
Confining Pressure (psi)	Pore Pressure (psi)	Measured Permeability (nD)
250	26.0	112.0 ± 6.75
250	27.9	102.0 ± 7.50
250	30.0	94.0 ± 7.00
250	31.8	91.5 ± 6.50
250	33.9	88.5 ± 6.50
250	36.3	86.0 ± 5.50
500	25.9	36.5 ± 4.00
500	27.8	28.5 ± 3.50
500	29.8	26.0 ± 2.50
500	32.0	24.0 ± 2.50
500	33.9	22.5 ± 2.50
500	36.3	21.0 ± 3.00
1000	25.9	10.5 ± 1.50
1000	27.8	9.0 ± 1.00
1000	29.9	8.1 ± 0.90
1000	31.6	7.8 ± 0.75
1000	33.8	7.0 ± 0.50
1000	36.3	6.9 ± 0.50
1500	27.9	5.0 ± 0.50
1500	29.9	4.6 ± 0.50
1500	31.9	4.0 ± 0.30
1500	33.7	3.9 ± 0.40
1500	36.1	3.6 ± 0.35

Table A.3.
Apparent permeability to air for sample SG-3.

Sample SG-3		
Confining Pressure (psi)	Pore Pressure (psi)	Measured Permeability (nD)
250	26.3	64.2 ± 5.00
250	28.2	62.0 ± 4.50
250	30.3	57.0 ± 4.50
250	32.1	55.5 ± 4.75
250	34.2	54.0 ± 4.00
250	36.7	52.5 ± 5.00
500	26.2	25.5 ± 3.00
500	28.1	21.5 ± 2.50
500	30.1	19.5 ± 2.00
500	32.3	19.0 ± 1.75
500	34.2	18.0 ± 2.00
500	36.6	17.2 ± 1.75
1000	26.2	8.8 ± 1.50
1000	28.0	8.2 ± 0.75
1000	30.2	7.6 ± 0.40
1000	31.8	7.1 ± 0.40
1000	34.1	6.5 ± 0.40
1000	36.6	6.4 ± 0.50
1500	28.2	4.8 ± 0.50
1500	30.2	4.3 ± 0.50
1500	32.2	4.0 ± 0.50
1500	33.9	3.7 ± 0.30
1500	36.4	3.6 ± 0.40

Table A.4.
Apparent permeability to air for sample SG-4.

Sample SG-4		
Confining Pressure (psi)	Pore Pressure (psi)	Measured Permeability (nD)
500	29.1	4.3 ± 0.20
500	30.5	4.1 ± 0.25
500	31.9	4.0 ± 0.25
500	34.9	3.7 ± 0.20
500	36.4	3.6 ± 0.25
1000	28.3	2.8 ± 0.50
1000	29.9	2.3 ± 0.40
1000	32.3	2.1 ± 0.30
1000	34.3	1.9 ± 0.25
1000	36.3	1.7 ± 0.20
1000	38.8	1.6 ± 0.20
1500	30.5	1.5 ± 0.20
1500	31.8	1.4 ± 0.25
1500	33.4	1.3 ± 0.25
1500	34.8	1.1 ± 0.20
1500	36.8	1.1 ± 0.15
1500	38.8	1.0 ± 0.15
2000	29.7	0.9 ± 0.15
2000	31.8	0.8 ± 0.10
2000	34.0	0.7 ± 0.10
2000	36.3	0.6 ± 0.10
2000	38.6	0.6 ± 0.10

Table A.5.
Apparent permeability to air for sample SG-5.

Sample SG-5		
Confining Pressure (psi)	Pore Pressure (psi)	Measured Permeability (nD)
250	26.0	172.5 ± 22.50
250	28.0	156.0 ± 20.00
250	29.9	150.0 ± 17.50
250	32.0	145.0 ± 17.50
500	26.0	80.0 ± 5.25
500	28.0	71.5 ± 6.00
500	30.0	66.5 ± 8.00
500	32.0	61.0 ± 3.00
500	33.9	59.5 ± 2.00
1000	25.8	28.0 ± 3.00
1000	28.0	26.0 ± 2.00
1000	29.8	24.0 ± 3.50
1000	32.0	21.5 ± 2.75
1000	33.9	20.6 ± 2.00
1000	36.5	19.4 ± 1.25
1500	26.1	16.5 ± 1.25
1500	28.0	14.0 ± 1.00
1500	29.9	13.5 ± 1.00
1500	32.0	12.0 ± 1.50
1500	34.1	11.1 ± 1.50
1500	36.4	11.0 ± 1.50
2000	26.0	10.5 ± 1.50
2000	27.7	9.5 ± 1.10
2000	30.0	8.8 ± 1.00
2000	31.7	8.4 ± 0.75
2000	33.9	7.8 ± 0.50
2000	36.3	7.4 ± 0.50

Table A.6.
Apparent permeability to air for sample SG-6.

Sample SG-6		
Confining Pressure (psi)	Pore Pressure (psi)	Measured Permeability (nD)
250	26.0	35.0 ± 2.25
250	28.2	32.6 ± 3.50
250	30.6	30.0 ± 2.75
250	32.8	28.6 ± 1.00
500	26.3	9.9 ± 1.50
500	28.2	8.7 ± 1.25
500	30.3	8.1 ± 1.00
500	32.3	7.5 ± 0.50
500	34.2	7.3 ± 0.50
1000	26.1	4.0 ± 0.30
1000	28.2	3.9 ± 0.30
1000	30.1	3.4 ± 0.30
1000	32.3	3.1 ± 0.30
1000	31.1	2.8 ± 0.25
1000	36.8	2.7 ± 0.25
1500	26.4	2.8 ± 0.30
1500	28.3	2.6 ± 0.30
1500	30.2	2.4 ± 0.25
1500	32.3	2.3 ± 0.25
1500	34.4	2.1 ± 0.25
1500	36.7	2.1 ± 0.25
2000	26.3	1.9 ± 0.30
2000	28.0	1.8 ± 0.25
2000	30.3	1.8 ± 0.25
2000	32.0	1.7 ± 0.20
2000	34.1	1.6 ± 0.20
2000	36.6	1.6 ± 0.20

APPENDIX B

Attributions

Testamanti, M. N. and Rezaee, R. (2017) **Determination of NMR T_2 cut-off for clay bound water in shales: A case study of Carynginia Formation, Perth Basin, Western Australia**. *Journal of Petroleum Science and Engineering*, *149*, 497–503.

Authors and attributions:

	Conception & Design	Method & Data Acquisition	Data Conditioning & Manipulation	Data Analysis	Interpretation & Discussion	Final Approval
M. N. Testamanti	X	X	X	X	X	X
I acknowledge that these represent my contribution to the above research output. Signed.						
Prof. R. Rezaee	X					X
I acknowledge that these represent my contribution to the above research output. Signed.						

Attributions (cont.)

Testamanti, M. N. and Rezaee, R. (2019) **Considerations for the Application of the NMR Technique in Shales**. *Journal of Petroleum Science and Engineering*, *174*, 177–188.

Authors and attributions:

	Conception & Design	Method & Data Acquisition	Data Conditioning & Manipulation	Data Analysis	Interpretation & Discussion	Final Approval
M. N. Testamanti	X	X	X	X	X	X
I acknowledge that these represent my contribution to the above research output. Signed.						
Prof. R. Rezaee						X
I acknowledge that these represent my contribution to the above research output. Signed.						

Attributions (cont.)

Testamanti, M. N. and Rezaee, R. and Yuan, Y. and Pan, D. (2017) **Determination of T_2 cut-off for Shale Reservoirs: A Case Study from the Carynginia Formation, Perth Basin, Western Australia**. Extended abstract, *The APPEA Journal*, *57*, 664–668. Poster presentation at the APPEA Annual Conference and Exhibition, May 14–17, 2017, Perth, Western Australia.

Authors and attributions:

	Conception, Design & Method	Data Acquisition	Data Conditioning & Manipulation	Data Analysis	Interpretation & Discussion	Final Approval
M. N. Testamanti	X	X	X	X	X	X
I acknowledge that these represent my contribution to the above research output.						
Signed.						
Prof. R. Rezaee						X
I acknowledge that these represent my contribution to the above research output.						
Signed.						
Y. Yuan		X				X
I acknowledge that these represent my contribution to the above research output.						
Signed.						
D. Pan		X				X
I acknowledge that these represent my contribution to the above research output.						
Signed.						

Attributions (cont.)

Testamanti, M. N. and Rezaee, R. and Wong, C. (2017) **Gas Permeability Measurement of Shales Using the Quasi Steady-State Technique**. Extended abstract, *The APPEA Journal*, *57*, 656–659. Presented at the APPEA Annual Conference and Exhibition, May 14–17, 2017, Perth, Western Australia.

Authors and attributions:

	Conception, Design & Method	Data Acquisition	Data Conditioning & Manipulation	Data Analysis	Interpretation & Discussion	Final Approval
M. N. Testamanti	X	X	X	X	X	X
I acknowledge that these represent my contribution to the above research output.						
Signed.						
Prof. R. Rezaee						X
I acknowledge that these represent my contribution to the above research output.						
Signed.						
C. Wong						X
I acknowledge that these represent my contribution to the above research output.						
Signed.						

Attributions (cont.)

Testamanti, M. N. and Rezaee, R. and Zou, J. (2017) **Porosity and Pore Size Distribution of Shales: A Case Study of the Carynginia Formation, Perth Basin, Western Australia**. Extended abstract, *The APPEA Journal*, *57*, 660–663. Presented at the APPEA Annual Conference and Exhibition, May 14–17, 2017, Perth, Western Australia.

Authors and attributions:

	Conception, Design & Method	Data Acquisition	Data Conditioning & Manipulation	Data Analysis	Interpretation & Discussion	Final Approval
M. N. Testamanti	X	X	X	X	X	X
I acknowledge that these represent my contribution to the above research output.						
Signed.						
Prof. R. Rezaee						X
I acknowledge that these represent my contribution to the above research output.						
Signed.						
J. Zou		X				X
I acknowledge that these represent my contribution to the above research output.						
Signed.						

Attributions (cont.)

Testamanti, M. N. and Rezaee, R. and Saeedi, A. (2016) **NMR T_2 cut-off Determination for Shales**. Poster presentation at *AAPG/SEG Annual International Conference and Exhibition*, 354–354, April 3–6, 2016, Barcelona, Spain.

Authors and attributions:

	Conception, Design & Method	Data Acquisition	Data Conditioning & Manipulation	Data Analysis	Interpretation & Discussion	Final Approval
M. N. Testamanti	X	X	X	X	X	X
I acknowledge that these represent my contribution to the above research output. Signed.						
Prof. R. Rezaee						X
I acknowledge that these represent my contribution to the above research output. Signed.						
A. Saeedi						X
I acknowledge that these represent my contribution to the above research output. Signed.						